

**A combined experimental and computational study of anthraquinone
dyes as guests in nematic liquid crystal hosts**

Mark Timothy Sims

PhD

University of York

Chemistry

September 2015

Abstract

A 1,5-diphenylthio-substituted anthraquinone, two 1,5-diphenylamino-substituted anthraquinones, and two 2,6-diphenyl-substituted anthraquinones have been studied in the context of the dyes as guests in nematic liquid crystal hosts, using a range of experimental and computational techniques.

UV-visible absorption spectroscopy showed that the dyes exhibit visible transitions at a range of wavelengths, and polarised UV-visible absorption spectroscopy of aligned samples of the dyes in the nematic host E7 yielded a range of dichroic order parameters. Redox potentials of the dyes obtained by cyclic voltammetry and spectroelectrochemistry showed significantly more variation between the oxidation potentials than the reduction potentials, and a correlation between colour and redox properties was shown. Visible electronic transitions were calculated by time dependent density functional theory, and order parameter contributions determined from angles between the calculated transition dipole moment orientations and the minimum moment of inertia axes matched the trend in experimental dichroic order parameters.

Molecular dynamics simulations of the dyes in E7 showed little variation in calculated orientational order parameters of the minimum moment of inertia axes of the dyes. The trend in experimental dichroic order parameters was replicated by calculated values, determined by combining the calculated orientational order parameters with the contributions from the transition dipole moment orientations. An assessment of various molecular alignment axes of the dyes indicated that the surface tensor model provided the most aligned axes of those tested, and improved the match with experimental dichroic order parameters. Incorporating dye flexibility into the calculations resulted in a further improvement in the match with experiment.

Isolated molecule simulations combined with a mean field approach enabled the calculation of order parameters at a reduced computational expense. Application of this approach to a variety of dyes from different classes demonstrated a generally good match with reported experimental alignment trends.

Contents

Abstract	3
Contents	5
List of Figures	13
List of Tables	26
Acknowledgements.....	35
Author's declaration	37
Chapter 1 Introduction.....	39
1.1 Liquid crystals	39
1.1.1 Background	39
1.1.2 Phases	40
1.1.3 Properties.....	43
1.1.4 Uses	43
1.2 Guest-Host Systems	45
1.2.1 Concept.....	45
1.2.2 Display applications	46
1.2.3 Other applications.....	49
1.2.4 Requirements	49
1.2.5 Order parameter.....	50
1.3 Choice of host.....	59
1.4 Choice of guest	60
1.4.1 Azo dyes	60
1.4.2 Anthraquinone dyes.....	62
1.4.3 Other dyes.....	69
1.5 Techniques.....	71

1.5.1	Electronic spectroscopy.....	71
1.5.2	Vibrational spectroscopy.....	73
1.5.3	Nuclear magnetic resonance spectroscopy.....	74
1.5.4	Electrochemistry.....	75
1.5.5	Electronic structure calculations.....	77
1.5.6	Molecular dynamics simulations.....	81
1.5.7	Ab-initio molecular dynamics simulations.....	85
1.6	Aims.....	88
Chapter 2 Experimental.....		91
2.1	Materials.....	91
2.2	Sample preparation.....	91
2.3	Experimental techniques.....	91
2.3.1	UV-visible absorption spectroscopy.....	91
2.3.2	Vibrational spectroscopy.....	92
2.3.2.1	IR spectroscopy.....	92
2.3.2.2	Raman spectroscopy.....	92
2.3.3	NMR spectroscopy.....	93
2.3.4	Dielectric permittivity.....	93
2.3.5	Electrochemistry.....	93
2.3.5.1	Cyclic voltammetry.....	93
2.3.5.2	Spectroelectrochemistry.....	94
2.4	Computational methods.....	94
2.4.1	Electronic structure calculations.....	94
2.4.2	MD simulations.....	95
2.4.3	Ab initio MD simulations.....	96
2.5	Molecular surfaces.....	96
2.6	Data analysis and processing.....	96

Chapter 3 Spectroscopy, structure and stability of dyes in isotropic systems..... 99

3.1	Introduction	99
3.1.1	Spectroscopy of anthraquinone dyes	99
3.1.1.1	UV-vis absorption spectroscopy	99
3.1.1.2	Vibrational spectroscopy	102
3.1.1.3	NMR spectroscopy	102
3.1.2	Structure of anthraquinone dyes	103
3.1.2.1	Characterisation of molecular structure	103
3.1.2.2	Molecular shape in the context of guest-host systems.....	103
3.1.3	Reactivity of anthraquinones	104
3.1.3.1	Electrochemical reactivity	104
3.1.3.2	Photochemical reactivity.....	106
3.1.4	Aims	109
3.2	Results and discussion	110
3.2.1	Spectroscopy	110
3.2.1.1	UV-vis absorption spectroscopy	110
3.2.1.2	Vibrational spectroscopy	113
3.2.1.3	NMR spectroscopy	113
3.2.2	Electronic structure calculations	114
3.2.2.1	DFT calculations and structural comparisons.....	114
3.2.2.2	TD-DFT calculations	120
3.2.3	Electrochemistry	128
3.2.3.1	Cyclic voltammetry.....	128
3.2.3.2	Spectroelectrochemistry.....	130
3.2.3.3	Calculations	133
3.2.3.4	Summary of experimental and calculated first redox potentials.....	137
3.2.4	Dye design considerations for guest-host applications	137

3.3	Conclusions	140
Chapter 4 Studies of liquid crystals and aligned guest-host systems		141
4.1	Introduction	141
4.1.1	Experimental order parameters	141
4.1.1.1	Polarised UV-vis absorption spectroscopy	141
4.1.1.2	Dielectric anisotropy.....	143
4.1.2	Molecular dynamics studies of liquid crystals	144
4.1.2.1	Coarse-grained simulations	144
4.1.2.2	United Atom Simulations	145
4.1.2.3	Fully Atomistic Simulations	146
4.1.3	Molecular dynamics studies of guest-host mixtures	147
4.2	Aims	148
4.3	Results and discussion.....	149
4.3.1	Experimental order parameters	149
4.3.1.1	Dielectric permittivity of E7	149
4.3.1.2	UV-visible absorption spectroscopy of dyes in E7.....	150
4.3.2	Molecular dynamics simulations.....	154
4.3.2.1	Simulations of E7 alone.....	154
4.3.2.2	Dye Force Constant Parameterisation	159
4.3.2.3	Guest-Host Simulations of dyes in E7.....	165
4.3.3	Combining MD with DFT results	175
4.4	Conclusions	179
Chapter 5 Molecular and transition dipole moment alignment		181
5.1	Introduction	181
5.1.1	Molecular alignment of solutes in liquid crystals	182
5.1.2	Implications of dye biaxiality on molecular and TDM alignment	187

5.1.3	Definitions of alignment axes.....	191
5.1.3.1	Moment of inertia	192
5.1.3.2	Elastic tube model.....	192
5.1.3.3	Surface tensor model	195
5.1.4	Molecular surface definitions.....	201
5.1.5	Molecular alignment in MD simulations.....	202
5.1.6	Transition dipole moment alignment	204
5.1.7	Aims	205
5.2	Results and discussion.....	206
5.2.1	Alignment axes.....	206
5.2.2	Basis for alignment.....	208
5.2.2.1	Minimum circumference.....	208
5.2.2.2	Minimum area.....	209
5.2.2.3	Maximum aspect ratio	209
5.2.2.4	Surface tensor	210
5.2.2.5	Comparison of principal molecular axis definitions.....	210
5.2.3	Application of the surface tensor model.....	211
5.2.3.1	Host order parameter	211
5.2.3.2	Consideration of molecular biaxiality.....	212
5.2.3.3	Reassessment of dichroic order parameters.....	214
5.2.4	Assessment of transition dipole moment orientations.....	218
5.2.4.1	Smaller molecular structures	218
5.2.4.2	Level of theory and basis sets.....	220
5.2.4.3	Fixed TDM orientations.....	221
5.2.4.4	Variable TDM orientations.....	223
5.3	Conclusions	231
Chapter 6 Isolated molecule studies		233

6.1	Introduction	233
6.1.1	Mean field theory and the surface tensor method	233
6.1.2	Ab initio molecular dynamics	236
6.2	Aims	238
6.3	Results and discussion.....	239
6.3.1	Classical MD simulations.....	239
6.3.1.1	Surface tensor analysis and molecular alignment.....	243
6.3.1.2	Molecular alignment order parameters	247
6.3.1.3	Transition dipole moment alignment.....	248
6.3.1.4	Benefits and drawbacks	251
6.3.2	Ab initio molecular dynamics simulations.....	253
6.3.2.1	Surface tensor analysis and molecular alignment.....	256
6.3.2.2	Transition dipole moment alignment.....	259
6.3.2.3	Benefits and drawbacks	262
6.3.3	DFT optimised structures	263
6.3.3.1	Surface tensor analysis and molecular alignment.....	263
6.3.3.2	Transition dipole moment alignment.....	264
6.3.3.3	Benefits and drawbacks	265
6.3.4	Overall comparison of methods	265
6.4	Conclusions	268
Chapter 7 Scope of computational methods		271
7.1	Introduction	271
7.1.1	Alignment prediction.....	271
7.1.2	Dyes exhibiting negative dichroism	272
7.1.2.1	Anthraquinone dyes	273
7.1.2.2	Azo dyes	275
7.2	Aims	276

7.3	Results and discussion.....	277
7.3.1	1,4-disubstituted anthraquinones: assessment of methods	277
7.3.1.1	DFT and TD-DFT calculations.....	277
7.3.1.2	Guest-host MD simulations	278
7.3.1.3	Isolated molecule MD simulations	282
7.3.1.4	Surface analysis of DFT optimised structures	284
7.3.2	Surface tensor analysis of DFT optimised structures: scope of methods	
7.3.2.1	Anthraquinone dyes	286
7.3.2.2	Azo dyes	291
7.3.2.3	Overall comparison.....	295
7.4	Conclusions	297
Chapter 8 Conclusions and further work		299
8.1	Structure, spectroscopy and stability.....	299
8.1.1	Structural comparisons	299
8.1.2	UV-visible absorption spectroscopy	299
8.1.3	Electrochemistry.....	300
8.1.4	Photochemistry.....	301
8.1.5	Solubility	301
8.2	Modelling alignment in liquid crystal hosts	302
8.2.1	Guest-host MD simulations.....	302
8.2.2	Isolated molecule studies.....	303
8.2.3	Scope of methods	305
8.2.4	Molecular biaxiality	305
8.2.5	Validation of alignment contributions.....	306
8.3	Interdependence of molecular properties	306
Appendix 1 Supplementary information relating to Chapter 3.....		307
A1.1	Determination of oscillator strengths	307

A1.2	Solvent dependence of λ_{max} values	308
A1.3	Concentration dependence of UV-vis absorption spectra	309
A1.4	Infrared spectroscopy	310
A1.5	Raman spectroscopy	311
A1.6	NMR spectroscopy	312
A1.7	Aspect ratios of unsubstituted dye structures	317
A1.8	Cyclic voltammetry	317
A1.9	Spectroelectrochemistry	318
Appendix 2	Supplementary information relating to Chapter 4	319
A2.1	UV-visible absorption of E7.....	319
A2.2	HF optimisations	319
A2.3	Atom types for MD simulations.....	320
A2.4	Potential energy wells of M2.....	338
A2.5	MD simulation verification	339
A2.6	Guest-host MD simulation from isotropic starting configuration.....	343
Appendix 3	Supplementary information relating to Chapter 5	345
A3.1	Wigner functions, $D_{m,n}^2(\alpha, \beta, \gamma)$	345
A3.2	Derivation of Equation (5.21)	346
A3.3	Derivation of $U(\beta, \gamma)$ using the surface tensor model.....	347
A3.4	Derivation of T from t	349
A3.5	Conversion between spherical and Cartesian tensors.....	351
Appendix 4	Supplementary information relating to Chapter 7	353
A4.1	Atom types for MD simulations.....	353
Definitions		357
References		359

List of Figures

Figure 1.1 Schematic diagram of a nematic liquid crystal phase and the director, n	40
Figure 1.2 Schematic diagram of a smectic A (left) and smectic C (right) liquid crystal phases and their director orientations.....	41
Figure 1.3 Schematic diagram of a chiral nematic liquid crystal phase and the local director orientations.	42
Figure 1.4 A general structure of a rod-like molecule including the ring groups (blue), linking group (yellow), terminal chain (orange), terminal polar group (red), and lateral substituents (green).	43
Figure 1.5 Schematic diagram of the bright “off” state (left) and dark “on” state (right) of a twisted nematic device.	45
Figure 1.6 Schematic diagram showing the orientation dependence of light transmission through an aligned guest-host mixture.	46
Figure 1.7 Schematic diagram of a Heilmeyer guest-host cell in the absorbing off state (left) and the transmitting on state (right).	47
Figure 1.8 Schematic diagram of a White-Taylor chiral nematic guest-host device in the coloured off state (left) and the colourless on state (right).	48
Figure 1.9 Schematic diagram of a double-layer guest-host device in the coloured off state (left) and the colourless on state (right).	49
Figure 1.10 Schematic diagram of the Euler angles, α , β and γ , used to describe molecular orientation against a cartesian reference frame.	51
Figure 1.11 The functional forms of the first four even Legendre polynomials of $\cos\beta$.	53
Figure 1.12 Distribution functions, $f(\beta)$, obtained for various values of $\langle P_2 \rangle$ using the maximum entropy approach.	56
Figure 1.13 Distribution functions, $f(\beta)$, obtained for various values of $\langle P_4 \rangle$ when $\langle P_2 \rangle = 0.4$ using the maximum entropy approach.	57
Figure 1.14 Schematic diagram defining the angles, θ_{host} and θ_{dye} , between the host and dye molecular axes, respectively, and the host director, n , and the angle, β , between the dye TDM and the dye molecular axis.	58
Figure 1.15 Components of the liquid crystal mixture E7 along with their abbreviations and their relative contributions by weight %.	60
Figure 1.16 The structure of the anthraquinone chromophore.	62

Figure 1.17 Structures and λ_{\max} values of some anthraquinone dyes in DCM. ⁵⁶	63
Figure 1.18 Schematic potential energy diagram of an electronic ground state (S_0) and excited state (S_1) and their harmonic vibrational levels and wave functions as a function of nuclear displacement, D.....	73
Figure 1.19 Structures and abbreviated names of the anthraquinone dyes studied in this work.	88
Figure 3.1 Typical colours of 1,4-, 1,5- and 1,4,5,8- phenylsulfide (top) and phenylamino-substituted anthraquinones.....	100
Figure 3.2 Two-step reversible electrochemical reduction of anthraquinone.....	104
Figure 3.3 First and second reduction potentials of some anthraquinones in acetonitrile, versus Ag/AgCl. ¹⁹⁴	105
Figure 3.4 Schematic excited state energy levels of 1-hydroxy- and 2-hydroxyanthraquinone. ²⁰⁴	107
Figure 3.5 Proton transfer in the S_1 state of 1-hydroxyanthraquinone. ^{159, 208}	108
Figure 3.6 Samples of the dyes in <i>p</i> -xylene at <i>ca.</i> 2×10^{-4} mol dm ⁻³	110
Figure 3.7 UV-vis absorption spectra of the dyes in <i>p</i> -xylene at 2.0×10^{-4} mol dm ⁻³ in 1 mm path-length cells. The spectra are offset for clarity.	111
Figure 3.8 UV-vis absorption spectra of the dyes in a range of solvents at <i>ca</i> 2×10^{-4} mol dm ⁻³ or at their solubility limits. The spectra are normalised to the peak absorbances of the visible bands.....	112
Figure 3.9 Optimised structures of the dyes in all- <i>trans</i> conformations at the B3LYP/6-31g(d) level of theory.....	114
Figure 3.10 Generalised structures and atom numbers used for labelling bond lengths and angles for the 1,5-disubstituted dyes (left) and the 2,6-disubstituted dyes (right).	115
Figure 3.11 End-views of the optimised structures of the dyes showing the angle made between the plane of the anthraquinone core (drawn vertically in each case) and the plane of the phenyl substituents for each of the dyes.	117
Figure 3.12 van der Waals structures and bounding boxes indicating the molecular lengths and widths from which the aspect ratios of the dyes were calculated.....	118
Figure 3.13 Comparison of the aspect ratios calculated for the dyes.	119
Figure 3.14 Calculated UV-vis absorption spectra of the dyes. Calculated transition energies and oscillator strengths are shown as vertical lines. Spectra are offset for clarity.	121

Figure 3.15 Optimised structures of the dyes and the orbitals involved in the visible transitions. HOMOs (left) and LUMOs (right) are shown except in the case of 26B3 where the HOMO–1 and LUMO are shown.....	122
Figure 3.16 Optimised structures of the dyes and the electron density changes on visible excitation obtained from the TD-DFT calculations. The shift occurs from the regions shown in purple to the regions shown in yellow. A cutoff threshold of $\pm 0.007 e \text{ Bohr}^{-3}$ was used.	123
Figure 3.17 Optimised structures of the dyes with vectors showing the orientations of the minimum moment of inertia axes (blue) and the visible transition dipole moment axes (red) with lengths proportional to the oscillator strengths.	124
Figure 3.18 Comparison of the S_{β} values calculated for the dyes.....	126
Figure 3.19 Optimised structure of 15NB3 with the TDM axis (red), the minimum MOI axis (blue) and the anthraquinone long axis (green) overlaid and the angles, δ_1 and δ_2 , between these vectors.....	126
Figure 3.20 Cyclic voltammograms of the dyes at $1 \times 10^{-3} \text{ mol dm}^{-3}$ in DCM with TBAHFP at 0.1 mol dm^{-3} using a scan rate of 100 mV s^{-1} , and corrected vs. the Fc/Fc ⁺ couple. The initial scan direction was to negative potential and the voltammograms are offset for clarity. Uncorrected cyclic voltammograms recorded after the addition of ferrocene are given in Figure A1.11 in Appendix 1.....	128
Figure 3.21 UV-vis absorption spectra of saturated solutions (<i>ca.</i> $5 \times 10^{-5} \text{ mol dm}^{-3}$) of the dyes in acetonitrile with TBAHFP at 0.1 mol dm^{-3} during electrochemical reduction (left) and oxidation (right). The insets are absorbance plots at single wavelengths (•) and the fits (—) used to estimate the redox potentials vs. the Fc/Fc ⁺ couple (see Figure A1.12 in Appendix 1.9). The dotted vertical lines indicate the redox potentials obtained from the fits, which are given in the plots.....	132
Figure 3.22 Structure of duroquinone.	135
Figure 3.23 Experimental (blue) and calculated (red) first redox potentials of the dyes in acetonitrile vs. Fc/Fc ⁺	137
Figure 3.24 HOMO and LUMO energies estimated from experimental redox potentials with UV-vis absorption spectra recorded in <i>p</i> -xylene (in eV) overlaid. The absorption spectra are plotted relative to the energies of the respective HOMOs of the dyes, with baselines extended to the HOMO energies. The colours indicate the observed colours of the dyes, <i>cf</i> Figure 3.6, which are complementary to the absorption characteristics....	139

Figure 4.1 Schematic diagram of the experimental set-up for recording polarised absorption spectra of aligned guest-host samples.	142
Figure 4.2 Plot of capacitance against applied RMS voltage of a homogeneously aligned sample of E7 in a cell with a path length of 7.35 μm at 25 $^{\circ}\text{C}$. The inset shows the capacitance plotted against $1/V$, along with the fit to obtain C_{\parallel}	149
Figure 4.3 Scaled UV-visible absorption spectra of the dyes at <i>ca</i> 1.5 wt % (except for 15NB3OH for which was at <i>ca</i> 0.75 wt % to ensure that the absorbance was within the instrument range) in E7 (black) and at $2 \times 10^{-4} \text{ mol dm}^{-3}$ in <i>p</i> -xylene (grey), shown for comparison.	150
Figure 4.4 Polarized UV-visible absorption spectra of aligned samples of the dyes at <i>ca</i> 1.5 wt % (except for 15NB3OH for which was at <i>ca</i> 0.75 wt % to ensure absorbance was within the instrument range) in E7, used to obtain their dichroic ratios. The spectra are offset for clarity.	151
Figure 4.5 Plots of dichroic ratio against wavelength for each of the dyes in E7, obtained from the polarized UV-visible absorption spectra presented in Figure 4.4 which are shown at the top of this figure for clarity. Highlighted grey bands show the full-width-half-maxima of the visible bands, except in the case of 26B3 due to the absorption of E7 below <i>ca</i> 370 nm.	152
Figure 4.6 Graphical comparison of the experimental order parameters of the dyes in E7, S_{exp} , and the values, S_{β} , obtained from the calculated β angles of the dyes.	153
Figure 4.7 Evolution of the order parameter over time of a simulation of 256 E7 component molecules, starting from an isotropic configuration. The region in black (>120 ns) represents the data averaged to obtain the order parameter value.	156
Figure 4.8 Evolution of the order parameter over time of a simulation of 400 E7 component molecules, starting from a pseudo-nematic configuration. The region in black (>30 ns) represents the data averaged to obtain the order parameter value.	157
Figure 4.9 Calculated densities during the simulations of E7 starting from isotropic and pseudo-nematic configurations, shown as 10 point averages alongside literature values of calculated ¹⁸⁵ and experimental ²⁷³ densities.	157
Figure 4.10 Normalised distribution functions of seven dihedral angles, 1-7, in the E7 component molecule 7CB, as defined in the structure shown above, calculated from a 256-molecule simulation of E7 alone with a pseudo-nematic starting geometry, obtained between 30 ns and 200 ns. (<i>cf.</i> equivalent Figure 3 in the work of Pelaez and Wilson ¹⁸⁵).	158

Figure 4.11 Evolution of the order parameter over time of a simulation of 3872 E7 component molecules, starting from a pseudo-nematic configuration. The region in black (>30 ns) represents the data averaged to obtain the order parameter value.	159
Figure 4.12 Model structures used for parameterisation of force constants for the C-S-C angle (top), the C-S-C-C dihedrals (left), and the C-N-C-C dihedrals and H-N-C-C dihedrals (right) required for dyes in the guest-host MD simulations.	160
Figure 4.13 Plots of HF energy vs. C-S-C bond angle at four different C-S-C-C torsion angles, ψ , alongside MD energies obtained after fitting the equilibrium angle, θ_0 , and bending force constant, k_θ , of M1.	162
Figure 4.14 Plots of potential energy surfaces for the two C-S-C-C dihedral angles of the model structure M2 shown in Figure 4.12 from the HF calculations (left) and from MD after fitting (right). The white dotted boundaries correspond to RT at 300 K (2.48 kJ mol ⁻¹).	163
Figure 4.15 Plots of potential energy surfaces for the two C-N-C-C dihedral angles of the model structure M3 shown in Figure 4.12 from the HF calculations (left) and from MD after fitting (right). The white dotted boundaries correspond to RT at 300 K (2.48 kJ mol ⁻¹).	164
Figure 4.16 Histograms of the angles, θ , between the long molecular axes of each of the five dye molecules (represented by different colours) and the host director, measured over the indicated time-periods for the five guest-host simulations starting from pseudo-nematic starting geometries, and normalised for each time range. Insets. Insets give S_θ values for each dye, 1-5, obtained by averaging over each time range.	167
Figure 4.17 Estimates of the orientations explored by the long molecular axis of each of the five 15NB3 molecules (represented by different colours, consistent with Figure 4.16) during the guest-host simulation. Orientations are drawn as unit vectors and viewed down the host director axis (central points in white), with the time ranges during which the orientations were obtained labelled above.	168
Figure 4.18 Population distribution of the two C-S-C-C dihedral angles in the five 15SB3 molecules during the guest-host MD simulation at 300 K, obtained between 30 ns and 500 ns.	170
Figure 4.19 Population distribution of the two C-N-C-C dihedral angles in the five 15NB3 molecules during the guest-host MD simulation at 300 K, obtained between 30 ns and 500 ns.	170

Figure 4.20 Population distribution of the two C-N-C-C dihedral angles in the five 15NB3OH molecules during the guest-host MD simulation at 300 K, obtained between 30 ns and 500 ns.....	170
Figure 4.21 Plots of the calculated order parameters, S_θ , of the minimum MOI axes of the host molecules determined from the guest-host MD simulations starting from pseudo-nematic configurations. Sections shown in black (> 30 ns) were used for the calculation of the average values.	171
Figure 4.22 Plots of the calculated order parameters, S_θ , of the minimum MOI axes of the dye molecules against the host director, determined from the MD simulations. Sections shown in black (> 30 ns) were used for the calculation of the average values.	172
Figure 4.23 Graphical comparison of the experimental order parameters of the dyes in E7, S_{exp} , with the calculated order parameters, S_ϕ , calculated as the product of S_θ and S_β values.	176
Figure 4.24 Plot of calculated dichroic order parameters, S_ϕ , vs. experimental order parameters, S_{exp} . The grey line indicates a perfect match between calculated and experimental values.....	176
Figure 4.25 Schematic diagram of the relative calculated alignments of the dye molecular axes, the host molecular axes and the dye TDMs using the values in Table 4.9 and Table 3.10.....	177
Figure 5.1 Schematic diagram of the principal axes of a shape of $D_{\infty h}$ symmetry (left), for which $S_{xx} = S_{yy}$, and a shape of D_{2h} symmetry (right), for which $S_{xx} \neq S_{yy}$	183
Figure 5.2 Schematic diagram showing the relative orientations of the laboratory frame axes (X , Y , and Z) and the molecular frame axes (x , y , and z), and the Euler angles, α , β and γ relating them.	185
Figure 5.3 Relative orientations of the electric polarisation of incident light, E , the orientation of the dye TDM, μ , the axes, X , Y , Z , defining the laboratory frame, and the axes x , y , z defining the molecular frame.	188
Figure 5.4 Schematic diagram of the elastic tube model applied to anthracene as a solute, in this example with an unfavourable configuration arising from a large circumference, C , when measured perpendicular to the director, n	193
Figure 5.5 Schematic diagram of the circumference band of an anthracene molecule between z and z' limits along the host director, n	195

Figure 5.6 Variation in energy, $U/k_B T$, for a vector normal to a surface element (shown above) with angle, ψ , against the director, n .	196
Figure 5.7 The surface of anthracene optimised at the B3LYP/6-31g(d) level (left), the triangulated surface with randomly coloured normal unit vectors shown for each surface element (centre), and the cuboid (rotated slightly out of the plane of the page for clarity) with face areas proportional to the eigenvectors of t (right).	197
Figure 5.8 Calculated orientational distribution function of anthracene using the surface tensor method with an orienting potential of $\varepsilon = 0.04 \text{ \AA}^{-2}$.	201
Figure 5.9 A 2D representation of a solvent excluded surface (SES) of a collection of fused spheres.	202
Figure 5.10 Comparison of the order parameters obtained for the alignment axes (a_{MOI}), minimum moment of inertia axes (MOI), minimum circumference (circ.), minimum area, maximum aspect ratio, and surface tensor axes.	210
Figure 5.11 Order parameter, S_θ , vs. time for a simulation of 400 E7 component molecules starting from an isotropic starting geometry, calculated for the axes of minimum MOI (left) and the principal surface tensor axes (right). Average values were determined between 120 ns and 500 ns, shown in black.	212
Figure 5.12 Histograms of the angles made between the principal, secondary and tertiary surface axes and the host director, of individual dye molecules (represented by different colours, consistent with those used in Chapter 4) measured from the five guest-host simulations.	213
Figure 5.13 DFT optimised structures of the dyes with vectors showing the orientations of the minimum MOI axes (blue), the principal surface tensor axes (turquoise), and the visible transition dipole moment axes (red) with lengths proportional to oscillator strengths.	215
Figure 5.14 Plot of calculated order parameters, S_ϕ , vs. experimental order parameters, S_{exp} . The grey line indicates a perfect match between calculated and experimental values.	216
Figure 5.15 Diagram of the molecular frame, defined by the x , y and z axes, the TDM axis, μ , and the angles α and β relating them.	217
Figure 5.16 Anthraquinone (AQ), carbonyl (CO) and orthogonal (ORTH) axes shown for 15NB3.	220

Figure 5.17 Plot of calculated order parameters, S_ϕ , obtained from the TDM orientations fixed against the anthraquinone cores during the MD simulations vs. experimental order parameters, S_{exp} .	223
Figure 5.18 Structures of the dyes with labels indicating bonds about which the dihedral angle distributions were calculated to have a FWHM $> 20^\circ$ during the guest-host MD simulations.	224
Figure 5.19 Plots of dihedral angle populations from the MD simulations for the dihedral angles labelled in Figure 5.18 with 1° histogram bin-widths. Angles used in geometries for the TD-DFT calculations of the TDM orientations are marked with blue dots. Shaded regions represent the “bins” used when assigning geometries from the MD trajectories to those for which the TDM orientations were calculated.	226
Figure 5.20 Views along the ORTH axes of structures used for calculating the influence of molecular conformation on the TDM orientations, with dihedral angles fixed at the most populated angles during the MD simulations. Red arrows are overlaid showing the orientations of the calculated TDMs, defined by scaled additions of the AQ, CO and ORTH unit vectors. TDM arrows are all of equal length, and the TDMs from conformations corresponding to $<5\%$ of the populations determined from the MD simulations are omitted here.	228
Figure 5.21 Views along the CO axes of structures used for calculating the influence of molecular conformations on the TDM orientations, with dihedral angles fixed at the most populated angles during the MD simulations. Red arrows are overlaid showing the orientations of the calculated TDMs, defined by scaled additions of the AQ, CO and ORTH unit vectors. TDM arrows are all of equal length, and the TDMs from conformations corresponding to $<5\%$ of the populations determined from the MD simulations are omitted here.	229
Figure 5.22 Plot of calculated order parameters, S_ϕ , obtained from the binned TDM orientations during the MD simulations vs. experimental order parameters, S_{exp} .	230
Figure 6.1 Plot of calculated order parameters, S_{calc} , obtained using the surface tensor model for the compounds listed in Table 6.1 vs. experimental order parameters, S_{exp} .	235
Figure 6.2 Structures of the dyes with labels indicating bonds about which the dihedral angle distributions were calculated to have a FWHM $> 20^\circ$ during the guest-host MD simulations, used for analysis of the isolated molecule MD simulations.	240

Figure 6.3 Plots of populations for the dihedral angles labelled in Figure 6.2 obtained from the the isolated molecule simulations (blue bars) and the guest-host MD simulations (dashed grey lines) using 1° bin widths.....	241
Figure 6.4 Inverse eigenvalues, t_{ii} , of the surface tensors, t , obtained from the MD simulations of the isolated dye molecules. Eigenvalues at every 50 th point of the trajectories are plotted for clarity.	244
Figure 6.5 Histograms of the surface tensor eigenvalues measured during the guest-host and the isolated molecule MD simulations. t_{zz} values are shown in blue, t_{xx} values are shown in green, and t_{yy} values are shown in red using bin widths of 2 Å ²	246
Figure 6.6 Cuboids, drawn to scale, with face areas proportional to $-t_{xx}$, $-t_{yy}$, and $-t_{zz}$, of each of the dyes, as determined from the MD simulations of isolated molecules.	247
Figure 6.7 Plot of calculated order parameters, S_{ϕ} , obtained from the TDM orientations fixed against the anthraquinone core during the isolated molecule MD simulations vs. experimental order parameters, S_{exp}	250
Figure 6.8 Plot of calculated order parameters, S_{ϕ} , obtained from the TDM orientations of binned conformers during the isolated molecule MD simulations vs. experimental order parameters, S_{exp}	251
Figure 6.9 Plots of dichroic order parameters calculated from the isolated molecule MD simulations, assuming fixed TDM orientations against the anthraquinone core (left) and using TDM orientations from binned geometries (right) against those calculated from principal surface tensor axes of the dyes in the guest-host simulations.....	252
Figure 6.10 Histograms of populations of the dihedral angles labelled in Figure 6.2 obtained from the CPMD simulations (blue bars, 3° bin-width) and the isolated molecule classical MD simulations (grey lines, 1° bin-width).	254
Figure 6.11 Inverse eigenvalues, $-t_{ii}$, of the surface tensors, t , obtained from the CPMD simulations of the isolated dye molecules.....	256
Figure 6.12 Histograms of the surface tensor inverse eigenvalues measured during the isolated molecule CPMD simulations alongside those from the isolated molecule classical MD simulations for comparison. t_{zz} values are shown in red, t_{xx} values are shown in green, and t_{yy} values are shown in blue, using 2° bin widths..	258
Figure 6.13 Plot of calculated order parameters, S_{ϕ} , obtained from the TDM orientations fixed against the anthraquinone core during the CPMD simulations vs. experimental order parameters, S_{exp}	261

Figure 6.14 Plot of calculated order parameters, S_ϕ , obtained from the TDM orientations of binned conformers during the CPMD simulations vs. experimental order parameters, S_{exp}	262
Figure 6.15 Plot of calculated order parameters, S_ϕ , obtained from the surface tensor analysis of the DFT optimised dye structures and the calculated TDM orientations vs. the experimental order parameters, S_{exp}	265
Figure 6.16 R^2 values of fits between calculated dichroic order parameters and experimental order parameters of the dyes.	266
Figure 6.17 Gradients of fits between calculated dichroic order parameters and experimental order parameters of the dyes. The dashed line indicates a gradient of 1.	266
Figure 6.18 Intercepts of fits between calculated dichroic order parameters and experimental order parameters of the dyes.	267
Figure 7.1 General structure of a 1,4-diamido-anthraquinone dye, derivatives of which have been shown to exhibit negative dichroism.	273
Figure 7.2 Structures of 1 and 2.....	274
Figure 7.3 Core structure of heteroaromatic azo dyes that have been shown to exhibit negative dichroism.	275
Figure 7.4 Optimised structures of 1 (left) and 2 (right) at the B3LYP/6-31g(d) level with red arrows overlaid, indicating the orientations of the TDMs associated with the strongly allowed visible transitions.....	277
Figure 7.5 Plots of the calculated order parameters, S_θ (MOI), of the minimum MOI axes of the host molecules of E7 during the guest-host MD simulations of 1 (left) and 2 (right). Sections shown in black (≥ 30 ns) were used to calculate the average values.	279
Figure 7.6 Plots of the calculated order parameters, S_θ (MOI), of the minimum MOI axes of the dye molecules during the guest-host MD simulations of 1 (left) and 2 (right). Sections shown in black (≥ 30 ns) were used to calculate the average values.	280
Figure 7.7 Plots of the calculated order parameters, S_θ (surface), of the principal surface tensor axes of the dye molecules during the guest-host MD simulations of 1 and 2. Sections shown in black (≥ 30 ns) were used to calculate the average values.	280
Figure 7.8 Cuboids, drawn to scale, with face areas proportional to $-t_{xx}$, $-t_{yy}$, and $-t_{zz}$, of 1 and 2, as determined from the MD simulations of isolated molecules.	283
Figure 7.9 Plot of calculated dichroic order parameters using optimised DFT structures and the surface tensor approach, S_{calc} , vs. experimental dichroic order parameters, S_{exp} ,	

for 1 to 9. The grey line shows a perfect match between calculated and experimental values.....	291
Figure 7.10 Plots of calculated dichroic order parameters, S_{calc} , vs. experimental dichroic order parameters, S_{exp} , for 10 to 19. The grey line shows a perfect match between calculated and experimental values.	295
Figure 7.11 Plot of calculated dichroic order parameters from single DFT optimised structures using the surface tensor method, S_{ϕ} , against experimental dichroic order parameters, S_{exp} , of anthraquinone dyes 1 to 9 (green), azo dyes 10 to 19 (orange) and the dyes studied in Chapters 3 – 6 (blue). The grey line shows a perfect match between calculated and experimental values.....	296
Figure A1.1 UV-vis absorption spectra of the dyes at 2.0×10^{-4} mol dm ⁻³ in <i>p</i> -xylene, with shaded regions showing the integrated areas used to determine the oscillator strengths, f , using direct integrals (left) and fitted gaussian bands (right).	307
Figure A1.2 Plots of λ_{max} of the dyes vs. solvent dielectric constant, polarizability and dipole moment, μ . ²¹⁷	308
Figure A1.3 Spectral profiles of the dyes in <i>p</i> -xylene (left) and DCM (right) at the concentrations indicated above. The peak absorbances are normalised for clarity.	309
Figure A1.4 Experimental IR absorption spectra of the dyes in KBr disks along with calculated spectra determined from geometries optimised at the B3LYP/6-31g(d) level and some assignments.	310
Figure A1.5 Experimental Raman spectra recorded of <i>ca</i> 5×10^{-4} mol dm ⁻¹ solutions of the dyes in DCM and an excitation wavelength of 514.5 nm, with regions corresponding to strong solvent peaks omitted. Calculated spectra are also shown, determined from geometries optimised at the B3LYP/6-31g(d) level.....	311
Figure A1.6 Structure of 15SB3 with numbering shown for NMR peak assignments, alongside experimental and calculated ¹ H NMR spectra recorded in DCM - <i>d</i> ₂	312
Figure A1.7 Structure of 15NB3 with numbering shown for NMR peak assignments, alongside experimental and calculated ¹ H NMR spectra recorded in DCM - <i>d</i> ₂	313
Figure A1.8 Structure of 15NB3OH with numbering shown for NMR peak assignments, alongside experimental and calculated ¹ H NMR spectra recorded in DCM - <i>d</i> ₂	314
Figure A1.9 Structure of 26B3 with numbering shown for ¹ H NMR peak assignments, alongside experimental and calculated ¹ H NMR spectra recorded in DCM - <i>d</i> ₂	315

Figure A1.10 Structure of 26B3OH with numbering shown for ^1H NMR peak assignments, alongside experimental and calculated NMR spectra recorded in DCM- d_2	316
Figure A1.11 Cyclic voltammograms of the dyes at $1 \times 10^{-3} \text{ mol dm}^{-3}$ in DCM with TBAHFP at 0.1 mol dm^{-3} and ferrocene at $ca\ 1 \times 10^{-3} \text{ mol dm}^{-3}$ using a scan rate of 100 mV s^{-1} . The initial scan direction was to negative potential and the voltammograms are offset for clarity.....	317
Figure A1.12 UV-vis absorption spectra of ferrocene at $ca. 5 \times 10^{-5} \text{ mol dm}^{-3}$ in acetonitrile during electrochemical reduction from $+0.76 \text{ V}$ to 0 V (left) and oxidation from 0 V to $+0.76 \text{ V}$ (right) vs. the Ag pseudo reference electrode. Inset are absorbance plots at single wavelengths (\bullet) and the fits (---) used to estimate the redox potential of Fc/Fc^+ . The dotted vertical lines indicate the redox potentials obtained from the fits, which are given in the plots.	318
Figure A1.13 UV-vis absorption spectra of duroquinone at $ca. 5 \times 10^{-5} \text{ mol dm}^{-3}$ in acetonitrile during electrochemical reduction (left) and oxidation (right). Inset are absorbance plots at single wavelengths (\bullet) and the fits (---) used to estimate the redox potentials vs. the Fc/Fc^+ couple. The dotted vertical lines indicate the redox potentials obtained from the fits, which are given in the plots.....	318
Figure A2.1 UV-visible absorption spectra of E7 in a thin film between quartz disks with no spacer, and in a cell between glass slides with a $20 \mu\text{m}$ pathlength, both recorded against a background of air.	319
Figure A2.2 Optimised structures of the dyes in all- <i>trans</i> conformations at the HF/6-31g(d) level of theory.....	319
Figure A2.3 Structure and atom numbering of 5CB for the MD simulations.	321
Figure A2.4 Structure and atom numbering of 7CB for the MD simulations.	322
Figure A2.5 Structure and atom numbering of 8OCB for the MD simulations.....	323
Figure A2.6 Structure and atom numbering of 5CT for the MD simulations.....	324
Figure A2.7 Structure and atom numbering of M1 for the MD force constant parameterisation.	325
Figure A2.8 Structure and atom numbering of M2 for the MD force constant parameterisation.	326
Figure A2.9 Structure and atom numbering of M3 for the MD force constant parameterisation.	327
Figure A2.10 Structure and atom numbering of 15SB3 for the MD simulations.	328

Figure A2.11 Structure and atom numbering of 15NB3 for the MD simulations.	330
Figure A2.12 Structure and atom numbering of 15NB3OH for the MD simulations. .	332
Figure A2.13 Structure and atom numbering of 26B3 for the MD simulations.	334
Figure A2.14 Structure and atom numbering of 26B3OH for the MD simulations. ...	336
Figure A2.15 Enlarged plots of the potential energy surfaces for the two C-N-C-C dihedral angles of the M3 from the HF calculations (left) and from MD after fitting (right), equivalent to Figure 4.15 but showing only the energy between 0 and 1.5 kJ mol ⁻¹ , illustrating the local minima in the base of each potential energy well.....	338
Figure A2.16 Estimates of the orientations explored by the long molecular axis of each of the five 15SB3 molecules (represented by different colours, consistent with Figure 4.16) during the guest-host simulation. Orientations are drawn as unit vectors and viewed down the host director axis (central points in white), with the time ranges during which the orientations were obtained labelled above.	339
Figure A2.17 Estimates of the orientations explored by the long molecular axis of each of the five 15NB3OH molecules (represented by different colours, consistent with Figure 4.16) during the guest-host simulation. Orientations are drawn as unit vectors and viewed down the host director axis (central points in white), with the time ranges during which the orientations were obtained labelled above.	340
Figure A2.18 Estimates of the orientations explored by the long molecular axis of each of the five 26B3 molecules (represented by different colours, consistent with Figure 4.16) during the guest-host simulation. Orientations are drawn as unit vectors and viewed down the host director axis (central points in white), with the time ranges during which the orientations were obtained labelled above.	341
Figure A2.19 Estimates of the orientations explored by the long molecular axis of each of the five 26B3OH molecules (represented by different colours, consistent with Figure 4.16) during the guest-host simulation. Orientations are drawn as unit vectors and viewed down the host director axis (central points in white), with the time ranges during which the orientations were obtained labelled above.	342
Figure A2.20 Plots of the calculated orientational order parameters, S_θ , of the host molecules (left) and the dye molecules (right) determined from the guest-host MD simulation of 26B3OH in E7 starting from an isotropic configuration. Sections shown in black (> 120 ns) were used for the calculation of the average values.	343
Figure A4.1 Structure and atom numbering of 1 for the MD simulations.	353
Figure A4.2 Structure and atom numbering of 2 for the MD simulations.	355

List of Tables

Table 1.1 Structures and order parameters of some azo dyes in the nematic host E7. ⁵⁰	61
Table 1.2 Structures, visible λ_{\max} values and order parameters of selected azo dyes in the nematic host GR-31. ¹²	62
Table 1.3 Visible λ_{\max} values of 1-aminoanthraquinone in several solvent systems with their solvent polarity functions (Δf) listed. ⁵⁷	63
Table 1.4 Structures, λ_{\max} values and order parameters of selected amino substituted anthraquinones in the nematic host E7. ⁵⁹	65
Table 1.5 Structures, λ_{\max} values and order parameters of selected sulfide substituted anthraquinones in the nematic host E43. ⁶⁰	66
Table 1.6 Structures, λ_{\max} values and order parameters of selected 2,6- and 2,7-disubstituted anthraquinones in the nematic hosts E43 ^a and NP1132 ^b . ^{60, 61}	67
Table 1.7 Structures and room temperature solubilities of selected anthraquinone dyes in the nematic host LIXON 5052XX. ^{65, 67}	68
Table 1.8 Structures and properties of examples of different dye classes analysed in nematic liquid crystal mixtures.	70
Table 3.1 Emission maxima, λ , and quantum yields, ϕ , of fluorescence and low temperature phosphorescence observed for hydroxyanthraquinones in propan-2-ol. ²⁰⁴	106
Table 3.2 Fluorescence observed from aminoanthraquinones in cyclohexane. ²⁰⁶	107
Table 3.3 Experimental visible absorption maxima and associated absorption coefficients and oscillator strengths, f , of the dyes in <i>p</i> -xylene at 2.0×10^{-4} mol dm ⁻³ .	111
Table 3.4 Visible λ_{\max} values of the dyes in a range of solvents.	112
Table 3.5 Approximate solubility limits of the dyes in a range of solvents based on absorption coefficients obtained in <i>p</i> -xylene.	113
Table 3.6 Selected bond lengths (Å) of the anthraquinone cores for the optimised dye structures shown in Figure 3.9 and from the crystal structures of anthraquinone (AQ), ¹⁷¹ anthraquinone-1,5-dithiol (15SH), ¹⁷³ <i>N,N'</i> -diphenyl-1,5-diaminoanthraquinone (15NB0) ²¹⁸ and 2,6-diphenyl-anthraquinone (26B0), ¹³⁷ using the numbering scheme shown in Figure 3.10.	115

Table 3.7 Bond lengths (\AA) between the anthraquinone cores and the directly substituted groups of the optimised dye structures shown in Figure 3.9 and for the crystal structures of related compounds, ^{137, 173, 218} using the numbering scheme shown in Figure 3.10...	116
Table 3.8 Molecular lengths, widths and aspect ratios of the dyes measured from the van der Waals surfaces of the optimised structures shown in Figure 3.12.	118
Table 3.9 Experimental and calculated visible absorption wavelengths and associated oscillator strengths of the dyes.	120
Table 3.10 Angles between the calculated minimum moment of inertia axes and TDM orientations, β , and associated order parameters, S_β	124
Table 3.11 Magnitudes of the angles δ_1 and δ_2 , calculated between the TDM and the minimum MOI axis, respectively, and the anthraquinone long axis axis for each of the dyes.	127
Table 3.12 Estimates of potentials, where observed, obtained from the CVs of the dyes in DCM vs. Fc/Fc ⁺ , presented in Figure 3.20.	129
Table 3.13 Experimental reduction and oxidation potentials of the dyes in acetonitrile obtained from the fits to the spectroelectrochemical data presented in Figure 3.21 and their differences ($\Delta E = E_{(\text{Dye}^{\bullet+}, \text{Dye})} - E_{(\text{Dye}, \text{Dye}^{\bullet-})}$), referenced vs. the Fc/Fc ⁺ couple. ..	132
Table 3.14 Calculated Gibbs energies, obtained from DFT optimised structures at the B3LYP/6-31g(d) level, of cationic, neutral and anionic forms of duroquinone and the five dyes studied in this work in an acetonitrile solvent field, and the associated calculated redox potentials, $E_{(\text{Dye}, \text{Dye}^{\bullet-})}$ and $E_{(\text{Dye}^{\bullet+}, \text{Dye})}$, of the dyes relative to the experimental potentials of duroquinone vs. Fc/Fc ⁺ , and the differences between them, ΔE	136
Table 3.15 HOMO (E_{HOMO}) and LUMO (E_{LUMO}) energies of the dyes, estimated from the experimental redox potentials of the dyes determined by spectroelectrochemistry. The energy gaps between the HOMO and LUMO levels (ΔE) and visible λ_{max} values in <i>p</i> -xylene converted to eV (E_{vis}) are also listed.	138
Table 4.1 Experimental λ_{max} values of the aligned samples of dye-E7 mixtures obtained from the polarised UV-vis absorption spectra. Values in <i>p</i> -xylene are also shown for comparison.	151
Table 4.2 Experimental dichroic ratios, R , and order parameters, S_{exp} , of aligned samples of the dyes in E7, obtained from the polarised UV-visible absorption spectra presented in Figure 4.4. Calculated S_β values presented and discussed in Chapter 3 (Table 3.10) are given here for comparison.	152

Table 4.3 The numbers of component E7 molecules used in the molecular dynamics simulations to match the experimental component weight % values.	155
Table 4.4 Dihedral force constants, $C_0 - C_5$, obtained from the dihedral angle fits presented in Figure 4.14 and Figure 4.15 for model structures M2 and M3.	165
Table 4.5 Calculated order parameters of the host molecules, S_θ (E7), and dye molecules, S_θ (dye), from the guest-host MD simulations, averaged between 30 ns and 500 ns.	172
Table 4.6 Calculated average molecular lengths, widths and aspect ratios of the dye molecules during the MD simulations, averaging over all dye molecules in each simulation between 30 ns and 500 ns, alongside the aspect ratios obtained for the DFT optimised structures. Standard deviations of lengths, widths and aspect ratios from MD were <i>ca</i> 0.05 Å, 0.03 Å and 0.10, respectively.	174
Table 4.7 Calculated average molecular lengths, widths and aspect ratios of the host molecules during the MD simulations averaging over each type of host molecule in the E7 simulation run from a pseudo-nematic starting configuration between 30 ns and 500 ns. Standard deviations of lengths, widths and aspect ratios were <i>ca</i> 0.05 Å, 0.04 Å and 0.20, respectively.	175
Table 4.8 Calculated dichroic order parameters, S_ϕ , of the dyes in E7 obtained from the product of calculated S_θ and S_β values.	176
Table 4.9 Angles, θ , obtained from the average order parameters of the host molecules and dye molecules from the guest-host MD simulations starting from pseudo-nematic configurations, calculated using Equation (4.12). β angles originally given in Table 3.10 are listed again here for clarity.	177
Table 5.1 Wigner functions defining the orientations of E in the laboratory frame, and μ in the molecular frame.	190
Table 5.2 Calculated order parameters, S_θ (MOI), of the minimum MOI axes of the dyes, originally presented in Chapter 4 (Table 4.5), and the order parameters S_θ (a_{MOI}) of the alignment axes of the dyes, against the host director, and the differences between these order parameters for each of the dyes, $\Delta S = S_\theta$ (a_{MOI}) - S_θ (MOI).	207
Table 5.3 Order parameters obtained for the alignment (a_{MOI}), minimum MOI, minimum circumference, minimum area, maximum aspect ratio and surface tensor axes. $\Delta = S_\theta$ (a_{MOI}) - S_θ . Average Δ values are also listed.	210
Table 5.4 Biaxial order parameters, $S_{xx} - S_{yy}$, of the dyes, determined from the guest-host MD simulations.	214

Table 5.5 Calculated angles, β , between the principal surface tensor axes and the visible TDMs of the dyes and their associated order parameters, S_β , and calculated uniaxial dichroic order parameters, S_ϕ (surface), determined as the product of S_θ and S_β (see Table 5.3). Uniaxial dichroic order parameters calculated using the minimum MOI axes, S_ϕ (MOI), presented in Chapters 3 and 4, are listed for comparison.....	215
Table 5.6 Calculated angles, α , between the secondary surface axis, x , and the projection of the TDM into the xy plane for each of the dyes along with values of the biaxial term used to calculate the overall dichroic order parameters.	217
Table 5.7 Calculated wavelengths, λ , and oscillator strengths, f , of the allowed visible electronic transitions of the propyl-substituted dyes and their hydrogen and methyl substituted analogues, along with their projections on to the AQ, CO and ORTH axes.	219
Table 5.8 Calculated allowed visible transitions and associated properties for 15SB0 using a range of levels of theory.	221
Table 5.9 Calculated angles, β and α , and their standard deviations, $+/-$, of the visible TDMs of the dyes, defined as fixed against the anthraquinone core. The associated biaxial terms and calculated overall dichroic order parameters, S_ϕ , are also listed.	222
Table 5.10 Most populated angles and associated FWHM values and ranges containing 95% of the populations for the dihedrals of the dyes labelled in Figure 5.18.	225
Table 5.11 Limits of the bins used to assign dye conformers in the MD simulations to those for which TD-DFT calculations had been run. The values correspond to the boundaries between shaded regions in Figure 5.19.	227
Table 5.12 Calculated angles, β and α , and their standard deviations, \pm , of the binned visible TDMs of the dyes. The associated biaxial terms and calculated overall dichroic order parameters, S_ϕ , are also listed.	229
Table 6.1 Experimental order parameters of solute molecules dissolved in nematic hosts alongside calculated values obtained using the surface tensor model, using an orienting potential of $\varepsilon = 0.05 \text{ \AA}^{-2}$. ²⁹⁷	234
Table 6.2 Experimental order parameters of CD bonds of alkanes dissolved in a nematic host, and calculated values obtained using the surface tensor model. ²⁹⁷	235
Table 6.3 Experimental order parameters of CD bonds in the aromatic rings of 5CB and in the 1-5 positions along the alkyl chains obtained from NMR experiments, and calculated order parameters obtained using the surface tensor model ($\varepsilon = 0.05 \text{ \AA}^{-2}$). ³⁰¹	236

Table 6.4 Most populated angles and associated FWHM values for the dihedrals of the isolated dye molecules labelled in Figure 6.2. Δ values indicate the differences between these there and the equivalent angles from the guest-host MD simulations given in Table 5.10.....	242
Table 6.5 Average inverse surface tensor eigenvalues, $-\langle t_{ii} \rangle$, and standard deviations obtained for the dye molecules during the guest-host MD simulations. The surface areas, SA, are also listed, calculated according to $SA = -\langle t_{xx} \rangle - \langle t_{yy} \rangle - \langle t_{zz} \rangle$	243
Table 6.6 Average inverse surface tensor eigenvalues, $-\langle t_{ii} \rangle$, and standard deviations obtained for the dye molecules during the isolated molecule MD simulations. The surface areas, SA, are also listed, calculated according to $SA = -\langle t_{xx} \rangle - \langle t_{yy} \rangle - \langle t_{zz} \rangle$. Δ values in each case are calculated as the difference between the value obtained from the isolated molecule simulation and the respective value from the guest-host simulation.	245
Table 6.7 Average values of the order parameters, S_{zz} and $S_{xx} - S_{yy}$, determined from the surface tensor eigenvalues at each frame of the trajectories of the isolated molecule MD simulations, using an orienting strength of $\varepsilon = 0.04 \text{ \AA}^{-2}$, and those obtained from the surface tensor axes in the guest-host simulations given in Tables 5.3 and 5.4 in Chapter 5.....	248
Table 6.8 Average β and α angles of the fixed visible TDMs of the dyes, calculated from the isolated molecule MD simulations and their standard deviations. The associated order parameters and calculated dichroic order parameters, S_ϕ , are also listed.	248
Table 6.9 Average angles, β and α , of the binned visible TDMs of the dyes, calculated from the classical isolated molecule MD simulations and their standard deviations. The associated order parameters and calculated dichroic order parameters, S_ϕ , are also listed.	250
Table 6.10 inverse surface tensor eigenvalues, $-\langle t_{ii} \rangle$, and standard deviations obtained for the isolated dye molecules during the CPMD simulations. The surface areas, SA, are also listed, calculated according to $SA = -\langle t_{xx} \rangle - \langle t_{yy} \rangle - \langle t_{zz} \rangle$. Δ values are calculated as the difference between the values obtained from the CPMD simulations and the isolated molecule MD simulations.	259
Table 6.11 Averages of the order parameters S_{zz} and $S_{xx} - S_{yy}$, determined from the surface tensor eigenvalues at each frame of the trajectories of the isolated molecule CPMD simulations, using and orienting strength of $\varepsilon = 0.04 \text{ \AA}^{-2}$	259

Table 6.12 Average angles, β and α , of the fixed visible TDMs of the dyes, calculated from the isolated molecule CPMD simulations and their standard deviations. The associated order parameters and calculated dichroic order parameters, S_ϕ , are also listed.	260
Table 6.13 Average angles, β and α , of the binned visible TDMs of the dyes, calculated from the isolated molecule CPMD simulations and their standard deviations. The associated order parameters and calculated dichroic order parameters, S_ϕ , are also listed.	261
Table 6.14 Order parameter, S_{zz} and $S_{xx} - S_{yy}$, determined from surface tensor analysis of the DFT optimised structures, using an orienting strength of $\varepsilon = 0.04 \text{ \AA}^{-2}$	264
Table 6.15 Calculated angles, β and α , of the binned visible TDMs of the dyes, calculated from the DFT optimised structures. The associated biaxial order parameters and calculated dichroic order parameters, S_ϕ , are also listed.	264
Table 6.16 R^2 values, gradients and intercepts of fits between calculated dichroic order parameters and experimental order parameters of the dyes.	266
Table 7.1 Reported dichroic order parameters, S_{exp} , of dyes 1 and 2, ^{332, 336} along with the wavelengths, λ , and nematic host mixtures ^{337, 338} used for the measurements.	274
Table 7.2 Calculated wavelengths, λ , of the allowed visible transitions of 1 and 2, and their associated oscillator strengths, f	278
Table 7.3 Average order parameters of the principal surface tensor axes of 1 and 2, calculated from the guest-host MD simulations.	281
Table 7.4 Average angles and standard deviations between the surface tensor alignment axes and the CO and AQ axes of 1 and 2.	281
Table 7.5 Average angles, β and α , and their standard deviations of the fixed visible TDMs of dyes 1 and 2 calculated from the guest-host MD simulations. The associated order parameter contributions and the calculated dichroic order parameters, S_ϕ , are also listed.	281
Table 7.6 Average surface tensor inverse eigenvalues, $-\langle t_{ii} \rangle$, and standard deviations obtained for the dye molecules during the isolated molecule simulations.	283
Table 7.7 Average values of the order parameters, S_{zz} and $S_{xx} - S_{yy}$, of 1 and 2 determined from the surface tensor eigenvalues at each frame of the trajectories of the isolated molecule MD simulations, using an orienting potential of $\varepsilon = 0.04 \text{ \AA}^{-2}$	283
Table 7.8 Average angles, β and α , and their standard deviations of the fixed visible TDMs of dyes 1 and 2 calculated from the isolated molecule MD simulations. The	

associated order parameter contributions and the calculated dichroic order parameters, S_ϕ , are also listed. 284

Table 7.9 Order parameter, S_{zz} and $S_{xx} - S_{yy}$, determined from surface tensor analysis of the DFT optimised structures of 1 and 2, using an orienting strength of $\varepsilon = 0.04 \text{ \AA}^{-2}$. Also listed are calculated angles, β and α , of the fixed visible TDMs and the associated order parameter contributions and the calculated dichroic order parameters, S_ϕ 285

Table 7.10 Dyes 3 and 4 and their reported experimental dichroic order parameters, S_{exp} , in Lixon 5052-XX measured at wavelengths, λ_{exp} .⁶⁴ Also shown are DFT optimised structures with calculated principal surface tensor axes (turquoise) and visible TDMs (red) overlaid, along with the calculated wavelengths, λ_{calc} , and oscillator strengths, f_{calc} of the allowed visible transitions. 287

Table 7.11 Dyes 5 – 7 and their reported experimental dichroic order parameters, S_{exp} , in Lixon GR 41 measured at wavelengths, λ_{exp} .²²⁹ Also shown are DFT optimised structures with calculated principal surface tensor axes (turquoise) and visible TDMs (red) overlaid, along with the calculated wavelengths, λ_{calc} , and oscillator strengths, f_{calc} of the allowed visible transition; those in italics are not shown on the optimised structures. 288

Table 7.12 Dyes 8 and 9 and their reported experimental dichroic order parameters, S_{exp} , in ZLI-1132 measured at wavelengths, λ_{exp} .³³² Also shown are DFT optimised structures with calculated principal surface tensor axes (turquoise) and visible TDMs (red) overlaid, along with the calculated wavelengths, λ_{calc} , and oscillator strengths, f_{calc} of the allowed visible transition; those in italics are not shown on the optimised structures. 289

Table 7.13 Order parameter, S_{zz} and $S_{xx} - S_{yy}$, determined from surface tensor analysis of the DFT optimised structures of 3 to 9, using an orienting strength of $\varepsilon = 0.04 \text{ \AA}^{-2}$. Also listed are calculated angles, β and α , of the fixed visible TDMs and the associated biaxial order parameters and calculated dichroic order parameters, S_ϕ 290

Table 7.14 Dyes 10 - 13 and dyes 14 -15 and their reported experimental dichroic order parameters, S_{exp} , in E7 and Lixon GR 41, respectively, measured at wavelengths, λ_{exp} .⁵⁰
²²⁹ Also shown are DFT optimised structures with calculated principal surface tensor axes (turquoise) and visible TDMs (red) overlaid, along with the calculated wavelengths, λ_{calc} , and oscillator strengths, f_{calc} of the allowed visible transitions; those in italics are not shown on the optimised structures. 292

Table 7.15 Dyes 16 - 18 and dye 19 and their reported experimental dichroic order parameters, S_{exp} , in E7 and 4OCB/4CB, respectively, measured at wavelengths, λ_{exp} .⁵⁰

³³⁹ Also shown are DFT optimised structures with calculated principal surface tensor axes (turquoise) and visible TDMs (red) overlaid, along with the calculated wavelengths, λ_{calc} , and oscillator strengths, f_{calc} of the allowed visible transitions; those in italics are not shown on the optimised structures.	293
Table 7.16 Order parameter, S_{zz} and $S_{xx} - S_{yy}$, determined from surface tensor analysis of the DFT optimised structures of 3 to 9, using an orienting strength of $\varepsilon = 0.04 \text{ \AA}^{-2}$. Also listed are calculated angles, β and α , of the fixed visible TDMs and the associated biaxial order parameters and calculated dichroic order parameters, S_{ϕ}	294
Table A1.1 Dielectric constants, polarizability volumes and dipole moments, μ , of the isotropic solvents used in this work. ²¹⁷	308
Table A1.2 Peak assignments of the experimental ^1H NMR spectrum of 15SB3 alongside calculated chemical shift values. Calculated shifts were averaged for protons shown to be equivalent in the experimental spectrum.	312
Table A1.3 Peak assignments of the experimental ^1H NMR spectrum of 15NB3 alongside calculated chemical shift values. Calculated shifts were averaged for protons shown to be equivalent in the experimental spectrum.	313
Table A1.4 Peak assignments of the experimental ^1H NMR spectrum of 15NB3OH alongside calculated chemical shift values. Calculated shifts were averaged for protons shown to be equivalent in the experimental spectrum.	314
Table A1.5 Peak assignments of the experimental NMR spectrum of 26B3 alongside calculated chemical shift values. Calculated shifts were averaged for protons shown to be equivalent in the experimental spectrum.	315
Table A1.6 Peak assignments of the experimental ^1H NMR spectrum of 26B3OH alongside calculated chemical shift values. Calculated shifts were averaged for protons shown to be equivalent in the experimental spectrum.	316
Table A1.7 Molecular lengths, widths and aspect ratios of optimised structures of the dyes with the terminal propyl chains replaced with hydrogen atoms, labelled “0” rather than “3”. The values were calculated using the same method as that presented in the main text.	317
Table A2.1 Atom numbers, OPLS atom types, charge groups and atomic charges (where default charges were not used) used for MD simulations of 5CB.	321
Table A2.2 Atom numbers, OPLS atom types, charge groups and atomic charges (where default charges were not used) used for MD simulations of 7CB.	322

Table A2.3 Atom numbers, OPLS atom types, charge groups and atomic charges (where default charges were not used) used for MD simulations of 8OCB.	323
Table A2.4 Atom numbers, OPLS atom types, charge groups and atomic charges (where default charges were not used) used for MD simulations of 5CT.	324
Table A2.5 Atom numbers, OPLS atom types, charge groups and atomic charges (where default charges were not used) used for MD simulations of M1.	325
Table A2.6 Atom numbers, OPLS atom types, charge groups and atomic charges (where default charges were not used) used for MD simulations of M2.	326
Table A2.7 Atom numbers, OPLS atom types, charge groups and atomic charges (where default charges were not used) used for MD simulations of M3.	327
Table A2.8 Atom numbers, OPLS atom types, charge groups and atomic charges (where default charges were not used) used for MD simulations of 15SB3.	328
Table A2.9 Atom numbers, OPLS atom types, charge groups and atomic charges (where default charges were not used) used for MD simulations of 15NB3.	330
Table A2.10 Atom numbers, OPLS atom types, charge groups and atomic charges (where default charges were not used) used for MD simulations of 15NB3OH.	332
Table A2.11 Atom numbers, OPLS atom types, charge groups and atomic charges (where default charges were not used) used for MD simulations of 26B3.	334
Table A2.12 Atom numbers, OPLS atom types, charge groups and atomic charges (where default charges were not used) used for MD simulations of 26B3OH.	336
Table A4.1 Atom numbers, OPLS atom types, charge groups and atomic charges (where default charges were not used) used for MD simulations of 1.	354
Table A4.2 Atom numbers, OPLS atom types, charge groups and atomic charges (where default charges were not used) used for MD simulations of 2.	356

Acknowledgements

First and foremost, I would like to acknowledge my supervisors, Dr John Moore and Prof. John Goodby, for providing me with the opportunity to work on this project, and for their help, advice and support over the last four years.

I would also like to thank Dr. Stephen Cowling for his practical advice in what was initially a very unfamiliar field, and particular thanks should go to Dr. Laurence Abbott, for both his willingness to share his extensive knowledge and experience, as well as for his enjoyable company in and outside the office. I am also grateful for the funding provided by the EPSRC for this project.

Additionally, thanks should go to the many people in both the Phys. Chem. and Materials groups for discussions, both related and unrelated to my work. In particular to James, whose presence has certainly been missed since he left.

This section would certainly not be complete without mentioning the many cavers (unfortunately too many to name) with whom I have shared some incredible and memorable experiences during my time at York. From grovelling under the Yorkshire Dales to entering the unknown in more exotic locations, our exploits have provided me with a welcome contrast to the office and the lab.

Finally, I would especially like to thank my family for their support and kindness, and Erin, for her company, encouragement and patience over the last few years.

Author's declaration

The research contained within this thesis was carried out in the Department of Chemistry at the University of York between October 2011 and September 2015. To the best of my knowledge, this research is original and my own, except where reference has been made to the work of others. This work has not previously been presented for an award at this, or any other, University.

Some of the material presented within this thesis has previously been published in:

M. T. Sims, L. C. Abbott, S. J. Cowling, J. W. Goodby and J. N. Moore, *Chem. - Eur. J.*, 2015, 21, 10123-10130.

Chapter 1

Introduction

The work reported in this thesis concerns the structure and properties of a set of anthraquinone dyes considered in the role of guests within liquid crystalline host systems. The dyes studied are closely related, enabling their behaviour to be considered in the context of their structural variation. For guest-host systems such as these to be designed with specific properties that may lead to their application in useful devices, it is desirable to obtain structure-function relationships and develop an understanding of the fundamental properties from which they arise. This work aims to make progress towards this goal by taking a combined experimental and computational approach to the problem.

This introductory chapter considers a range of background information on liquid crystal phases, and more specifically the principles, applications, and theory of the guest-host effect. The properties of dyes used in such systems are then considered, followed by an overview of the techniques used in this work and their underlying principles. The final section of the chapter describes the aims of the project.

1.1 Liquid crystals

1.1.1 Background

The observation of an intermediate state of matter between the solid crystalline phase and the isotropic liquid phase was first recorded in the late 1800s when “double melting” behaviour was observed in cholesteryl acetate and cholesteryl benzoate. Subsequent work revealed such phases to flow like a liquid, whilst maintaining characteristics of a solid, and the term “liquid crystal” was first used in 1889 to describe these systems. Further research revealed a wider range of compounds that exhibited this phase, which became associated primarily with rod-like molecular structures, and it was observed for the first time in the early 1900s that some compounds exhibited multiple liquid crystalline phases. Subsequently, the field of research expanded, particularly after the discovery of technological applications in the 1960s.

1.1.2 Phases

Liquid crystalline phases of matter lie between fully isotropic liquids that exhibit little or no short or long range order, and crystalline solids that exhibit both short range and long range positional and orientational order. Hence, it follows that the subdivision of phases within liquid crystals is primarily determined by the degree of ordering of the system. Thermotropic liquid crystals, which are defined by phases largely dictated by the temperature of the system, are discussed in this thesis. Lyotropic liquid crystals, in which the phase behaviour is largely dictated by the concentration of the species within a solvent, do not fall within the scope of this work.

The simplest of the liquid crystal phases is the nematic phase, in which the molecules exhibit a degree of short range orientational order, i.e. neighbouring molecules have a tendency to orient in the same direction, as shown in Figure 1.1. Typically, this phase is formed by calamitic (rod-like) molecules. In a nematic phase, domains of aligned molecules form, although the domains themselves may not be aligned with each other, giving the bulk material no net alignment. However, alignment of the bulk material may be induced by an external influence such as the presence of an aligned surface or the application of an electric field, and the resulting average molecular orientation is termed the director, \mathbf{n} . The alignment in a nematic phase may generally be considered to be uniaxial, meaning that the alignment in the phase is cylindrically symmetric around the director.

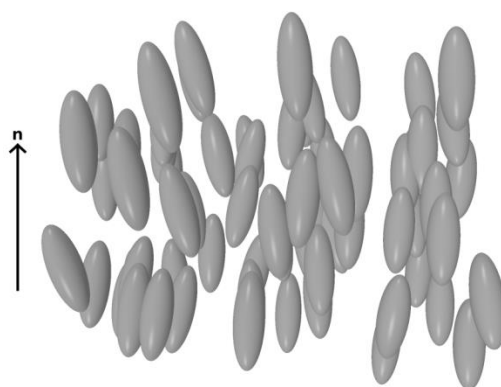


Figure 1.1 Schematic diagram of a nematic liquid crystal phase and the director, \mathbf{n} .

Smectic phases are also formed by rod-like molecules and exhibit orientational order, similar to that observed in nematic phases. In addition, they exhibit a degree of positional order in which the molecules form layers, as shown in Figure 1.2. The

relationship between the orientational order and the positional order gives rise to several subdivisions of smectic phases, such as the smectic A phase in which the layers are perpendicular to the director, and the smectic C phase in which the layers lie at an angle other than 90° to the director, as also shown in Figure 1.2. Additional order such as positional ordering within the layers gives rise to further subdivisions of smectic phases.

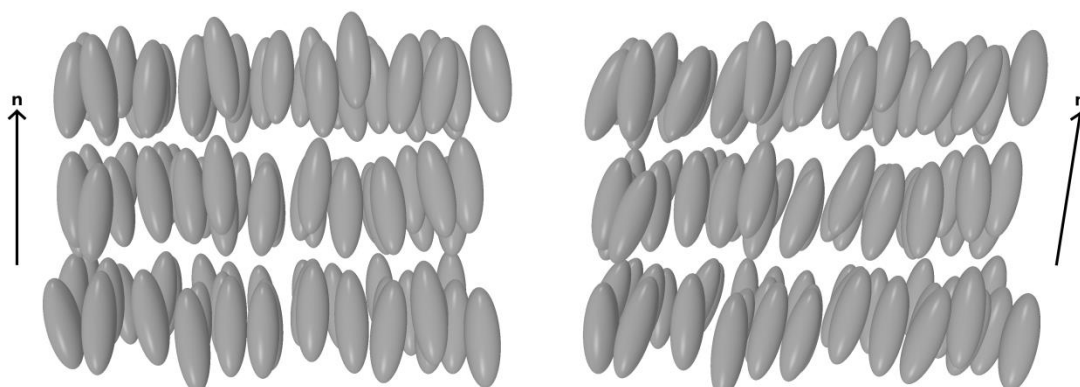


Figure 1.2 Schematic diagram of a smectic A (left) and smectic C (right) liquid crystal phases and their director orientations.

Specific phases formed by chiral molecules are also observed, and have similarities to those formed by achiral species. The chiral nematic phase, for example, exhibits short range orientational order, but the local director orientation rotates around an axis perpendicular to this director, as shown in Figure 1.3. Chiral smectic phases are also observed in which the orientation of the tilt angle described above rotates around an axis normal to the layers.

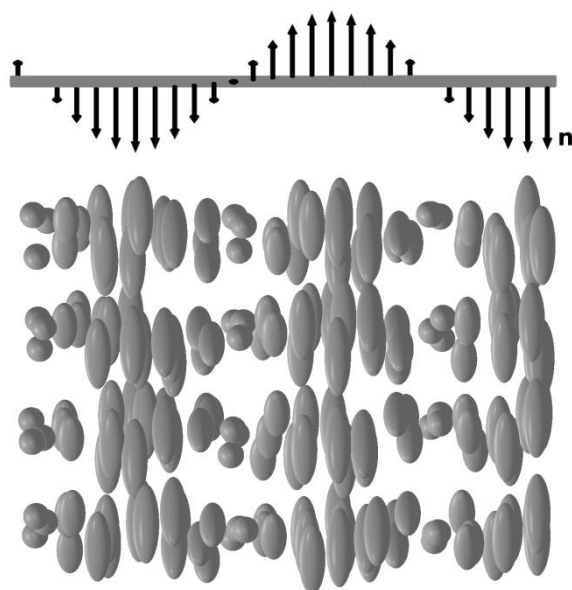


Figure 1.3 Schematic diagram of a chiral nematic liquid crystal phase and the local director orientations.

In addition to the phases described above, many other phases have been characterised, such as discotic phases formed by disc-like molecules, defect-driven blue phases that lie between the isotropic and nematic phases, ferroelectric phases, and phases formed by bent-core molecules. All of these phases demonstrate subtly different properties due to the variations in their degrees of ordering and symmetry, and, although they may be divided into many different categories, they share an underlying basis for the formation of the phases: molecular anisotropy.

To exhibit one or more of the liquid crystalline phases shown in Figures 1.1 - 1.3 above, a molecule must not only have a rod-like structure, but it must also be relatively rigid in order to maintain this shape. Typically, such structures comprise a core of two or more connected aromatic or cyclohexane rings. Not only does this molecular design provide the overall rod-like shape and a degree of rigidity, but the presence of extended conjugation through aromatic ring systems can also result in strong intermolecular interactions that can aid alignment. The ring systems may be bonded directly or via linking groups to alter the overall molecular shape and conjugation within the molecule. Alkyl and alkoxy chains are commonly appended as terminal groups on the ring systems to provide the molecule with a degree of flexibility, favouring the formation of liquid crystalline phases in comparison with less flexible structures lacking such groups. Polar terminal groups can be used in order to increase intermolecular interactions,

favouring alignment between neighbouring molecules. Lateral substituents may also be added to the ring systems in order to tune the phase behaviour and dielectric properties. A schematic diagram showing a generalised structure of a rod-like molecule that may exhibit liquid crystal behaviour is shown in Figure 1.4.

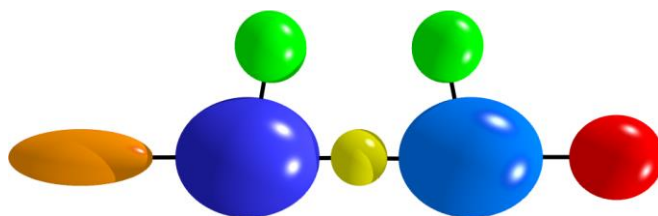


Figure 1.4 A general structure of a rod-like molecule including the ring groups (blue), linking group (yellow), terminal chain (orange), terminal polar group (red), and lateral substituents (green).

1.1.3 Properties

The order exhibited by liquid crystalline materials, along with the molecular anisotropy of their constituents, means that many of their bulk physical properties are also characterised by anisotropy. Properties including elasticity, magnetic susceptibility, electric permittivity, viscosity, and optical properties can vary significantly depending on the orientation in which they are measured relative to the director. It is the combination of the optical properties and the electric properties that has given rise to most of the current applications of liquid crystals.

1.1.4 Uses

Currently, the primary application for liquid crystals is in display technology. Such displays vary in their construction and mode of operation, but all rely on the optical anisotropy of aligned liquid crystal systems. Typically, a cell is constructed from two glass plates coated with a transparent electrode layer to enable an electric field to be applied across the cell. The inner surfaces of the glass plates are usually coated with an alignment layer, such as polyimide or nylon, to induce bulk alignment of the mixture, and polarisers may be present on one or both of the plates depending on the mode of operation of the device. A cell typically has a path length of the order of *ca* 10 μm and is filled with the liquid crystal.

The first practical liquid crystal display (LCD) that was commercially successful was produced in 1973, and utilised an ion-doped liquid crystal mixture. In the “off” state of an ion-doped system, the liquid crystal is uniformly aligned and transparent, but on the application of an electric field, movement of the ions disrupts the liquid crystal alignment, causing light to scatter and the transparency to be lost. In spite of its initial success, this technology was limited by its power consumption and operating temperatures, and was soon superseded by a device utilising an alternative mode of operation: the twisted nematic (TN) display.

TN displays rely on the behaviour of plane polarised light passing through a liquid crystalline material that exhibits a helical twist much larger than the wavelength of the incident light. This mesophase configuration is typically achieved by sandwiching a nematic liquid crystal between two orthogonally aligned surfaces of a cell, as depicted in Figure 1.5. Due to the differences in the refractive indices of the liquid crystal measured parallel and perpendicular to the director, when the incident light is polarised with the electric component parallel to the director, the effect of the twist in the director orientation is to rotate the polarisation of the light as it passes through the cell. By placing polarisers parallel with the direction of molecular alignment on each surface of the device, a situation is achieved in which linearly polarised light may pass through the perpendicular polarisers and be transmitted through the device. On the application of an electric field between the surfaces, the dielectric anisotropy of the molecules causes them to rotate to lie perpendicular to the plane of the surfaces. In this configuration, the polarisation of the incident light is not rotated and is blocked by the second polariser, producing a dark state, as also shown in Figure 1.5.

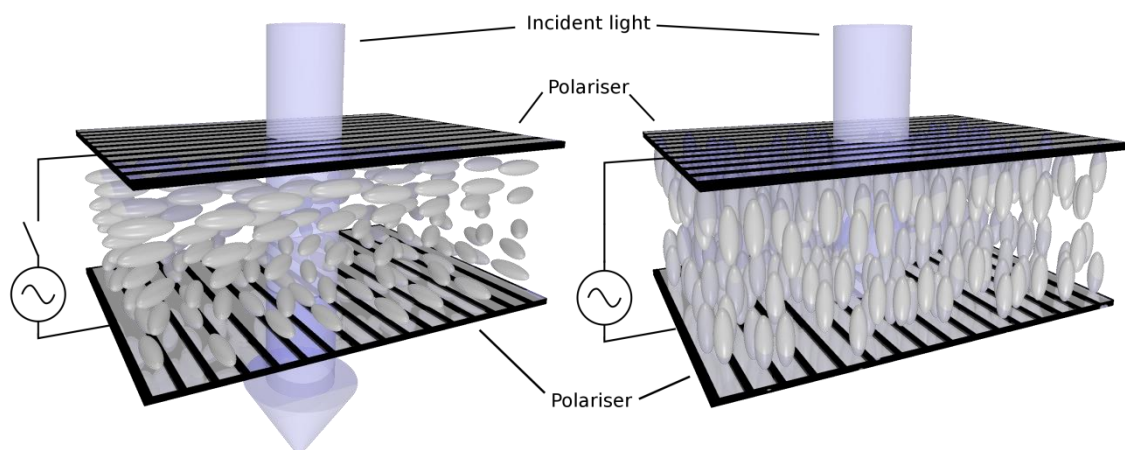


Figure 1.5 Schematic diagram of the bright “off” state (left) and dark “on” state (right) of a twisted nematic device.

This TN mode of operation overcame some shortcomings of the earlier scattering device, providing significantly lower power consumption and improved contrast between the off and on states. Further improvements have been made to the materials used, and TN displays comprise the majority of commercial LCDs produced.¹

Aside from their use in displays, liquid crystals have also been used in more diverse commercial applications, often utilising the temperature dependence of chiral nematic liquid crystals, with examples including thermometers, medical screening devices, battery testers, and jewellery.² Research is ongoing into further applications for liquid crystals including, but certainly not limited to, electrically switchable lenses,³ lasers,⁴ optoelectronic devices⁵ and biological applications.⁶

1.2 Guest-Host Systems

1.2.1 Concept

The guest-host effect in liquid crystal systems was first observed in 1964, when it was realised that the application of an electric field to a cell containing a nematic liquid crystal-dye mixture resulted in an observed colour change.^{7, 8} The underlying reasons for this observation were twofold: firstly, the dye was dichroic, meaning that its absorption was strongly dependent on the relative orientation of the dye molecules and the polarisation of the incident light, and secondly the dye molecules exhibited a

tendency to align with the host material. In the absence of an applied field, the sample exhibited no net bulk alignment, but on the application of an electric field the guest-host system aligned with the director parallel to the direction of observation, resulting in the colour change.⁷ Figure 1.6 shows the orientation dependence of the light transmitted by an aligned guest-host mixture. The observation of this effect was the basis for a substantial amount of subsequent work into such systems that was largely aimed at optimising the properties of guest-host mixtures for use in display technology.

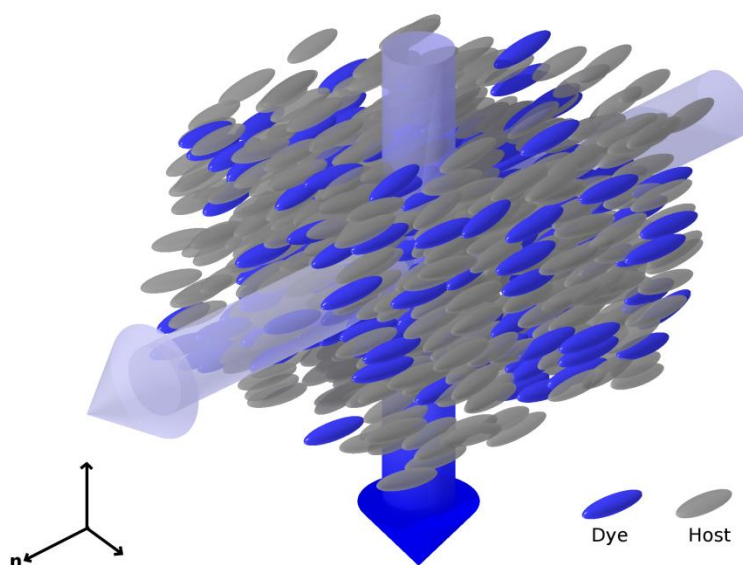


Figure 1.6 Schematic diagram showing the orientation dependence of light transmission through an aligned guest-host mixture.

1.2.2 Display applications

There are many configurations of guest-host devices that enable switching between absorbing and transmitting states. The first of these was the Heilmeyer device, shown in Figure 1.7, in which uniform alignment of the liquid crystal mixture in the plane of the cell (homogeneous alignment) maximises absorption in the “off” state, and the application of an electric field orients the mixture to align the molecules along the direction of light propagation to produce the transmitting state. This design produces a display that is dark or coloured in the off state, and colourless in the on state. Variations on this mode of operation include using host mixtures aligned perpendicular to the plane of the cell (homeotropic alignment) that twist into the plane of the cell on the application of an electric field, providing a colourless off state and a coloured on state;

the same effect may be achieved by switching to a dye with an absorption axis perpendicular to the alignment axis.⁹

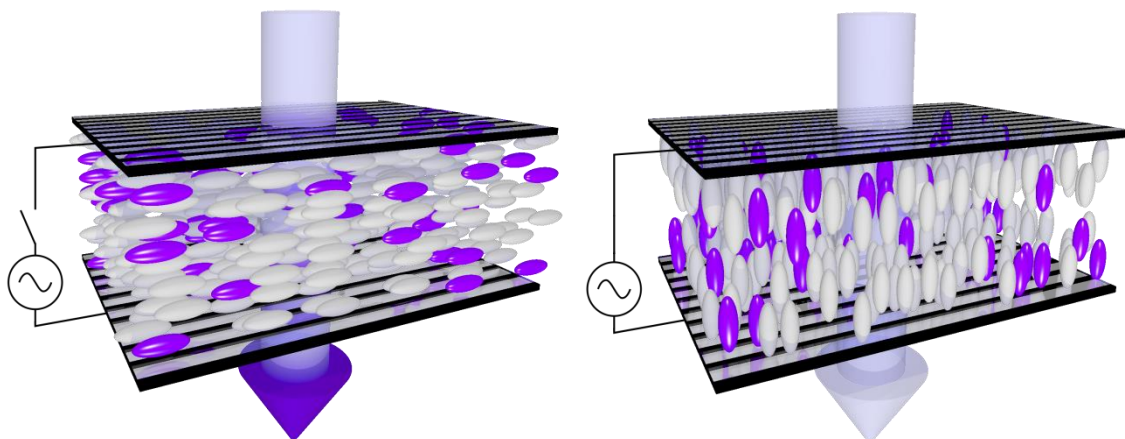


Figure 1.7 Schematic diagram of a Heilmeyer guest-host cell in the absorbing off state (left) and the transmitting on state (right).

The problem these systems share is that they all typically operate using polarisers, resulting in more than 50% of the light being lost, even in the transmitting state, and giving no increase in brightness compared with simple TN devices, which also suffer from narrow viewing angles caused by the polarisers. Although it is possible for these systems to work without polarisers to increase the brightness and viewing angle of the devices, the absence of polarisers significantly decreases the contrast ratio between the absorbing and transmitting states.

There have been efforts to try to increase the brightness without compromising the colour contrast and viewing angle, using a variety of approaches. The first of these approaches was developed by White and Taylor,¹⁰ who utilised a chiral nematic host, as shown in Figure 1.8. In the off state, the rotation of the director results in all polarisations of incident light being absorbed, and the application of an electric field induces a phase change that results in homeotropic alignment to give the transmitting on state. This design produces a device without the requirement for polarisers, resulting in improved viewing angle and brightness when compared with the Heilmeyer-type device, whilst maintaining an acceptable contrast ratio.¹⁰ There were drawbacks to this device, most notably the high voltages required to induce the switch between the absorbing and transmitting states, and the inability of the device to be multiplex driven, increasing the complexity and power consumption of the device.⁹

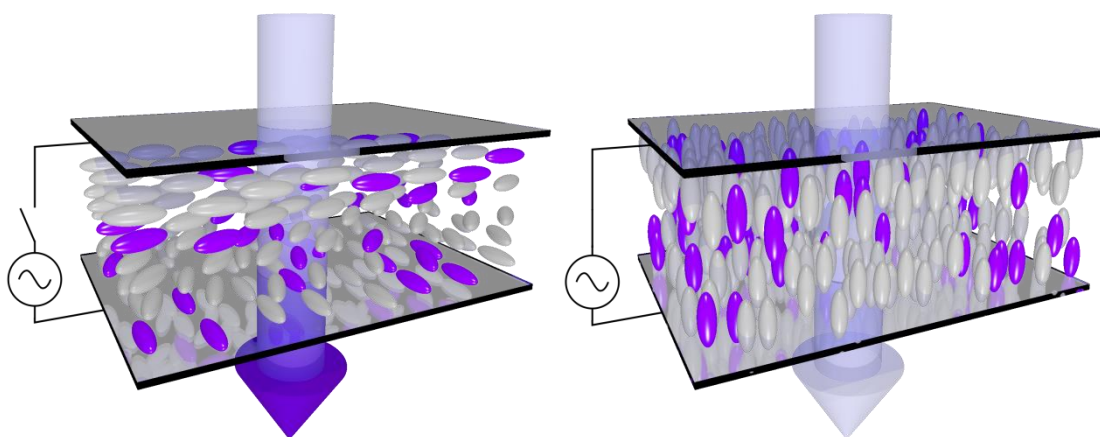


Figure 1.8 Schematic diagram of a White-Taylor chiral nematic guest-host device in the coloured off state (left) and the colourless on state (right).

In an attempt to overcome these barriers, Cole and Kashnow developed a reflective display mode based on the Heilmeyer device, but utilising a quarter-wave plate on a back reflector.¹¹ This device causes the polarisation of the reflected light to be rotated by 90° with respect to the incident light, again enabling the device to operate without polarisers, but without the need for the higher operating voltages of the White and Taylor device. The notable drawback to this mode of operation is the viewing angle, which is dictated by the narrow operating angle of the quarter-wave plate, as well as only being able to operate in a reflective mode.

Uchida *et al.* then developed a double-layer guest-host device in order to improve on the shortcomings of the previous devices by using two layers of perpendicular homogeneously aligned guest-host mixtures, as shown in Figure 1.9.¹² Hence, a device without the need for polarisers and high driving voltages was realised, giving an acceptable contrast ratio in addition to good brightness and wide viewing angle, but at the cost of the added complexity of constructing a multi-layered system.

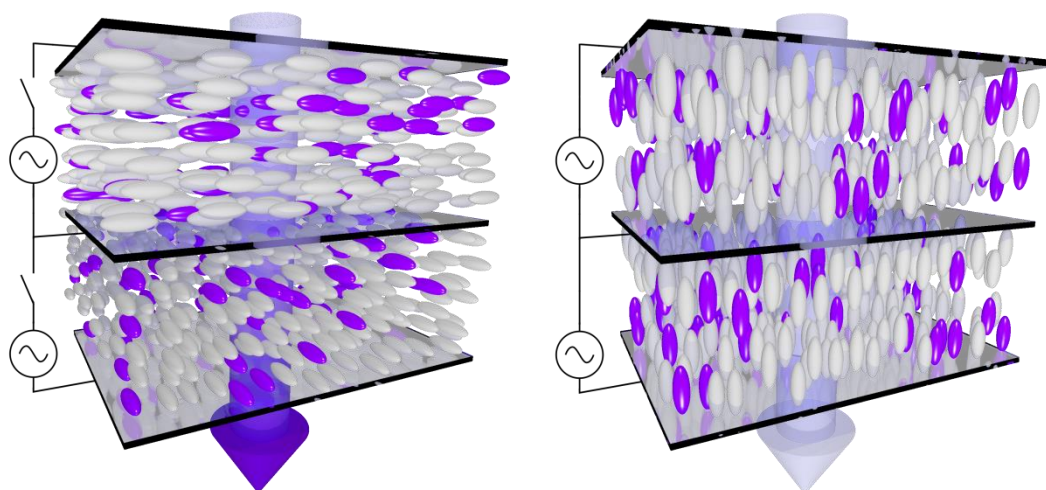


Figure 1.9 Schematic diagram of a double-layer guest-host device in the coloured off state (left) and the colourless on state (right).

Further work into guest-host systems has aimed to improve the performance of such devices, for example by the use of smectic systems,¹³ liquid crystal gels,¹⁴ and hosts with low refractive index anisotropy,¹⁵ but there are few guest-host systems currently used in commercial devices for reasons discussed below in Sections 1.3 and 1.4.

1.2.3 Other applications

Aside from the obvious potential for use in display applications, guest-host systems have also been proposed for use in a wide variety of other diverse applications, including precursors for high performance thin-film polarizers,¹⁶ optical storage devices utilising photochemical dye isomerisation¹⁷ optically controlled diffraction gratings,¹⁸ security devices,¹⁹ switchable solar windows using fluorescent guest molecules,²⁰ and 3D imaging of micellar systems also using fluorescent dyes.²¹ Studies of the behaviour of guest-host systems are also of particular interest for biological applications due to the use of fluorescent dye molecules as probes for the investigation of alignment in biological membranes.^{22, 23}

1.2.4 Requirements

In the context of display applications, it is vital that any guest-host system fulfils a number of criteria in order to be of practical use. The dyes used must exhibit visible absorption transitions with high absorption coefficients, ideally with tuneable

wavelengths of maximum absorption obtained by accessible synthetic approaches that enable their optical properties to be optimised. The solubility of the dyes must also be high, in order for intense colours to be realised, and ideally the presence of the dyes must not compromise the liquid crystal mixture in terms of the viscosity and switching times. The expected lifetime of a display device is on the order of several years, and consequently the system must exhibit sufficient stability to ensure that the performance of the device is not compromised during its lifetime; limited stability has been a significant barrier to the use of some classes of dye in such applications.²⁴ Regardless of the mode of operation of a guest-host device, the dye should exhibit a high degree of alignment within the host system in order to maximise the difference between the absorbing and transmitting states. In the context of a display, it is primarily the alignment that determines the contrast ratio of a device, and therefore it is vital that this property is optimised.²⁴

1.2.5 Order parameter

The measurement and quantification of dye alignment is crucial to the assessment of guest-host systems. Prior to consideration of dye alignment, background information on the quantification of liquid crystal alignment in general is introduced.

In order to describe the molecular order in a liquid crystal phase, all the molecules in a sample must be considered. The spatial configuration of a single molecule within a system may be described in terms of the positions, r , of the molecules, their orientations, Ω , and their conformational states, Φ . If the probabilities of these three quantities, $f(r, \Omega, \Phi)$, are known for a system then the average value of the property, $g(r, \Omega, \Phi)$, may be expressed in terms of Equation (1.1), where angular brackets are used to denote an ensemble average, and $f(r, \Omega, \Phi)$ is normalised according to Equation (1.2).²⁵

$$\langle g(r, \Omega, \Phi) \rangle = \int g(r, \Omega, \Phi) f(r, \Omega, \Phi) dr d\Omega d\Phi \quad (1.1)$$

$$\int f(r, \Omega, \Phi) dr d\Omega d\Phi = 1 \quad (1.2)$$

Each of these three parameters may be split further into vectors to describe the position, angles to describe the orientation, and a number of conformational variables to describe the conformational state.

To take the simplest case of a uniaxial nematic liquid crystal phase modelled with rigid molecules of $D_{\infty h}$ symmetry, fewer terms need to be considered. By definition there is no translational order in the system, so the molecular orientations and conformations may be considered independently from the molecular positions. Furthermore, the treatment of the molecules as being rigid means only the molecular orientation quantity, Ω , needs to be considered to fully describe the phase.

The orientation of any given molecule may be described in terms of the three Euler angles, α , β and γ , as defined in Equation (1.3) and shown graphically in Figure 1.10, where the z axis defines the director.

$$f(\Omega) = f(\alpha, \beta, \gamma) \quad (1.3)$$

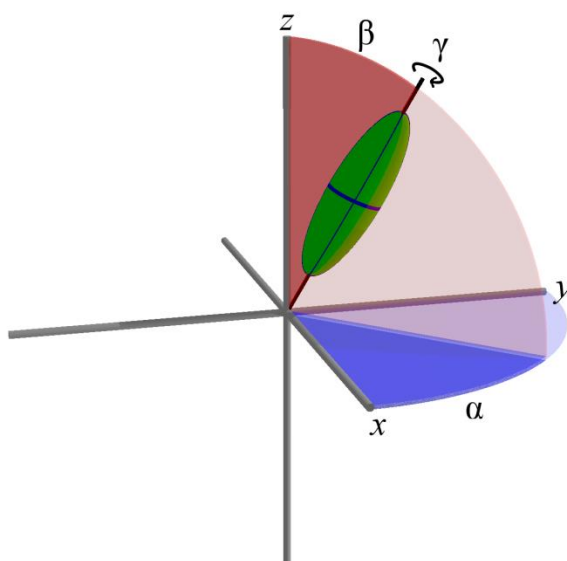


Figure 1.10 Schematic diagram of the Euler angles, α , β and γ , used to describe molecular orientation against a cartesian reference frame.

Given the $D_{\infty h}$ symmetry constraint imposed in this model, it can be seen that rotation about the molecular axis, γ , will have no effect on the distribution. Additionally, because the uniaxial nematic phase is being considered, the probability of the

orientation, β , of a molecule should also be unaffected by the angle, α , and this leads to the simplification expressed in Equation (1.4).

$$f(\Omega) = f(\alpha, \beta, \gamma) \equiv f(\beta) \quad (1.4)$$

This expression gives rise to the singlet orientational distribution function, $f(\beta)$, which is a fully comprehensive description of the molecular orientation given the symmetry constraints imposed. Normalisation of this function is carried out according to Equation (1.5).^{25, 26}

$$\int_0^\pi f(\beta) \sin \beta \, d\beta = 1 \quad (1.5)$$

Due to the constraints imposed, the form of the distribution must be symmetric, as defined in Equation (1.6).

$$f(\beta) = f(\pi - \beta) \quad (1.6)$$

Determining this complete distribution experimentally is extremely challenging, but simplified forms of the distribution may be more readily obtained, such as the original expression used to measure the order parameter, S , of a system, given by Equation (1.7).²⁷

$$S = \frac{3\langle \cos^2 \beta \rangle - 1}{2} \quad (1.7)$$

Using this description of nematic ordering, $S = 1$ for a fully ordered system in which $\beta = 0$ for all molecules, $S = 0$ for a completely disordered (isotropic) system, and $S = -0.5$ for a system in which all molecules lie perpendicular to the director. This parameter is often readily obtainable from experiment, which makes it extremely useful. However, although this quantity is determined by the full orientational distribution function, the value itself is far from sufficient to describe the distribution in full. For example, a positive value of S between 0 and 1 may arise from a wide distribution of molecular orientations centred around 0 degrees, or it may arise from all molecules lying at a single angle, β , against the director.²⁸

The full orientational distribution function may be described in terms of an expansion of Legendre polynomials, as given by by Equations (1.8) and (1.9),^{34, 38} where the angular brackets around P_L indicate the average value of $P_L(\cos\beta)$ for the distribution. Only even coefficients need be considered because the distribution has been defined as symmetric. The first four even terms of the expansion are given in Equations (1.10) - (1.13) and shown in Figure 1.11. It can be seen that the order parameter, S , given in Equation (1.7) corresponds to the second term of this expansion.^{25, 29}

$$f(\beta) = \sum_L f_L P_L(\cos\beta) ; (L \text{ even}) \quad (1.8)$$

$$f_L = \left(\frac{2L+1}{2} \right) \langle P_L \rangle \quad (1.9)$$

$$P_0(\cos\beta) = 1 \quad (1.10)$$

$$P_2(\cos\beta) = \frac{(3\cos^2\beta - 1)}{2} \quad (1.11)$$

$$P_4(\cos\beta) = \frac{(35\cos^4\beta - 30\cos^2\beta + 3)}{8} \quad (1.12)$$

$$P_6(\cos\beta) = \frac{(231\cos^6\beta - 315\cos^4\beta + 105\cos^2\beta - 5)}{16} \quad (1.13)$$

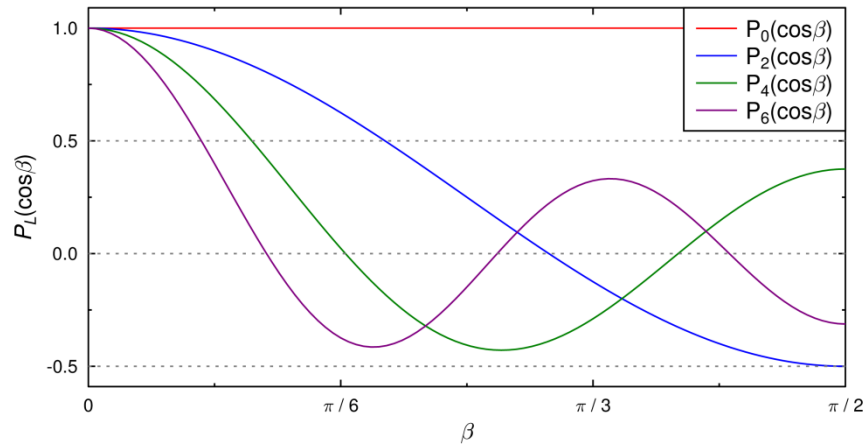


Figure 1.11 The functional forms of the first four even Legendre polynomials of $\cos\beta$.

For the specific case described here, the full singlet orientational distribution function may be described as the infinite expansion given in Equation (1.14), which is obtained by substituting Equations (1.9) - (1.13) into Equation (1.8).

$$f(\beta) = \frac{1}{2} + \frac{5}{2}(\langle P_2 \rangle P_2(\cos \beta)) + \frac{9}{2}(\langle P_4 \rangle P_4(\cos \beta)) + \frac{13}{2}(\langle P_6 \rangle P_6(\cos \beta)) \dots \quad (1.14)$$

A value of $\langle P_L \rangle$ may be obtained from a given orientational distribution function using Equation (1.15),²⁶ or from an ensemble of molecular orientations using Equation (1.16).

$$\langle P_L \rangle = \int_0^\pi P_L(\cos \beta) f(\beta) \sin \beta \, d\beta \quad (1.15)$$

$$\langle P_L \rangle = \langle P_L(\cos \beta) \rangle \quad (1.16)$$

As mentioned previously, the full orientational distribution function, $f(\beta)$, is extremely difficult to measure experimentally, and although such distributions have been derived from X-ray and neutron scattering experiments, a number of approximations have to be made.³⁰ However, a value of $\langle P_2 \rangle$, may be readily deduced from experiment because it can be elucidated from the measurement of a property that transforms under rotation in the same way as a second rank tensor, and is often referred to as a second-rank order parameter.²⁶ Examples of such properties are birefringence, magnetic susceptibility and linear dichroism.³¹ These properties are dependent on the relative orientations of two vectors; for example, for linear dichroism arising from polarised UV-vis absorption, the vectors are the electric vector of the polarised incident light and the electronic transition dipole moment vector of the molecule. Measurement of $\langle P_4 \rangle$ from experiment is also feasible, from the measurement of a property that transforms as a fourth-rank tensor under rotation. Examples of such properties are polarised Raman scattering³² and fluorescence depolarisation.^{33, 34}

Although knowledge of higher order parameters increases the knowledge of the distribution function, the full distribution cannot be obtained exactly from a finite number of $\langle P_L \rangle$ values. One method of deriving a full orientational distribution function from a limited number, M , of $\langle P_L \rangle$ values is to assume a particular form for the distribution. A common example is the maximum entropy approach, which provides the most random distribution for a given set of known $\langle P_L \rangle$ values, as expressed in Equation (1.17),³⁰ where λ_L are coefficients to be determined and normalisation of the function is carried out according to Equation (1.5).

$$f(\beta) = e^{\left(\sum_{L=0}^M \lambda_L P_L(\cos \beta)\right)} \quad (1.17)$$

For example, in the case of known $\langle P_2 \rangle$ and $\langle P_4 \rangle$ values, λ_2 and λ_4 values are obtained by numerically solving Equations (1.18) and (1.19).²⁸

$$\frac{\int_0^\pi e^{\lambda_2 P_2(\cos \beta) + \lambda_4 P_4(\cos \beta)} P_2(\cos \beta) \sin \beta d\beta}{\int_0^\pi e^{\lambda_2 P_2(\cos \beta) + \lambda_4 P_4(\cos \beta)} \sin \beta d\beta} = \langle P_2 \rangle \quad (1.18)$$

$$\frac{\int_0^\pi e^{\lambda_2 P_2(\cos \beta) + \lambda_4 P_4(\cos \beta)} P_4(\cos \beta) \sin \beta d\beta}{\int_0^\pi e^{\lambda_2 P_2(\cos \beta) + \lambda_4 P_4(\cos \beta)} \sin \beta d\beta} = \langle P_4 \rangle \quad (1.19)$$

Methods such as this are particularly useful to calculate distribution functions that would give rise to particular values of $\langle P_L \rangle$. For example, Figure 1.12 shows distribution functions, $f(\beta)$, calculated using Equation (1.17) for various values of $\langle P_2 \rangle$ according to the maximum entropy principle, and Figure 1.13 shows distribution functions calculated for various $\langle P_4 \rangle$ values for a given value of $\langle P_2 \rangle$, again assuming a maximum entropy distribution. The plots of $f(\beta)$ in Figure 1.12 and Figure 1.13 are taken from functions that have been normalised according to Equation (1.5).

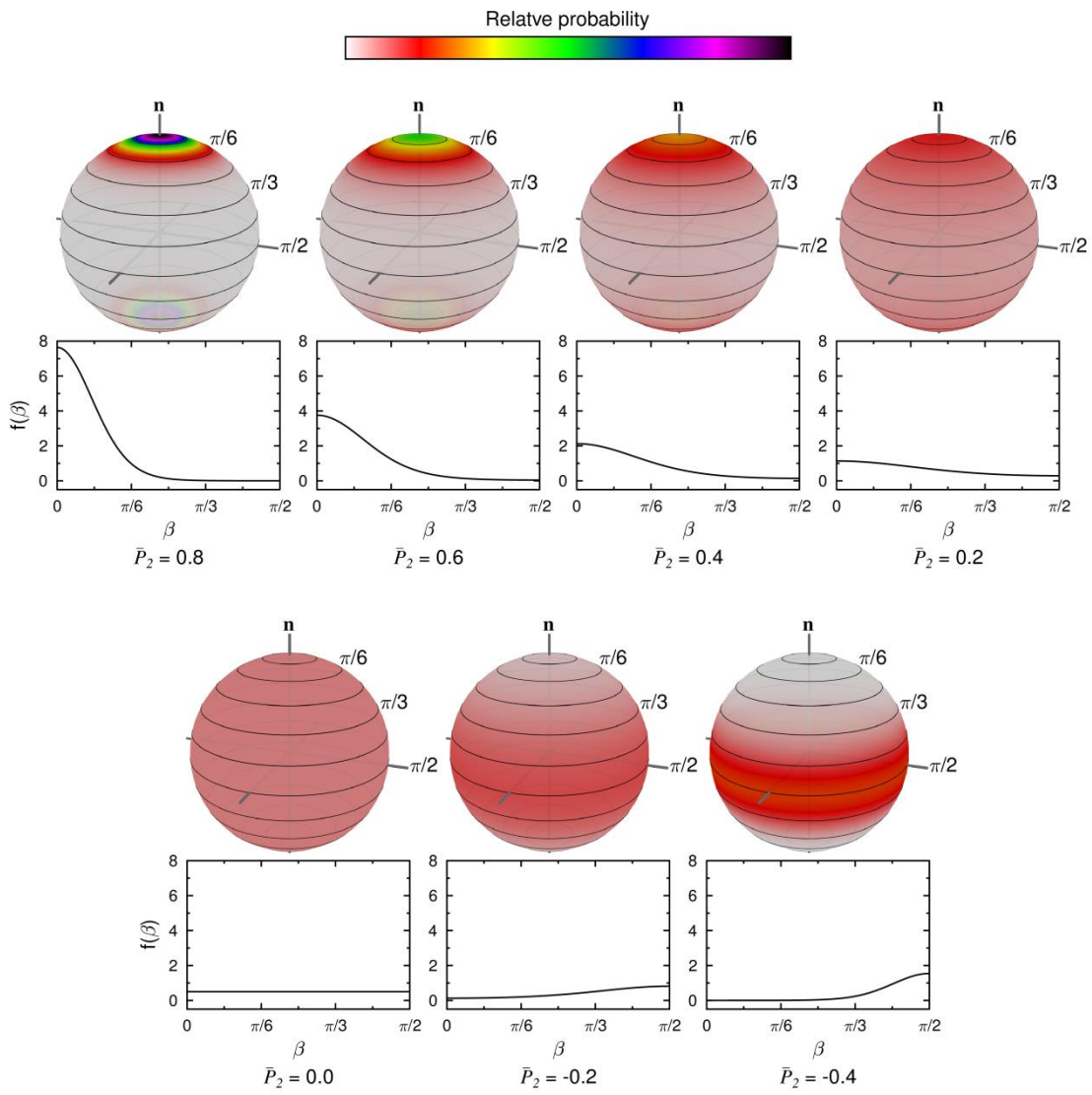


Figure 1.12 Distribution functions, $f(\beta)$, obtained for various values of $\langle P_2 \rangle$ using the maximum entropy approach.

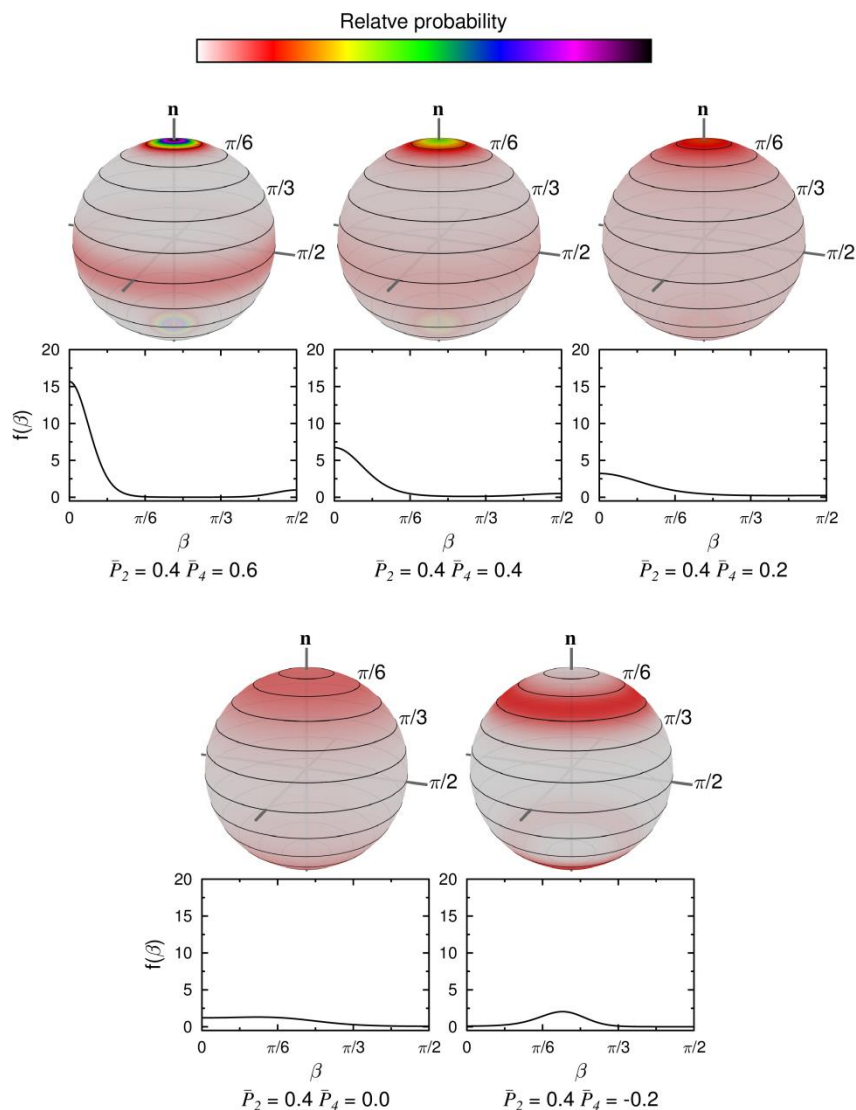


Figure 1.13 Distribution functions, $f(\beta)$, obtained for various values of $\langle P_4 \rangle$ when $\langle P_2 \rangle = 0.4$ using the maximum entropy approach.

A well-established example of an approach that uses a fixed functional form to obtain a full distribution is provided by Maier-Saupe theory, which predicts an orientational distribution function from a single $\langle P_2 \rangle$ value using an equation with a similar form to Equation (1.17), that also includes the temperature.^{26, 30} The variation in Figure 1.13 demonstrates the limitations of $\langle P_2 \rangle$ as a measure of the order of a system, showing that a single $\langle P_2 \rangle$ value may arise from a variety of distributions,²⁸ but the success of Maier-Saupe theory indicates the validity of such an approach across a range of systems.³⁵ However, in some contexts it is important to consider the different distribution functions that may give rise to a measured value of $\langle P_2 \rangle$, and guest-host systems are generally considered to fall into this category.

The alignment of a liquid crystal-dye mixture is typically characterised by polarised UV-visible absorption spectroscopy, and it is therefore the alignment of the electronic transition dipole moments (TDMs) of the dye molecules that is measured. In the context of guest-host devices, this is useful because it is the order parameter of the TDM that largely determines the contrast ratio of a device.²⁴ The alignment of the TDM is usually considered to arise from two contributions: the molecular orientations of the guest dyes within the host, and the orientations of the TDMs within the dye molecules. The angles defining the relative orientations in a guest-host system are shown schematically alongside the host director in Figure 1.14.

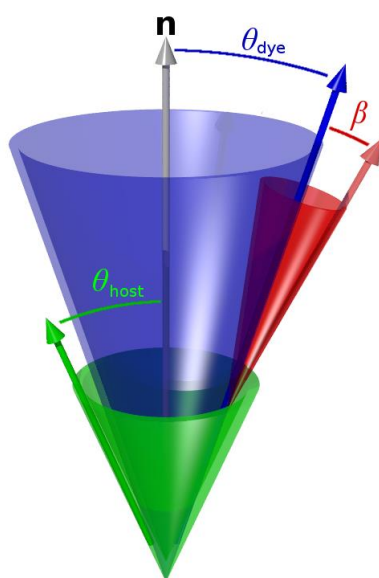


Figure 1.14 Schematic diagram defining the angles, θ_{host} and θ_{dye} , between the host and dye molecular axes, respectively, and the host director, \mathbf{n} , and the angle, β , between the dye TDM and the dye molecular axis.

Although Figure 1.14 shows the orientations as single angles for clarity to define them, in the case of θ for the host and the dye, this is not indicative of the actual distribution function, in which the host and dye molecules are expected to adopt a range of angles. In contrast, β is commonly assumed to be a fixed angle between the molecular axis and the TDM for a given dye, and therefore it is generally considered to have a δ -distribution against this molecular axis.²⁴

Hence, the alignment of the TDM of the dye molecules in a guest-host system arises from two contributions: the alignment of the dyes within the mixture, defined by a range of angles θ_{dye} , and the alignment of the TDM within the dye, defined by a fixed angle β .

If the alignment of the dye molecules is assumed to be axially symmetric, then the overall order parameter, S_ϕ , of the TDM of the dye measured against the host director may simply be expressed as a product of the two individual order parameters, given by Equation (1.20).³⁶

$$S_\phi = S_\theta S_\beta = \langle P_2(\cos \theta) \rangle (P_2(\cos \beta)) \quad (1.20)$$

1.3 Choice of host

For use in a practical guest-host device, a suitable host must fulfil a variety of criteria. The choice of mesophase may be determined by the mode of operation for which the mixture is intended; for example, a White-Taylor device (Figure 1.8) requires a chiral nematic host for operation. The host must exhibit the desired mesophase over an appropriately wide range of temperatures to allow a device to be of practical use, and it should have dielectric properties suited to the mode of switching desired. It is also important for a suitable host mixture to dissolve a sufficient concentration of dye to achieve a mixture with an intense colour. The alignment of the dye molecules within a host is influenced strongly by the alignment of the host molecules themselves, and for many applications it is therefore desirable for the host also to exhibit a high order parameter.

A variety of liquid crystalline host materials have been used in studies of guest-host systems. Amongst the most widely studied are cyanobiphenyl-based nematic systems,³⁷⁻⁴⁵ although some studies have been carried out on smectic systems, which tend to have higher order parameters that increase the order parameter of guest molecules.^{46, 47} In general, liquid crystal hosts comprise a mixture of component molecules, the type and concentration of which are designed to optimise the switching properties and the operating temperature range of the system. The components of the commonly used liquid crystal mixture E7, and their relative concentrations, are shown in Figure 1.15.

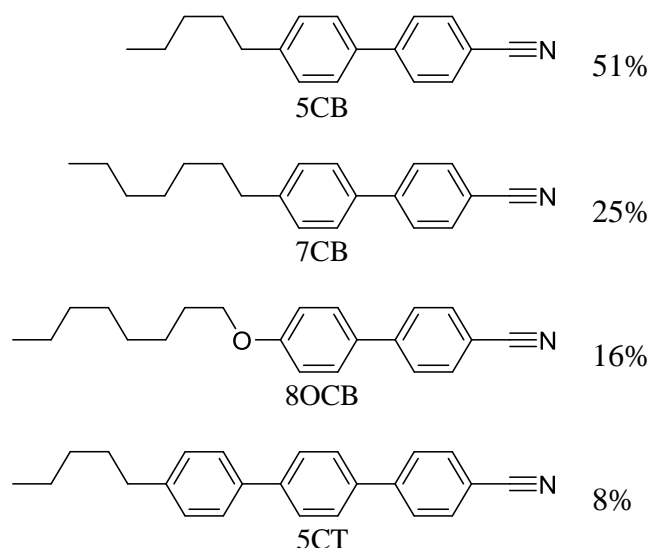


Figure 1.15 Components of the liquid crystal mixture E7 along with their abbreviations and their relative contributions by weight %.

In general, the order parameter of a guest in a host is more dependent on the order parameter of the host than on the particular chemical nature of the host, in the absence of any particularly strong guest-host interactions.²⁴ It is for this reason that the relative alignments of dyes within a single host are likely to be indicative of their behaviour in guest-host systems in general.

1.4 Choice of guest

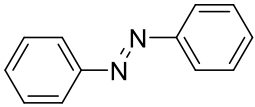
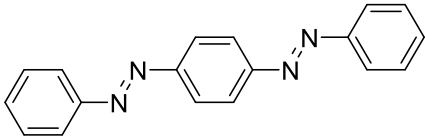
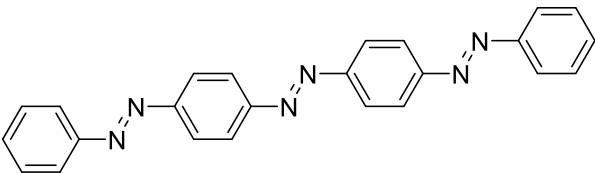
1.4.1 Azo dyes

Azo dyes containing the azo ($-N=N-$) linkage group are the largest class of commercial dyes, and they produce coloured compounds due to the electron delocalisation that arises from aromatic substituents appended to both ends of the azo group. Their widespread use in a range of applications is principally due to the ease and versatility of their synthesis, enabling a wide range of structures and resultant colours to be obtained, as well as due to the intense colours they exhibit.⁴⁸

After having been used in the first report of the guest-host effect,⁷ azo dyes have subsequently been widely studied as candidates for guest-host systems. Their use has been largely due to the rod-like shape of the chromophore, which generally results in both good alignment of the molecules within a liquid crystalline host and good

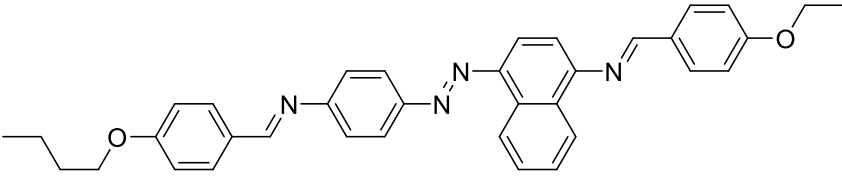
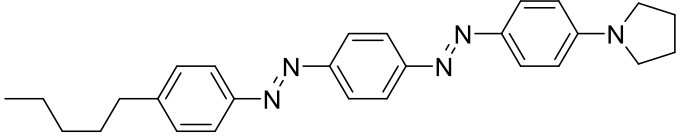
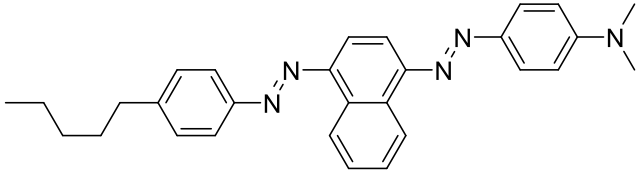
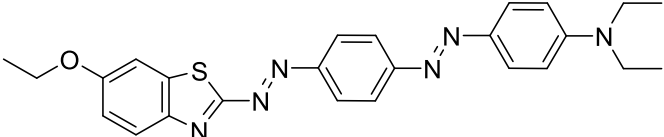
alignment of the TDMs within the dyes.^{10, 49} The ability to readily synthesise elongated molecules enables the molecular aspect ratios (length/breadth ratios) to be modified to obtain high order parameters, as illustrated by the experimental order parameter values, S_{exp} , given in Table 1.1.

Table 1.1 Structures and order parameters of some azo dyes in the nematic host E7.⁵⁰

Structure	S_{exp}
	0.37
	0.62
	0.64

The range of accessible synthetic modifications enables the optical properties of azo dyes to be tuned by using a variety of substituents. Early studies yielded azo dyes with a range of absorption maxima, λ_{max} , and colours, which exhibit order parameters of >0.7 in nematic hosts,¹² as given in Table 1.2. Further work incorporating ester groups into the structures has yielded azo dyes with order parameters > 0.8 .⁵¹

Table 1.2 Structures, visible λ_{\max} values and order parameters of selected azo dyes in the nematic host GR-31.¹²

Structure	λ_{\max} / nm	S_{exp}
	447	0.79
	507	0.78
	533	0.73
	570	0.78

As well as their good optical and alignment properties, the solubilities of azo dyes in liquid crystalline hosts tend to be high,^{37, 41} enabling devices using azo compounds to exhibit intense colours and high contrast ratios. However, despite the positive characteristics outlined here, azo dyes are generally considered to be impractical for applications in commercial devices due to their poor stability. The stability within the azo dye class has been shown generally to be better for red and yellow dyes than for blue and violet dyes, although there is still a tendency for all of the dyes to degrade over time.^{24, 49, 52, 53}

1.4.2 Anthraquinone dyes

Anthraquinone dyes are another important class of commercial dyes, and they are based upon the fused ring chromophore shown in Figure 1.16. A range of substituents may be used around the structure to obtain a full range of colours, although typically the colours of anthraquinone dyes are weaker than those of azo dyes.⁴⁸

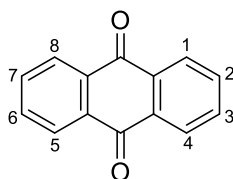


Figure 1.16 The structure of the anthraquinone chromophore.

Anthraquinone itself does not exhibit a strong colour,⁵⁴ but the addition of electron-donating groups to the chromophore results in relatively strong visible absorption bands, attributable to $\pi \rightarrow \pi^*$ intramolecular charge-transfer transitions between the substituent(s) and the carbonyl groups. This colour may be observed in the context of the absorption wavelengths of simple anthraquinone dyes such as those shown in Figure 1.17. The addition of more electron-donating substituents results in a red shift of the visible absorption band, as does the presence of hydrogen bonds with the carbonyl groups, which can be obtained by using appropriate donors in the 1-, 4-, 5-, and 8-positions, stabilising the charge-transfer state.⁵⁵

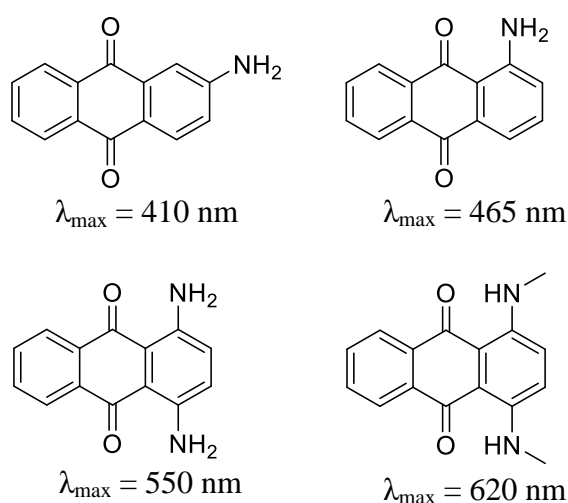


Figure 1.17 Structures and λ_{\max} values of some anthraquinone dyes in DCM.⁵⁶

Red shifts are also observed on going to more polar solvents, again as a result of stabilisation of the charge transfer excited state, as shown in Table 1.3,⁵⁷ although deviations from this trend are observed in structures that can form intramolecular hydrogen bonds.⁵⁸

Table 1.3 Visible λ_{\max} values of 1-aminoanthraquinone in several solvent systems with their solvent polarity functions (Δf) listed.⁵⁷

Solvent	Δf	$\lambda_{\max} / \text{nm}$
Cyclohexane	0.000	452
Decalin	0.002	454
Cyclohexane: Ethyl Acetate (90:10)	0.046	463
Ethyl Acetate	0.201	467

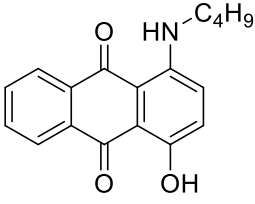
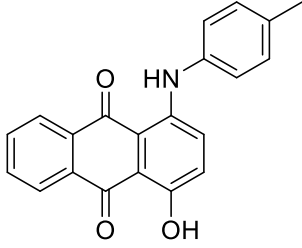
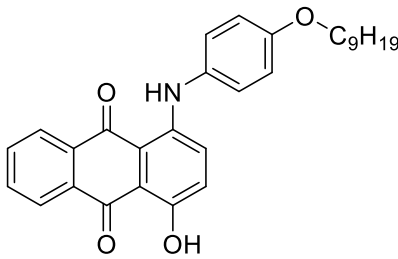
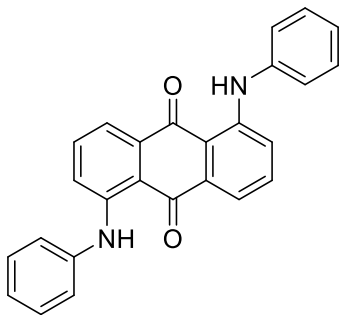
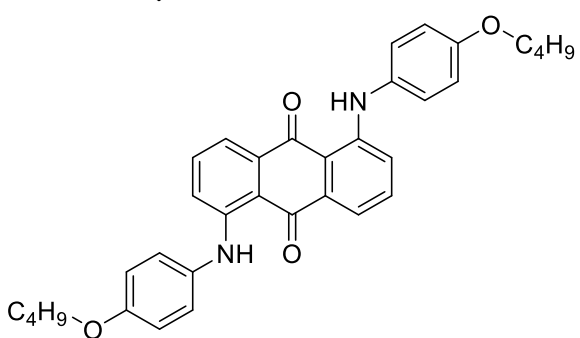
In the context of guest-host systems, anthraquinone dyes are attractive due to their stability. In particular, their light-fastness properties are generally superior to those of

azo dyes,⁴⁸ resulting in a significant amount of research into anthraquinone dyes in the context of liquid-crystal applications.

The molecular structure of the anthraquinone chromophore does not lend itself as readily to creating rod-like structures as the azo chromophore does. This possible drawback is evident from order parameters in the region of 0.6 in nematic hosts obtained for anthraquinone dyes with a range of colours, obtained from using various hydroxyl and amine substituents in the 1-,4-,5-,8- positions.²⁴

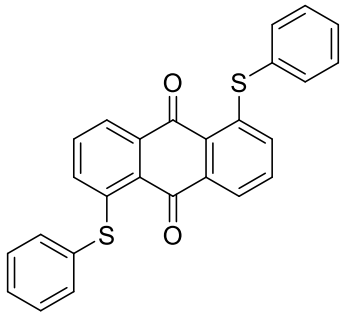
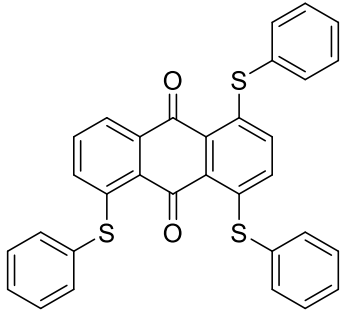
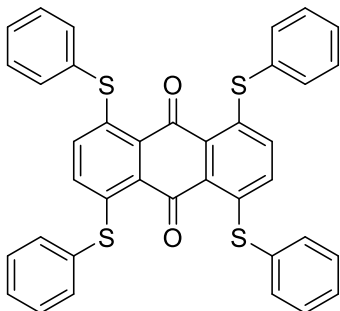
Much of the early work on anthraquinone-liquid crystal mixtures was carried out on compounds based on 1-phenylamino-4-hydroxy-anthraquinone, as shown in Table 1.4, after it was found that they exhibited both satisfactory solubility in liquid crystals and higher order parameters than their alkylamino counterparts.⁵⁹ Both elongation of the phenyl alkyl substituent and addition of a second phenylamino substituent in the 5-position were shown to result in an increased order parameter, as can be seen from the values in Table 1.4, and order parameters of up to 0.7 were achieved for compounds with a range of colours in nematic hosts.

Table 1.4 Structures, λ_{\max} values and order parameters of selected amino substituted anthraquinones in the nematic host E7.⁵⁹

	$\lambda_{\max} / \text{nm}$	S_{exp}
	570 ^a	0.43 ^a
	596	0.62
	596	0.65
	544	0.58
	556	0.66

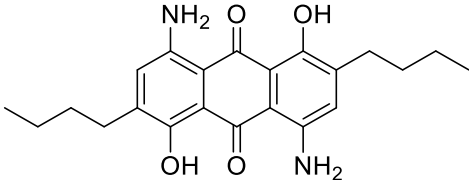
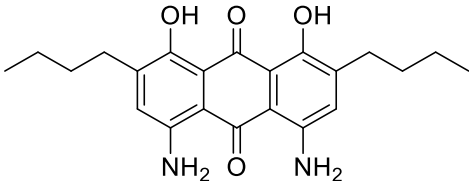
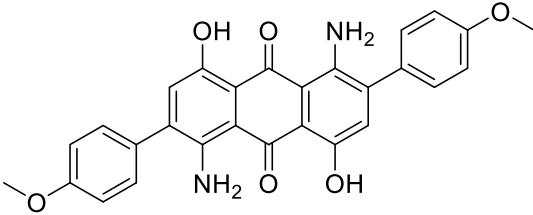
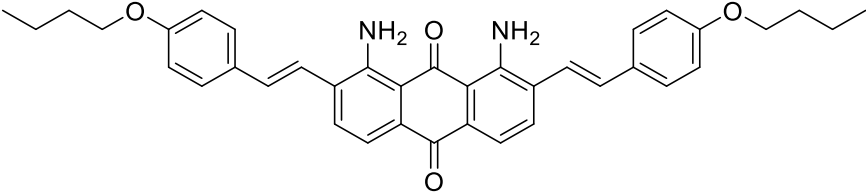
It was subsequently found that similar structures with a sulfide linking group instead of an amine linking group yielded materials exhibiting order parameters higher than 0.8 in nematic hosts in some cases, as shown in Table 1.5.⁶⁰ The complex nature of alignment in anisotropic systems is illustrated by these structures, because the tetra-substituted compound exhibits the same experimental order parameter as the di-substituted compound, but is much less rod-like in shape.

Table 1.5 Structures, λ_{\max} values and order parameters of selected sulfide substituted anthraquinones in the nematic host E43.⁶⁰

	$\lambda_{\max} / \text{nm}$	S_{exp}
	465	0.80
	520	0.79
	550	0.80

Anthraquinone compounds that are more rod-like have been investigated by adding substituents in the 2-, 3-, 6- and 7- positions, providing relatively high order parameters in nematic hosts, as shown in Table 1.6. However, the high degree of alignment displayed by these compounds is not obtained as readily with as wide a range of colours as that obtained with azo dyes.^{60, 61}

Table 1.6 Structures, λ_{\max} values and order parameters of selected 2,6- and 2,7- disubstituted anthraquinones in the nematic hosts E43^a and NP1132^b.^{60, 61}

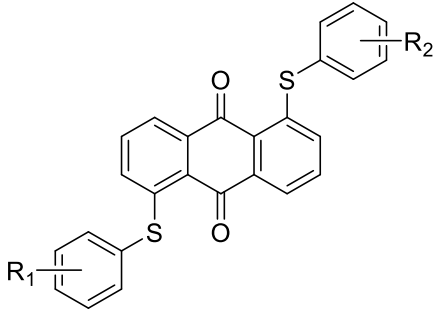
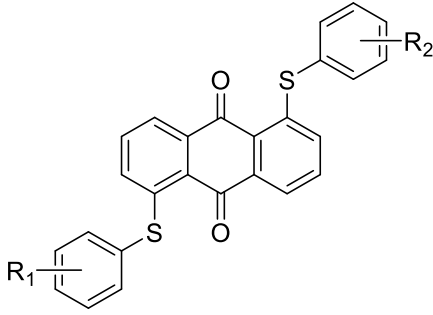
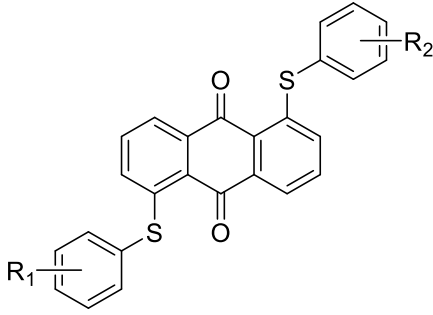
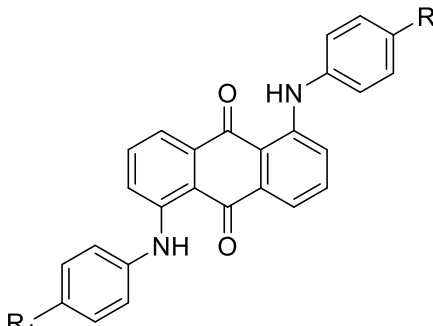
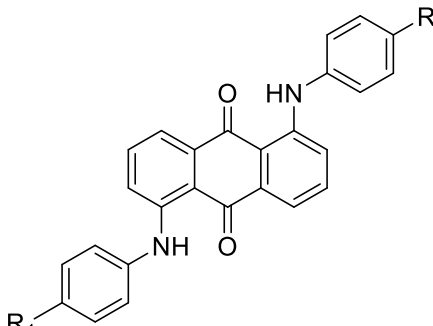
Structure	λ_{\max} / nm	S_{exp}
		0.72 ^a
		0.73 ^a
	612 ^b	0.73 ^b
	536 ^b	0.74 ^b

Another property that has proven challenging to optimise for anthraquinone-based dyes is their solubility in liquid crystal hosts. This property is particularly important because anthraquinone compounds commonly have significantly lower absorption coefficients than azo dyes,⁴⁸ consequently requiring higher concentrations than azo dyes to achieve the same colour intensity in a device. However, in general, anthraquinone dyes typically exhibit lower solubility than azo dyes,³⁷ especially in the case of sulfide substituted anthraquinones.⁶²

Due to the strong dependence of both order parameter and solubility on molecular structure, an alteration to optimise one parameter will generally have an effect on the other; for example, the addition of biphenyl substituents to anthraquinones has been shown to increase order parameters whilst decreasing the solubility.⁶³ However, in the case of some naphthylsulfide-substituted anthraquinones, both the order parameters and the solubilities were found to be higher than for the phenyl sulfide equivalents.⁶⁴

Typically, the trends described above have not been rationalised quantitatively, although some properties have been linked to specific structural units. For example, it has been suggested that the typically lower order parameters of amino-anthraquinones than sulfide-anthraquinones arise from the sulfide linkage being more flexible than the amine linkage.^{65, 66} Greater flexibility has also been suggested to enhance solubility in para-substituted phenyl sulfide compounds over their ortho-substituted analogues.⁶⁶ A general effect that has been observed is the significant increase of solubility for asymmetric dyes compared with symmetrically substituted dyes, but at the cost of ease of synthesis;^{60, 65-67} examples of this effect are shown in Table 1.7. The variation in solubility of a number of anthraquinone compounds has been correlated with the enthalpies of fusion and melting points of the dyes.⁶⁸

Table 1.7 Structures and room temperature solubilities of selected anthraquinone dyes in the nematic host LIXON 5052XX.^{65, 67}

Structure	Substituents	Solubility / wt %
	R ₁ = t-Bu (para) R ₂ = t-Bu (para)	0.05
	R ₁ = CF ₃ (meta) R ₂ = CF ₃ (meta)	0
	R ₁ = H R ₂ = H	0.07
	R ₁ = t-Bu (para) R ₂ = CF ₃ (meta)	5.4
	R ₁ = t-Bu (para) R ₂ = H	1.7
		R ₁ = t-Bu R ₂ = t-Bu
	R ₁ = t-Bu R ₂ = H	1.6

Eutectic mixtures of a set of anthraquinone dyes have also recently been shown to exhibit a variety of mesophases themselves, without the presence of any solvent.⁶⁹

1.4.3 Other dyes

In addition to research on azo and anthraquinone dyes, work has also been carried out on the behaviour of other chromophores in liquid crystal hosts, albeit to a lesser extent. The scope of this reported work is very wide, but example structures of some different classes of dyes and their properties are given in Table 1.8, and each class is discussed briefly below.

Tetrazine dyes have typically been found to exhibit low absorption coefficients, but their high solubilities in nematic hosts of *ca* 20 wt % means that intense colours can still be obtained. Two-ring species tend to have low order parameters of *ca* 0.5, whereas three-ring species have been shown to have higher order parameters of up to 0.8. These compounds also offer better stability than azo dyes, although they do not tend to be as stable as anthraquinones.⁷⁰

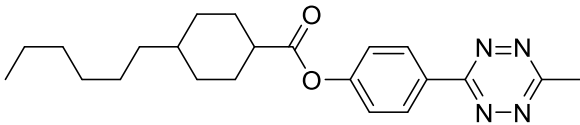
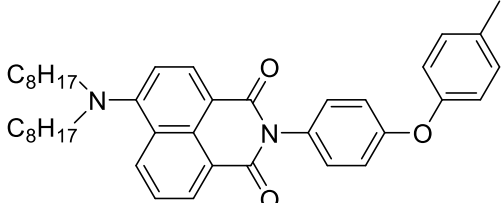
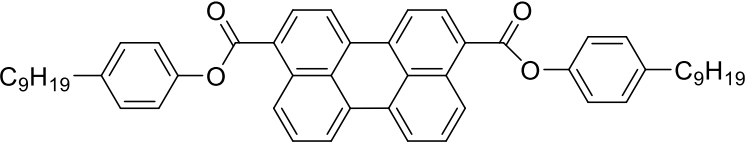
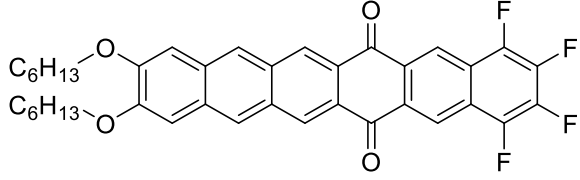
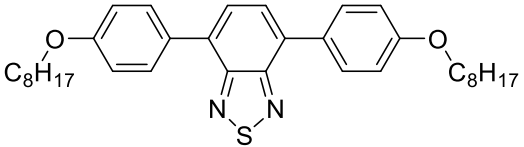
Some naphthalimide dyes exhibit order parameters of between 0.4 and 0.6 in nematic hosts, with solubilities of up to *ca* 5 wt%, and have good stability. They also exhibit strong fluorescence in the visible region, which can enable more visually appealing displays.⁷¹⁻⁷⁴

Research into perylene dyes as guests have shown that order parameters of up to 0.7 may be achieved by elongation of the structures with substituents containing rigid aromatic groups. These dyes also exhibit fluorescence and have solubilities in nematic hosts of up to *ca* 5 wt %.⁴²

Another class of dye displaying strong emission characteristics that have been analysed in nematic mixtures are acenequinones, which are similar in structure to anthraquinone dyes. Yellow dyes have been produced with order parameters above 0.7 with tuning of the emission properties possible by functionalisation of the core.⁷⁵

Substituted benzothiadiazole yellow dyes studied in this context exhibit absorption and emission, with order parameters of over 0.7 and high quantum yields of emission.⁷⁶

Table 1.8 Structures and properties of examples of different dye classes analysed in nematic liquid crystal mixtures.

Dye	Colour	S_{exp}	Solubility / wt %
 <p>Tetrazine</p>	red-violet	0.73	$\approx 20^a$
 <p>Naphthalimide</p>	yellow	0.53	$\approx 5^b$
 <p>Perylene</p>	yellow	0.69	$\approx 5^c$
 <p>Acenequinone</p>	yellow	0.75	
 <p>Benzothiadiazole</p>	yellow	0.73	

^a "Mi 24" host; ^b "ZLI 1695" host; ^c 8OCB host

1.5 Techniques

1.5.1 Electronic spectroscopy

Electronic spectroscopy is used as a method to obtain information about the electronic states of atoms and molecules. On irradiation of a sample with UV or visible light, a photon may be absorbed by a molecule when the photon energy matches the energy difference between the ground and excited states. In the context of dye molecules, it is electronic transitions occurring in the visible region of the electromagnetic spectrum, typically promoting an electron from the highest occupied molecular orbital (HOMO) to the lowest unoccupied molecular orbital (LUMO), which gives rise to the colours of the compounds.

A UV-visible absorption spectrum is usually measured by shining a beam of white light, between *ca* 190 and 900 nm, through a sample. The transmittance at any particular wavelength is defined as the ratio of the intensities of light having passed through the sample, I , to the incident light, I_0 . The absorbance of the sample, A , may then be obtained according to Equation (1.21).

$$A = \log\left(\frac{I_0}{I}\right) = -\log(T) \quad (1.21)$$

In a double-beam experiment, the incident light is split and passed through two samples, usually one containing the species of interest plus solvent and the other containing solvent alone. The transmittance may then be determined as the ratio of the intensities of the two beams after passing through the samples. In a single-beam experiment, the measurements of the solvent and sample of interest must be carried out sequentially and the transmittance determined subsequently.

The Beer-Lambert law, given in Equation (1.22), relates the absorbance of a sample to the concentration of the absorbing species in the sample, c , and the path length of the sample, l , using the molar absorption coefficient, ϵ , typically expressed in units of $\text{dm}^3 \text{mol}^{-1} \text{cm}^{-1}$.

$$A = \epsilon cl \quad (1.22)$$

The molar absorption coefficient enables quantitative comparison of the absorption strength of different samples at a given wavelength, but does not take into account the shape or the width of a given electronic absorption band.

An alternative parameter to quantify the absorption strength is the oscillator strength, f , which expresses the probability of a transition occurring. It may be obtained by measuring the integral of an entire absorption band in wavenumber, $\tilde{\nu}$, given by Equation (1.23), where n is the refractive index of the sample and k is a constant ($4.32 \times 10^{-9} \text{ dm}^{-3} \text{ mol cm}$).⁷⁷

$$f = (k / n) \int_{\nu} \epsilon(\nu) d\nu \quad (1.23)$$

The shape of an absorption band has a significant influence on the observed colour of a dye: a narrow, sharp band will give rise to a very bright colour, whereas a broad absorption band causes the colour to be dull.⁴⁸ The primary reason for the variation in shape of visible absorption bands is the coupling of the electronic transitions with vibrational transitions; on excitation, the electron density distribution within a molecule changes, resulting in a change in structure compared with the ground state.⁷⁸ According to the Franck-Condon principle, electronic transitions may be considered to take place instantaneously on the timescale of nuclear motion. An electronic transition may therefore be considered to occur between the equilibrium ground state geometry and the same geometry in the electronic excited state, in which the nuclei are no longer at an equilibrium position. The probability, and therefore the intensity, of a transition depends on the overlap integral between the ground and excited state vibrational wave functions, as shown in Figure 1.18. The number and separation of vibrational transitions associated with an electronic transition is the cause of the variation in electronic band shapes, and is dependent on the specific system in question. In gas phase spectra the vibrational structure may be resolved, but in solution samples intermolecular interactions with solvent molecules typically causes bands to broaden, often into a single peak.

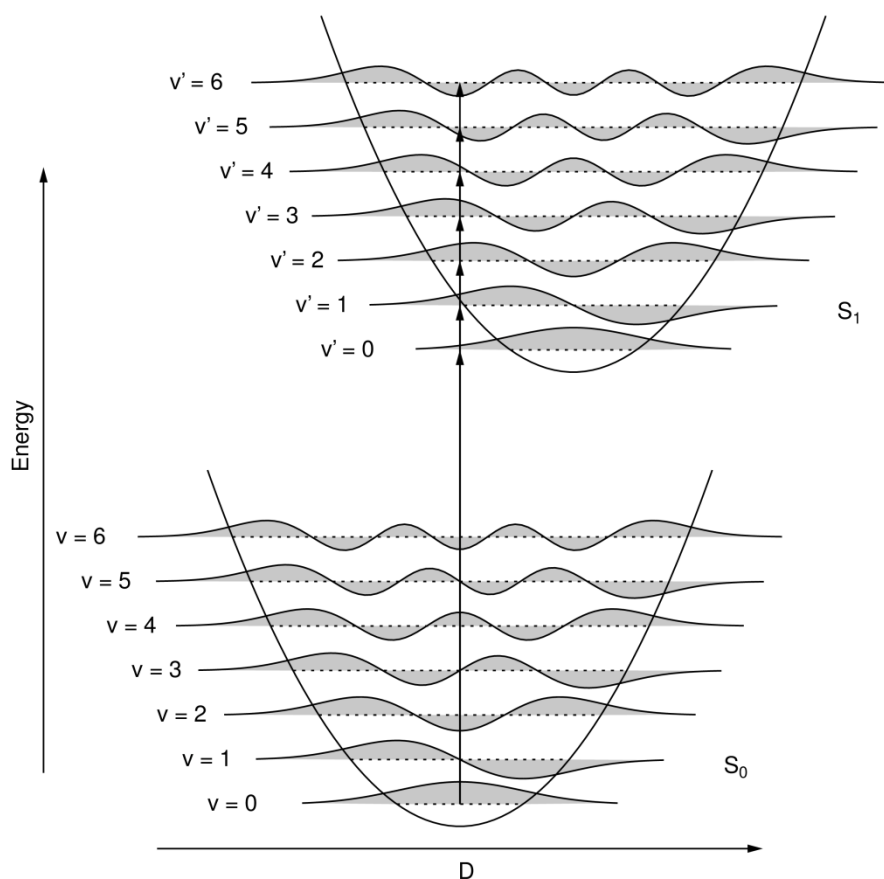


Figure 1.18 Schematic potential energy diagram of an electronic ground state (S_0) and excited state (S_1) and their harmonic vibrational levels and wave functions as a function of nuclear displacement, D .

1.5.2 Vibrational spectroscopy

The study of molecular vibration uses measurements of absorption or inelastic scattering of light resulting from changes in molecular vibrational energy. For a polyatomic molecule containing a number of atoms, N , the location of each atom may be expressed in terms of three coordinates, for example the cartesian x , y and z coordinates. Each atomic location may be specified independently of the positions of all the others, and therefore a molecule may be considered to have $3N$ degrees of freedom. Three of these degrees of freedom correspond simply to translation through space, and another three are accounted for by molecular rotation, leaving $3N-6$ degrees of freedom for a non-linear molecule that are accounted for by internal molecular vibration.⁷⁹ The separation of vibrational energy levels typically corresponds to the infrared region of the electromagnetic spectrum.

Vibrational transitions typically lie in the region between ≈ 300 and 3500 cm^{-1} , and in infrared (IR) absorption spectroscopy they are measured using a comparable method to that for recording UV-visible absorption spectra. Vibrational modes are IR active if the vibration gives a change in the dipole moment of a molecule, and the energy of the absorbed radiation corresponds to the difference in energies of the two vibrational states involved in the transition. Some vibrational modes may be considered to be local to particular functional groups, typically occurring above 1500 cm^{-1} , whereas other modes may be considered to arise from collective motions of many or all of the atoms.⁷⁸

Raman spectroscopy, which can also measure transitions between vibrational energy levels, is a complementary technique to IR absorption due to the fact that it relies on a different selection rule: for a vibrational mode to be Raman active, there must be a change in polarisability on vibration, and hence some modes may be IR inactive but Raman active and vice versa. Rather than an absorption technique, Raman spectroscopy is a scattering technique where incident monochromatic light is scattered inelastically by the sample, the difference in energy between the incident and scattered light corresponding to the energy of the vibrational transition. By using incident radiation coincident with the energy of an electronic transition, the intensity of scattered radiation from vibrational modes within the chromophore may be greatly increased, resulting in a large increase in the sensitivity of the technique; this approach is known as resonance Raman spectroscopy.

1.5.3 Nuclear magnetic resonance spectroscopy

Nuclear magnetic resonance (NMR) spectroscopy is a technique that utilises the property of nuclear spin to detect nuclei in different magnetic environments. For a nucleus with a spin quantum number $I > 0$ (e.g. ^1H), its angular momentum vector will have more than one possible orientation. The states arising from these orientations are typically degenerate, but on the application of an external magnetic field this degeneracy is lost and their energies become inequivalent. To utilise this practically, a sample is placed in a magnetic field and irradiated with a pulse of radio-frequency radiation to align the bulk magnetic moment of the sample. As the sample relaxes back to its equilibrium state, the emitted radiation is detected and Fourier transformed to produce an NMR spectrum.

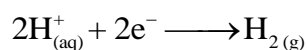
Variation in the frequency of emitted radiation from different nuclear environments is caused by deviations in the local magnetic field resulting from variation in electron density within a molecule. Nearby NMR-active nuclei may also influence the local magnetic field, causing splitting of NMR resonances into multiple signals depending on the number, nature and proximity of the nearby nuclei. The combination of the frequency of a resonance, the extent of the splitting, and the integration of the peak relating to the number of nuclei in the environment, can enable a large amount of structural information to be obtained from an NMR spectrum.⁷⁹

1.5.4 Electrochemistry

Electrochemical methods involve the measurement of electron-transfer processes, i.e. redox reactions. In general these processes are extremely important because they underpin many biological and industrial processes.⁷⁸ In the context of dye chemistry, their importance is particularly significant in terms of the stability of dye molecules, because electron-transfer processes are significant in dye degradation pathways.⁸⁰

Oxidation processes in which electrons are lost from a molecule, and reduction processes in which electrons are gained by a molecule, may be measured by electrochemical techniques. Measurements of the oxidation and reduction of a species may be carried out using a three-electrode cell. In this set-up, three electrodes are immersed in a solution of the compound of interest along with an electrolyte to ensure that the solution is conductive. The potential difference between a reference electrode and a working electrode is set by passing current through a counter electrode; the presence of the counter electrode negates the need to pass current through the reference electrode, enabling a stable potential to be obtained.

Ideally, the reference electrode should have a known, stable electrode potential vs. the standard hydrogen electrode, which is based on the following half-cell reaction, and is the standard against which electrode potentials are compared.



For aqueous samples, the reference electrode is most commonly the silver-silver chloride (Ag/AgCl) redox couple; however, this is not always practical for nonaqueous samples, and therefore a pseudo-reference electrode such as a silver wire may be used, along with a system of known potential such as the ferrocene (Fc/Fc⁺) redox couple that provides an in-situ calibration.^{81, 82} Working and counter electrodes are typically made from an inert metal such as platinum.

The electrode potential of a system is related to the position of equilibrium by the Nernst equation, given by Equation (1.24), where E is the electrode potential, E^\ominus is the standard electrode potential, R is the universal gas constant, T is the temperature, F is the Faraday constant, and a is the activity of the reduced/oxidised species.⁸¹

$$E = E^\ominus - \left(\frac{RT}{F} \right) \ln \left(\frac{a_{\text{red}}}{a_{\text{ox}}} \right) \quad (1.24)$$

The electrode potential may also be related to the Gibbs energy of the redox process, ΔG , according to Equation (1.25) where n is the number of electrons involved in the process.

$$\Delta G = -nFE \quad (1.25)$$

Cyclic voltammetry (CV) is one of the most common electrochemical techniques and uses a three-electrode cell. Typically, the potential of the working electrode is swept linearly from an initial voltage to a final voltage and back to the initial voltage, and the current is measured as a function of this applied potential. On the occurrence of an oxidative or reductive process, current flow is observed. Because the solution in a CV experiment is not agitated, the electrochemical processes at an electrode are diffusion controlled, resulting in the direction of the potential sweep affecting the voltage at which the peak current occurs. For this reason, electrode potentials from CV experiments are determined as the average of the voltages at which the forward and reverse peak currents occur. For a fully reversible and fast process, the peak potentials of the forward and reverse scans will be separated by $56/n$ mV and the oxidative and reductive peak currents will be identical.⁸¹

Spectroelectrochemistry is another electrochemical technique that uses a three-electrode cell, but rather than sweeping the potential at a constant rate, the potential is set to a fixed value, the system allowed to equilibrate, and a spectrum of the sample at the working electrode is recorded. The process is repeated for a number of applied potentials and the spectra may be plotted as a function of the applied potential. This method may therefore be used to characterise species undergoing redox reactions, in addition to determining redox potentials, and variants include UV-visible, IR and EPR spectroscopic monitoring. In particular, the use of UV-visible spectroelectrochemistry enables redox processes to be observed selectively and with high sensitivity for strongly absorbing compounds.

1.5.5 Electronic structure calculations

A fundamental basis of quantum mechanics is that for a chemical system there exists a wave function, Ψ , upon which appropriate functions or operators (\mathbf{O}) may act to yield observable scalar properties (o), as expressed in Equation (1.26). The square of the wave function, Ψ^2 , for a real wave function, corresponds to the probability density of the system.⁸³

$$\mathbf{O}\Psi = o\Psi \quad (1.26)$$

More specifically, the operator that yields the energy, E , of a system is termed the Hamiltonian operator, \mathbf{H} , yielding Equation (1.27), the time-independent Schrödinger equation.

$$\mathbf{H}\Psi = E\Psi \quad (1.27)$$

The Hamiltonian operator contains kinetic and potential terms, shown in Equation (1.28) in blue and red, respectively, for a molecular system containing nuclei (I, J) and electrons (i, j). The kinetic energy is a sum of the Laplacians, ∇^2 , for all the electrons and nuclei, where \hbar is the reduced Planck constant and m is the mass of an electron. The potential energy is the sum of the Coulombic forces between electrons and nuclei, where Z is the atomic number of a nucleus, e is the charge of an electron, and r is the distance between particles.

$$\mathbf{H} = - \sum_i^{\text{electrons}} \frac{\hbar^2}{2m_e} \nabla_i^2 - \sum_I^{\text{nuclei}} \frac{\hbar^2}{2m_I} \nabla_I^2 - \sum_i^{\text{electrons}} \sum_I^{\text{nuclei}} \left(\frac{Z_I e^2}{\Delta r_{iI}} \right) + \sum_i^{\text{electrons}} \sum_{j>i}^{\text{electrons}} \left(\frac{e^2}{\Delta r_{ij}} \right) + \sum_I^{\text{nuclei}} \sum_{J>I}^{\text{nuclei}} \left(\frac{Z_I Z_J e^2}{\Delta r_{IJ}} \right) \quad (1.28)$$

Exact solutions to the Schrödinger equation for anything other than the simplest systems cannot be obtained, but a number of constraints and approximations can simplify the problem. The probability density of the system, Ψ^2 , may be normalised because the probability density in all space is equal to 1. The wave function, Ψ , must also be antisymmetric according to the Pauli exclusion principle; hence, any valid wave function must also satisfy Equation (1.29), which shows that swapping any two electrons results in inversion of the sign of the wave function for a system of n electrons in n orbitals with coordinates r_n .⁸³

$$\Psi(r_1, \dots, r_i, \dots, r_j, \dots, r_n) = -\Psi(r_1, \dots, r_j, \dots, r_i, \dots, r_n) \quad (1.29)$$

For a given system there are many or potentially infinite acceptable solutions for Ψ to satisfy Equation (1.27). The variational principle states that the wave function best describing the ground state of a system will be that which yields the lowest energy; hence, when searching for the optimum solution to Equation (1.27), a wave function with a lower associated energy may be defined as a better description of the ground state than a wave function with a higher associated energy.⁸³

In electronic structure calculations, the Born-Oppenheimer approximation is usually applied, which enables the wave function of a molecule to be split into separate nuclear and electronic components. The approximation is based on the assumption that the speed of electrons is far faster than that of the nuclei, so on the timescale of nuclear motion the electronic wave function may be considered to relax to its ground state dependent on a “fixed” set of nuclear coordinates. Practically, this means that an electronic Hamiltonian, \mathbf{H}^{elec} , may be constructed that does not include the kinetic energy of the nuclei and does not include nuclear repulsion energy, which is readily calculated from the nuclear charges and their fixed positions. This electronic Hamiltonian may be used in the Schrödinger equation to obtain the electronic wave function, Ψ^{elec} , dependent on the positions of the electrons (\mathbf{r}) in a system of fixed nuclei (\mathbf{R}), and is related to the electronic energy, E^{elec} , by Equation (1.30).

$$\mathbf{H}^{\text{elec}}\Psi^{\text{elec}}(\mathbf{r}, \mathbf{R}) = E^{\text{elec}}(\mathbf{R})\Psi^{\text{elec}}(\mathbf{r}, \mathbf{R}) \quad (1.30)$$

A further approximation that may be applied is based on molecular orbital theory, which describes Ψ in terms of normalised orthogonal molecular orbitals. The simplest representation of a combination of molecular orbitals that generates an antisymmetric function is a Slater determinant, and it is this approximation that underpins the Hartree Fock (HF) method.^{83, 84}

Electronic structure calculations use basis sets, where the molecular orbitals are defined as linear combinations of specific normalised one-electron basis functions, each with associated molecular orbital coefficients. These basis functions are commonly gaussian-type functions for ease of calculation.⁸⁴ For example, the 6-31G(d) basis set used in this work models each atom using six gaussian functions for each core orbital, valence orbitals are described by two basis functions comprising 3 and 1 gaussian functions, respectively, and d functions are added to non-hydrogen atoms.⁸⁴ The lowest-energy solution for the wave function given these constraints is achieved by calculating the combination of molecular orbital coefficients that results in the minimum energy.

In order to carry out this minimisation using the HF method, the equality shown in Equation (1.31) is used, which arises from the variational principle. This equation relates a diagonal matrix of orbital energies, ϵ , to the Fock matrix, F , which represents the effect of all the electrons on each orbital, the overlap matrix, S , which represents the overlap between orbitals, and the molecular orbital coefficients, C .

$$FC = SC\epsilon \quad (1.31)$$

The Fock matrix and the molecular orbitals both depend on the orbital coefficients, meaning that the equation must be solved iteratively; this is known as the self-consistent field (SCF) method. At convergence, the molecular orbitals produce a Fock matrix, which in turn produces the same orbitals, within given convergence criteria.

Hartree-Fock theory has seen widespread use for many years, but there are some significant limitations that arise from the method. By describing the wave function as a single determinant, electron correlation (specific electron-electron interaction) is not

taken into account other than by exchange energy. Additionally, there is poor scaling with basis-set and system size, limiting the basis sets that are of practical use.⁸³

Density functional theory (DFT) methods are based on the Hohenberg-Kohn theorem that the ground state electronic energy of a system may be defined uniquely by minimising the energy using a functional of the electron density.⁸⁵ This utilisation of the 3-dimensional electron density provides a significant simplification compared with consideration of a $3N$ dimensional system of N electrons. It was also demonstrated that the density obeys a variational principle.

The Kohn-Sham method defines a set of component energies that are summed to give the energy functional of the electron density. This method is based on a system of fictitious non-interacting electrons to overcome the difficulty of calculating the kinetic energy of an interacting system of electrons. The energy functional takes the form of Equation (1.32), where E^T is the kinetic energy of the electrons in a system with the same density as the real system with no interactions, E^V includes Coulombic interactions involving electrons and nuclei, E^J includes Coulombic interactions involving only electrons, and E^{XC} is the exchange correlation term and includes the non-Coulombic electron-electron interactions, such as the antisymmetry of the wave function and the dynamic correlation in the motions of electrons.

$$E = E^T + E^V + E^J + E^{XC} \quad (1.32)$$

In order to obtain a solution for the minimum energy, a set of orbitals is defined in an analogous way to the HF method in which a Kohn-Sham determinant is constructed from a set of orbitals, themselves obtained from a combination of basis functions. This method enables minimisation of the energy to be carried out in a way that is comparable to the self-consistent HF method, but at much less computational expense.⁸⁶

The key limitation of DFT is the definition of the E^{XC} functional in Equation (1.32), which is usually divided into separate terms described by exchange functionals and correlation functionals. These functionals may each be of two main types: local functionals that depend only on the electron density, and gradient-corrected functionals that depend on both the electron density and its gradient. In practice, many

combinations of these exchange and correlation functionals are used, and a DFT method is defined by the particular combination used. For example, in this work, the B3LYP functional is employed, which is a combination of a Becke 3-parameter hybrid functional and the LYP correlation functional.^{87, 88}

After minimising the electronic energy of a given structure, a geometry optimisation may be carried out by changing the molecular coordinates, typically after calculating or estimating the derivative of the energy with respect to the nuclear coordinates to determine the gradient of the potential energy surface, and then iterating. A geometry is considered to be optimised when the forces on the nuclei fall below a given threshold and the calculated displacement for the next step of the calculation is also below a specified threshold.⁸⁴

An optimised structure and its associated wave function can be used to obtain further information about a molecular system. Molecular vibrational frequencies are dependent on the second derivatives of the energy with respect to the nuclear coordinates, and thus vibrational frequencies may be obtained from optimised structures.⁸⁴ Information about electronic transitions to excited states may be obtained by time-dependent DFT (TD-DFT) methods, which can provide excitation energies, oscillator strengths, and quantitative descriptions of the excitations in terms of changes in orbital occupancy and electron density distributions.⁸³

1.5.6 Molecular dynamics simulations

Molecular dynamics (MD) simulations are based on a very different principle from the electronic structure calculations described in Section 1.5.5 because, rather than typically considering static systems (i.e. systems without momentum at 0 K), MD calculations evaluate equations of motion of particles over time in order to model dynamic systems at specified temperatures. MD methods are based on the ergodic hypothesis, which states that, over an infinite period of time, the average properties of an observable of a system will match that of a statistical average. When applied in the context of a chemical system in which energy is conserved, this hypothesis means that simulating a system for a sufficient period of time will allow information to be obtained that is representative of a statistical energy distribution of the system.

In contrast to the quantum mechanical foundation of most electronic structure methods, systems of interacting particles are typically described using classical mechanics based on Newton's equations of motion. The relationships between the position, q , and momentum, p , of a particle of mass, m , at two different times, t_1 and t_2 , with acceleration, a , are given by Equations (1.33) and (1.34).⁸³

$$q(t_2) = q(t_1) + \int_{t_1}^{t_2} \frac{p(t)}{m} dt \quad (1.33)$$

$$p(t_2) = p(t_1) + m \int_{t_1}^{t_2} a(t) dt \quad (1.34)$$

Analytical expressions for the positions and momenta, are not easily obtained for anything other than the simplest systems, but Equations (1.33) and (1.34) may be approximated as Equations (1.35) and (1.36) using finite time-steps, Δt , providing a method of simulating a trajectory.

$$q(t + \Delta t) = q(t) + \frac{p(t)}{m} \Delta t \quad (1.35)$$

$$p(t + \Delta t) = p(t) + ma(t) \Delta t \quad (1.36)$$

A commonly used scheme in practice is the Verlet algorithm, based on Equation (1.37), which is obtained from taking the sum of the first two terms of the Taylor expansion for forward and backward time-steps, resulting in a step that is determined by the current, $q(t)$, and previous, $q(t - \Delta t)$, positions. An adaptation of the Verlet algorithm is the leapfrog algorithm, as used in this work.⁸³

$$q(t + \Delta t) = 2q(t) - q(t - \Delta t) + a(t)(\Delta t)^2 \quad (1.37)$$

The acceleration, a , can be calculated from the forces acting on a particle, which are obtained from the derivatives of the potential energy functions defined by the force field that is used to describe the interactions between particles, which is discussed further below.

MD simulations may vary considerably in terms of their treatment of a chemical system: atomistic simulations consider each atom in the system as one particle, united atom simulations combine multiple atoms into single particles, and coarse grain simulations treat molecules as one or more larger particles, representing, for example a molecular group.^{83, 89} Approaches combining atoms or groups into single entities are typically employed to reduce the computation time required for an adequate simulation of the system. All such systems require the definition of potential functions to describe the interactions between the particles in the system.

For atomistic simulations, as is the case in this work, the potential functions are split into bonded terms in which interactions along defined chemical bonds are considered, and non-bonded terms that are through-space interactions that may be inter- and/or intra-molecular interactions. Bonded interactions usually include bond stretching, bond angle bending and dihedral torsional potentials, whereas non-bonded interactions typically comprise Coulombic potentials between the charges assigned to the atoms, and non-Coulombic potentials that include both short-range repulsion and long-range attraction between atoms.⁹⁷

Defining the forms of the potentials is only part of the solution to defining the behaviour of the system, however. In order to model the system, coefficients for use in all these terms must be defined. Some of these quantities are relatively straightforward to define; for example, the Coulombic forces rely only on the charges assigned to each atom, which may be readily obtained from a variety of experimental or computational methods, but defining other terms such as torsional force constants may be significantly more challenging, and time consuming. To overcome these challenges, molecular force-fields have been developed in which values for specific atoms and groups are defined. These force fields are based on the principle of transferability, in which it is assumed that properties of particular atoms and groups, such as equilibrium bond-lengths and angles and their associated force constants, will be the same or similar for comparable groups in different molecular environments. The success of MD simulations shows that this assumption may be considered valid in a wide variety of chemical systems,⁹⁰ but the validity of the assumption must be carefully considered before applying variables from a force field to components of a simulation. Force field variables are typically parameterised to enable simulations to replicate experimental observables; for example,

the OPLS force field used generally in this work was parameterised against experimental properties of liquids, such as density and enthalpy of vaporisation.⁹¹

MD simulations may be used to model a variety of ensembles, as defined by the properties of the system that are held constant. Common examples of these are: the canonical (N, V, T) ensemble in which the number of particles, N , the system volume, V , and the temperature, T , are kept constant; the microcanonical (N, V, E) ensemble in which the energy of the system, rather than the temperature of the system, is constant; and the isothermal-isobaric (N, P, T) ensemble in which the pressure and temperature are both constant. The choice of ensemble is determined by the intention of the simulation, and the isothermal-isobaric ensemble is typically the best representation of an experimental system under atmospheric pressure and temperature. In order to maintain constant pressure or temperature in a system, thermostats and barostats are also commonly applied while running simulations.

In general, the longer the simulation time, the better the description of the statistical ensemble that is obtained, due to the ergodic principle on which MD simulations are based. In practice, the simulation time is often limited by the computation time, and verification is required to demonstrate that a simulation time is sufficient to give an adequate measure of the variable(s) of interest. MD simulations are run with fixed time-steps that define the interval between which the forces on all the particles in the system are evaluated. These time-steps must be shorter than the shortest timescale in the simulated system, which typically corresponds to the oscillation of bond stretching motion for a fully atomistic simulation. In some cases, constraints may be used if they do not significantly affect the outcome of the intended simulation analysis; for example, constraining bonds to their equilibrium distances may allow longer time steps to be used, which may significantly reduce the overall computation time of a simulation.

Another key consideration for the computation time is the size of the system to be simulated. The constraints of computation time typically limit the system size to one in which surface effects at the boundary of the simulation box would dominate the system, or are at least significant. To overcome this limitation, periodic boundary conditions are often used, in which the simulation box is assumed to be a unit of an infinite number of identical cells in all directions. Under these conditions, a molecule on the edge of the

simulation box will not interact with a surface, but rather will interact with the molecules at the opposite side of the box. Although this allows smaller system sizes to be used in many cases, care must still be taken to ensure that the box size is large enough for artefacts arising from system size to be avoided.

1.5.7 Ab-initio molecular dynamics simulations

The electronic structure methods and molecular dynamics methods described above are both enormously successful and in widespread use, but there is no overlap between the two approaches as described. The electronic structure calculations described in Section 1.5.5 are typically ab-initio, reliant only on an input of atom types, coordinates, charge and multiplicity to obtain chemical information on a static system. Molecular dynamics simulations are far from ab-initio because the use of force fields, typically parameterised to replicate experimental observables, is inherent to the method, and there are additional assumptions associated with treating species classically. Nevertheless, MD methods do allow the simulation of dynamic systems experiencing user-defined conditions, which is extremely useful when making comparisons with experimental conditions. Ab-initio molecular dynamics (AIMD) simulations bridge this gap to some extent, enabling the simulation of dynamic systems requiring only the input of the fundamental information required in electronic structure calculations.^{83, 92} The major hurdle in applying AIMD methods is that of computation time; adding time as an additional dimension to ab-initio calculations means that computation times are inherently extremely long unless approximations are made.

Ehrenfest molecular dynamics is a method based on the time-dependent Schrödinger equation in which the nuclear and electronic contributions to the total wave function of a system are separated. The motion of the nuclei is calculated classically and the time-dependent electronic wave function is solved self-consistently and simultaneously, enabling a trajectory to be modelled, but the required time steps are necessarily very small due to the high speed of the electronic motion.⁹²

An alternative but intuitive approach to calculating a trajectory by an ab-initio method is to optimise the time-independent wave function of a system, calculate the forces on each nucleus, apply a thermostat to the nuclear motion if required, and displace the

nuclei for each step of the simulation.⁹³ This approach is the basis for Born-Oppenheimer Molecular Dynamics (BOMD), which assumes that the propagation of the electronic wave function through time is adiabatic and defined only by the classical motion of the nuclei without the feedback present in Ehrenfest molecular dynamics. This method overcomes the time-step limits because only the much slower nuclear motion limits the step size, but optimisation of the wave function at each step is computationally expensive in its own right.

An approach that incorporates the benefits of each of these methods is Car-Parrinello molecular dynamics (CPMD),⁹⁴ as used in the latter part of the work reported here. This approach treats the systems of electrons and nuclei classically, taking advantage of the adiabaticity caused by the differences in timescale of electronic and nuclear motion that forms the basis of the Born-Oppenheimer approximation.

In classical mechanics, the forces acting on a system may be calculated by taking the derivative of a suitable Lagrangian; in its simplest classical case, the Lagrangian would simply be the kinetic energy minus the potential energy of the system. In order to apply this to a system of nuclei and electrons, Car and Parrinello introduced a Lagrangian to take into account the various components of kinetic and potential energy present. The kinetic energy of the nuclei may be calculated classically, and the potential energy of the total system may be obtained using the appropriate Hamiltonian of the wave function as described in Section 1.5.5. The kinetic energy of the electrons is more complicated, but to make the calculation feasible a fictitious electron mass, μ , was introduced that is assigned to molecular orbital coefficients, enabling them to be treated classically.⁸³ Additionally, constraints are imposed to maintain orthonormality of the orbitals.⁹² The time-steps of simulations utilising these methods are still constrained by the motion of the electrons, but the constraints are much less than those imposed by Ehrenfest molecular dynamics due to the introduction of μ . Although the time steps must be smaller than those that may be achieved using BOMD, the classical consideration of the electrons negates the need to reoptimise the wave function at each time-step, providing a significant computational advantage over both methods.

The CPMD method is typically implemented using DFT functionals and Kohn-Sham orbitals, described using plane-wave basis sets alongside pseudopotentials. In contrast

to gaussian-type basis sets, plane-wave basis sets describe the wave function not as localised functions centred on nuclear coordinates, but as an expansion of a discrete set of plane waves.⁹⁵ Plane-wave basis sets allow easier calculation of the integrals required to obtain the forces and are particularly well suited to simulations utilising periodic boundary conditions.⁸³ For plane-wave basis sets to be used, pseudopotentials are employed, which approximate the chemically inert core electrons by treating them as rigid non-polarizable cores. By explicitly considering only the valence electrons, the degrees of freedom in the Hamiltonian are reduced, resulting in a significant reduction in the basis set size, particularly for heavier elements.⁹² In this work, the BLYP functional is employed, along with Vanderbilt ultrasoft pseudopotentials.⁹⁶

In principle, a trajectory using the CPMD method should match that obtained using BOMD, and in order to ensure that this is the case, the nuclear and electronic sub-systems must not exchange energy, i.e. the fictitious temperature of the electrons must remain constant and much lower than the temperature of the ionic system. This condition is typically achieved by choosing a low enough value for the fictitious mass, alongside independent thermostating of the electronic and nuclear sub-systems. Fluctuations still occur compared with the true Born-Oppenheimer energy surface, but these are small and very rapid, so on the timescale of the nuclear motion the effect is negligible due to cancellation of these fluctuations.⁹²

1.6 Aims

A set of five rod-like anthraquinone dyes, shown in Figure 1.19, formed the basis of the work reported in this thesis. These dyes formed part of a wider set of high purity anthraquinone dyes that had recently been synthesised in York,⁶⁹ and were chosen to provide a closely related set of structures, all terminating with propyl groups, but with variations in the linking groups and other substituent groups on the anthraquinone core to provide a range of colours. Compounds based on the sulfide and amine substituted species, 15SB3, 15NB3 and 15NB3OH, have been the subject of several previous studies in liquid crystal hosts,^{60, 62-65, 67, 97, 98} whereas the direct phenyl substituted structures, 26B3 and 26B3OH, have been the subject of much less work.

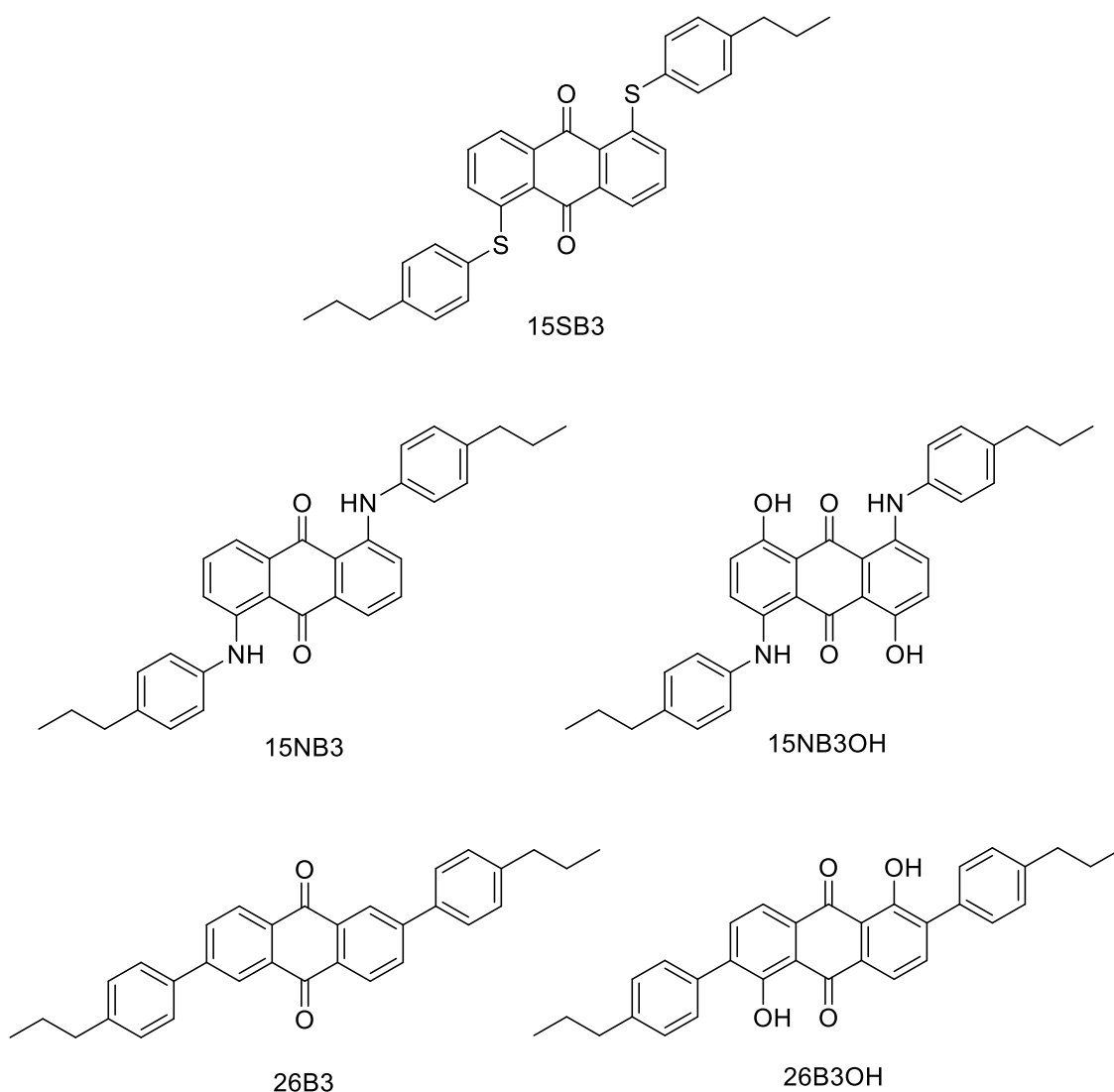


Figure 1.19 Structures and abbreviated names of the anthraquinone dyes studied in this work.

The overall aim of the project was to apply a variety of experimental and computational methods to these compounds in order to assess and rationalise their behaviour in solution and in liquid crystal hosts. The intention was to explore the possibility of elucidating structure-property relationships for these dyes, both qualitatively and quantitatively, and to try to understand the fundamental features from which such relationships derive; in a broader context, the intention was to assess the usefulness of developing such an approach to aid in the rational design of new dyes intended for guest-host applications.

The initial aim was to study the dyes in isotropic solutions using a range of spectroscopic and electrochemical methods, allied with DFT calculations to aid interpretation of the results, and thereby to gain information on the molecular structures, properties and stabilities of the dyes, and this work is described in Chapter 3.

A further aim was to extend both the experimental and computational methods to study the dyes within liquid crystal hosts, primarily through the use of polarised UV-visible spectroscopy of aligned samples, and to attempt to model these guest-host systems using molecular dynamics simulations, and this work is described in Chapter 4. By measuring these properties and modelling the systems computationally, the intention was to identify structural features that are critical to determining properties such as the colour, the stability, the orientation of the TDMs, the molecular shape, and the overall alignment of the dye molecules within liquid crystalline systems.

The implications arising from the results of Chapters 3 and 4 are assessed in Chapter 5, and extensions and improvements of the methods developed are considered in Chapter 6, before the scope of the methods is considered in Chapter 7. Chapter 8 draws together the conclusions from the work as a whole and outlines potential future work arising from this project.

Chapter 2

Experimental

2.1 Materials

The synthesis, purification and characterisation of 15SB3, 15NB3, 15NB3OH, 26B3 and 26B3OH has been reported previously.⁶⁹ E7 and KBr (>99.5%) were used as received from Merck and Fisons, respectively. Ethanol (analytical grade), methanol (>99.9%) and dichloromethane (DCM; >99.9%) were used as received from Fisher. *p*-xylene (>99%), acetonitrile (anhydrous, 99.8%), duroquinone (97%) and tetrabutylammonium hexafluorophosphate (TBAHFP; >99%) were used as received from Sigma Aldrich. The ferrocene used had been previously purified by sublimation.

2.2 Sample preparation

Guest-host mixtures were prepared by heating samples of the dyes in E7 above the clearing point of E7 to ensure full dissolution of the dyes, before cooling to room temperature and sonicating for *ca.* 2 minutes. Visual inspection of the samples and viewing under a microscope showed no evidence of dye precipitation.

Slides for aligned mixtures were prepared by spin coating glass microscope slides with a saturated solution of nylon-6,6 in formic acid, before drying the slides in an oven at 100 °C. The slides were rubbed in a single defined direction to align the surface coating, and cells with a path length of *ca.* 20 μm were constructed from two slides with parallel inward-facing alignment layers. Observation through a microscope with crossed-polarizers confirmed alignment of nematic samples within the cells.

2.3 Experimental techniques

2.3.1 UV-visible absorption spectroscopy

UV-visible absorption spectra were recorded using a Hitachi U-3010 spectrophotometer with a scan rate of 600 nm min^{-1} and slit widths of 2 nm. Matched quartz cuvettes (1

mm or 1 cm) were used to measure spectra of isotropic samples versus solvent at room temperature (*ca.* 298 K).

Polarised spectra of aligned samples were recorded at 300 K versus air with a Glan-laser polarizer (Newport 10GL08) fixed between the lamp and the sample. Each guest-host sample was rotated to obtain the maximum absorbance at the visible wavelength of maximum absorption for the parallel absorbance measurement, A_{\parallel} . The sample was then rotated by 90° for the perpendicular absorbance measurement, A_{\perp} . Polarised spectra of an aligned sample of E7 alone recorded using the same method were subtracted from the guest-host spectra, scaled according to the cell path lengths, to obtain the data presented.

2.3.2 Vibrational spectroscopy

2.3.2.1 IR spectroscopy

IR spectra were recorded using a Perkin-Elmer Impact 1000 FTIR spectrometer and a resolution of 4 cm⁻¹, referenced against air. Samples were prepared as KBr disks by adding 0.5 mg of dye to 20 mg of KBr and pressing to *ca.* 5 tonnes.

2.3.2.2 Raman spectroscopy

The Raman apparatus used has been described in detail previously.⁹⁹ All spectra were recorded using an excitation wavelength of 514.5 nm from a Spectra Physics 2025 argon ion laser. The scattered light was collected at 90° to the incident beam, dispersed through a Spex 1403 double monochromator with a 30 μm slit width, and detected using a liquid nitrogen cooled CCD detector. The resolution was *ca.* 4 cm⁻¹ and the accuracy was ±2 cm⁻¹. Solution phase spectra were recorded using a spinning cell and with concentrations of *ca.* 5 × 10⁻⁴ mol dm⁻³. Spectra were recorded using four 300 s exposures giving a total acquisition time of 20 minutes. Fluorescence backgrounds were then subtracted from the spectra, which were calibrated against spectra of 1,4-dioxane, acetone and benzene. UV-visible absorption spectra were recorded before and after each Raman experiment to monitor the sample for bleaching due to the laser irradiation, and the Raman spectra were also monitored throughout the data acquisition. The UV-visible

absorption of the samples were shown to be consistent before and after each Raman experiment, and Raman spectra were consistent between each of the exposures.

2.3.3 NMR spectroscopy

^1H (500 MHz) NMR spectra were recorded using a Bruker AV500 spectrometer at 300 K and peaks were referenced against residual solvent bands. Spectra were recorded from dyes at a concentration of $1 \times 10^{-2} \text{ mol dm}^{-3}$ in deuterated dichloromethane.

2.3.4 Dielectric permittivity

The capacitance values were measured using an INSTRON ALCT Property Tester at 25 °C. Initially, the capacitance of an empty cell with an aligned surface coating was determined. The cell was then filled via capillary action with E7, heated to produce the isotropic phase and then cooled to 25 °C. The capacitance was measured as a function of the applied AC voltage (1 kHz), and the permittivity of E7 defined as the ratio of the capacitance of the filled cell to that of the empty cell.

2.3.5 Electrochemistry

2.3.5.1 Cyclic voltammetry

Cyclic voltammograms were recorded from solutions of the dyes at $1 \times 10^{-3} \text{ mol dm}^{-3}$ in DCM, in the presence of TBAHFP at 0.1 mol dm^{-3} as an electrolyte. The samples were purged for 10 minutes with nitrogen prior to measurements being taken and a positive pressure of nitrogen was maintained during the measurements. Voltammograms were recorded using an EG&G Princeton Applied Research potentiostat (model 273) with its associated software for recording voltage and current. A platinum wire counter electrode, a silver wire pseudo-reference electrode and a platinum disk working electrode were used. The applied potentials were swept linearly at a rate of 100 mV s^{-1} , initially to negative potential. Electrode potentials were referenced against the potential of the ferrocene/ferricenium (Fc/Fc^+) couple,^{100, 101} which was determined as the average of the forward and reverse peaks of this couple

within a voltammogram recorded after the addition of ferrocene to each dye sample at *ca.* $1 \times 10^{-3} \text{ mol dm}^{-3}$ immediately after the measurement of each dye solution.¹⁰⁰

2.3.5.2 Spectroelectrochemistry

UV-visible spectroelectrochemical measurements were recorded from samples at room temperature in a custom cell consisting of a Pt gauze working electrode in a 1 mm pathlength quartz cell, a Pt wire counter electrode, and a silver wire pseudo-reference electrode. An EG&G Princeton Applied Research potentiostat (model 273) was used to control the potential. The spectra were recorded from saturated solutions of the dyes in acetonitrile, in the presence of TBAHFP at 0.1 mol dm^{-3} as an electrolyte. The solutions were purged with nitrogen for 15 minutes and remained under a positive pressure of nitrogen for the duration of each experiment. After applying each potential, the sample was left to equilibrate for 10 minutes prior to recording a spectrum. The measurements of duroquinone were carried out in the same way. All redox potentials are reported vs. the Fc/Fc^+ redox couple,^{100, 101} measured from a solution of ferrocene using the same method as for the dyes (described in the main text) and baseline-corrected spectra are presented.

2.4 Computational methods

2.4.1 Electronic structure calculations

All DFT and HF calculations were performed using the Gaussian 09 software package.¹⁰²

Optimisations for structural studies, vibrational calculations and subsequent TD-DFT calculations were carried out using the B3LYP functional^{87, 103} and the 6-31G(d) basis set. The structures were optimised for the molecules in the gas phase with the propyl chains in their all-*trans* configurations. Structures of neutral and charged species for the calculation of electrode potentials were obtained from structures optimised in an acetonitrile solvent field using the SMD solvation model.¹⁰⁴ Structures for MD force

constant parameterisations were optimised at the HF/6-31g(d) level in the gas phase with the propyl chains in their all-*trans* configurations.

Calculated vibrational wavenumbers were scaled by a factor of 0.9614¹⁰⁵ and the resultant calculated vibrational spectra were created by adding a gaussian profile of 12 cm⁻¹ width (full-width at half-maximum) to each line, with peak heights proportional to the calculated intensities.

TD-DFT calculations of the gas phase structures were carried out at the same level of theory as the structural optimisations, and calculated UV-visible absorption spectra were subsequently produced by summing gaussian bands of 50 nm width (full-width at half-maximum) with peaks at the calculated transition wavelengths and with the respective oscillator strength.

Calculated ¹H NMR resonances of the gas phase structures were obtained using the GIAO method,¹⁰⁶ and are reported relative to tetramethylsilane calculated to the same level of theory. Peaks were split into multiplets according to coupling constants calculated by DFT, and calculated spectra were then produced by adding gaussian profiles of 0.002 ppm linewidth (full-width-half-maximum).

2.4.2 MD simulations

Fully atomistic *NPT* MD simulations of the host and of guest-host mixtures were carried out using the GROMACS 4.5.5 package¹⁰⁷⁻¹¹⁰ and the OPLS AA force field,^{91, 111} except for inter-ring biphenyl torsions for which reported force constants were used,¹¹² or where stated in the main text. Atomic charges of the dyes for use in the MD simulations were determined using the HLY method for the DFT optimised structures,¹¹³ which is a method that has been shown to demonstrate little dependence on the specific molecular geometry. The simulations for analysis were run at 300 K using a velocity-rescale thermostat,¹¹⁴ 2-fs time-steps, with periodic boundary conditions, and were maintained at a pressure of 1 bar with Parinello-Rahman pressure coupling.¹¹⁵ A cut-off of 9 Å for van der Waals interactions was used without dispersion correction, and electrostatic interactions were calculated using the Particle Mesh Ewald method,^{116, 117} also with a cut-off of 9 Å. All bonds were constrained to their equilibrium lengths during the

simulations using the P-LINCS algorithm.¹¹⁸ Further details about the simulations are described in the main text. The simulation trajectories were sampled every 10 ps and were analysed using Gromacs analysis tools or software written in Perl as part of the work reported here.

NVT simulations of isolated molecules were carried out in cubic cells of $4 \times 4 \times 4$ nm without periodic boundary conditions and using infinite van der Waals and Coulomb cut-offs. Other parameters used were identical to the guest-host simulations. The trajectories were sampled every 1 ps.

2.4.3 Ab initio MD simulations

Simulations of isolated dye molecules were carried out using the CPMD program, version 3.17.1.¹¹⁹ The molecules were simulated in cells of $32 \times 16 \times 16$ Å with periodic boundary conditions, using the BLYP functional^{103, 120} and Vanderbilt ultrasoft pseudopotentials,⁹⁶ with a wave function cut off of 30 Ry. All hydrogen atoms were assigned the mass of deuterium to enable the use of longer time-steps than for hydrogen in accordance with standard methods.¹²¹⁻¹²³ Initial equilibration runs of 2 ps were used, followed by production runs of 50 ps using time-steps of 5 a.u. (0.121 fs), and the trajectory was sampled every 20 steps. The temperature was maintained at 300 K using a Nose-Hoover thermostat,¹²⁴⁻¹²⁶ and a fictitious electron mass of 400 a.u. was employed. The total energy of each system was monitored and found to vary by less than 1×10^{-4} % during the course of each production run.¹²⁷

2.5 Molecular surfaces

Molecular surfaces were calculated using the MSMS algorithm¹²⁸ applied to structures comprising spheres of radii defined as the atomic van der Waals radii¹²⁹ centred at the calculated atomic coordinates. Further details are provided in the main text.

2.6 Data analysis and processing

Spectra were generally processed using Grams 32AI software (Galactic Industries). All NMR analysis was carried out using Bruker TOPSPIN 3.2. Non-linear regression analyses were performed using R.¹³⁰

Axes of minimum moment of inertia were defined as the eigenvector associated with the minimum eigenvalue of the inertia tensor for all structures studied.¹³¹ Aspect ratios were calculated from molecular lengths defined as the maximum distance between points on the molecular van der Waals surface along the axes of minimum moment of inertia, and widths were calculated as twice the distance from the furthest point on the molecular van der Waals surface to the axis of minimum moment of inertia using self-written software in Perl.

Optimised structures and MD trajectories were visualised using VMD.¹³² All Cartesian axes used were defined as right-handed, in which the orientation of the z axis is defined as pointing towards the observer when the x axis points to the right, and the y axis points upwards. For each dye geometry for which a set of molecular axes was constructed, the z and x axes were defined as both having positive projections on to the anthraquinone axis, itself defined as the minimum moment of inertia of the 14 carbon atoms of the anthraquinone core. The exception to this rule was for the DFT optimised structures in Section 7.3.2, for which the principal and secondary molecular axes were defined as having positive projections along the vector defined by the TDM.

Chapter 3

Spectroscopy, structure and stability of dyes in isotropic systems

This chapter focuses on studies of the dyes in isotropic solutions, assessing their spectroscopy, structure and stability by using a range of experimental spectroscopic methods allied with results from DFT calculations. The results of these studies are also considered in the context of how they may relate to anthraquinones as guests within anisotropic systems, for which studies are reported in Chapter 4.

3.1 Introduction

This introductory section presents a background summary of the reported spectroscopy, structure and reactivity of anthraquinone dyes, including both experimental studies and computational methods that have been used to provide comparisons with the experimental results where applicable. This section builds on the introduction to anthraquinone dyes given in Chapter 1 (Section 1.4.2), highlighting some of the properties that are most relevant to guest-host systems, and concludes with the aims of the work presented in this chapter.

3.1.1 Spectroscopy of anthraquinone dyes

3.1.1.1 UV-vis absorption spectroscopy

Anthraquinone dyes may exhibit a wide range of visible absorption maxima depending on the position and nature of the substituent groups, as introduced in Chapter 1, enabling their visible absorption characteristics to be tuned. This tunability arises from the influence of the substituents on the energies of the HOMOs and LUMOs of anthraquinone dyes, which largely determine the energies of the visible electronic absorption bands, and thus the perceived colours of the dyes. Additional effects may arise from associated vibronic transitions giving rise to broad visible absorption bands that may have multiple peaks, which can be significant in terms of the perceived dye colour,¹³³ and which may be observed in hydroxy- and amino-substituted anthraquinones.¹³⁴ Solvent effects on the visible absorption spectra may also be

observed in anthraquinone dyes, as discussed in Chapter 1, resulting in subtle changes in their perceived colours with solvent environment.

Considering dyes that are related to the specific compounds studied in this work, those based on phenylsulfide-substituted anthraquinone structures are generally yellow in the case of 1,4- and 1,5-disubstituted species, and magenta in the case of 1,4,5,8-tetra-substituted species, as summarised in Figure 3.1.^{64-66, 68, 135} Phenylamino-substituted anthraquinone dyes tend to be magenta in the case of 1,4- and 1,5-disubstituted species, and cyan for 1,4,5,8-tetra-substituted species, as also summarised in Figure 3.1.^{63, 65, 136}

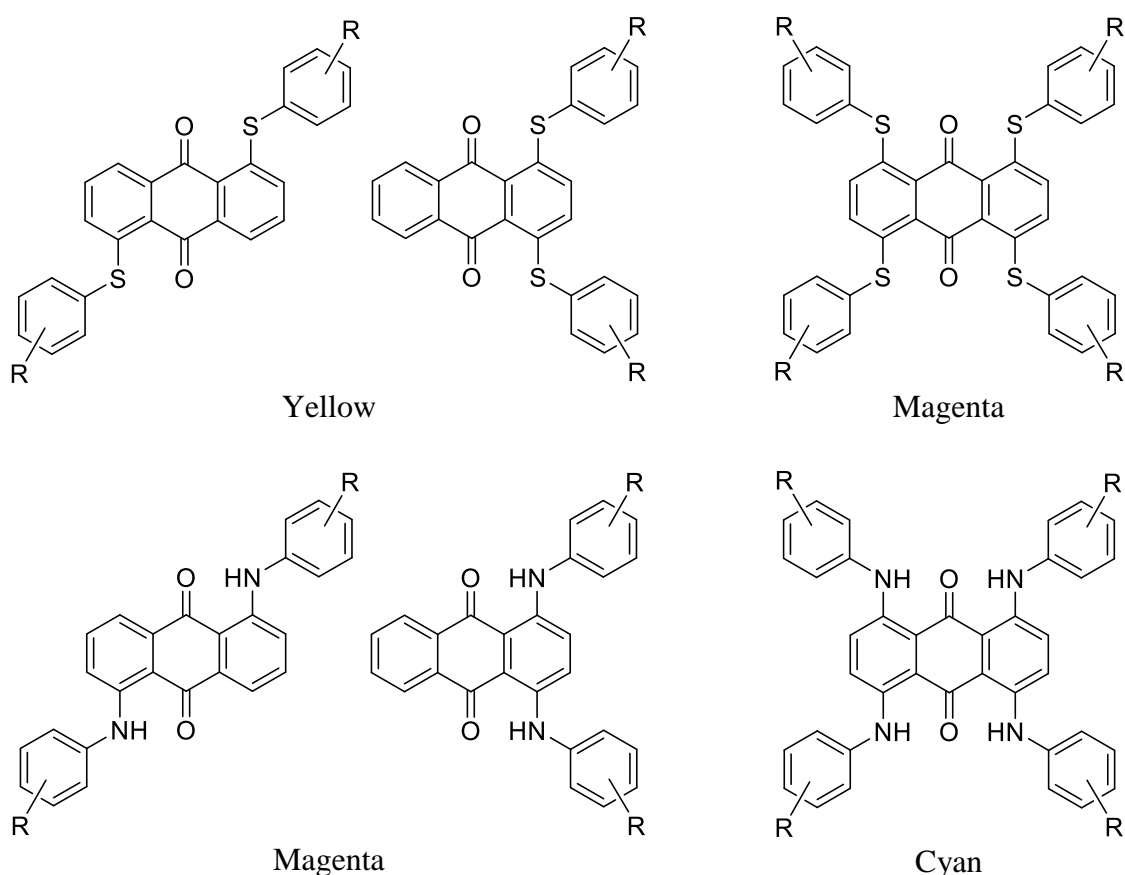


Figure 3.1 Typical colours of 1,4-, 1,5- and 1,4,5,8- phenylsulfide (top) and phenylamino-substituted anthraquinones.

The occurrence of longer wavelength absorption bands for the amino-substituted dyes than the sulfide-substituted dyes, which results in the different colours, may be attributed both to the greater electron-donating characteristics of the amine substituents and the ability of the protons of the amine groups in these positions to hydrogen bond with the oxygen atoms of the anthraquinone carbonyl groups.^{55, 57} The addition of

hydroxyl groups to diamino-substituted anthraquinone dyes has been shown to yield blue dyes,⁶⁰ which again is attributable to the electron-donating characteristics and hydrogen-bonding capability of the added substituent groups. 2,6-Diphenyl substituted anthraquinone dyes have been the subject of much less research, but those in which the phenyl groups are attached directly to the anthraquinone core have generally been shown to be yellow/orange in colour.^{69, 137}

Many computational studies of anthraquinone dyes have focused on the simulation of UV-visible absorption spectra, due to the uses of these compounds generally being based on their colours, and good matches between DFT calculated and experimental visible absorption wavelengths have been obtained for a variety of anthraquinone dyes.^{138, 139} More recently, vibrationally resolved UV-visible absorption spectra have been calculated to try to rationalise the different spectral profiles observed experimentally from different substituted anthraquinone dyes, and good matches with experimental band shapes as well as band positions have been obtained.^{133, 140}

The polarisation of the visible absorption band(s) of a dye is particularly relevant in considering dyes within anisotropic hosts because the orientation of the transition dipole moment (TDM) associated with the visible absorption of a dye is crucial to obtaining a high dichroic order parameter.²⁴ For rod-like dyes of high symmetry, it is often assumed that the angle, β , between the long molecular axis and the TDM is equal to 0° , although the lower dichroic order parameters obtained from some anthraquinone dyes have been attributed to their lower symmetry resulting in larger values of β .^{24, 141}

A limited number of studies have assessed the alignment of the transition dipole moments in dichroic dyes by calculating the orientations of the visible TDMs of optimised dye structures,¹⁴²⁻¹⁴⁵ but the β angles have typically been measured against a long molecular axis which is not unambiguously defined, making a comparison of the orientations between different structures difficult. Additionally, the level of theory used for some reported calculations does not match the level(s) which have been shown to reproduce experimental electronic absorption properties well.^{133, 140}

3.1.1.2 Vibrational spectroscopy

Several early vibrational studies were carried out on anthraquinone and many of its derivatives, with peaks in their IR spectra initially assigned on the basis of characteristic skeletal and group frequencies, and by comparison between similar structures.¹⁴⁶⁻¹⁴⁸ More in-depth studies have revealed discrepancies in the earlier assignments of some anthraquinone bands, which have since been resolved using polarised studies of dyes aligned in stretched polythene and also computational studies, which have provided good matches between calculated and experimental data.¹⁴⁹⁻¹⁵¹

More recently, the vibrational spectroscopy of anthraquinone dyes has been used in a variety of applied contexts, such as analysing the structures of solvated anthraquinones in supersonic jets,¹⁵² characterising the nature of adsorption of anthraquinones onto metal surfaces,^{153, 154} and analysing dye-fibre interactions in a range of anthraquinones.¹⁵⁵ Vibrational spectroscopy has also been used relatively extensively in the analysis of excited-state processes,¹⁵⁶⁻¹⁶⁰ which are discussed in Section 3.1.3.2 below.

Calculated vibrational spectra of anthraquinones have not only provided more comprehensive band assignments of experimental spectra than have been possible from purely experimental studies, but they have also been used for comparisons between computational methods, showing that DFT generally provides more accurate vibrational spectra than the semi-empirical methods used.^{150, 151}

3.1.1.3 NMR spectroscopy

¹H and ¹³C NMR spectroscopy has been relatively widely used for structural studies of anthraquinones, including those of naturally occurring compounds.¹⁶¹⁻¹⁶⁴ Some reported ¹³C NMR studies on simpler anthraquinones have focussed on assignments,¹⁶⁵⁻¹⁶⁷ and on ¹⁴N nuclear quadrupole coupling to determine internuclear geometry using known quadrupole data of an aminoanthraquinone.¹⁶⁸ Hydroxy- and ethoxy-anthraquinones have also been suggested as ¹³C chemical shift assignment tools for other anthraquinone species for which full assignments have been reported to be difficult.¹⁶⁹

3.1.2 Structure of anthraquinone dyes

3.1.2.1 Characterisation of molecular structure

The structure of anthraquinone itself has been characterised by multiple X-ray crystallography studies and shown to be planar with all the hydrogen atoms also lying in the plane of the rings,^{170, 171} and with the molecule having overall D_{2h} symmetry. The C-C bond lengths were found to be very similar throughout the two terminal phenyl rings, demonstrating their aromatic nature, whereas the C-C bond-lengths within the central ring were shown to exhibit more variation, demonstrating the “quinoidal” nature of the central ring.¹⁷⁰⁻¹⁷² Crystallography studies have shown that simple substituted anthraquinone species may also retain a central planar structure.^{173, 174}

Anthraquinone and its substituted derivatives have been used as model compounds for several comparisons of both ab initio and semi-empirical computational methods for structure optimisations, and then structures have been used to generate calculated spectra.^{138, 139, 175, 176} Very good matches between experimental and calculated visible absorption energies were obtained for structures optimised using hybrid DFT functionals.

3.1.2.2 Molecular shape in the context of guest-host systems

The overall molecular shape of anthraquinone dyes for guest-host applications is important because the alignment of guest molecules within anisotropic hosts is typically considered to be driven by molecular anisotropy in the same way as it is for the liquid crystal mixtures themselves. This importance of molecular shape has been observed for many dyes, with higher order parameters typically being observed for more elongated structures.²⁴ The molecular aspect ratio, defined as the molecular length divided by the molecular width, has become a standard way of quantifying the anisotropy of molecular shape, both for guests dissolved in liquid crystal hosts,¹⁷⁷⁻¹⁸⁰ and for host molecules alone. For example, aspect ratios have been used widely as a variable in coarse-grain molecular dynamics simulations of liquid crystal mixtures.^{178, 181-184}

The axis along which molecules in liquid crystalline systems align is typically termed the long axis or the molecular axis, but for non-linear molecules these terms lack unambiguous quantitative definition. The specific case of anthraquinone dyes is also made more complex by their typically less rod-like structures in comparison with many azo dyes used in liquid crystal mixtures, as introduced in Chapter 1, making an intuitive definition of such an axis less clear for substituted anthraquinones.⁹⁸ A common approach taken in situations where the axis of minimum moment of inertia of a molecule needs to be quantified,¹⁸⁵⁻¹⁸⁸ is to define it as the eigenvector associated with the minimum eigenvalue of the inertia tensor of a given structure.¹³¹

3.1.3 Reactivity of anthraquinones

3.1.3.1 Electrochemical reactivity

The electrochemical properties of anthraquinone-based compounds have been the subject of a significant amount of research, partly due to the utilisation of anthraquinone redox processes in wood pulping,¹⁸⁹ the role of quinone moieties in charge-transfer processes in photosynthesis,¹⁹⁰ and their use as sensitizers in studies of charge-transfer in DNA.^{191, 192} Electrochemical studies have shown that in oxygen-free aprotic nonaqueous environments, quinones undergo two 1-electron reductions to a dianion, the first of which is typically fully reversible and the second of which is quasi-reversible under typical conditions, as shown in Figure 3.2 for anthraquinone.¹⁹³

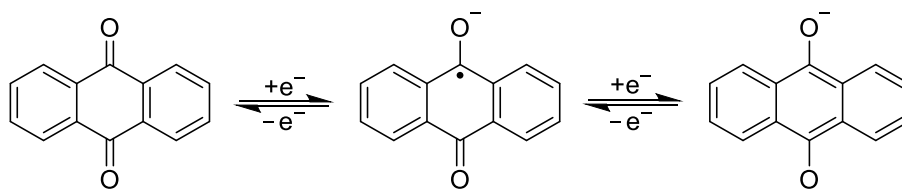
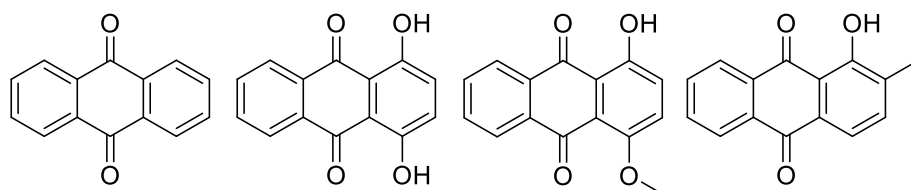


Figure 3.2 Two-step reversible electrochemical reduction of anthraquinone.

Similar reductions have been observed for substituted anthraquinones, and their reduction potentials have been shown to be highly dependent on the position and nature of the substituents, as shown by the reduction potentials given in Figure 3.3.¹⁹⁴ In the presence of oxygen, only the first reduction step is observed because the anthraquinone

radical anion may react directly with oxygen to re-form the anthraquinone and produce the superoxide anion, $O_2^{\bullet-}$.^{195, 196}



$E_{(\text{Dye}, \text{Dye}^{\bullet-})} / \text{V}$	-0.911	-0.757	-0.750	-0.639
$E_{(\text{Dye}^{\bullet-}, \text{Dye}^{2-})} / \text{V}$	-1.410	-1.175	-1.260	-1.198

Figure 3.3 First and second reduction potentials of some anthraquinones in acetonitrile, versus Ag/AgCl.¹⁹⁴

Oxidation studies of anthraquinone compounds have been much less reported, which may be attributable to their relatively high oxidation potentials; for example, the oxidation potential of anthraquinone itself has been measured to be +2.25 V versus Ag/AgCl in 1,1,1,3,3,3-hexafluoropropan-2-ol.¹⁹⁷ A notable exception is provided by amino-substituted anthraquinones, which have been of interest due to the electrochemical polymerisation of such compounds being used to form conducting polymers.¹⁹⁸⁻²⁰⁰ In these polymerisation processes, the relatively accessible oxidation of the amine group(s), occurring at *ca* +1.4 V versus Ag/AgCl for 1-aminoanthraquinone,²⁰⁰ is reported to be followed by a sequence of radical cation dimerisations and deprotonation steps to form the polymeric species.¹⁹⁹

The electrochemical properties of many anthraquinones have been investigated using computational methods and, as with the vibrational and UV-vis calculations, comparisons of different theoretical approaches have been carried out. Redox potentials and quantitative structure-function relationships have been determined from the calculated thermodynamic properties, enabling the prediction of electrochemical properties of new systems, and demonstrating a good match between experimental and calculated redox potentials obtained using DFT methods.^{194, 196, 201}

3.1.3.2 Photochemical reactivity

The photochemical characteristics of anthraquinone itself are markedly different from those of many substituted anthraquinones which also have different UV-vis absorption characteristics to anthraquinone. The fluorescence of anthraquinone itself is rarely observed because there is efficient intersystem crossing from the $^1(\pi\pi^*)$ state to produce a $^3(\pi\pi^*)$ state, resulting in strong phosphorescence in alkane solutions and in the crystalline form at room temperature.^{202, 203} Amino- and hydroxy- substituted anthraquinones have received much attention in the literature and provide good examples of how the photochemistry of anthraquinones varies with substituent, illustrated by the fluorescence and phosphorescence properties of a variety of hydroxy-substituted anthraquinones listed in Table 3.1.²⁰⁴ A wide range of hydroxyanthraquinones are reported to fluoresce, with the position of the hydroxyl group(s) determining the quantum yield.²⁰⁵ Phosphorescence is typically reported only for 2-hydroxyanthraquinones, which has been attributed to the $^3(\pi\pi^*)$ state lying slightly lower in the energy than the $^1(\pi\pi^*)$ state, favouring intersystem crossing; the relative energy levels in 1-hydroxyanthraquinone are reported to be unfavourable to intersystem crossing, hence phosphorescence is generally not observed from these species, as shown in Figure 3.4.²⁰⁴

Table 3.1 Emission maxima, λ , and quantum yields, ϕ , of fluorescence and low temperature phosphorescence observed for hydroxyanthraquinones in propan-2-ol.²⁰⁴

Substituents	Fluorescence		Phosphorescence	
	λ / nm	ϕ_f	λ / nm	ϕ_p
2-hydroxy	472, 500	$\sim 10^{-5}$	515	0.06
2,6-dihydroxy	463, 505	$\sim 10^{-5}$	532, 560	0.23
1-hydroxy	570, 597	0.004	-	-
1,5-dihydroxy	575, 605	0.006	-	-
1,2-dihydroxy	570, 590	0.004	-	-
1,2,5,8-tetrahydroxy	550, 561, 591	0.004	-	-

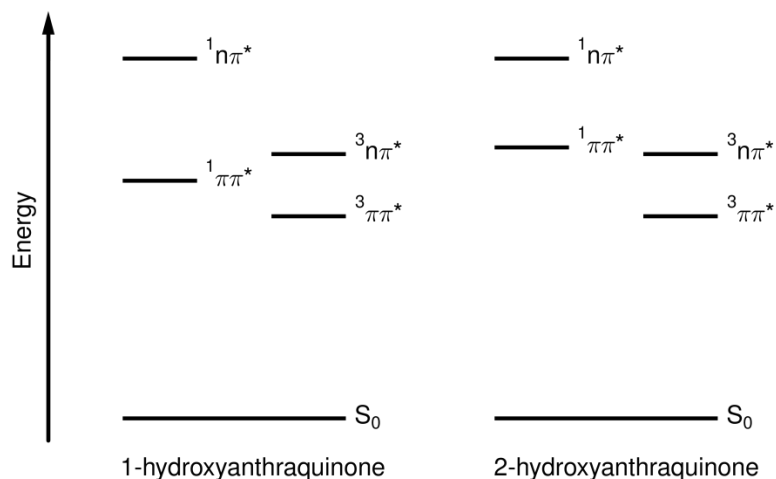


Figure 3.4 Schematic excited state energy levels of 1-hydroxy- and 2-hydroxyanthraquinone.²⁰⁴

The influence of amine substituent groups on the photochemical pathways is significantly more complicated than that of hydroxyl groups because the nature of the substituents on the amine groups have an effect, in addition to the position of the amine group on the anthraquinone core. This effect can be seen from the quantum yields of fluorescence of 1-aminoanthraquinones listed in Table 3.2, which decrease with increasing alkylation of the amine group.²⁰⁶

Table 3.2 Fluorescence observed from aminoanthraquinones in cyclohexane.²⁰⁶

Substituent	Fluorescence	
	λ / nm	ϕ_f
1-amino	590	0.003
1-methylamino	612	10^{-4}
1-piperidino	-	$<10^{-5}$

Radiationless deactivation from the S_1 state of aminoanthraquinones to the ground state has been found to be much accelerated when the amine group is in the 1-position and has a hydrogen substituent, such that intramolecular hydrogen bonding plays a role in the non-radiative decay.²⁰⁷ An increase in the rate of radiationless deactivation in ethanol, especially for 2-aminoanthraquinones, also shows that intermolecular hydrogen bonding can accelerate the process, supported by analysis of deuterated ethanol solutions.⁵⁴

Radiationless deactivation to the ground state is also a major pathway from the S_1 state of 1-hydroxyanthraquinones. The fluorescence of these hydroxy compounds has been observed to have a much greater Stokes shift than their amino counterparts, and has

been rationalised by an intra-molecular proton transfer mechanism in the S_1 state, as shown in Figure 3.5.^{159, 208} It is proposed that this effect is observed for the hydroxyl species but not for the amine species due to the relatively weak hydrogen bond donating characteristics of NH groups relative to OH groups.^{57, 207, 209, 210}

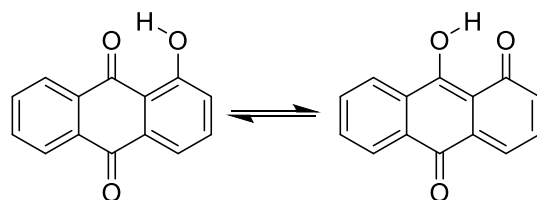


Figure 3.5 Proton transfer in the S_1 state of 1-hydroxyanthraquinone.^{159, 208}

Another mechanism of non-radiative decay from the S_1 state of aminoanthraquinones was first observed as quenching via exciplex formation in benzene,²⁰⁹ which has since been observed in a variety of aromatic solvents.²¹¹

The photochemical reactions of anthraquinones are important in respect to the light-fastness of dyes. The T_1 state of anthraquinone itself may undergo a variety of reactions, depending on the conditions: in isopropanol, a concentration-dependent, wavelength-independent photochemical reduction to 9,10-dihydroxyanthraquinone is observed,²¹² and more detailed mechanistic studies have shown that this is due to an initial hydrogen atom abstraction by the T_1 state of anthraquinone to form the semiquinone radical.²¹³ More recently, it has been shown by time-resolved UV-vis absorption and time-resolved EPR studies, that hydrogen atom abstraction from other alcohols and amines occurs.^{214, 215} Due to the efficient non-radiative relaxation of the substituted anthraquinones discussed above, the reactions of their triplet states are less commonly observed than those of anthraquinone itself.²¹⁶

The photochemical properties of anthraquinones are related to their electrochemical properties because electron transfer to the triplet state of some anthraquinones results in the formation of the semiquinone radical anion.²¹⁴ Hence, the stability of photochemically produced anthraquinone radicals and their subsequent reactions may parallel that observed on electrochemical reduction.

3.1.4 Aims

The overall aim of the work reported in this chapter was to study the spectroscopy, structure and reactivity of the dyes in isotropic phases, and to elucidate structure-property relationships from experimental measurements allied with computational studies of the dyes.

More specifically, the aim was to use UV-visible absorption spectroscopy, vibrational spectroscopy and NMR spectroscopy to study the dyes in isotropic systems in order to assess the visible absorption characteristics and molecular structures of the dyes, and to combine these experimental results with those of DFT calculations to assess the properties that may determine their alignment in liquid crystal hosts. A further aim was to use cyclic voltammetry and spectroelectrochemical methods to assess the redox behaviour and stabilities of the dyes in isotropic solutions, again allied with the results of DFT calculations. By combining the results from these different techniques, the aim was to gain information on the variation and interdependence of these various properties with dye substituents and structure, with the results from the calculations enabling a more detailed interpretation than available from using the experimental results alone.

In addition, a further general aim was to assess the quality of the computational studies in order to evaluate their predictive capabilities for the design of dyes for guest-host applications more generally.

3.2 Results and discussion

3.2.1 Spectroscopy

3.2.1.1 UV-vis absorption spectroscopy

The dyes studied in this work exhibit a range of colours from pale yellow through to blue in isotropic solution, as can be seen from the photograph of the dyes in *p*-xylene solutions shown in Figure 3.6.



Figure 3.6 Samples of the dyes in *p*-xylene at *ca.* 2×10^{-4} mol dm⁻³.

The UV-visible absorption spectra of the dyes in *p*-xylene are presented in Figure 3.7, and they show that the colours arise from a single strong visible absorption band for each of the dyes. Table 3.3 lists the wavelengths of maximum absorption, λ_{\max} , and oscillator strengths, f , of the visible bands in *p*-xylene calculated using Equation (3.1),⁷⁷ where the constant $k = 4.32 \times 10^{-9}$ dm⁻³ mol cm and the refractive index $n = 1.50$.²¹⁷ Figure A1.1 in Appendix 1.1 shows the integrated peak areas used to determine these oscillator strengths.

$$f = (k/n) \int \varepsilon(\tilde{\nu}) d\tilde{\nu} \quad (3.1)$$

The band positions may be rationalised in terms of the substituents on the anthraquinone core. Dye 26B3 exhibits the shortest wavelength absorption, consistent with it having the fewest and least electron-donating substituents of the dyes. A comparison of 15SB3 with 15NB3 shows that the more electron-donating amine substituents, which are also capable of intramolecular hydrogen bonding with the anthraquinone carbonyl groups,

result in an absorption band at a longer wavelength for 15NB3 than for 15SB3. A comparison of 15NB3OH and 26B3OH with their respective non-hydroxylated counterparts, 15NB3 and 26B3, shows that the addition of the electron-donating hydroxyl groups, which are also capable of hydrogen bonding with the anthraquinone carbonyl groups, again results in absorption occurring at longer wavelength, manifested as a red-shift of > 100 nm in both cases. The absorption coefficients and oscillator strengths obtained from these visible absorption bands also show that the hydroxyl-substituted dyes exhibit stronger visible absorption bands than their non-hydroxylated counterparts, which is consistent with their transitions having a stronger charge-transfer character.

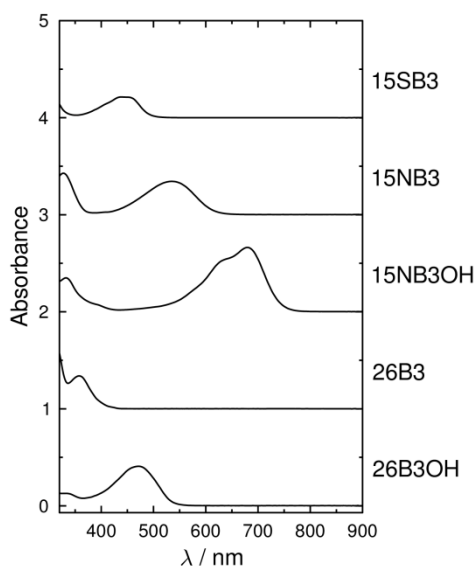


Figure 3.7 UV-vis absorption spectra of the dyes in *p*-xylene at $2.0 \times 10^{-4} \text{ mol dm}^{-3}$ in 1 mm path-length cells. The spectra are offset for clarity.

Table 3.3 Experimental visible absorption maxima and associated absorption coefficients and oscillator strengths, f , of the dyes in *p*-xylene at $2.0 \times 10^{-4} \text{ mol dm}^{-3}$.

Dye	$\lambda_{\text{max}} / \text{nm}$	$\epsilon_{\text{max}} / 10^4 \text{ dm}^3 \text{ mol}^{-1} \text{ cm}^{-1}$	f
15SB3	439	1.05	0.14
15NB3	535	1.70	0.21
15NB3OH	680	3.51	0.32
26B3	358	1.71	0.18
26B3OH	471	2.04	0.28

UV-vis absorption spectra of the dyes were recorded in a range of solvents, enabling the solvent dependence of the visible absorption bands to be assessed, along with the solubilities of the dyes in the different solvents. The band shapes observed for each respective dye in the various solvents were consistent, as shown in Figure 3.8, and the

visible λ_{\max} values, listed in Table 3.4, showed no strong solvent dependence; these characteristics suggest that strong solvent-solute interactions are not present in these systems. Plots of these small shifts in absorption maxima with solvent dielectric constants, dipole moments and polarizability (see Table A1.1 and Figure A1.2 in Appendix 1.2) did not show any strong correlation with these properties. UV-vis absorption spectra recorded from each of the dyes in DCM and in *p*-xylene showed no significant variation in profile between $ca\ 2 \times 10^{-5}\ \text{mol dm}^{-3}$ and $ca\ 4 \times 10^{-3}\ \text{mol dm}^{-3}$ and within the solubility limits, suggesting that dye aggregation does not occur under the conditions used (see Figure A1.3 in Appendix 1.3).

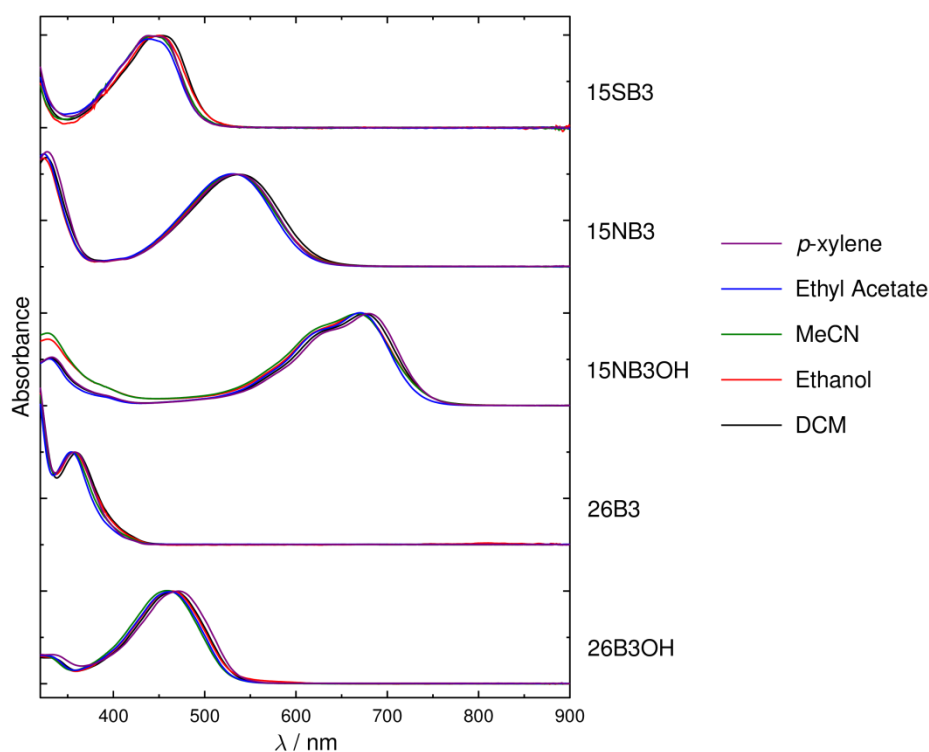


Figure 3.8 UV-vis absorption spectra of the dyes in a range of solvents at $ca\ 2 \times 10^{-4}\ \text{mol dm}^{-3}$ or at their solubility limits. The spectra are normalised to the peak absorbances of the visible bands.

Table 3.4 Visible λ_{\max} values of the dyes in a range of solvents.

	$\lambda_{\max} / \text{nm}$				
	DCM	Ethanol	Acetonitrile	Ethyl Acetate	<i>p</i> -Xylene
15SB3	453	451	445	437	439
15NB3	538	534	532	531	535
15NB3OH	675	669	668	670	680
26B3	360	357	355	354	358
26B3OH	466	464	459	462	472

The solubilities of the dyes were estimated from the absorbances of the visible absorption peaks obtained from saturated solutions of the dyes in the different solvents, using the molar absorption coefficients obtained from the respective spectra in *p*-xylene. These estimates are listed in Table 3.5 and demonstrate that 15NB3 generally has the highest solubility of the dyes in the range of solvents used, whereas 15SB3 generally has the lowest solubility. No strong correlations were evident between solubility and the solvent properties identified above, but it can be seen that the solubility is significantly higher in the solvents of low dielectric constant (DCM, *p*-xylene) than in the solvents of high dielectric constant (ethanol, acetonitrile).

Table 3.5 Approximate solubility limits of the dyes in a range of solvents based on absorption coefficients obtained in *p*-xylene.

	Solubility limit / 10^{-5} mol dm ⁻³				
	DCM	Ethanol	Acetonitrile	Ethyl Acetate	<i>p</i> -xylene
15SB3	>100	4	2	9	27
15NB3	>100	3	8	54	74
15NB3OH	>100	1	4	25	38
26B3	>100	1	6	37	32
26B3OH	>100	2	6	49	32

3.2.1.2 Vibrational spectroscopy

IR spectra of the dyes in KBr disks and Raman spectra of solutions of the dyes in DCM were recorded and are presented in Figure A1.4 in Appendix 1.4 and Figure A1.5 in Appendix 1.5, respectively. These experimental data were used as an aid to assessing the validity of the DFT calculated optimised structures of the dyes, as discussed below.

3.2.1.3 NMR spectroscopy

NMR spectra of solutions of the dyes in DCM were recorded and are presented in Figures A1.6–A1.10 in Appendix 1.6, and associated values are listed in Tables A1.2–A1.6 in Appendix 1.6. These spectra confirm the high degree of organic purity of all of the dyes, and they were also used as an aid to assess the validity of the DFT optimised structures of the dyes, as discussed below.

3.2.2 Electronic structure calculations

3.2.2.1 DFT calculations and structural comparisons

Optimised structures of the dyes with all-*trans* conformations of the propyl chains were obtained from DFT calculations and are shown in Figure 3.9. These optimised structures were used to obtain calculated IR, Raman and NMR spectra, and a comparison with the respective experimental spectra, presented in Appendix 1.4-1.6, shows a good match generally between experiment and calculation, providing support for the quality of these optimised structures.

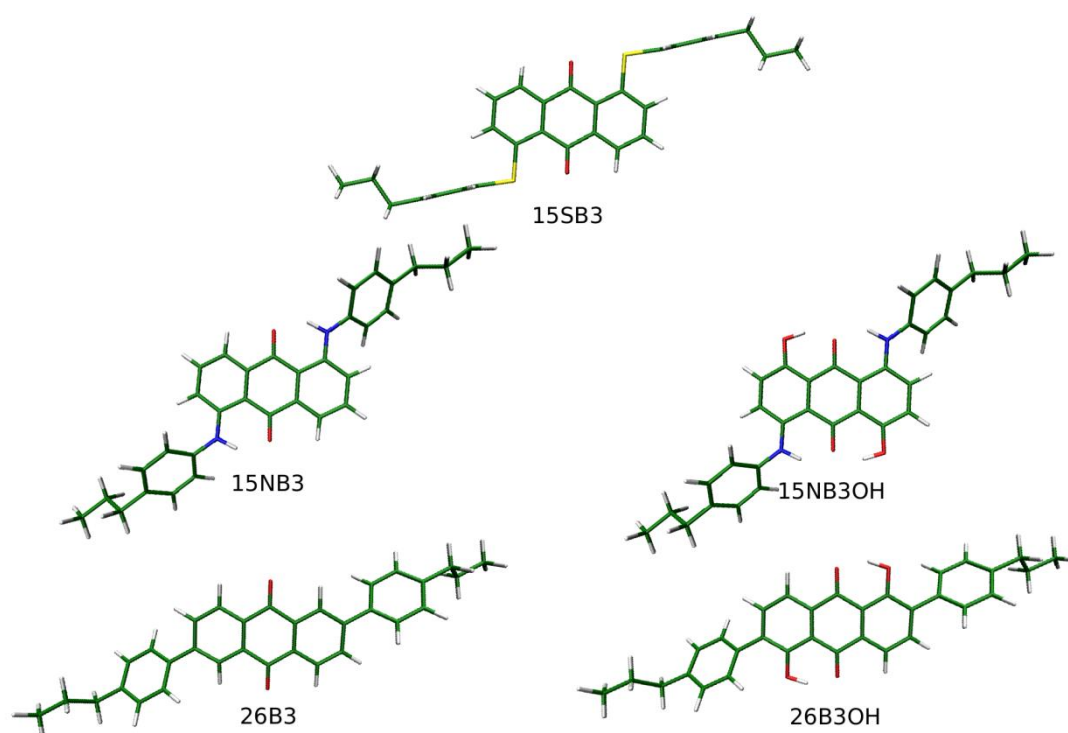


Figure 3.9 Optimised structures of the dyes in all-*trans* conformations at the B3LYP/6-31g(d) level of theory.

All of the optimised dye structures exhibit an essentially planar anthraquinone core. Using the numbering system shown in Figure 3.10, the calculated bond lengths between the non-hydrogen atoms in the anthraquinone core of the five dyes are listed in Table 3.6, along with those from experimental crystal structures of related compounds, which also show essentially planar cores. The calculated structures were not symmetry-constrained but, as can be seen from Figure 3.9, they may all be considered to exhibit approximately C_{2h} symmetry when all the substituent phenyl conformations are

considered. Thus, one half of the anthraquinone core was considered in the analysis of bond lengths.

The bond lengths within the anthraquinone cores are generally consistent between the dyes, both from the calculated structures and the crystal structures. In general, the longest C–C bonds are the C⁹–C¹³ and C¹⁰–C¹⁴ bonds in the central ring, and the shortest bonds are those around the outer ring. The presence of C¹³–C¹⁴ bonds that are shorter than the other C–C bonds in the central ring is indicative of the quinoidal nature of the central rings in all these anthraquinone compounds.¹⁷² Closer inspection of the bond lengths within the central ring of the anthraquinones shows that the C¹³–C¹⁴ bond lengths increase on going from less electron-donating substituents (e.g. 26B3 and 15SB3) to more electron-donating substituents (e.g. 15NB3 and 15NB3OH), whereas the C⁹–C¹³ and C¹⁴–C¹⁰ bonds show a slight tendency for the opposite behaviour. The C¹³–C¹ bond lengths are also shown to increase with increasing electron-donating character of the substituent at the 1- position.

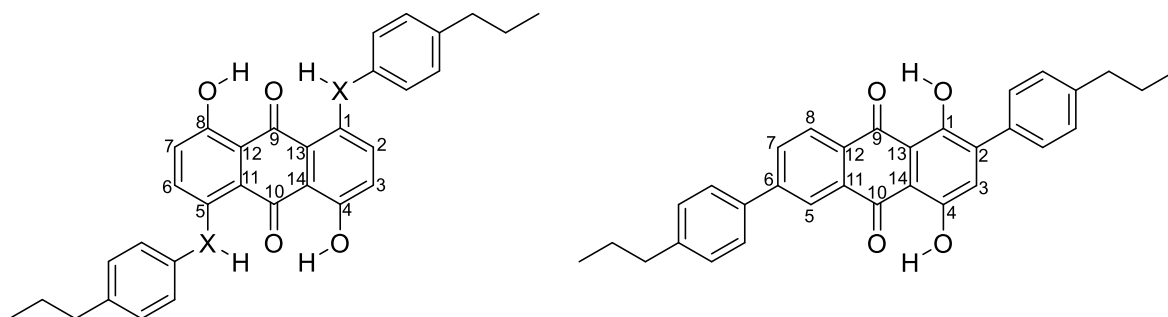


Figure 3.10 Generalised structures and atom numbers used for labelling bond lengths and angles for the 1,5-disubstituted dyes (left) and the 2,6-disubstituted dyes (right).

Table 3.6 Selected bond lengths (Å) of the anthraquinone cores for the optimised dye structures shown in Figure 3.9 and from the crystal structures of anthraquinone (AQ),¹⁷¹ anthraquinone-1,5-dithiol (15SH),¹⁷³ *N,N'*-diphenyl-1,5-diaminoanthraquinone (15NB0)²¹⁸ and 2,6-diphenylanthraquinone (26B0),¹³⁷ using the numbering scheme shown in Figure 3.10.

Dye	CO	9-13	10-14	13-14	13-1	1-2	2-3	3-4	4-14
15SB3	1.231	1.475	1.496	1.414	1.421	1.405	1.391	1.392	1.390
15NB3	1.244	1.465	1.496	1.419	1.435	1.417	1.383	1.399	1.390
15NB3OH	1.271	1.455	1.465	1.435	1.427	1.423	1.371	1.413	1.411
26B3	1.227	1.493	1.488	1.409	1.396	1.403	1.410	1.389	1.400
26B3OH	1.248	1.467	1.482	1.417	1.419	1.425	1.398	1.396	1.390
AQ	1.230	1.472	1.495	1.401	1.383	1.390	1.388	1.381	1.380
15SH	1.207	1.498	1.496	1.403	1.400	1.373	1.388	1.374	1.385
15NB0	1.256	1.449	1.510	1.409	1.415	1.414	1.386	1.372	1.382
26B0	1.223	1.490	1.488	1.404	1.392	1.400	1.400	1.385	1.395

Table 3.7 lists the bond lengths between the anthraquinone core and the directly attached substituent groups, from which it can be seen that the calculated C-S, C-N and C-C bond lengths of the dye-substituent groups generally match well with the respective bond lengths obtained from crystal structures of comparable compounds. The C-O and O-H bonds are calculated to be 1.34 Å and 1.00 Å, respectively, for both 15NB3OH and 26B3OH, showing that there is little difference between the bond lengths of either the carbonyl or the hydroxyl groups in these structures.

Table 3.7 Bond lengths (Å) between the anthraquinone cores and the directly substituted groups of the optimised dye structures shown in Figure 3.9 and for the crystal structures of related compounds,^{137, 173, 218} using the numbering scheme shown in Figure 3.10.

	C ¹ -S ¹	C ¹ -N ¹	C ² -C
15SB3	1.792	-	-
15NB3	-	1.370	-
15NB3OH	-	1.372	-
26B3	-	-	1.483
26B3OH	-	-	1.484
15SH	1.738	-	-
15NB0	-	1.368	-
26B0	-	-	1.487

The slight variations in the calculated structures of the anthraquinone cores between the dyes show changes in bonding that link to electronic, vibrational and related effects but these changes are relatively subtle, such that the variation in the overall molecular shapes evident in Figure 3.9 largely arises from the orientation and structural variation within the substituent groups. For the 1,5-disubstituted structures, there is a significant difference between the C-S-C and the C-N-C bond angles, which are calculated as 102° for 15SB3, and 129° for both 15NB3 and 15NB3OH, such that the phenyl rings and alkyl chains are oriented further from the anthraquinone core in 15NB3 and 15NB3OH than in 15SB3.

The angles between the planes of the substituent phenyl rings and the plane of the anthraquinone core vary between all five structures, as shown in Figure 3.9 and also by the end-views of the structures shown in Figure 3.11. The molecular planes of the anthraquinone core and phenyl substituent rings were defined as the planes containing the axes of minimum and secondary moments of inertia of the respective sets of constituent carbon atoms to obtain the angles given in Figure 3.11. In the case of

15SB3, the phenyl rings lie at 90° to the plane of the anthraquinone core (as shown also in Figure 3.9), whereas in 15NB3, 15NB3OH, 26B3 and 26B3OH the phenyl rings lie at 45° , 45° , 35° and 41° to the plane of the anthraquinone core, respectively. These calculated values are not entirely consistent with those of *ca.* 60° and 30° measured from crystal structures of 15NB0 and 26B0, respectively,^{137, 218} but this difference may be attributable to comparing the experimental geometries obtained from crystal structures with calculated gas-phase structures.

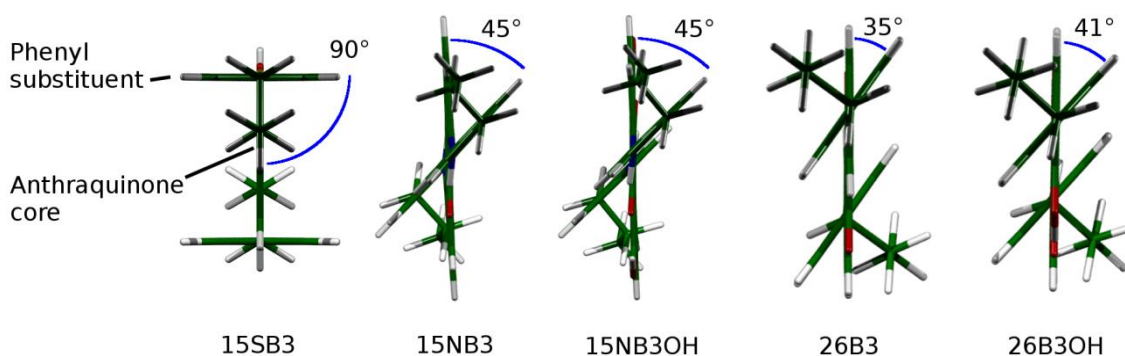


Figure 3.11 End-views of the optimised structures of the dyes showing the angle made between the plane of the anthraquinone core (drawn vertically in each case) and the plane of the phenyl substituents for each of the dyes.

Considering the overall molecular shapes, it can be seen qualitatively from Figure 3.9 that the 2,6-disubstituted structures are the most “rod-like” of the dyes studied, and this property may be quantified in terms of the calculated aspect ratios of the molecules. In order to calculate the aspect ratios, the long axes of the dyes were defined as the minimum moment of inertia (MOI) axes of the optimised structures. The van der Waals structures of the dyes are shown in Figure 3.12, along with bounding dimensions calculated parallel and perpendicular to the minimum moment of inertia axes to define the molecular lengths and widths, respectively, from which the aspect ratios were determined.

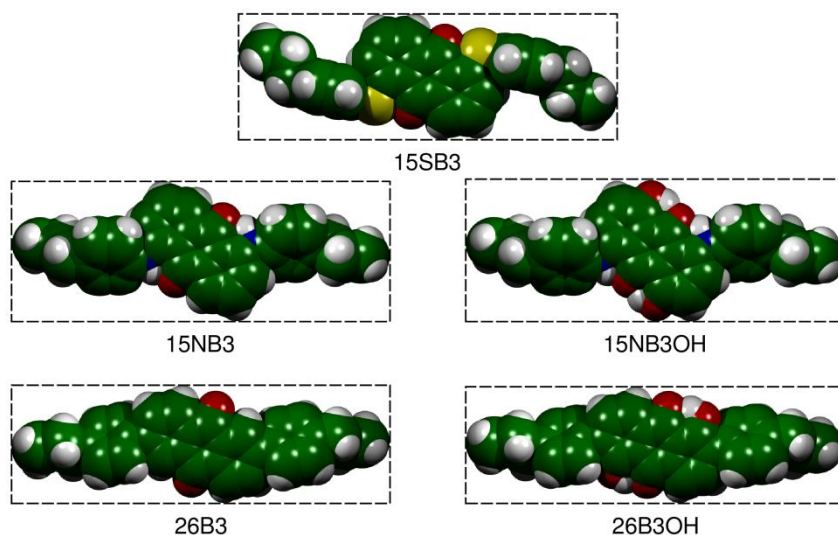


Figure 3.12 van der Waals structures and bounding boxes indicating the molecular lengths and widths from which the aspect ratios of the dyes were calculated.

These calculated lengths, widths and aspect ratios are listed in Table 3.8, and a comparison of the aspect ratio values is shown graphically in Figure 3.13. It is evident from the structures in Figure 3.12 that, for the dyes studied in this work, the presence of the terminal alkyl chains has a significant influence on the molecular lengths and hence on the aspect ratios of the dyes. Optimisations of equivalent dye structures with the terminal propyl groups replaced with hydrogen atoms were carried out and the trend in aspect ratios was found to be the same as that listed in Table 3.8 (see Table A1.7 in Appendix 1.7), indicating that the variation in the aspect ratios between the dyes is due to the differences in the nature of the anthraquinone substituents rather than the specific conformations or lengths of the terminal propyl chains on the phenyl substituent groups.

Table 3.8 Molecular lengths, widths and aspect ratios of the dyes measured from the van der Waals surfaces of the optimised structures shown in Figure 3.12.

Dye	Length / Å	Width / Å	Aspect ratio
15SB3	26.44	8.84	2.99
15NB3	26.93	10.13	2.66
15NB3OH	26.92	10.62	2.53
26B3	26.99	8.48	3.18
26B3OH	27.10	8.37	3.24

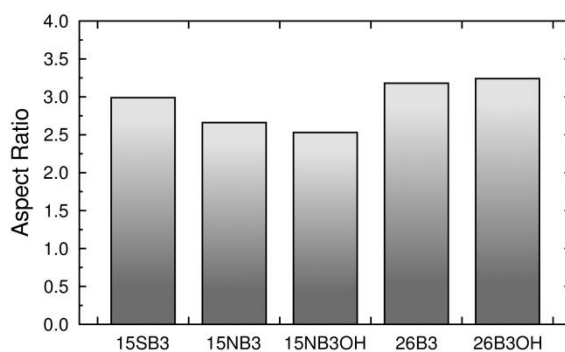


Figure 3.13 Comparison of the aspect ratios calculated for the dyes.

The aspect ratio values show quantitatively that the 2,6-disubstituted species are the most rod-like of the five dyes, and they also indicate that the amine dyes are less rod-like than the sulfide dye. This latter comparison is consistent with the experimental observations that, in general, the order parameters of sulfide-substituted anthraquinone dyes are higher than those of amino-substituted anthraquinone dyes.^{59, 65, 66}

For the 1,5-disubstituted structures, the difference in aspect ratios between the dyes may be rationalised in terms of the specific structural units: the C-S-C bond angle is calculated to be smaller than the C-N-C angle, and hence the phenyl rings and alkyl chains lie closer to the long axis of the anthraquinone core in 15SB3 than in both of the amine dyes, resulting in a more rod-like structure for 15SB3 than 15NB3 and 15NB3OH. In addition, the perpendicular orientation of the phenyl rings in 15SB3 with respect to the plane of the anthraquinone core reduces the molecular width, causing an additional slight increase in the aspect ratio. The effect of the hydroxyl groups in 15NB3OH is to decrease the aspect ratio slightly compared with 15NB3, because the oxygen atoms directly increase the molecular width, albeit only by a small amount. By contrast, the effect of the hydroxyl groups in 26B3OH is to slightly increase the aspect ratio compared with 26B3. This is an indirect effect, because the position of substitution means the hydroxyl groups do not directly influence the molecular dimensions, as can be seen in Figure 3.12, but the relatively high atomic mass of the oxygen causes a slight change in the axis of minimum moment of inertia along which the aspect ratio is measured, resulting in 26B3OH having both a longer length and a narrower width than 26B3.

When analysed in the context of the colours of the dyes, the interplay between the molecular shape and colour may be seen. In the case of the 1,5-diphenylamino substituted dyes, the addition of hydroxyl groups to 15NB3 to form 15NB3OH results in absorption at a longer wavelength, but decreases aspect ratio and hence the rod-like nature of the molecular shape. In the case of the 2,6-diphenyl substituted dyes, the addition of hydroxyl groups to 26B3 to form 26B3OH also results in longer wavelength absorption but, by contrast, it results in a slight increase in the aspect ratio and hence the rod-like nature of the molecular shape.

3.2.2.2 TD-DFT calculations

TD-DFT calculations on the DFT optimised structures of the dyes enabled the electronic excitation energies to be calculated, providing a comparison with those obtained from experimental UV-vis absorption spectra. The calculated visible absorption wavelengths and associated oscillator strengths are listed in Table 3.9, alongside the experimental λ_{\max} values for comparison; simulated UV-vis absorption spectra are shown in Figure 3.14.

Table 3.9 Experimental and calculated visible absorption wavelengths and associated oscillator strengths of the dyes.

	Experimental		Calculated	
	λ_{\max} / nm	f	λ / nm	f
15SB3	439	0.14	453	0.28
15NB3	535	0.21	552	0.35
15NB3OH	680	0.32	634	0.55
26B3	358	0.18	390 ^a	0.29 ^a
26B3OH	472	0.28	492	0.57

^aa weaker transition ($f = 0.07$) is also calculated at 385 nm

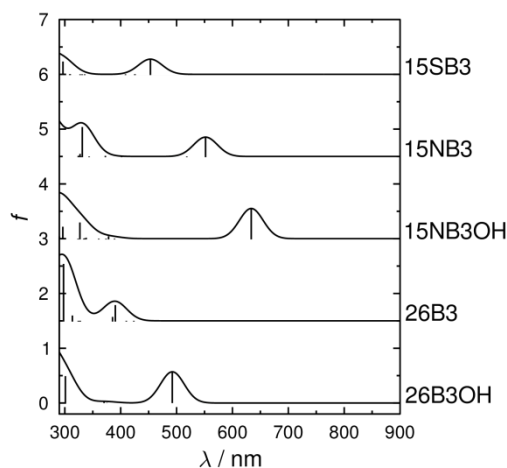


Figure 3.14 Calculated UV-vis absorption spectra of the dyes. Calculated transition energies and oscillator strengths are shown as vertical lines. Spectra are offset for clarity.

A comparison of the calculated absorption wavelengths and oscillator strengths with the experimental λ_{\max} and f values shows a reasonable match. The calculated wavelengths are generally longer and the calculated oscillator strengths are higher than those obtained experimentally, but the trend between the dyes is generally consistent between the sets of values. The calculation of absorption wavelengths that are generally longer than the experimental wavelengths is consistent with the calculations representing 0-0 transitions in which there is no gain in vibrational energy, whereas the experimental λ_{\max} values arise from a set of vibronic transitions that include some with an increase in vibrational as well as electronic energy. Overall, these favourable comparisons provide further support for the DFT optimised structures and illustrate the predictive capacity of the TD-DFT calculations in the context of these dyes.

The TD-DFT calculations indicate that the visible absorption bands are due to single HOMO \rightarrow LUMO transitions, other than for 26B3 for which the strongest visible band is largely due to a HOMO-1 \rightarrow LUMO transition. These transitions are predominantly $\pi \rightarrow \pi^*$ intramolecular charge transfer in character for all of the dyes, as can be seen from both the representation of the orbitals involved in the transitions, shown in Figure 3.15, and the electron density changes on excitation, shown in Figure 3.16.

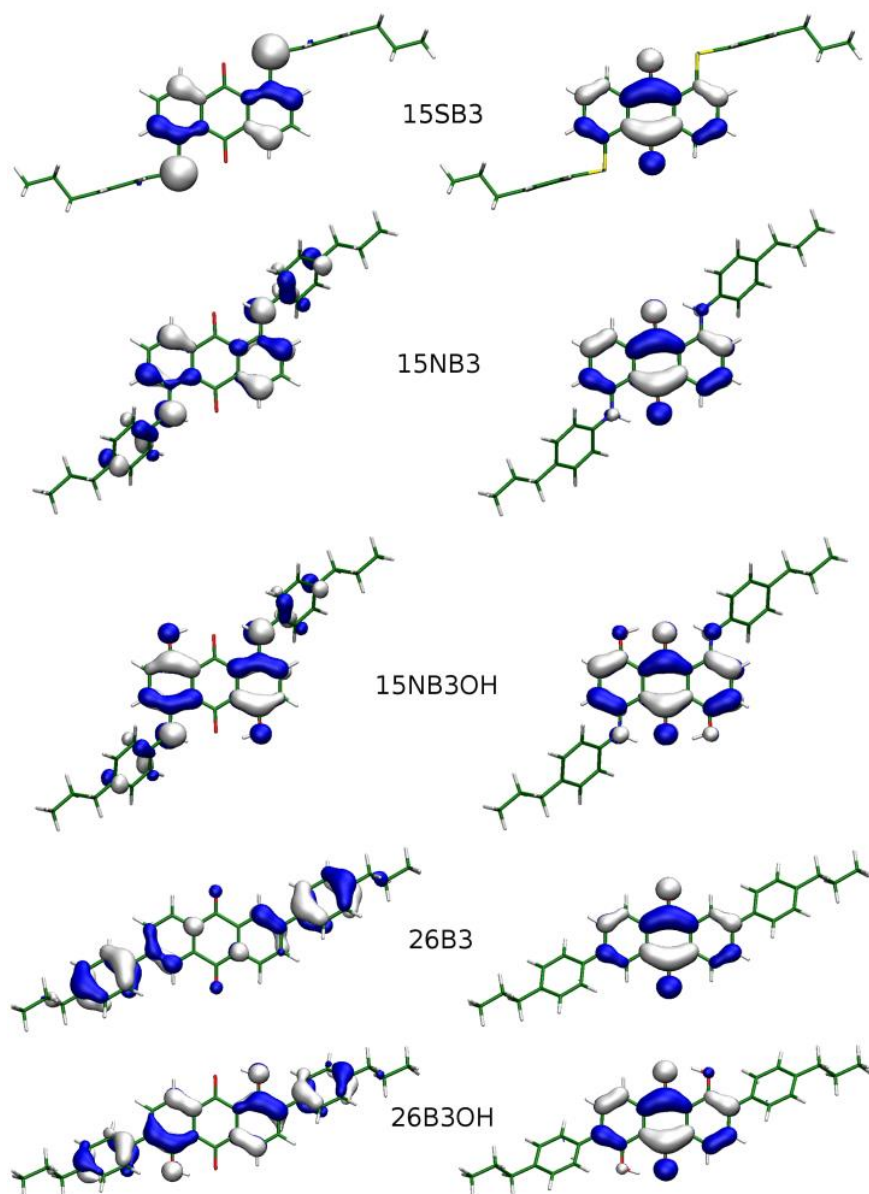


Figure 3.15 Optimised structures of the dyes and the orbitals involved in the visible transitions. HOMOs (left) and LUMOs (right) are shown except in the case of 26B3 where the HOMO-1 and LUMO are shown.

In all cases, it can be seen that the orbitals from which the transitions originate are mainly located on the outer anthraquinone rings and their substituents, and away from the carbonyl groups, whereas the LUMOs are mainly located on the central anthraquinone rings and carbonyl groups. This character is also reflected in the electron density changes on excitation, which show a shift in electron density from the substituents to the carbonyl groups for all of the dyes. The contribution of the hydroxyl groups to the visible transitions can be seen for 15NB3OH and 26B3OH, in both Figure

3.15 and Figure 3.16, and some $n \rightarrow \pi^*$ character can be seen for the transition in 26B3 in Figure 3.16

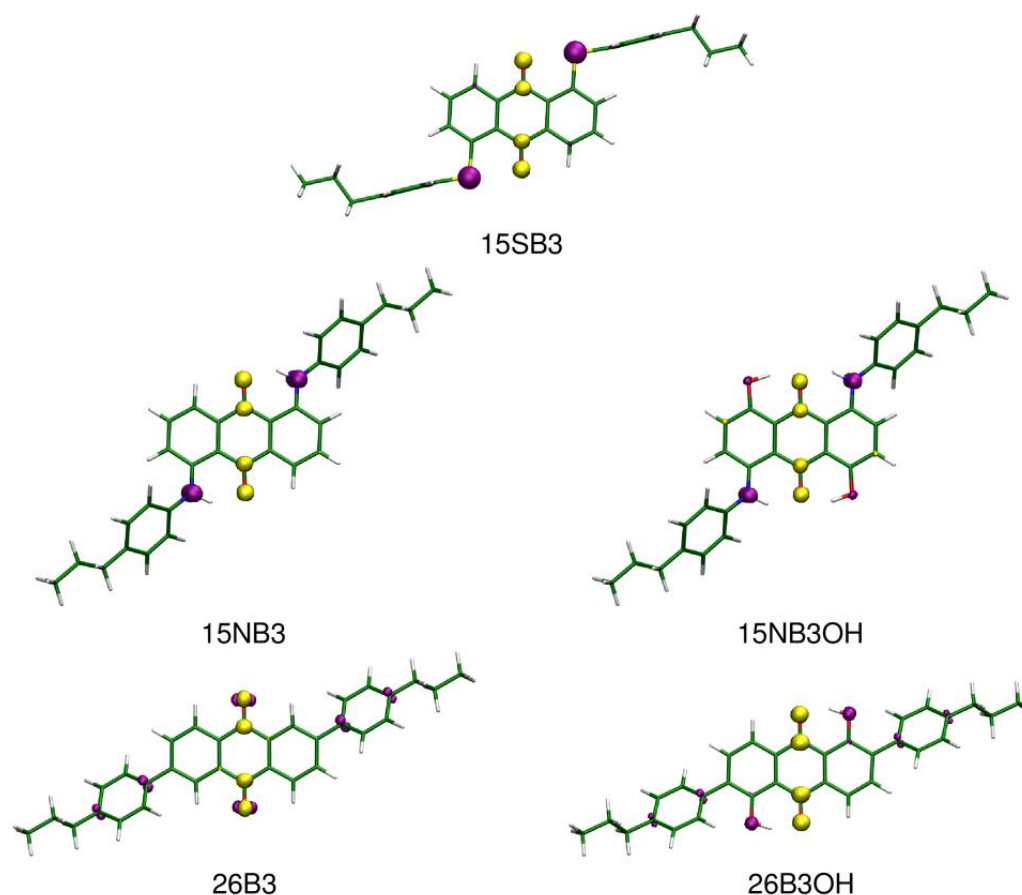


Figure 3.16 Optimised structures of the dyes and the electron density changes on visible excitation obtained from the TD-DFT calculations. The shift occurs from the regions shown in purple to the regions shown in yellow. A cutoff threshold of $\pm 0.007 e \text{ Bohr}^{-3}$ was used.

The orientation of the TDM associated with the visible transition is of direct relevance to the use of anthraquinone dyes in liquid crystal applications, because it is the angle between this TDM orientation and the molecular alignment axis of the dye in the liquid crystal that determines one of the two contributions to the observed order parameter, as expressed in Equation (1.30) in Chapter 1. The orientations of the TDMs obtained from the TD-DFT calculations are shown in Figure 3.17, along with the axes of minimum moment of inertia that may be used to represent of the long molecular axes of the dyes. The magnitudes of the angles, β , between these axes and their resultant contributions, S_β , to the overall calculated uniaxial order parameters, determined using Equation (3.2), are listed in Table 3.10.

$$S_\beta = \frac{3\cos^2 \beta - 1}{2} \quad (3.2)$$

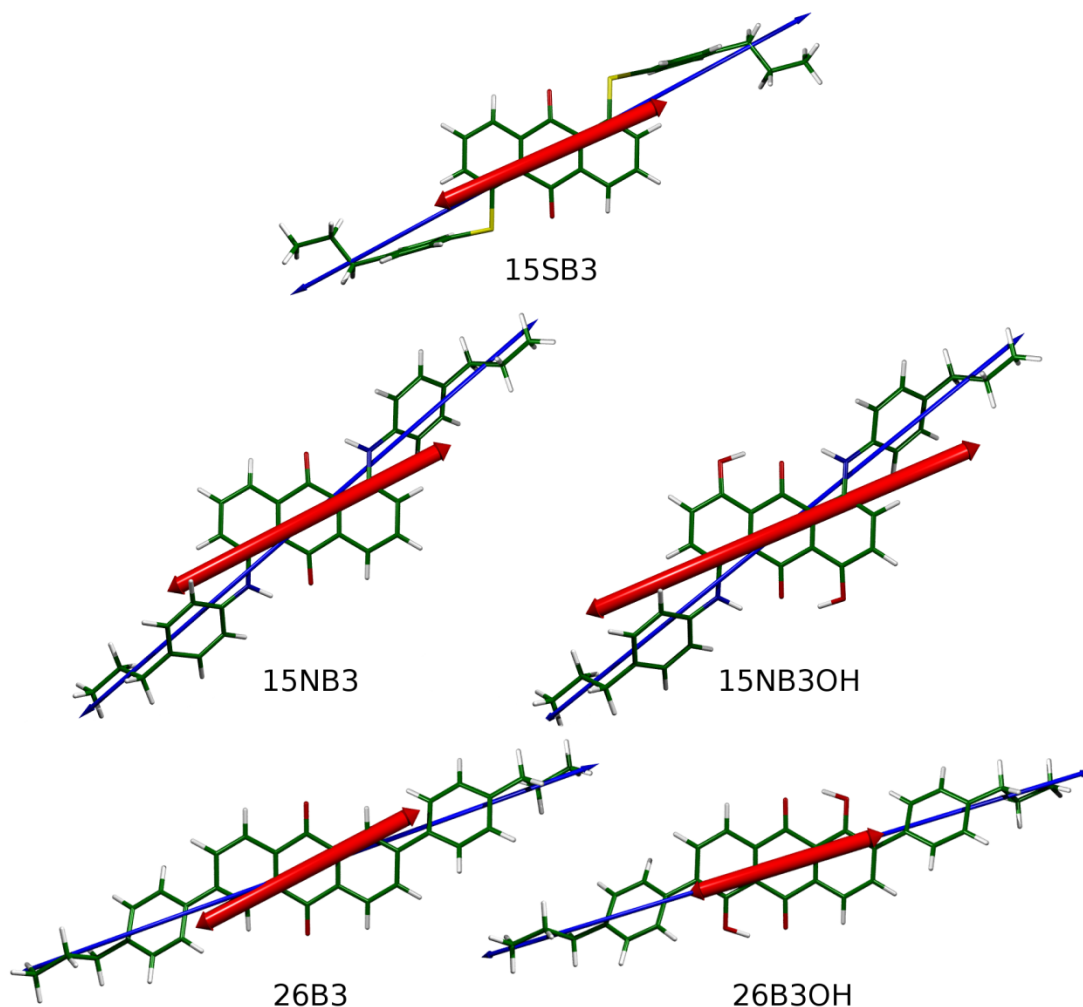


Figure 3.17 Optimised structures of the dyes with vectors showing the orientations of the minimum moment of inertia axes (blue) and the visible transition dipole moment axes (red) with lengths proportional to the oscillator strengths.

Table 3.10 Angles between the calculated minimum moment of inertia axes and TDM orientations, β , and associated order parameters, S_β .

Dye	$\beta / ^\circ$	S_β
15SB3	4.4	0.991
15NB3	13.8	0.914
15NB3OH	15.9	0.887
26B3 ^a	8.4	0.968
26B3OH	1.7	0.999

^aA weaker transition at 385 nm makes an angle of $\beta = 8.8^\circ$ with a corresponding value of $S_\beta = 0.965$.

The orientations of the axes in Figure 3.17 show that the TDMs are generally aligned in similar orientations to the minimum moment of inertia axes of the dyes. However, there is a clear variation in the degree of the alignment of these axes between the dyes, evident from the range of calculated β angles in Table 3.10.

The significantly smaller β angle calculated for 15SB3 than for 15NB3 and 15NB3OH is consistent with reported experimental studies which indicate that the dichroic order parameters of phenylsulfide anthraquinones are generally higher than those of phenylamine anthraquinones.²⁴ This consistency with experimental data suggests that the deviation of the TDM alignment from that of the molecular alignment axis may be a significant contributory factor in the observed experimental dichroic order parameters, in addition to the likely influence from the less rod-like molecular shapes exhibited by the amine dyes than the sulfide dye discussed in Section 3.2.2.

The relatively small β values calculated for 26B3 and 26B3OH suggest that 2,6-substitution in anthraquinone dyes is an effective way of aligning the TDM with the minimum MOI axis of the dye, and is consistent with the relatively high overall order parameters obtained for similar structures experimentally.⁶¹ An additional consideration of TDM alignment is highlighted by the example of 26B3, for which two visible transitions are calculated. In the particular case of 26B3, the calculated TDMs exhibit very similar orientations, and the second transition has only a small oscillator strength associated with it, such that it has little influence on the overall order parameter. However, this cannot be assumed in a general case where additional transitions could have a significant influence on the overall order parameter of a dye.

A comparison of the calculated S_β values is shown graphically in Figure 3.18, from which it is evident that the trend between the dyes is similar to that exhibited by the calculated aspect ratios in Figure 3.13. This similarity suggests that both the molecular shape and the TDM alignment may contribute to the higher order parameters reported generally for phenylsulfide than phenylamine anthraquinone dyes. It also highlights the fact that although the 2,6-disubstituted dyes may intuitively appear more rod-like than any of the 1,5-disubstituted dyes, and therefore better candidates for guest-host applications, substitution with phenylsulfide groups in the 1,5 positions appears to result in similar characteristics to substitution with phenyl groups in the 2,6 positions in terms of both the molecular shape and the TDM alignment.

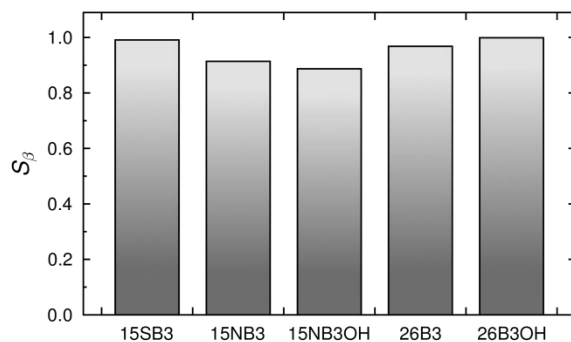


Figure 3.18 Comparison of the S_β values calculated for the dyes.

The TDM orientations and the MOI orientations of the dyes may be assessed in a more absolute way against a common consistent internal reference by comparing how their alignments vary against the orientation of the anthraquinone group. The long axis of the anthraquinone core (AQ) was defined as the minimum moment of inertia axis of the 14 carbon atoms comprising the anthraquinone core, enabling the angle between the AQ axis and the visible TDM vector, δ_1 , and the angle between the AQ axis and the minimum MOI axis, δ_2 , to be defined for each dye. Figure 3.19 shows the relative alignments of the AQ, TDM and MOI axes of 15NB3 as an example and the angles between the axes are listed for all the dyes in Table 3.11. The difference between δ_1 and δ_2 for each dye is approximately equal to β , because the vectors are approximately coplanar, and thus δ_1 and δ_2 should be approximately equal for a dye to exhibit good alignment between the TDM and the minimum MOI axis.

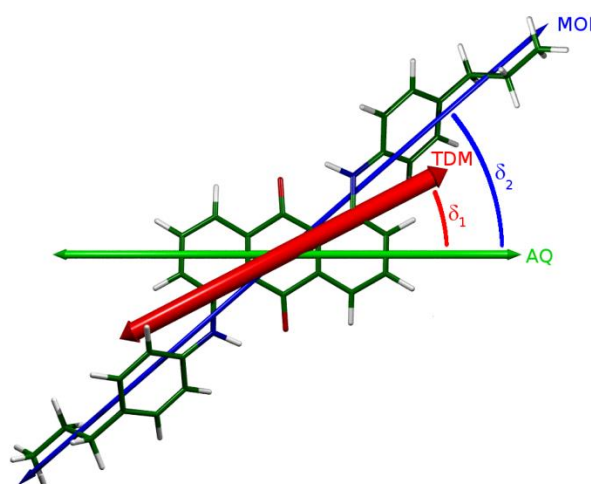


Figure 3.19 Optimised structure of 15NB3 with the TDM axis (red), the minimum MOI axis (blue) and the anthraquinone long axis (green) overlaid and the angles, δ_1 and δ_2 , between these vectors.

Table 3.11 Magnitudes of the angles δ_1 and δ_2 , calculated between the TDM and the minimum MOI axis, respectively, and the anthraquinone long axis axis for each of the dyes.

Dye	$\delta_1 / ^\circ$	$\delta_2 / ^\circ$
15SB3	23.4	27.8
15NB3	26.7	40.5
15NB3OH	24.3	40.2
26B3	27.0	19.0
26B3OH	17.2	19.8

A comparison of the angles in Table 3.11 shows the five dyes exhibit a variation of 21.5° in the δ_2 angles between the MOI and AQ axes, which is significantly greater than the variation of 9.8° in the δ_1 angles between the TDM and AQ axes. However, a comparison of the two hydroxy-substituted dyes with their non-hydroxylated counterparts shows that the addition of the hydroxyl groups reduces δ_1 but has much less of an effect on δ_2 . These trends suggest that altering the nature and position of bulky substituents on the anthraquinone core results in a significant shift in the minimum MOI axis of the dye with respect to the anthraquinone core, and a less significant shift in the alignment of the TDM axis with respect to the anthraquinone core. This observation helps to rationalise why phenylamino-substituted anthraquinones generally give lower experimental order parameters than phenylsulfide and 2,6-diphenyl-substituted anthraquinones: the geometry of the 1,5-diamino substituents causes the moment of inertia axis to lie significantly further from the anthraquinone axes (given by δ_2) than the other dyes studied here, whilst having relatively little influence on the orientation of the TDM against the anthraquinone axis (given by δ_1). Overall, the substituents on the 15SB3 dye and the two 2,6-disubstituted dyes result in relatively small δ_2 angles, which better align the minimum MOI axes of these dyes with the TDM axes.

A more detailed analysis of the effect of the hydroxyl groups shows that due to the fact that $\delta_1 < \delta_2$ for 15NB3, the decrease in δ_1 caused by the addition of hydroxyl groups to form 15NB3OH results in the minimum MOI and TDM axes becoming less aligned, manifested as a larger β in 15NB3OH than in 15NB3. Conversely, $\delta_1 > \delta_2$ for 26B3 such that the decrease in δ_1 on hydroxylation causes the TDM and minimum MOI axes to become better aligned, manifested as a smaller β angle in 26B3OH than in 26B3.

Overall, the calculations indicate that there is a subtle interplay between the nature and positions of substituent groups and the relative orientations of the AQ, TDM and minimum MOI axes, which may aid in understanding the trends in experimental dichroic order parameters.

3.2.3 Electrochemistry

3.2.3.1 Cyclic voltammetry

Cyclic voltammograms obtained from the dyes in DCM are shown in Figure 3.20; DCM was used as the solvent due to the relatively high dye concentrations required (Table 3.5). The reduction and oxidation potentials obtained from these data, estimated as the average voltage of the forward and reverse peak currents for each redox process, are listed in Table 3.12.

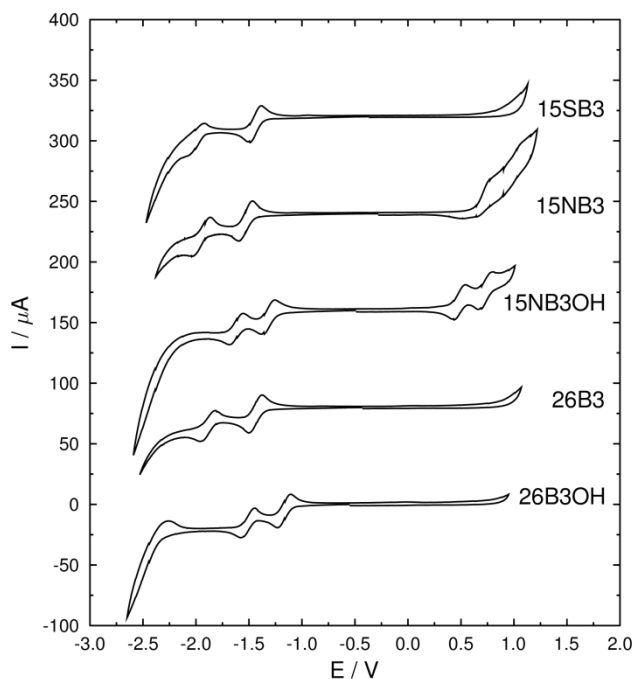


Figure 3.20 Cyclic voltammograms of the dyes at $1 \times 10^{-3} \text{ mol dm}^{-3}$ in DCM with TBAHFP at 0.1 mol dm^{-3} using a scan rate of 100 mV s^{-1} , and corrected vs. the Fc/Fc^+ couple. The initial scan direction was to negative potential and the voltammograms are offset for clarity. Uncorrected cyclic voltammograms recorded after the addition of ferrocene are given in Figure A1.11 in Appendix 1.

Table 3.12 Estimates of potentials, where observed, obtained from the CVs of the dyes in DCM vs. Fc/Fc⁺, presented in Figure 3.20.

Dye	$E_{(\text{Dye}, \text{Dye}^{\bullet-})} / \text{V}$	$E_{(\text{Dye}^{\bullet-}, \text{Dye}^{2-})} / \text{V}$	$E_{(\text{Dye}^{\bullet+}, \text{Dye})} / \text{V}$	$E_{(\text{Dye}^{2+}, \text{Dye}^{\bullet+})} / \text{V}$
15SB3	-1.44	-1.99		
15NB3	-1.54	-1.96	0.73 ^a	1.10 ^a
15NB3OH	-1.31	-1.62	0.49	0.74
26B3	-1.42	-1.86		
26B3OH	-1.13	-1.47		

^a estimated

From the peaks at negative potential, it is evident that each of the dyes exhibits two sequential reduction processes, consistent with the general behaviour of quinones in solution.¹⁹³ The separation between the forward and reverse peaks was estimated to be *ca* 100-150 mV at 100 mV s⁻¹, and was found to increase with increasing scan-rate, which suggests that these are quasi-reversible reductions, because a fully reversible process should exhibit forward and reverse peak separations of 56 mV that are independent of the scan rate.⁸¹ The quasi-reversible nature of the reductions of the dyes indicates that, under the conditions used, the species formed are relatively stable and that no significant degradation of the dyes occurs. Estimates of the peak currents for the forward and reverse peaks were found to be approximately equal for each reduction process, but in some cases the proximity of the reduction peaks to one another and to the edge of the solvent window (see Figure 3.20), precluded the determination of accurate values.

The first reduction potentials of 15SB3, 15NB3 and 26B3 were similar at $E_{(\text{Dye}, \text{Dye}^{\bullet-})} \approx -1.4$ to -1.5 V, whereas the values for 15NB3OH and 26B3OH were at -1.31 V and -1.13 V, respectively, which are *ca.* 0.2-0.3 V less negative than their non-hydroxylated counterparts. Comparable trends between hydroxylated and non-hydroxylated counterparts were also observed for the second reduction potentials. These differences may be attributed to the stabilising effect of the hydrogen-bonding OH groups in the anionic forms of the dyes.¹⁹⁴

The only oxidation potentials observed within the solvent window were for the two phenylamino dyes, which is consistent with the accessible potentials reported for aminoanthraquinones.¹⁹⁸⁻²⁰⁰ 15NB3OH exhibits two quasi-reversible oxidation processes under the conditions used, whereas the lack of defined peaks at positive

potential from the 15NB3 solution suggests that the oxidation of 15NB3 is not fully reversible,⁸¹ which again is consistent with previous studies demonstrating that reactions of some aminoanthraquinones can occur after oxidation.

3.2.3.2 Spectroelectrochemistry

The redox processes of the dyes were also studied by UV-visible spectroelectrochemistry using acetonitrile as the solvent. The use of acetonitrile provided a larger solvent window at positive potential than DCM,²¹⁹ potentially enabling the observation of oxidation peaks at higher potentials than those reported by cyclic voltammetry in Section 3.2.3.1, for which the solubility in acetonitrile was too low (Table 3.5). In addition, the use of spectroelectrochemistry provided selective detection of the dyes via their UV-vis absorption spectra.

The UV-visible absorption spectra of the dyes in acetonitrile solutions recorded at different applied potentials are presented in Figure 3.21 and the insets show plots of absorbance against the applied potential at specific wavelengths. The spectral changes observed on the application of negative and positive potentials demonstrate that both reduction and oxidation processes are observed for each of the dyes. On reduction, each of the dyes exhibits an increase in absorbance at long wavelength, consistent with the behaviour of anthraquinone itself on reduction,²²⁰ along with a decrease of the visible absorption band of the neutral dye. On oxidation, the visible absorption bands of each of the dyes decrease, with no distinct visible absorption bands arising from the product(s) of oxidation.

Reduction and oxidation potentials were obtained from the absorbances using Equation (3.3),²²¹ derived for a reversible equilibrium where A_0 is the absorbance of the neutral species, A_∞ is the absorbance of the species formed on oxidation/reduction, n is the number of electrons associated with the redox process, E° is the redox potential, E is the applied potential, R is the gas constant and T is the temperature.

$$A = \frac{A_0 + A_\infty e^{\left(\frac{nF(E^\ominus - E)}{RT}\right)}}{1 + e^{\left(\frac{nF(E^\ominus - E)}{RT}\right)}} \quad (3.3)$$

The fits to Equation (3.3) shown in the inset plots in Figure 3.21 were carried out with no constraints on the values of n and gave values of n between 0.32 and 1.54, suggesting that the redox processes may not be fully reversible under the conditions used. However, additional fits to Equation (3.3) with values of n constrained to 1 resulted in essentially identical fitted potentials that were within 0.01 V of those obtained without constraints. Equivalent fits at different wavelengths also resulted in essentially identical fitted potentials that were typically within 0.02 V of those from the fits shown in Figure 3.21. The fitted redox potentials of the dyes in acetonitrile are listed in Table 3.13 alongside the differences between the potentials for the first oxidation and reduction processes of the dyes.

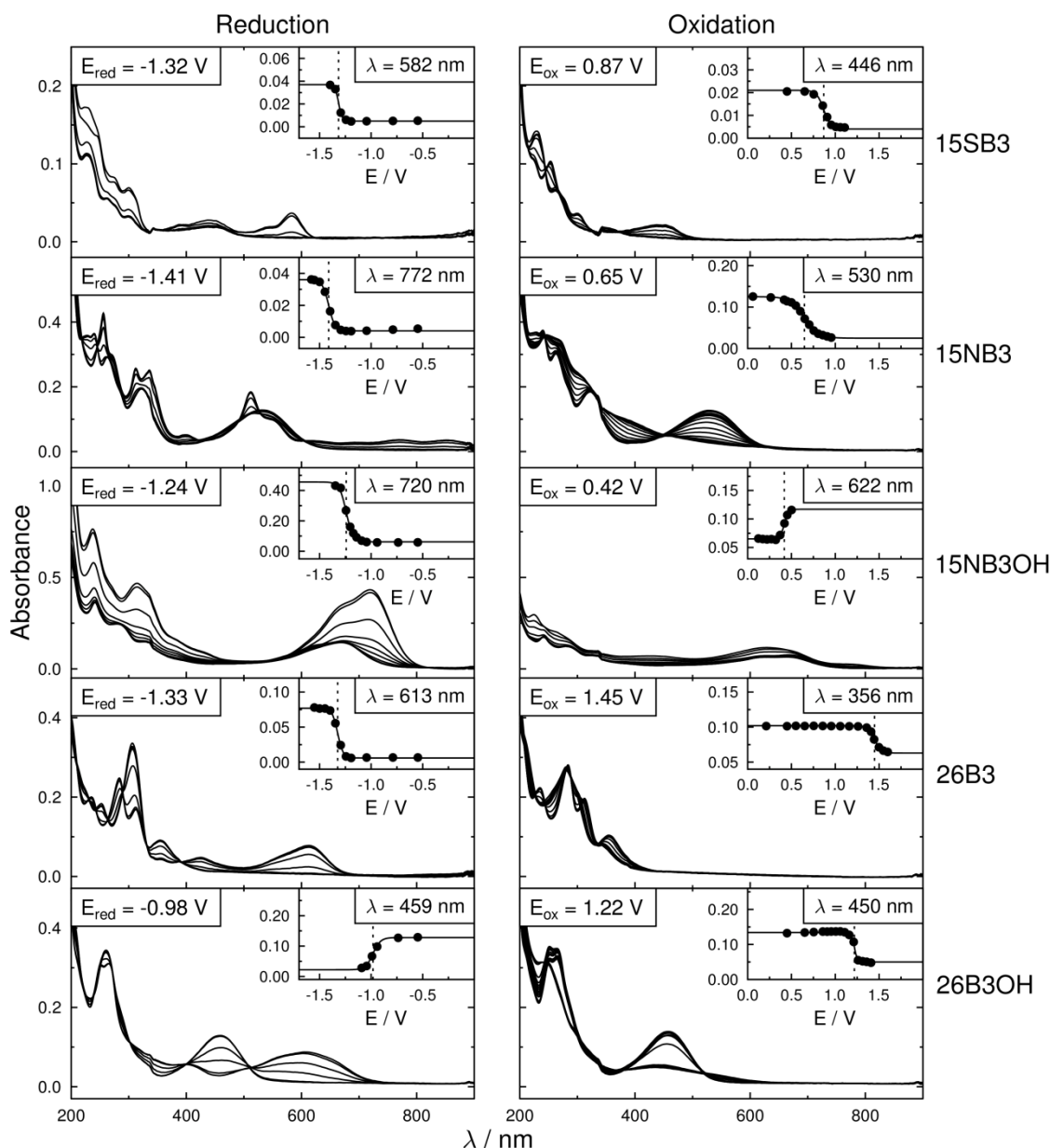


Figure 3.21 UV-vis absorption spectra of saturated solutions (*ca.* 5×10^{-5} mol dm $^{-3}$) of the dyes in acetonitrile with TBAHFP at 0.1 mol dm $^{-3}$ during electrochemical reduction (left) and oxidation (right). The insets are absorbance plots at single wavelengths (•) and the fits (—) used to estimate the redox potentials vs. the Fc/Fc $^{+}$ couple (see Figure A1.12 in Appendix 1.9). The dotted vertical lines indicate the redox potentials obtained from the fits, which are given in the plots.

Table 3.13 Experimental reduction and oxidation potentials of the dyes in acetonitrile obtained from the fits to the spectroelectrochemical data presented in Figure 3.21 and their differences ($\Delta E = E_{(Dye^{\bullet+}, Dye)} - E_{(Dye, Dye^{\bullet-})}$), referenced vs. the Fc/Fc $^{+}$ couple.

Dye	$E_{(Dye, Dye^{\bullet-})} / V$	$E_{(Dye^{\bullet+}, Dye)} / V$	$\Delta E / V$
15SB3	-1.32	0.87	2.19
15NB3	-1.41	0.65	2.06
15NB3OH	-1.24	0.42	1.66
26B3	-1.33	1.45	2.78
26B3OH	-0.98	1.22	2.20

The trends in the redox potentials between the dyes from the spectroelectrochemical data are essentially the same as those obtained by cyclic voltammetry, despite being recorded in a different solvent, and with the magnitudes of the values being slightly smaller in acetonitrile than in DCM.

The oxidation potentials presented in Table 3.13 exhibit significantly more variation between the dyes than the reduction potentials. This observation is consistent with the HOMO and LUMO plots shown in Figure 3.15. The LUMOs, to which an electron is added on reduction, are largely located on the central anthraquinone core and carbonyl groups of each of the dyes, and the lack of variation in the reduction potentials is consistent with the similarity of these orbitals; the dyes without hydroxyl groups show a variation of *ca* 0.09 V, with the addition of hydroxyl groups lowering the magnitude by *ca* 0.2-0.3 V, as described above in discussing the CV results. In contrast, the HOMOs, from which an electron is removed on oxidation, are largely located on the outer anthraquinone rings and the substituents, and the variation in the nature and position of the substituents between the dyes is evidently reflected in the greater variation of 1.03 V in the observed oxidation potentials.

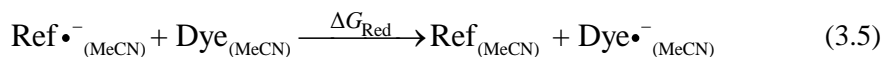
The trend in the oxidation potentials of the dyes may also be considered in the context of the electronic nature of the substituents. 26B3, which may be considered to have the least electron-donating substituents of the dyes studied, exhibits the largest oxidation potential of the dyes. In contrast, the presence of the most electron-donating hydroxyl and amine groups of the dyes in 15NB3OH results in it having the smallest oxidation potential of the dyes. The trends in the redox potentials are discussed further in Section 3.2.4.

3.2.3.3 Calculations

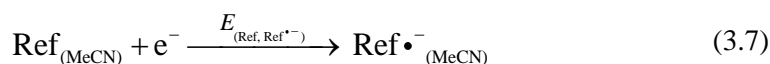
The redox potentials of the dyes were calculated in order to provide a comparison with the experimental values obtained from the spectroelectrochemical data. The relationship between the Gibbs energy change, ΔG , of a reduction or oxidation process and its associated redox potential, E , is expressed by Equation (3.4), where n is the number of electrons involved in the process and F is the Faraday constant.

$$\Delta G = -nFE \quad (3.4)$$

The reduction of a dye to a radical anion in MeCN is given in an isodesmic reaction in Equation (3.5), in which the only process occurring is an electron transfer between the dye and a reference compound, Ref.



This reaction may be considered to be a sum of two half-reactions, Equations (3.6) and (3.7), each with an associated potential. These potentials are combined in Equation (3.8) to give the reduction potential for the overall reaction, E_{Red} . Equation (3.9) may then be derived from Equations (3.4) and (3.8) enabling the reduction potential of the dye, $E_{(\text{Dye}, \text{Dye}\cdot^-)}$, to be calculated from known experimental value of $E_{(\text{Ref}, \text{Ref}\cdot^-)}$ and a calculated value of ΔG_{Red} , obtained from calculated Gibbs energies of each of the individual species in the reaction.^{194, 201, 222}

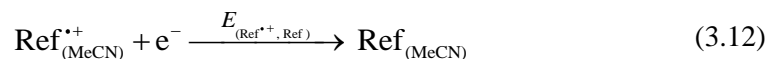


$$E_{\text{Red}} = E_{(\text{Dye}, \text{Dye}\cdot^-)} - E_{(\text{Ref}, \text{Ref}\cdot^-)} \quad (3.8)$$

$$\Delta G_{\text{Red}} = -nF \left(E_{(\text{Dye}, \text{Dye}\cdot^-)} - E_{(\text{Ref}, \text{Ref}\cdot^-)} \right) \quad (3.9)$$

A similar approach may be taken for the isodesmic oxidation process given by Equation (3.10), which may be expressed as the half reactions in Equations (3.11) and (3.12). Using the same approach as described above, Equation (3.13) may derived, enabling the potential, $E_{(\text{Dye}\cdot^+, \text{Dye})}$, to be determined from an experimental value of $E_{(\text{Ref}\cdot^+, \text{Ref})}$ and a calculated value of value of ΔG_{Ox} .





$$\Delta G_{\text{Ox}} = -nF \left(E_{(\text{Ref}^{\bullet+}, \text{Ref})} - E_{(\text{Dye}^{\bullet+}, \text{Dye})} \right) \quad (3.13)$$

In this work, duroquinone, the structure of which is shown in Figure 3.22, was used as the reference compound because it is closely related structurally to the dyes studied, and it has accessible reduction and oxidation potentials that were measured here to be $E_{(\text{Ref}, \text{Ref}^{\bullet-})} = -1.21 \text{ V}$ and $E_{(\text{Ref}^{\bullet+}, \text{Ref})} = +2.15 \text{ V}$, respectively, in acetonitrile vs. Fc/Fc^+ using the same spectroelectrochemical method as used for the dyes, as shown in Figure A1.13 in Appendix 1.8. The reduction potential of duroquinone obtained here is consistent with that of -1.228 V reported previously vs. Fc/Fc^+ in acetonitrile using cyclic voltammetry.²²³ The oxidation of duroquinone has been studied less, but a value of $E_{\text{ox}} = 2.46 \text{ V}$ vs Ag/AgCl has been reported for duroquinone in 1,1,1,3,3,3-hexafluoropropan-2-ol.¹⁹⁷

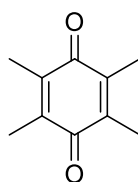


Figure 3.22 Structure of duroquinone.

Calculated Gibbs energies of each of the neutral, cationic and anionic forms of the dyes and of duroquinone were obtained from DFT optimised structures in an acetonitrile solvent field. These values are listed in Table 3.14 along with the calculated redox potentials of the dyes obtained using Equations (3.9) and (3.13). A comparison of the calculated values with the experimental values obtained from the spectroelectrochemical studies (Table 3.13) shows that the trend in the experimental oxidation and reduction potentials is replicated well by the calculated values; the calculated reduction potentials, $E_{(\text{Dye}, \text{Dye}^{\bullet-})}$, are within 0.12 V of the experimental

values, whereas the magnitudes of the calculated oxidation potentials, $E_{(\text{Dye}\bullet+, \text{Dye})}$, are slightly larger than the experimental values and show more variation.

Table 3.14 Calculated Gibbs energies, obtained from DFT optimised structures at the B3LYP/6-31g(d) level, of cationic, neutral and anionic forms of duroquinone and the five dyes studied in this work in an acetonitrile solvent field, and the associated calculated redox potentials, $E_{(\text{Dye}, \text{Dye}\bullet-)}$ and $E_{(\text{Dye}\bullet+, \text{Dye})}$, of the dyes relative to the experimental potentials of duroquinone vs. Fc/Fc^+ , and the differences between them, ΔE .

Compound	Gibbs Energy / Ha			$\Delta G / 10^{-3}$ Ha		Potential / V		
	Cation	Neutral	Anion	ΔG_{Red}	ΔG_{Ox}	$E_{(\text{Dye}, \text{Dye}\bullet-)}$	$E_{(\text{Dye}\bullet+, \text{Dye})}$	ΔE
Duroquinone	-538.35735	-538.58859	-538.7044					
15SB3	-2182.52642	-2182.72858	-2182.8421	2.29	-29.1	-1.27	+1.36	2.63
15NB3	-1496.86517	-1497.04612	-1497.1590	2.93	-50.3	-1.29	+0.78	2.07
15NB3OH	-1647.32281	-1647.49448	-1647.6118	-1.51	-59.6	-1.17	+0.53	1.70
26B3	-1386.16007	-1386.37176	-1386.4842	3.37	-19.5	-1.30	+1.62	2.92
26B3OH	-1536.61145	-1536.81791	-1536.9407	-6.98	-24.8	-1.02	+1.48	2.50

The match between the experimental and calculated values is better for the reduction potentials than the oxidation potentials, which may be attributed to the choice of duroquinone as the reference compound: the location of the LUMOs of the dyes on the central anthraquinone core and carbonyl groups is likely to be similar to that of duroquinone, whereas the location of the dye HOMOs on the outer anthraquinone rings and substituents will not be similar to duroquinone, which does not contain these structural units.

3.2.3.4 Summary of experimental and calculated first redox potentials

A comparison of all the experimental and calculated first redox potentials is shown graphically in Figure 3.23.

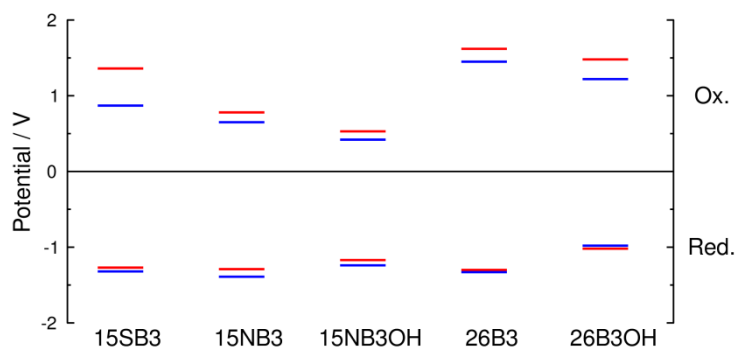


Figure 3.23 Experimental (blue) and calculated (red) first redox potentials of the dyes in acetonitrile vs. Fc/Fc^+ .

The experimental and calculated redox potentials both indicate that there is significant variation in the oxidation potentials of the dyes, arising from the variation in the nature of the LUMOs with substituent, whereas the reduction behaviour of the dyes is fairly similar between the dyes, consistent with the similarities observed in the HOMOs. A comparison of the sizes of the redox windows, ΔE , of the dyes shows that the trend from both experimental and calculated data, largely follows that of the oxidation potentials, providing further indication that the variation in the oxidation potentials dominates the variation in the redox properties of the dyes.

3.2.4 Dye design considerations for guest-host applications

The experimental and computational work described in this chapter highlights the strongly interdependent nature of the properties that must be optimised for dyes to be of use in guest-host systems, which is an extremely important consideration from the perspective of molecular design. In the work reported here, it is the nature and position of the substituents on the anthraquinone core that controls these properties for the dyes studied.

The electronic properties of the substituents are crucial to determining the colours of the dyes via the relative HOMO and LUMO energies, which define the energy gaps giving

rise to the visible transitions, and this aspect is typically the primary reason for the choice of substituents. Here, changes in substituent have also been shown to markedly alter the redox potentials of the dyes, which are also critically dependent on the HOMO and LUMO energies. In accordance with the literature,²²⁴⁻²²⁷ the HOMO and LUMO energies can be estimated from experimental redox potentials of the dyes according to $E_{\text{HOMO}} = -(E_{\text{ox}}^1 + 4.8) \text{ eV}$ and $E_{\text{LUMO}} = -(E_{\text{red}}^1 + 4.8) \text{ eV}$, where -4.8 eV is the reported redox potential of the Fc/Fc^+ couple vs. the zero vacuum level. These calculated orbital energies are listed in Table 3.15 along with the HOMO-LUMO energy gaps, ΔE , and the energies, E_{vis} , in eV of the experimental visible absorption maxima.

Table 3.15 HOMO (E_{HOMO}) and LUMO (E_{LUMO}) energies of the dyes, estimated from the experimental redox potentials of the dyes determined by spectroelectrochemistry. The energy gaps between the HOMO and LUMO levels (ΔE) and visible λ_{max} values in *p*-xylene converted to eV (E_{vis}) are also listed.

	$E_{\text{HOMO}} / \text{eV}$	$E_{\text{LUMO}} / \text{eV}$	$\Delta E / \text{eV}$	$E_{\text{vis}} / \text{eV}$
15SB3	-5.67	-3.48	2.19	2.82
15NB3	-5.45	-3.39	2.06	2.32
15NB3OH	-5.22	-3.56	1.66	1.82
26B3	-6.25	-3.47	2.78	3.46
26B3OH	-6.02	-3.82	2.20	2.63

The correlation between the estimated HOMO and LUMO energy gaps, ΔE , and the energies, E_{vis} , corresponding to the visible absorption maxima is evident from the values in Table 3.15 and from Figure 3.24, which shows the visible absorption spectra plotted on an eV scale relative to the respective HOMO energies of the dyes. For each of the dyes the energy corresponding to the visible absorption maximum is greater than that of the HOMO-LUMO energy gap, which is consistent with the absorption peaks occurring above the electronic transition origin, i.e. with the transitions occurring with a change in vibrational energy, but the trends within the sets of values are consistent.

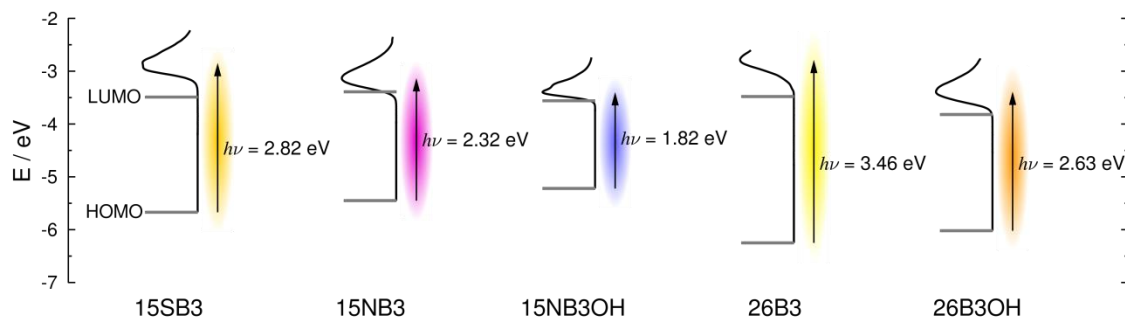


Figure 3.24 HOMO and LUMO energies estimated from experimental redox potentials with UV-vis absorption spectra recorded in *p*-xylene (in eV) overlaid. The absorption spectra are plotted relative to the energies of the respective HOMOs of the dyes, with baselines extended to the HOMO energies. The colours indicate the observed colours of the dyes, *cf* Figure 3.6, which are complementary to the absorption characteristics.

For the set of dyes studied here, it is evident that altering the substituents to obtain absorption at longer wavelength (lower energy) results in a compound with a higher HOMO energy, which consequently is more susceptible to oxidation but with relatively little change in its LUMO energy and consequently its susceptibility to reduction. It is therefore evident that if it were desirable to achieve long-wavelength absorption characteristics whilst retaining a high resistance to oxidation, it may be necessary to utilise an alternative chromophore to anthraquinone, in which the LUMO is of lower energy, or in which the energy of the LUMO may be modified by altering the structure.

As noted in the introduction to this chapter, the photostability of anthraquinones is closely related to their electrochemical properties, and hence such considerations may also extend to photochemical aspects that are beyond the scope of this thesis.

It is also evident that the subtle changes in molecular structure that influence the colour and electrochemical properties of these dyes, discussed in Sections 3.2.1 and 3.2.3, also result in significant variation in the molecular properties that define alignment, as discussed in Section 3.2.2. Although the aspect ratio and β angles are not as closely linked to the colours of the dyes as the redox properties, it is apparent that structural variations that might be made to the dyes to modify their colour and redox properties are very likely to influence the molecular shape and the TDM alignment.

3.3 Conclusions

The combination of experimental and computational studies of the dyes presented in this chapter provides an insight into how variations in the molecular structure of anthraquinone dyes influence a variety of properties that are relevant to their use in guest-host applications, particularly in terms of the substituent effect on colour, molecular shape, TDM alignment and redox behaviour. Of particular significance is the clear interdependence of these properties, and the result that straightforward substituent effects cannot be assumed in the design of molecules for these applications.

The comparisons between the experimental and calculated UV-visible absorption properties and redox potentials of the dyes generally showed a good match. In addition, the trends in the calculated aspect ratios and TDM alignments were consistent with experimental trends in the alignment of similar dyes in guest-host systems reported in the literature. This consistency between calculated and experimental results suggests that calculations such as those reported in this work may be a valuable tool to aid the molecular design of dyes for guest-host systems, potentially providing a more time and cost-effective approach than the more traditional synthetic approaches typically reported in the literature. The calculation methods used here required no input of experimental data from the dyes themselves, illustrating the predictive power of the approaches; which may readily be extended to the analysis of hypothetical structures prior to synthesis being carried out.

Chapter 4

Studies of liquid crystals and aligned guest-host systems

The work reported in this chapter focuses on studies of the dyes in aligned liquid crystal systems, quantifying their alignment through experimental spectroscopic studies. MD simulations of guest-host systems are also described, providing an aid with which to rationalise the experimental alignment trends and a method of assessing molecular structure in the context of room temperature guest-host systems.

4.1 Introduction

This introduction section gives an outline of experimental methods that are relevant to the work reported in this chapter, and which may be used to characterise orientational order in liquid crystal systems; it also gives background information on molecular dynamics simulations carried out on liquid crystals. The section concludes with the aims of the work presented in this chapter.

4.1.1 Experimental order parameters

4.1.1.1 Polarised UV-vis absorption spectroscopy

As mentioned in Chapter 1, the experimental uniaxial dichroic order parameter of a guest-host mixture, S_{exp} , may be obtained by using polarised UV-visible absorption spectroscopy to study an aligned guest-host mixture. The absorbance of the sample is measured with the electric vector of incident polarised light oriented parallel (A_{\parallel}) and perpendicular (A_{\perp}) to the orientation of the host director, as shown in Figure 4.1.

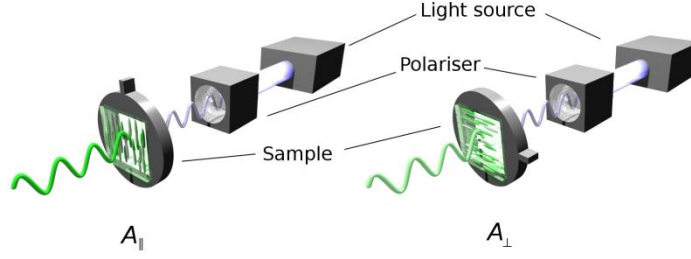


Figure 4.1 Schematic diagram of the experimental set-up for recording polarised absorption spectra of aligned guest-host samples.

In the literature on guest-host systems, the angular dependence of the absorbance of a uniaxially aligned sample, $A(\beta, \psi)$, has often been given by Equation (4.1),^{9, 24, 228, 229} where β is the angle between the transition dipole moment (TDM) and the molecular axis of the dye, ψ is the angle between the host director and the electric vector of the polarised light, S_θ is the order parameter of the dye molecules against the host director, and $S_\beta = P_2(\cos\beta)$, as defined in Section 1.2.5.

$$A(\beta, \psi) = \epsilon cl \left[\frac{S_\theta}{2} \sin^2 \beta + \frac{1 - S_\theta}{3} + S_\theta S_\beta \cos^2 \psi \right] \quad (4.1)$$

Equation (4.1) may be rearranged into a much simpler form, given by Equation (4.2), where $S_\psi = P_2(\cos\psi)$.

$$A(\beta, \psi) = \epsilon cl \frac{1}{3} (2S_\psi S_\theta S_\beta + 1) \quad (4.2)$$

The parallel and perpendicular absorbance measurements correspond to $\psi = 0^\circ$ and $\psi = 90^\circ$, respectively, and the ratio of the two, termed the dichroic ratio, R , may be expressed according to Equation (4.3).²⁴

$$R = \frac{A_{\parallel}}{A_{\perp}} = \frac{2 + 4S_\theta - 6S_\theta \sin^2 \beta}{2 - 2S_\theta + 3S_\theta \sin^2 \beta} \quad (4.3)$$

The experimental dichroic order parameter, $S_{\text{exp}} = S_\theta S_\beta$, may therefore be expressed in terms of the dichroic ratio, and hence the parallel and perpendicular absorbances, by Equation (4.4).²⁴

$$S_{\text{exp}} = \frac{R-1}{R+2} = \frac{A_{\parallel} - A_{\perp}}{A_{\parallel} + 2A_{\perp}} \quad (4.4)$$

An intuitive approach based on the $\cos^2\psi$ dependence of A would be to measure the absorbance at many values of ψ , and fit the resultant absorbances to a $\cos^2\psi$ function in order to obtain a more accurate order parameter than that obtained from the approach described above, for which just two absorbance values, measured at $\psi = 0^\circ$ and $\psi = 90^\circ$, are used. This approach may be appropriate for a non-birefringent sample, but most liquid crystal hosts exhibit birefringence, and consequently the absorbance of an aligned sample does not simply vary as a function of $\cos^2\psi$.²³⁰⁻²³² However, at $\psi = 0^\circ$ and $\psi = 90^\circ$, the electric vector of the polarised light is aligned with one of the two optical axes of a birefringent sample, such that Equation (4.1) holds under these two conditions.

4.1.1.2 Dielectric anisotropy

The host mixtures used in guest-host devices are generally colourless to provide a transparent material for guest dyes, and so UV-visible absorption spectroscopy is generally not a suitable method to obtain the orientational order parameter of a host. However, the order parameter of a host may be obtained by alternative techniques, such as measurement of the dielectric permittivity. The combination of molecular anisotropy and bulk alignment causes a bulk aligned sample to exhibit dielectric anisotropy $\Delta\varepsilon$, which is the difference in the dielectric permittivity measured parallel, ε_{\parallel} , and perpendicular, ε_{\perp} , to the sample director, given by equation (4.5). Using this anisotropy, and the average dielectric permittivity of the sample, $\bar{\varepsilon}$, given by Equation (4.6), the order parameter, S , may be estimated according to Equation (4.7).²³³

$$\Delta\varepsilon = \varepsilon_{\parallel} - \varepsilon_{\perp} \quad (4.5)$$

$$\bar{\varepsilon} = \frac{\varepsilon_{\parallel} + 2\varepsilon_{\perp}}{3} \quad (4.6)$$

$$S = \frac{\Delta\varepsilon}{3(\bar{\varepsilon} - 3)} \quad (4.7)$$

In practice, the dielectric anisotropy of a liquid crystalline material known to have positive dielectric anisotropy may be measured by applying an AC field between the plates of a cell containing a homogeneously aligned liquid crystal sample, and measuring the capacitance as a function of applied voltage. At low voltage, the alignment of the phase is not disrupted by the applied field, and therefore the capacitance may be considered to be measured perpendicular to the director of the phase. At higher voltage, the applied field causes reorientation of the phase in the direction of the applied field, so at infinite voltage, the director may be considered to be aligned with the applied field, and the capacitance would be that measured parallel to the director; practically, the capacitance curve obtained on increasing the voltage may be fitted to find the upper limit of the capacitance. In each case, the ratio of the capacitance to that of the empty cell gives the dielectric permittivity of the sample.²³⁴

4.1.2 Molecular dynamics studies of liquid crystals

The use of MD simulations to aid the understanding of liquid crystalline systems is increasing as a result of the increasing capability and availability of computational resources, and the development of modelling approaches. Conceptually, reproducing a phase of matter is a simple task, but the nature of liquid crystalline phases means that, practically, a relatively large number of molecules are required for a simulation to be of sufficient size to avoid boundary effects dominating, as discussed in Chapter 1, and liquid crystal phase behaviour has been shown to be sensitive to the intermolecular potentials employed.²³⁵ Research in this area is extensive and varied, and this introductory section aims to cover a brief background based on different fundamental approaches to MD simulations, giving context and highlighting aspects of particular relevance to the work reported here.

4.1.2.1 Coarse-grained simulations

In the context of liquid crystal simulations, a common coarse-grained approach is to model individual molecules as hard particles such as spherocylinders or ellipsoids.²³⁶ In purely repulsive models, a simulated phase may be considered to be dictated by shape alone, and such models have resulted in the simulation of stable liquid crystalline

phases,²³⁷ but this approach does not account for the temperature dependence of all thermotropic phases. To include the temperature dependence of liquid crystal phases, attractive and repulsive interactions must be considered, such as the successful Gay-Berne potential, which can be considered as a modified Lennard-Jones interaction.^{235, 238} This type of approach is well suited to conceptual studies, such as studying the influence of variation of particle shape, or variation of the precise nature of the attractive and repulsive terms of the potential on the phase behaviour observed in the simulation, because it enables huge simplification of complex chemical systems. Studies based on this approach have not only provided successful simulations of experimentally observed systems, but they have also provided simulations of hypothesised liquid crystal phases, enabling the molecular features required for such phases to form to be elucidated from the parameters of the simulations.⁶ Conversely, parameterisation must be carried out to optimise the variables in the simulations in order to replicate experimental observables from a particular chemical system, as the method is not based on specific chemical information.

Coarse-grained methods inherently require fewer calculations per time-step than atomistic simulations for a given number of molecules, and therefore they offer the advantage of shorter computation time, and hence the capability of simulating large systems. This capability has led to recent work studying systems including the interaction of liquid crystals with colloidal particles,²³⁹ and liquid crystal droplets in an aqueous environment,²⁴⁰ which would be largely inaccessible by the methods described below due to the large system sizes required.

4.1.2.2 United Atom Simulations

Combining multiple atoms into single interacting sites enables simulations to be based on specific chemical components, unlike those in coarse-grained simulations, whilst requiring shorter simulation times than methods that treat each atom specifically. Such united atom (UA) approaches are relatively widespread in liquid crystal simulations, typically through combining CH, CH₂, and CH₃ groups into single interaction sites. The consideration of these transferable chemical units enables simulations to be analysed in

much more detail than those using coarse-grained methods, and enables structure-function relationships and design features to be elucidated.

One of the most widely studied groups of nematogens using UA methods is cyanobiphenyls, due to the large number of experimental studies concerning them. Reports of such liquid crystal simulations using standard force fields parameterised for non-liquid-crystalline compounds have been successful in generating liquid crystal phases observed experimentally, but the simulated systems have tended to exhibit phase transition temperatures much higher than those observed experimentally, along with higher order parameters.²⁴¹⁻²⁴³ By adjusting the Lennard-Jones interaction parameters, it has been found that experimental transition temperatures can be reproduced, as well as densities and order parameters of liquid crystal phases.²⁴⁴ Further studies based on this force field have yielded good matches with experiment for properties of the nematic and smectic phases exhibited by 8CB.²⁴⁵ Studies of cyanobiphenyl compounds adjacent to solid surfaces have replicated experimentally observed behaviour,²⁴⁶ and the influence of surface roughness on molecular alignment has been analysed.¹⁸⁸ This force field has been extremely successful in replicating a wide variety of experimental observations, but the initial parameterisation against experimental observables limits the transferability of the force field to closely related systems.

Ab-initio methods have also been used to parameterise intermolecular force fields for UA simulations of 5CB, and they have been extended to structurally similar cyanobiphenyls, resulting in good matches between calculated and experimental thermodynamic and structural properties, including the experimentally observed smectic phase of 8CB.²⁴⁷⁻²⁵⁰

4.1.2.3 Fully Atomistic Simulations

Simulations of liquid crystal systems treating all of the atoms explicitly are also relatively widespread, and they may be considered to be the most detailed classical description of liquid crystal phases. Like united atom simulations, much of the work has focussed on cyanophenyl based compounds. Early studies focussed on simulating order parameters,²⁵¹ including simulation of the formation of liquid crystalline phases from

initial isotropic molecular configurations, demonstrating the thermodynamic stability of the simulated phase.²⁵² Specific behaviour such as rotational viscosity, anti-parallel molecular arrangements, radial distribution functions and the effect of molecular conformations have been studied.^{253, 254} The local structure of cyanobiphenyl molecules capable of hydrogen bonding has been investigated, and shown to be markedly different from those that cannot hydrogen bond.²⁵⁵ Specific interatomic interactions such as this highlight the theoretical advantages of fully atomistic simulations over those that do not treat all atoms explicitly.

Simulation of the commonly used nematic liquid crystal mixture E7 using standard inter-molecular parameters has yielded individual dipole correlations and the order parameters of individual component molecules, which are not readily available experimentally, although, as in the UA simulations, the calculated order parameter obtained was much higher than that measured experimentally.¹⁸⁵ The apparent requirement for longer timescales in atomistic simulations compared with those adopting a UA approach has also been highlighted,¹⁸⁵ which is particularly relevant given the greater computational expense of fully atomistic simulations.

4.1.3 Molecular dynamics studies of guest-host mixtures

MD simulations of liquid crystal guest-host mixtures are not common, but a few examples have been reported on studies of guest molecules other than dyes dissolved in liquid crystals. These examples include calculations of EPR spectra from studies a spin probe,²⁵⁶ studies of the influence of electrostatic interactions on the alignment of small organic molecules,²⁵⁷ replication of experimental NMR data from studies of solute molecules,²⁵⁸ and studies of the conformation and order exhibited by biphenyl solute molecules,²⁵⁹ all simulated in nematic hosts. Each of these MD studies considered the host molecules using either coarse-grained or united-atom approaches. Fully atomistic guest-host simulations are less common, but successful replication of EPR spectra of spin probes in cyanobiphenyl hosts based on fully atomistic simulations have been reported.^{260, 261}

Studies of fluorescent probes in biological membranes are also relevant to this work, because probe molecules can exhibit optical anisotropy, as observed in liquid crystal guest-host systems. Molecular dynamics studies of dye molecules within lipid bilayers have shown, amongst other properties, the occurrence of molecular alignment of the dyes within the layers, enabling experimentally observed alignment to be rationalised.^{23, 262-264}

4.2 Aims

One aim of the work presented in this chapter was to carry out experimental studies to assess the order exhibited by aligned samples of both the nematic host mixture E7 alone, and guest-host mixtures of the dyes in E7. The intention was to analyse the guest-host mixtures by polarised UV-visible absorption spectroscopy, enabling the dye alignment to be quantified and a comparison with the absorption characteristics in isotropic solution to be made.

A further aim was to explore the possibility of modelling guest-host systems using molecular dynamics simulations which, if successful, would enable a comparison of the dyes in terms of their relative molecular alignments within the host systems. In addition, the intention was to explore the dynamic behaviour of the dyes in room-temperature systems, provided by the simulations, enabling a comparison to be made with the results of the electronic structure calculations and optimised geometries presented in Chapter 3.

4.3 Results and discussion

4.3.1 Experimental order parameters

4.3.1.1 Dielectric permittivity of E7

The experimental dielectric properties of E7 alone were obtained by measuring the capacitance of a homogeneously aligned sample as a function of the applied voltage, as shown in Figure 4.2.

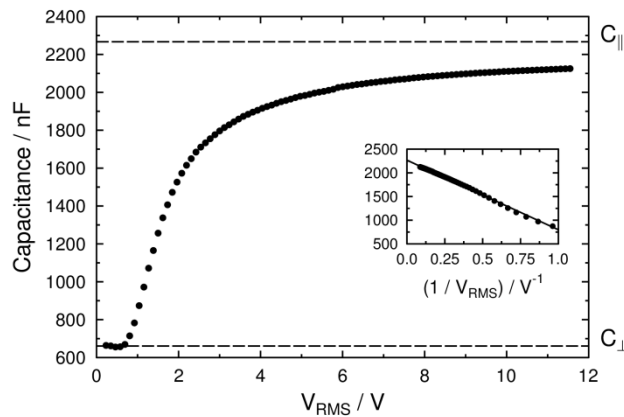


Figure 4.2 Plot of capacitance against applied RMS voltage of a homogeneously aligned sample of E7 in a cell with a path length of $7.35 \mu\text{m}$ at $25 \text{ }^\circ\text{C}$. The inset shows the capacitance plotted against $1/V$, along with the fit to obtain C_{\parallel} .

The value of the capacitance measured perpendicular to the phase director, $C_{\perp} = 661 \text{ pF}$, was obtained by averaging the capacitance measured between 0 and 0.7 V. The value of the capacitance parallel to the director, $C_{\parallel} = 2267 \text{ pF}$, was obtained by fitting the capacitance to $C = 1/V$, for $V > 1 \text{ V}$,²⁶⁵ as shown in the inset in Figure 4.2. Using these values and that of $C_0 = 120.7 \text{ pF}$, measured for the empty cell, gave values of $\epsilon_{\perp} = 5.5$ and $\epsilon_{\parallel} = 18.8$ for the dielectric permittivity perpendicular and parallel to the director, respectively, which are consistent with values reported in the literature.^{266, 267} Using Equations (4.5) - (4.7), the order parameter of E7 was estimated to be 0.64, consistent with the experimental order parameter of *ca* 0.65 reported in the literature.^{185, 268}

4.3.1.2 UV-visible absorption spectroscopy of dyes in E7

Polarised UV-visible absorption spectra were recorded from aligned samples of the dyes in E7 with the electric vector of the polarised light oriented parallel with the host director, as shown in Figure 4.3, along with those obtained from *p*-xylene solutions. It is evident from the spectra presented in Figure 4.3 that the visible absorption profiles of the dyes do not change significantly between the isotropic *p*-xylene and nematic E7 solvents. This match between the band shapes is consistent with the TD-DFT calculations, which indicated that the visible absorption band of each dye arises from a single electronic transition, or from transitions with very similar TDM orientations. Additionally, the consistency in band shapes between the samples in *p*-xylene and E7 is indicative that aggregation of the dyes is unlikely to have occurred in the E7 samples, because molecular aggregation is typically associated with changes in spectral profile.²⁶⁹ The aggregation of an anthraquinone dye in 5CB has been reported in the literature,²⁷⁰ but no evidence of the hair-like structures described in this report was observed in the samples when viewed under a microscope. This observation is consistent with the structures of the five dyes studied here, in which the terminal alkyl chains typically confer greater dye solubility than that of unsubstituted structures²⁴ such as that for which aggregation has been reported.

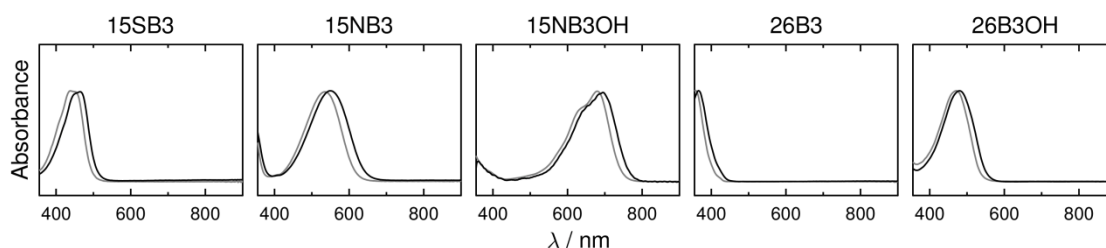


Figure 4.3 Scaled UV-visible absorption spectra of the dyes at *ca* 1.5 wt % (except for 15NB3OH for which was at *ca* 0.75 wt % to ensure that the absorbance was within the instrument range) in E7 (black) and at 2×10^{-4} mol dm⁻³ in *p*-xylene (grey), shown for comparison.

A comparison of the λ_{max} values of the dyes in E7 with those in *p*-xylene, listed in Table 4.1, shows a red shift in going to E7 for each of the dyes, and comparison with the dyes in other isotropic solvents (Table 3.4) shows that the same offset is observed with respect to all of the isotropic solvents used. This behaviour is consistent with red-shifts reported for many dyes on going from non-polar isotropic solvents to cyanobiphenyl-

based liquid-crystalline solvents.^{37, 45, 271} The shift has been assigned to the polarisability of the cyanobiphenyl hosts being higher than those of the isotropic solvents in the case of an oxazine dye,²⁷² although no strong trends were observed between solvent polarisability and λ_{\max} values within the isotropic solvents used in the work reported here (see Appendix 1.2).

Table 4.1 Experimental λ_{\max} values of the aligned samples of dye-E7 mixtures obtained from the polarised UV-vis absorption spectra. Values in *p*-xylene are also shown for comparison.

Dye	λ_{\max} / nm	
	E7	<i>p</i> -xylene
15SB3	460	439
15NB3	548	535
15NB3OH	693	680
26B3	367	358
26B3OH	477	471

Polarised UV-visible absorption spectra of aligned samples of the dyes in E7 with the director oriented parallel (A_{\parallel}) and perpendicular (A_{\perp}) to the electric vector of the incident light are presented in Figure 4.4.

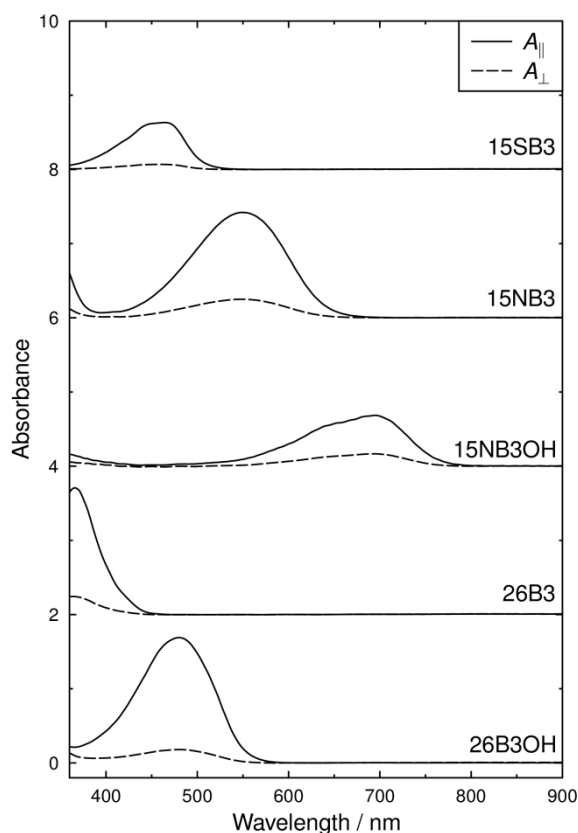


Figure 4.4 Polarized UV-visible absorption spectra of aligned samples of the dyes at *ca* 1.5 wt % (except for 15NB3OH for which was at *ca* 0.75 wt % to ensure absorbance was within the instrument range) in E7, used to obtain their dichroic ratios. The spectra are offset for clarity.

The spectra in Figure 4.4 show that the value of A_{\parallel} is greater than that of A_{\perp} for each of the dyes in E7, and this positive dichroism is consistent with the reported alignment of comparable structures studied previously.^{59, 60} Plots of the dichroic ratios, R , across the full range of the visible spectrum are presented for each of the dyes in Figure 4.5, and they show that the dichroic ratios are approximately constant over the range of each of the visible bands. This observation is consistent with the TD-DFT calculations and with the comparison of spectral profiles in Figure 4.3, indicating that the bands arise from single electronic transitions, discussed in Chapter 3.

The dichroic ratios and associated order parameters, S_{exp} , determined using Equation (4.4) are listed in Table 4.2, and a comparison of the order parameter values is shown graphically in Figure 4.6. The dichroic ratios were calculated at the absorption maxima for each of the dyes, except for 26B3 for which the dichroic ratio was determined at 390 nm to avoid overlap with E7 absorption below *ca* 370 nm (see Figure A2.1 in Appendix 2.1).

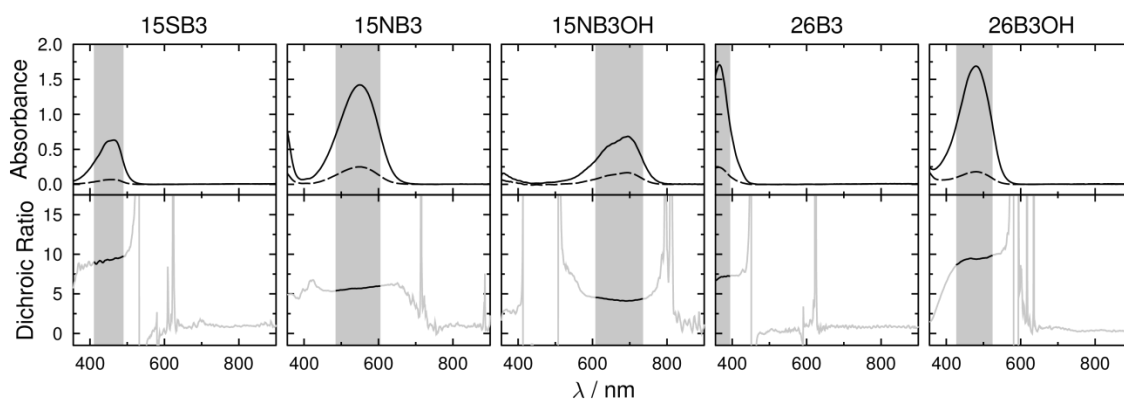


Figure 4.5 Plots of dichroic ratio against wavelength for each of the dyes in E7, obtained from the polarized UV-visible absorption spectra presented in Figure 4.4 which are shown at the top of this figure for clarity. Highlighted grey bands show the full-width-half-maxima of the visible bands, except in the case of 26B3 due to the absorption of E7 below *ca* 370 nm.

Table 4.2 Experimental dichroic ratios, R , and order parameters, S_{exp} , of aligned samples of the dyes in E7, obtained from the polarised UV-visible absorption spectra presented in Figure 4.4. Calculated S_{β} values presented and discussed in Chapter 3 (Table 3.10) are given here for comparison.

Dye	Experimental		Calculated
	R	S_{exp}	S_{β}
15SB3	9.32	0.73	0.991
15NB3	5.69	0.61	0.914
15NB3OH	4.10	0.51	0.887
26B3	7.26	0.68	0.968
26B3OH	9.40	0.74	0.999

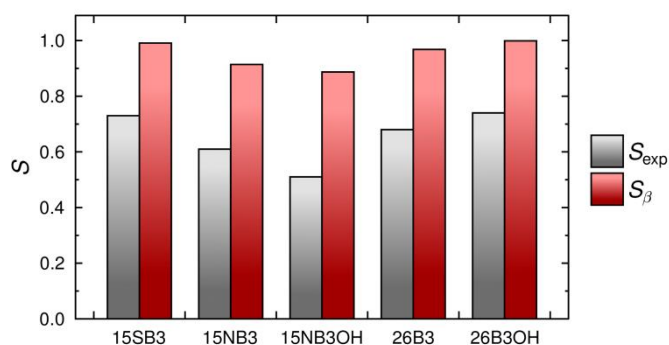


Figure 4.6 Graphical comparison of the experimental order parameters of the dyes in E7, S_{exp} , and the values, S_{β} , obtained from the calculated β angles of the dyes.

The experimental order parameters in E7 show significant variation between the dyes despite their relatively similar structures. A relatively high experimental order parameter is observed for 15SB3, consistent with measurements of other 1,5-disubstituted sulfide anthraquinones reported in the literature.^{64, 65, 68} Replacement of the sulfide linking group with an amine group causes a significant decrease in dichroic ratio, shown in going to 15NB3 and 15NB3OH, which is again consistent with values for 1,5-disubstituted aminoanthraquinones reported previously.^{59, 65, 66} The two 2,6-disubstituted dyes exhibit high order parameters, which is also consistent with reported order parameters of similar structures.⁶¹

A comparison of the experimental order parameters with the order parameters, S_{β} , obtained from the calculated β angles, listed in Table 4.2 and shown in Figure 4.6, shows a good match in the trends between the dyes. This match indicates that the relative orientations of the TDMs within the dyes are significant in terms of the observed alignment of this set of dyes in E7, although the observation that the experimental values are lower than the calculated S_{β} values indicate that there is also likely to be a significant contribution from the molecular alignment within the host for each of the dyes.

A comparison of the experimental order parameters of the dyes in E7 with the experimental order parameter of 0.64 for E7 alone shows that the order parameters of the amine dyes (15NB3 and 15NB3OH) are lower than that of the host, whereas the order parameters of the sulfide and 2,6-disubstituted dyes (15SB3, 26B3 and 26B3OH) are higher than that of the host. This type of behaviour has been linked with the relative sizes of the host and guest molecules, with dyes that are longer than the host molecules

typically exhibiting higher order parameters than the host alone.²⁴ This observation is discussed further in Section 4.3.2.3.

4.3.2 Molecular dynamics simulations

A comparison of S_{exp} with S_{β} , such as that discussed above, is only of limited use because it neglects the contribution of the molecular alignment to the experimental order parameter, as discussed in Chapter 1. Therefore, it is desirable to be able to calculate the molecular alignment contribution, S_{θ} , to the overall order parameter in order to be able to make a more meaningful comparison between experimental and calculated order parameters. The molecular alignment is of particular relevance to the dyes studied in this work because of the variation in shapes between the dyes, highlighted by the electronic structure calculations discussed in Chapter 3. In principle, the order parameter, S_{θ} , arising from the molecular alignment of the dyes within the host should be obtainable from guest-host molecular dynamics simulations. Prior to consideration of such guest-host systems, MD studies on the host alone were carried out, and are presented first in this section.

4.3.2.1 Simulations of E7 alone

A fully atomistic simulation of E7 has been reported in the literature previously,¹⁸⁵ and it was used as the starting point for the work reported here; the intention was first to replicate the previous simulation results on E7 to verify the methods used here.

A regular lattice of E7 component molecules in the correct component concentrations (given in Figure 1.15), listed in Table 4.3, was arranged in a random head-tail orientation with parallel minimum moment of inertia axes, and was used as the initial geometry for the simulations. The lattice consisted of $8 \times 8 \times 4$, $10 \times 10 \times 4$, or $22 \times 22 \times 8$ component molecules for simulations of 256, 400, and 3872 host molecules, respectively. The geometries of the host molecules used to construct the lattice were obtained by DFT optimisations at the B3LYP/6-31G(d) level. Their long axes were aligned parallel with each other, with a regular intermolecular spacing of *ca.* 10 Å along each axis corresponding to a gas-phase density, which provided an approximately cubic

simulation box for these lattices. An energy minimisation was then carried out using a steepest descent algorithm.

Table 4.3 The numbers of component E7 molecules used in the molecular dynamics simulations to match the experimental component weight % values.

	Number of molecules		
E7 total	256	400	3872
5CB	141	220	2130
7CB	62	97	941
8OCB	36	56	542
5CT	17	27	259

To obtain a starting geometry for the full simulation corresponding to an isotropic liquid configuration, an NVT run of 20 ps at a nominal temperature of 1000 K was carried out, enabling the lattice system to evolve into a randomised system for which the order parameter was ≈ 0 , before rapidly compressing the system with a nominal pressure of 5×10^4 bar until the system reached a density of $\approx 1 \text{ g cm}^{-3}$, corresponding to a condensed-phase, randomised system. The system was subsequently relaxed, again using a steepest descent method, before running the full MD simulation at 300 K.

The order parameter of the simulated system was calculated as the largest eigenvector of the ordering tensor, $Q_{\alpha\beta}$, and the director, \mathbf{n} , was defined as the associated eigenvector, as given by Equation (4.8) where N is the number of molecules, δ , is the Kronecker delta, j is the molecule number in the simulation, α and β represent the Cartesian x , y and z axes, and a represents the component of the long molecular axis vector. The long molecular axis of each component molecule of E7 was defined as the axis of minimum moment of inertia. The ordering tensor was calculated for the ensemble at each trajectory frame of the simulation.

$$Q_{\alpha\beta} = \frac{1}{N} \sum_{j=1}^N \frac{3a_{j\alpha}a_{j\beta} - \delta_{\alpha\beta}}{2} \quad (4.8)$$

The evolution of the order parameter over time for a simulation of 256 component molecules of E7, starting from an isotropic configuration, is shown in Figure 4.7, demonstrating evolution of the nematic phase over approximately 100 ns and giving an average order parameter of $S_\theta = 0.884$ between 120 and 500 ns. This S_θ value is significantly higher than the experimental value of $S_{\text{exp}} = 0.64$, but it is similar to the

previous reported calculated value of 0.81,¹⁸⁵ and the overestimation of the calculated order parameter is likely to be largely due to the default non-bonded interaction parameters discussed in Section 4.1.2.2. Additional contributions to the overestimation may arise from redefining the internal director, \mathbf{n} , of the system at each time frame, inherently maximising the calculated order parameter of the ensemble, and from using the minimum moment of inertia axes of the molecules to calculate the order parameter.

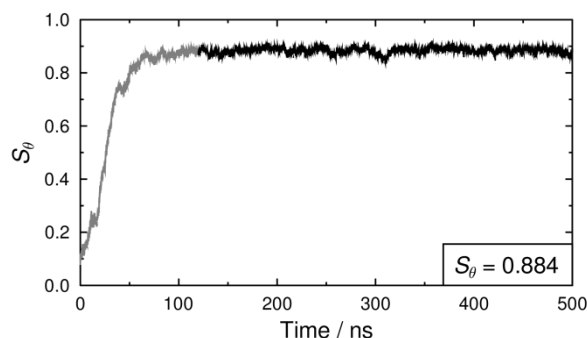


Figure 4.7 Evolution of the order parameter over time of a simulation of 256 E7 component molecules, starting from an isotropic configuration. The region in black (>120 ns) represents the data averaged to obtain the order parameter value.

As also described in the previous report,¹⁸⁵ a simulation was also run here from a “pseudo-nematic” starting configuration. This configuration was generated using the same method as that for the isotropic starting point, but omitting the initial, randomising NVT step. This starting point, therefore, has a comparable density to that of the isotropic starting point, but the initial order parameter is comparable to that of the equilibrated sample, providing a more rapid generation of the nematic phase and reducing the computation time required to obtain this phase. The evolution of the order parameter in a simulation of 400 component molecules of E7, starting from a pseudo-nematic geometry, is shown in Figure 4.8; the order parameter reaches an approximately constant value of $S_\theta = 0.878$ after *ca* 30 ns, matching that obtained from the isotropic starting point, and comparable to that of 0.83 reported in the literature.¹⁸⁵

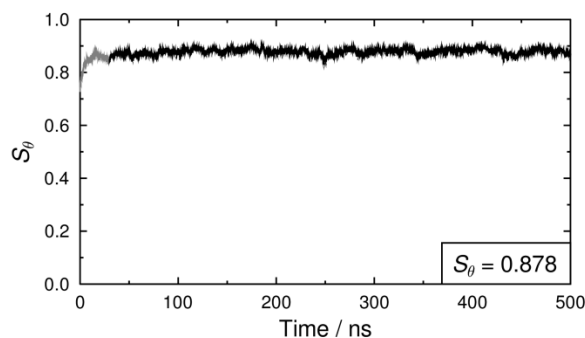


Figure 4.8 Evolution of the order parameter over time of a simulation of 400 E7 component molecules, starting from a pseudo-nematic configuration. The region in black (>30 ns) represents the data averaged to obtain the order parameter value.

The densities of the two simulations of E7 reported above were calculated and are shown plotted against time in Figure 4.9, alongside a calculated density of 1.06 g cm^{-3} from previous MD studies¹⁸⁵ and an experimental density of 1.028 g cm^{-3} ²⁷³ reported in the literature. The simulations from both the pseudo-nematic and isotropic starting configurations result in an average system density of 1.015 g cm^{-3} , comparable to the calculated and experimental values reported in the literature.

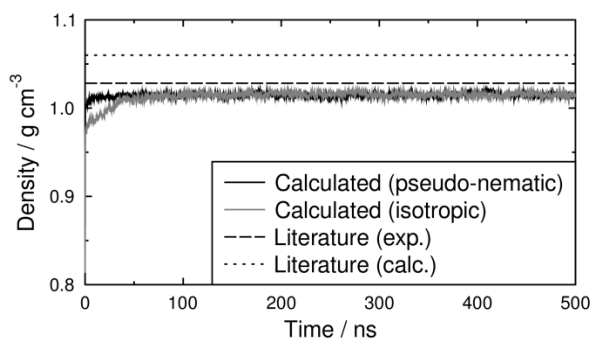


Figure 4.9 Calculated densities during the simulations of E7 starting from isotropic and pseudo-nematic configurations, shown as 10 point averages alongside literature values of calculated¹⁸⁵ and experimental²⁷³ densities.

A final comparison made between this work and the previous work on E7 was an analysis of the dihedral angle distributions within the molecules. Figure 4.10 shows the dihedral distributions about selected bonds within 7CB, demonstrating the tendency of the alkyl chains to exhibit all-*trans* conformations, and the phenyl rings to have an inter-ring angle distribution centred at *ca* 33° , consistent with that of $34 \pm 1^\circ$ measured experimentally for biphenyl in a nematic host.²⁷⁴ The distributions in Figure 4.10 also show a close match with the equivalent distributions reported in the literature from MD simulations.¹⁸⁵

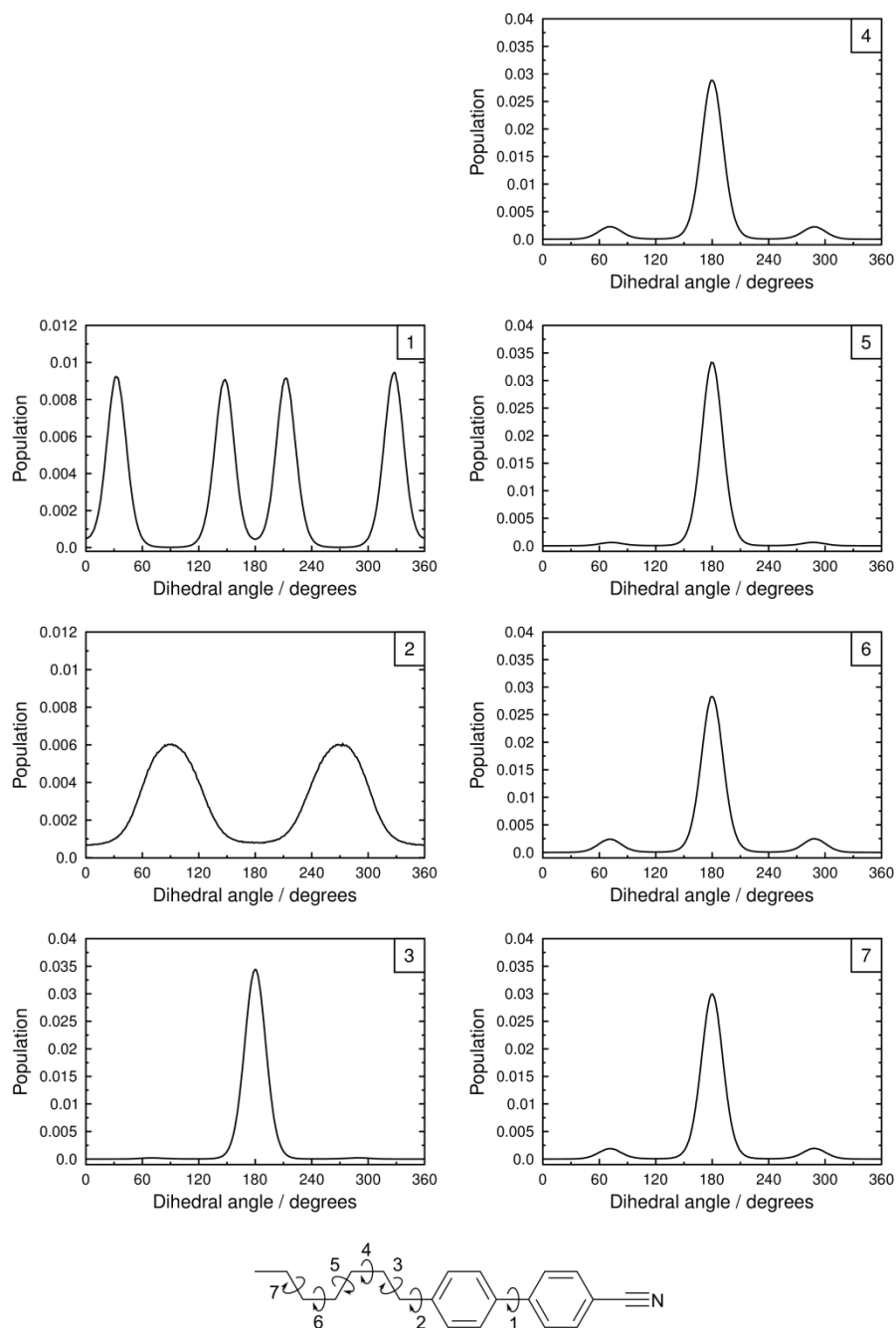


Figure 4.10 Normalised distribution functions of seven dihedral angles, 1-7, in the E7 component molecule 7CB, as defined in the structure shown above, calculated from a 256-molecule simulation of E7 alone with a pseudo-nematic starting geometry, obtained between 30 ns and 200 ns. (*cf.* equivalent Figure 3 in the work of Pelaez and Wilson¹⁸⁵).

The possible influence of the system size on the calculated order parameters was assessed by simulating a system of 3872 component molecules of E7, starting from a pseudo-nematic configuration. This larger system evolved to give an order parameter of $S_\theta = 0.869$, obtained between 30 and 50 ns, shown in Figure 4.11, which suggests that the influence of the system size on the calculated order parameter is small.

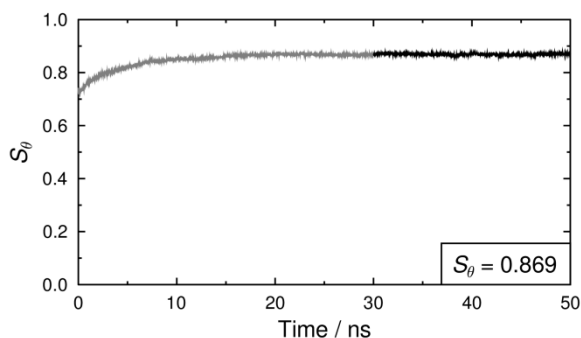


Figure 4.11 Evolution of the order parameter over time of a simulation of 3872 E7 component molecules, starting from a pseudo-nematic configuration. The region in black (>30 ns) represents the data averaged to obtain the order parameter value.

The calculations presented in this section demonstrate successful simulations of the nematic phase of E7, both from isotropic and pseudo-nematic starting geometries, with the pseudo-nematic starting geometry enabling the simulated nematic phase to be obtained more rapidly than the isotropic starting geometry. The methods were therefore considered suitable for simulating the host mixture in guest-host simulations. There is scope for improving the E7 simulations, most notably in terms of the overestimation of the order parameter of the system, but such an improvement would be likely to require parameterisation of intermolecular force constants to improve the match with experimental data. In the work presented here, the focus was on the comparison of dye behaviour within a nematic host, and therefore the simulation methods outlined above were considered suitable for providing a nematic environment within which to compare the behaviour of different guest dye molecules.

4.3.2.2 Dye Force Constant Parameterisation

Prior to the simulation of guest-host mixtures, it was necessary to allocate atom types from the force field to the atoms of the dye molecules, and subsequently to parameterise any intramolecular force constants not present in the default OPLS force field used in this work. The overall potential energy, E_{tot} , of a given configuration in the OPLS force field is defined by Equation (4.9) where E_{bond} is the bond stretching term, E_{angle} is the angle bending term, E_{dihedral} is the dihedral torsion term, and $E_{\text{nonbonded}}$ is the energy term arising from non-bonded interactions.

$$E_{\text{tot}} = E_{\text{bond}} + E_{\text{angle}} + E_{\text{dihedral}} + E_{\text{non-bonded}} \quad (4.9)$$

Of the intramolecular terms, force constants related to E_{bond} were not required because bond lengths were constrained during the simulations. The functional form of the angle bending energy term for a given bond angle is given by Equation (4.10), where k_{θ} is the force constant, θ is the bond angle, and θ_0 is the equilibrium bond angle.

$$E_{\text{angle}} = \frac{1}{2} k_{\theta} (\theta - \theta_0)^2 \quad (4.10)$$

The functional form of the dihedral torsion energy term for a given dihedral may be given by Equation (4.11), where C_n are the Ryckaert-Bellemans coefficients and ψ is the dihedral angle.

$$E_{\text{dihedral}} = \sum_{n=0}^5 C_n (\cos(\psi - \pi))^n \quad (4.11)$$

Specifically, parameterisation was required for the C-S-C bond angle and the C-S-C-C dihedral angles in 15SB3, and for the C-N-C-C and H-N-C-C dihedral angles in 15NB3 and 15NB3OH. In order to simplify the parameterisation process, model structures, **M1**, **M2** and **M3**, were used for the parameterisations, as shown in Figure 4.12 where they are labelled with the angles and dihedrals for which force constants were determined.

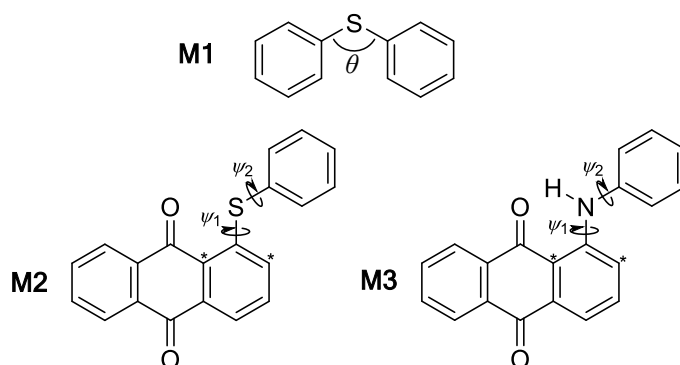


Figure 4.12 Model structures used for parameterisation of force constants for the C-S-C angle (top), the C-S-C-C dihedrals (left), and the C-N-C-C dihedrals and H-N-C-C dihedrals required for dyes in the guest-host MD simulations.

For determining the angle bending and dihedral torsion force constants, a series of HF optimisations of the model structures were carried out, stepping around the bond angle or dihedral of interest, providing a series of conformational “HF energies”. Dihedral angles within the aromatic systems were constrained to keep the carbon atoms in a planar configuration. The HF/6-31g(d) level of theory was used here to provide consistency with that used in the development of the OPLS force field,⁹¹ and to provide acceptable computation times for the large number of optimisations performed. Optimised structures of the five dyes at the HF/6-31g(d) level are shown in Figure A2.2 in Appendix 2.2 demonstrating comparable geometries to those optimised at the B3LYP/6-31g(d) level discussed in Chapter 3. The “MD energy”, given by Equation (4.9), was then determined for each of these conformations but with the force constants relating to the angle or dihedral being fitted set to zero. The force constant(s) and equilibrium angles were then determined by fitting the difference between calculated HF and MD energies to Equation (4.10) in the case of bond angle force constant parameterisation and Equation (4.11) in the case of the dihedral angle force constant parameterisation.

Potential energy curves for fitting the C-S-C angle force constants were obtained by calculating conformational HF and MD energies of **M1**. Due to the fact that the C-S-C-C dihedral force constants had not been parameterised at this point, four potential energy plots were produced with the C-S-C-C dihedrals fixed at angles of $\psi = 90, 120, 150$ and 180° , shown in Figure 4.13, enabling the effect of variation of the C-S-C angle to be considered independently of the dihedral angles. The constants, θ_0 and k_θ , were then fitted for each of the four dihedral angles, and the average values were determined as $\theta_0 = 101.572^\circ$ and $k_\theta = 556.089 \text{ kJ mol}^{-1} \text{ rad}^{-1}$. The MD energies of the conformations, calculated by using these average fitted force constant and equilibrium angle values, are also shown in Figure 4.13, demonstrating a good match between the HF and MD conformational energies for each of the fixed dihedral angles.

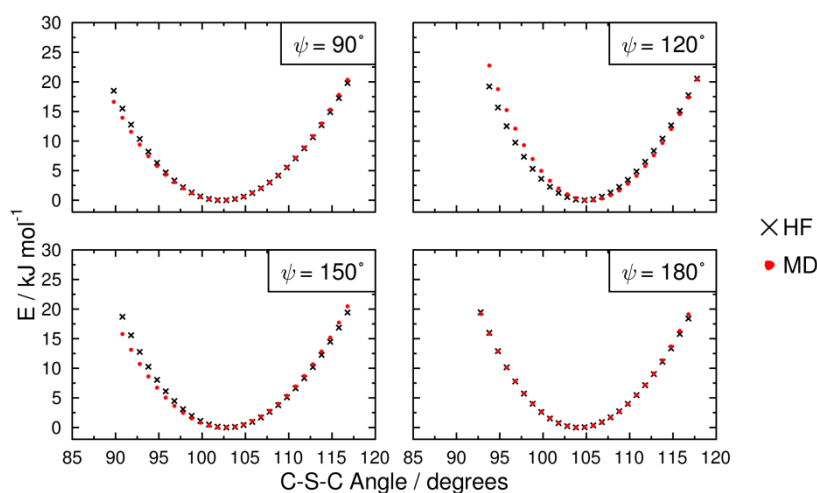


Figure 4.13 Plots of HF energy vs. C-S-C bond angle at four different C-S-C-C torsion angles, ψ , alongside MD energies obtained after fitting the equilibrium angle, θ_0 , and bending force constant, k_θ , of **M1**.

Initial studies on fitting the force constants for dihedrals ψ_1 and ψ_2 showed that these two torsions were not equivalent in the case of either the sulfide or the amine compounds, **M2** and **M3**, and so the carbon atoms marked ‘*’ in Figure 4.12 were defined as different atom types from the unmarked carbon atoms in order to distinguish between torsions about ψ_1 and ψ_2 . A complete list of the atom-types used in the simulations is given in Appendix 2.3. The major difficulty in the parameterisations of both **M2** and **M3** was the inter-dependence of the parameters to be fitted, so they could not be fitted entirely independently of each other.

The potential energy surface obtained from conformations of **M2** from HF calculations using 5° steps about both ψ_1 and ψ_2 is shown in Figure 4.14. These surfaces show a minimum energy conformations at $\psi_1 = 180^\circ$ and $\psi_2 = 90^\circ$, and at $\psi_1 = 180^\circ$ and $\psi_2 = 270^\circ$, which are consistent with the HF optimised geometry of 15SB3 shown in Appendix 2.2. The force constants C_0 to C_5 for the C-S-C-C dihedral rotation, ψ_2 , were fitted using Equation (4.11) for $20^\circ < \psi_2 < 160^\circ$, and a fixed value of $\psi_1 = 180^\circ$, which was the minimum energy angle for ψ_1 from the optimised geometry. A subsequent fit over the C*-C-S-C dihedral angles for $90^\circ < \psi_1 < 270^\circ$ was carried out, with ψ_2 unconstrained and using the previously fitted force constants. The fitted force constants are listed in

Table 4.4 and the resultant MD potential energy surface calculated using these force constants is also shown in Figure 4.14. A comparison of the HF energy surface and the MD energy surface after fitting the force constants shows a good match between the two, with each surface showing comparable energy minima and energy profiles. The main differences are the energy barriers corresponding to dihedral angles of $\psi_2 \approx 0^\circ$ and $\psi_2 \approx 180^\circ$, at energies $>30 \text{ kJ mol}^{-1}$. The similarity in the shapes of the regions defined by RT at 300 K in Figure 4.14, provide support that the fitted force constants are suitable for simulations at 300 K.

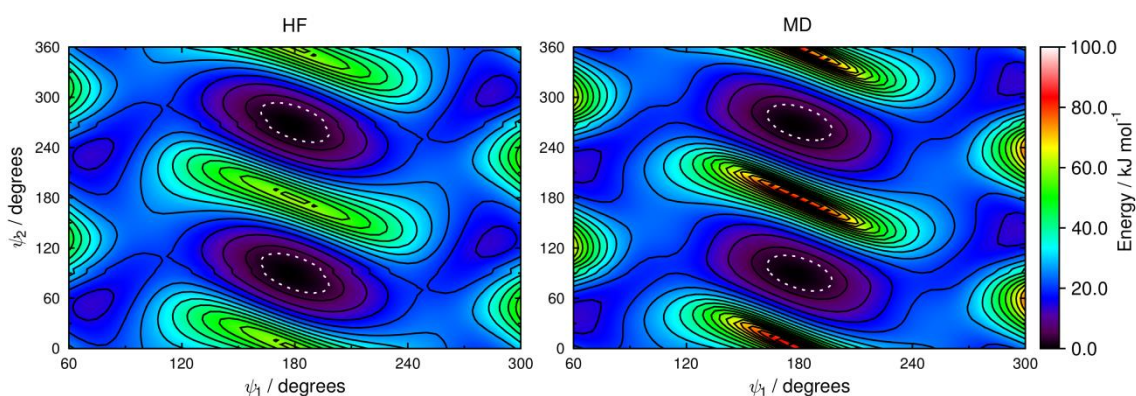


Figure 4.14 Plots of potential energy surfaces for the two C-S-C-C dihedral angles of the model structure **M2** shown in Figure 4.12 from the HF calculations (left) and from MD after fitting (right). The white dotted boundaries correspond to RT at 300 K (2.48 kJ mol^{-1}).

The potential energy surface relating to torsions about ψ_1 and ψ_2 in **M3** obtained from the HF calculations is shown in Figure 4.15. The surface shown in Figure 4.15 appears to have equivalent minimum energy conformations at $\psi_1 = 180^\circ$ and $\psi_2 = 90^\circ$, and at $\psi_1 = 180^\circ$ and $\psi_2 = 270^\circ$, but close inspection shows the presence of minima at *ca* $\psi_1 = 180^\circ$ and $\psi_2 = 70^\circ$, and at $\psi_1 = 180^\circ$ and $\psi_2 = 110^\circ$, with the energy of the conformations at $\psi_1 = 180^\circ$ and $\psi_2 = 90^\circ$, and to $\psi_1 = 180^\circ$ and $\psi_2 = 270^\circ$ calculated to be higher in energy by *ca* 0.1 kJ mol^{-1} , as shown in Figure A2.15 in Appendix 2.4. These minima are again consistent with the optimised geometry of **M3**, shown in Figure A2.2 in Appendix 2.2.

The fitting of the dihedral force constants was more complex for **M3** than **M2** due to the presence of the hydrogen atom on the amine group, resulting in two additional sets of force constants required to describe torsion about the H-N-C-C and H-N-C-C* dihedrals. The force constants describing the C-N-C-C torsion about ψ_2 were fitted first

over angles of $20^\circ < \psi_2 < 160^\circ$, with ψ_1 fixed at 180° , and the force constants for the ψ_2' H-N-C-C torsion were then fitted for the same geometries. Fitting was then carried out for the force constants describing the C-N-C-C* torsion about ψ_1 for values of $90^\circ < \psi_1 < 270^\circ$, with the torsions about ψ_2 unconstrained and for which the previously fitted force constants were used; the force constants describing the ψ_1' H-N-C-C* torsion were then also fitted for these geometries. The resultant MD potential energy surface corresponding to torsion about the ψ_1 C-N-C-C and ψ_2 C-N-C-C* dihedrals after fitting of the force constants is shown in Figure 4.15 and the fitted force constants are listed in Table 4.4.

A comparison of the HF and MD potential energy surfaces in Figure 4.15 shows a good match between the two, with the general shapes of the surfaces consistent with each other. The dimensions of the regions within the dashed lines corresponding to RT at 300 K are consistent between the energy surfaces in Figure 4.15, demonstrating that the potential energy wells in both the ψ_1 and the ψ_2 dimensions of the fitted MD energies match those calculated from HF, although the slight difference in the shapes of the potential energy wells suggests that the interdependence of the dihedral torsions is not exactly replicated by the fitted force constants. The potential energy wells in the fitted MD energy surface exhibit double minima, consistent with the HF energy surface, as shown in Figure A2.15 in Appendix 2.4; the minima do occur at slightly different values of ψ_1 and ψ_2 , but the absolute energy differences between these regions of the HF and MD surfaces are very small.

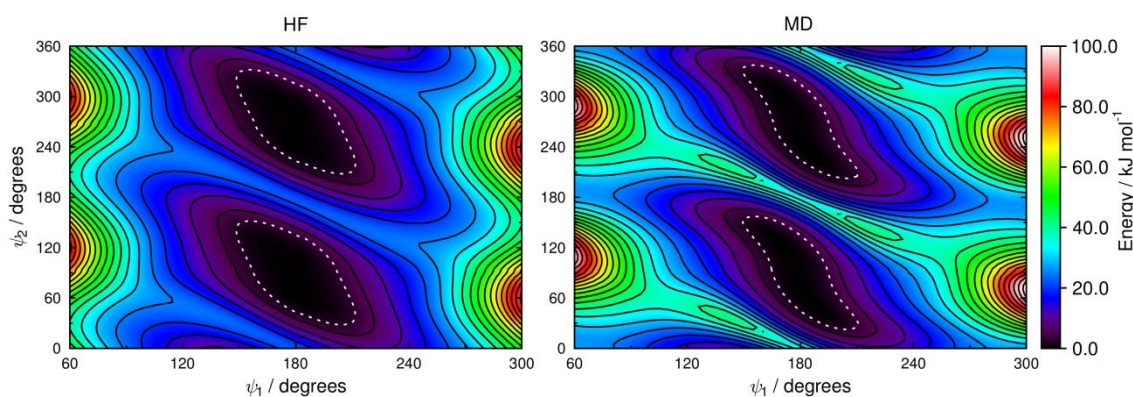


Figure 4.15 Plots of potential energy surfaces for the two C-N-C-C dihedral angles of the model structure **M3** shown in Figure 4.12 from the HF calculations (left) and from MD after fitting (right). The white dotted boundaries correspond to RT at 300 K (2.48 kJ mol^{-1}).

Table 4.4 Dihedral force constants, $C_0 - C_5$, obtained from the dihedral angle fits presented in Figure 4.14 and Figure 4.15 for model structures **M2** and **M3**.

	Dihedral	Dihedral force constants / kJ mol^{-1}					
		C_0	C_1	C_2	C_3	C_4	C_5
M2	ψ_2 C-C-S-C	18.27654	0.00001	2.51901	-0.00001	-5.57075	0.00001
	ψ_1 C*-C-S-C	25.61956	-0.00001	-13.22398	0.00000	-12.73441	0.00001
M3	ψ_2 C-C-N-C	18.05799	0.01619	-5.53203	0.01654	-5.84963	-0.02760
	ψ_2' C-C-N-H	6.70517	-0.01274	-0.40420	0.03014	0.64107	-0.02561
	ψ_1 C*-C-N-C	20.58734	0.00008	-8.84758	-0.00038	-11.67430	0.00027
	ψ_1' C*-C-N-H	-13.11104	-0.05736	32.32178	0.05109	-18.77205	-0.02023

A comparison of the HF potential energy surfaces of **M2** in Figure 4.14 and **M3** in Figure 4.15 provides a comparison of the relative flexibilities of the sulfide and amine linking groups, and it indicates that there is a significant difference between the two. The range of angles defined by the boundaries of the energy wells described by RT at 300 K, shown as the dashed lines in Figure 4.14 and Figure 4.15, enable a comparison of the sizes of the potential energy wells with the same energy boundaries. In the case of **M2**, the dimensions are 36° (ψ_1) and 46° (ψ_2), and for **M3** the dimensions are 62° (ψ_1) and 124° (ψ_2). The differences in these dimensions indicate that the calculated flexibility about the amine substituent is significantly greater than that about the sulfide substituent, and this difference may be a major factor in the different order parameters observed for these compounds. This flexibility contrasts the conclusions drawn from the calculation of bond orders in similar sulfide and amine substituted anthraquinone dyes, from which it was proposed that the higher calculated bond order of an amine substituent compared with that of a sulfide substituent was indicative of less flexibility in the amine substituent than the sulfide substituent.^{65, 66}

4.3.2.3 Guest-Host Simulations of dyes in E7

The guest-host MD simulations for all the dyes were run from a pseudo-nematic starting configuration, as described in Section 4.3.2.1. For each simulation the gas-phase density lattice of 400 E7 molecules was used, and five dye molecules were added in random mid-positions between the host molecules, with the long axes aligned parallel with those of the host molecules. This ratio of dye molecules to host molecules gave effective concentrations of *ca* 2 wt %, which is comparable to that of *ca* 1.5 wt % used experimentally, and provided a sufficient number of dye molecules for meaningful

analysis to be carried out whilst maintaining a system size that was small enough for the computation times to be feasible.

A simulation of 26B3OH in E7 run from an isotropic starting geometry was also carried out to check for consistency with the equivalent simulation started from the pseudo-nematic configuration.²⁷⁵ This additional simulation is reported briefly below, with the main focus in this thesis being on the full set of simulations from pseudo-nematic configurations for all the dyes.

Verification of the simulation methods was carried out in a number of ways. The first of these was to determine the simulation time necessary to provide adequate data for meaningful analysis of the dye behaviour. This aspect of the simulations was particularly important due to the necessarily small number of dye molecules (five) present in the simulations. Histograms of the θ angles made between the dye molecular axes and the host director during different time-periods of the simulations are shown in Figure 4.16, from which it is evident that during the early sections of the simulations, between 30 and 100 ns, the alignment of the five dye molecules within each simulation varies widely. In contrast, when the simulation is analysed between 30 and 500 ns, the alignment of the five dye molecules is much more consistent within each simulation. This time-dependence demonstrates that averages obtained over a relatively short run of *ca* 100-200 ns would be unlikely to provide an adequate simulation of the behaviour of the alignments of the dyes.

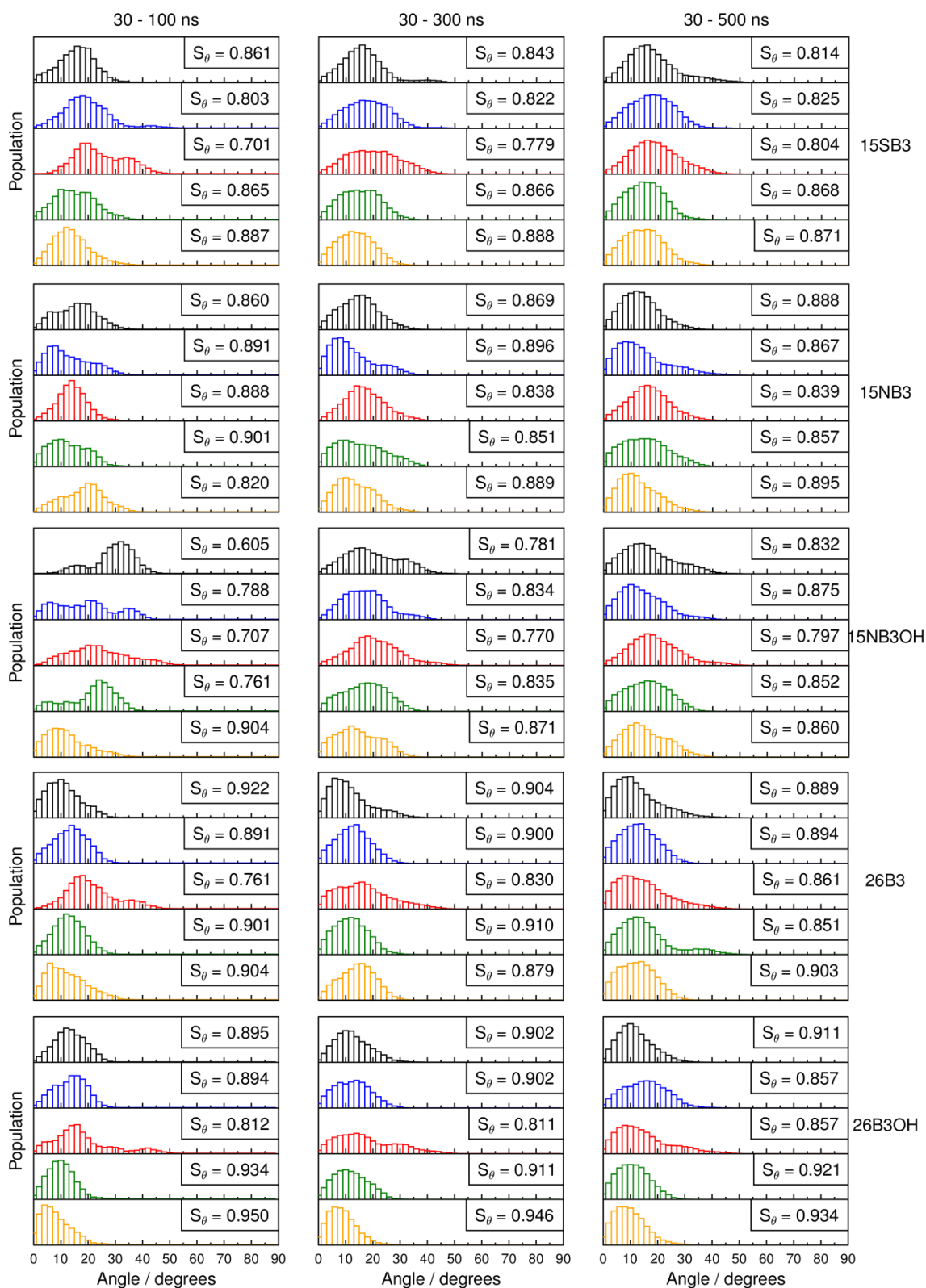


Figure 4.16 Histograms of the angles, θ , between the long molecular axes of each of the five dye molecules (represented by different colours) and the host director, measured over the indicated time-periods for the five guest-host simulations starting from pseudo-nematic starting geometries, and normalised for each time range. Insets give S_θ values for each dye, 1-5, obtained by averaging over each time range.

In the context of the theoretical treatment of dye alignment, it is important to consider the model introduced in Section 1.25, in which dye molecules within a host are considered to explore all orientations about the director, as represented by the α angles in the x, y plane shown in Figure 1.10. A qualitative assessment of the simulations in this context is presented in Figure 4.17, which shows the orientations of the molecular axes of the dye molecules as viewed down the host director during different time periods of the 15NB3 guest-host simulation. The equivalent plots for the simulations for the other guest-host simulations are shown in Figures A2.16-A2.19 in Appendix 2.5.

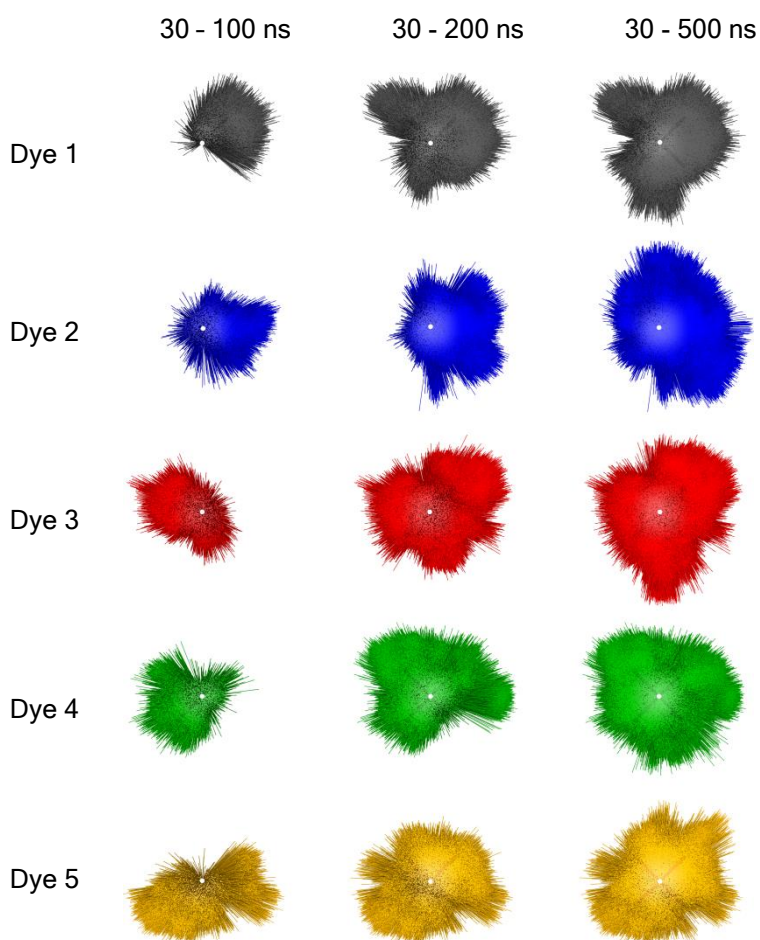


Figure 4.17 Estimates of the orientations explored by the long molecular axis of each of the five 15NB3 molecules (represented by different colours, consistent with Figure 4.16) during the guest-host simulation. Orientations are drawn as unit vectors and viewed down the host director axis (central points in white), with the time ranges during which the orientations were obtained labelled above.

The orientations of the directors were not constrained during the MD simulations, in which the molecules were allowed to move freely, such that the systems did not have a fixed reference/laboratory frame against which the director and perpendicular axes were

defined. Hence, the plots in Figure 4.17 and the equivalent figures in Appendix A2.5 were generated by transforming the z -axis of the simulation box to align with the calculated host director at each time interval, by sequential rotation about x and then y axes. Consequently, these plots show estimates rather than “true” orientations explored around the director. The calculated host directors were found to remain in relatively constant orientations within the axes of the simulation boxes, varying at most by around $\pm 10^\circ$ between 30 ns and 500 ns, and suggesting that this approach provides a useful qualitative analysis.

From Figure 4.17 it is evident that during the early part of the simulation, the regions explored around the director vary significantly between the dyes, and the distributions are not very uniform, whereas after 500 ns the dyes have explored a full range of angles and the distributions are more uniform, supporting the suitability of this time period for analysis of the dyes in the guest-host mixture.

The populations of the dihedral angles, ψ_1 and ψ_2 , within the sulfide dye (15SB3) and the amine dyes (15NB3 and 15NB3OH) were analysed in order to compare them with the potential energy plots against which the force constants described in Section 4.3.2.2 had been parameterised. Figure 4.18, Figure 4.19 and Figure 4.20 show 2D populations of these dihedral angles, and a comparison with Figure 4.14 and Figure 4.15 shows that the shapes of the distributions give a close match with the HF potential energy wells. This consistency suggests that the greater flexibility of the amine substituent than the sulfide substituent calculated for isolated model structures using electronic structure calculations is also valid for the dyes in guest-host environments.

Figure 4.18 and Figure 4.19 show that the two potential wells corresponding to a 180° twist about ψ_2 were not explored equally on the timescale of the simulations of 15SB3 and 15NB3 in E7, and this bias was determined by the configurations of the starting geometries. However, because these conformations are equivalent, this asymmetry of the distributions is not indicative of an insufficient simulation time. A comparison of Figure 4.19 with Figure 4.20 shows that there is little difference in the conformations explored in 15NB3 and 15NB3OH.

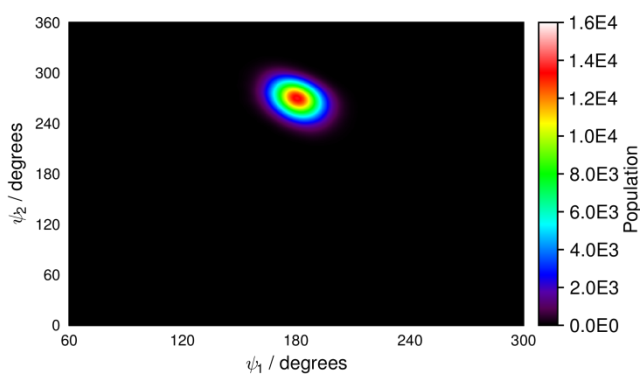


Figure 4.18 Population distribution of the two C-S-C-C dihedral angles in the five 15SB3 molecules during the guest-host MD simulation at 300 K, obtained between 30 ns and 500 ns.

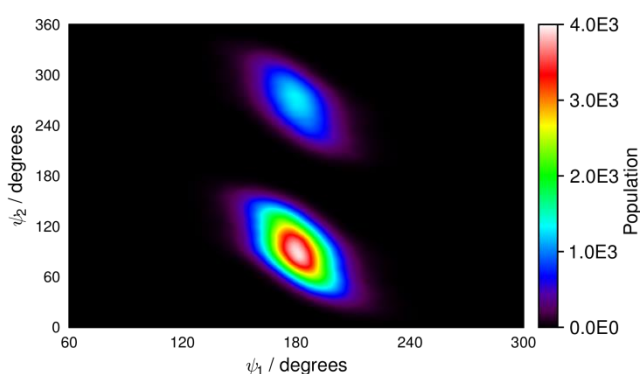


Figure 4.19 Population distribution of the two C-N-C-C dihedral angles in the five 15NB3 molecules during the guest-host MD simulation at 300 K, obtained between 30 ns and 500 ns.

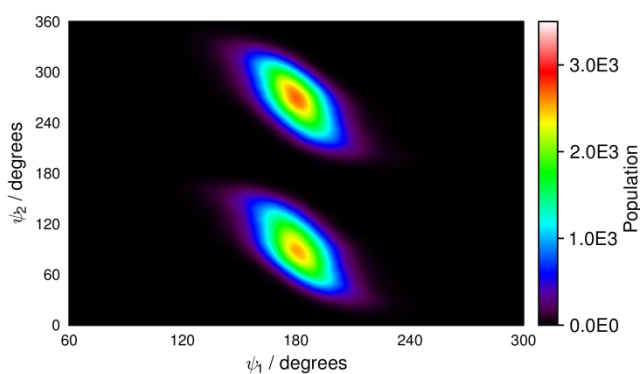


Figure 4.20 Population distribution of the two C-N-C-C dihedral angles in the five 15NB3OH molecules during the guest-host MD simulation at 300 K, obtained between 30 ns and 500 ns.

Figure 4.21 shows plots of the molecular order parameters, S_θ , of the minimum MOI axes of the host molecules, calculated using Equation (4.8), during the course of the guest-host simulations. These plots demonstrate a stable nematic phase in each case, with each of the simulations exhibiting comparable host alignment. The average order parameters obtained from the plots are listed in Table 4.5, showing the order parameters

to be comparable between the different simulations, and comparable with the order parameter of $S_\theta = 0.878$ obtained from the equivalent simulation of the host alone (Figure 4.8). These order parameters are discussed further below. Analysis of an equivalent guest-host simulation of 26B3OH in E7 starting from an isotropic starting configuration is given in Appendix A2.6, demonstrating consistency between the E7 order parameters obtained from the two approaches.

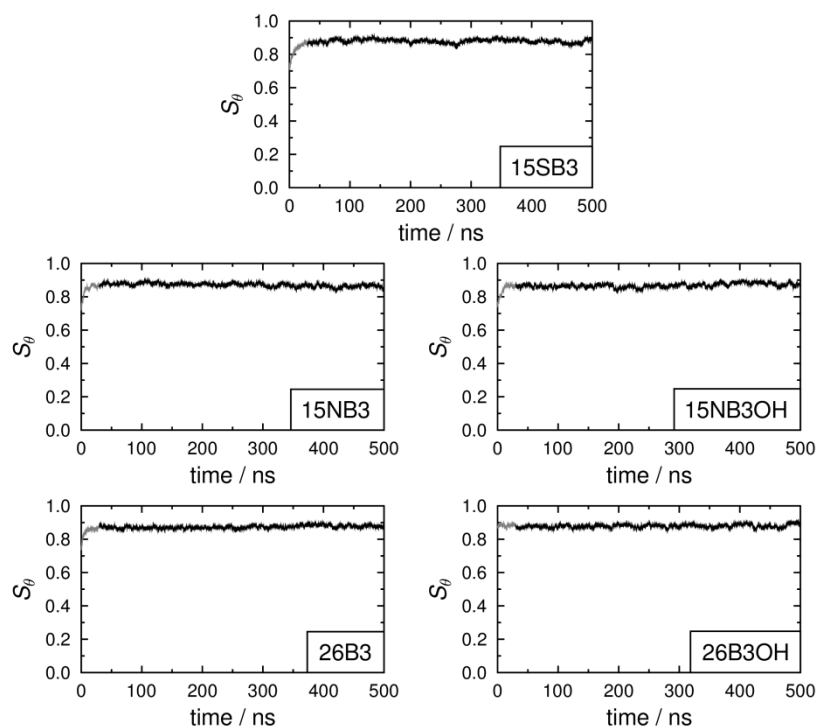


Figure 4.21 Plots of the calculated order parameters, S_θ , of the minimum MOI axes of the host molecules determined from the guest-host MD simulations starting from pseudo-nematic configurations. Sections shown in black (> 30 ns) were used for the calculation of the average values.

Plots of the molecular order parameters, S_θ , of the minimum MOI axes of the dye molecules during the guest-host simulations calculated according to Equation (1.16), against the host director are shown in Figure 4.22, and the average values obtained between 30 ns and 500 ns are listed in Table 4.5, alongside the molecular order parameters of the host molecules shown in Figure 4.21. The equivalent plot for the guest-host simulation of 26B3OH in E7 starting from an isotropic starting configuration is given in Appendix A2.6, again demonstrating consistency between the approaches.

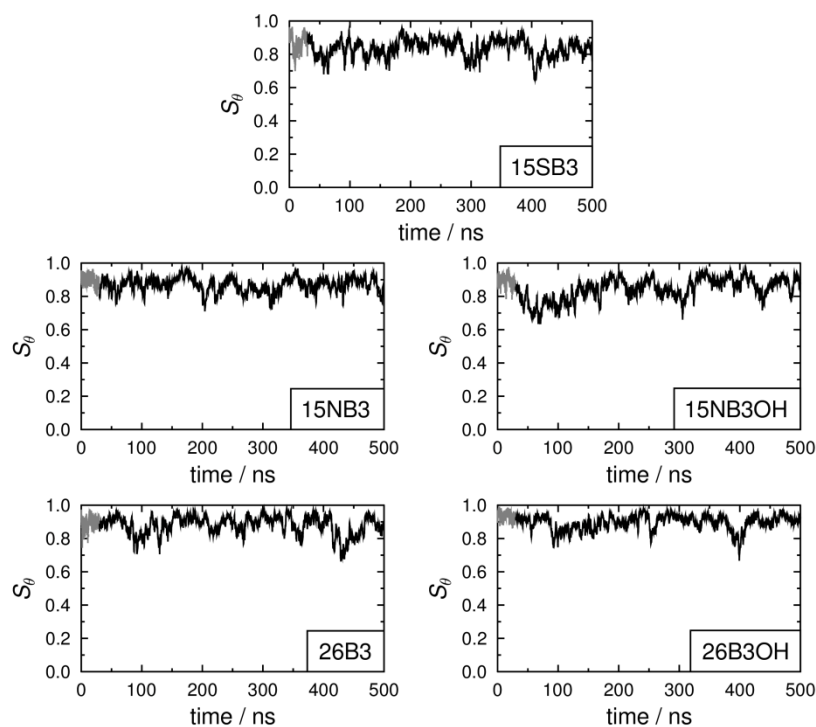


Figure 4.22 Plots of the calculated order parameters, S_θ , of the minimum MOI axes of the dye molecules against the host director, determined from the MD simulations. Sections shown in black (> 30 ns) were used for the calculation of the average values.

Table 4.5 Calculated order parameters of the host molecules, S_θ (E7), and dye molecules, S_θ (dye), from the guest-host MD simulations, averaged between 30 ns and 500 ns.

Dye	$\langle S_\theta(\text{E7}) \rangle$	$\langle S_\theta(\text{dye}) \rangle$
15SB3	0.880	0.836
15NB3	0.871	0.869
15NB3OH	0.868	0.843
26B3	0.873	0.880
26B3OH	0.879	0.896

A comparison of the molecular order parameters, S_θ , of the dyes in Table 4.5 suggests that there is little variation between the molecular alignments of the different dyes within the host. However, slight differences are evident, most notably that the two 2,6-disubstituted dyes exhibit slightly higher calculated molecular order parameters than those of the 1,5-disubstituted dyes. Although the differences between the dyes are only subtle, it is evident that the trend in the experimental order parameters listed in Table 4.2 is matched by the trend of the calculated molecular order parameters with the exception of 15SB3, suggesting that the observed variation in experimental order parameters may be influenced by θ as well as β in these dyes.

An analysis of the host order parameters, S_θ , from the guest-host simulations, also listed in Table 4.5, shows very slight variation between the five simulations, with the E7 order parameters all lying within a range of 0.012, but the variation does again match that of the observed experimental order parameters of the dyes listed in Table 4.2, with the exception of 15SB3. This result is consistent with reported experimental work showing that the presence of dyes has a slight effect on the host order parameter.²⁴ This effect has been linked to the relative sizes of the guest and host species: guest dye molecules that are significantly longer than the host molecules have been shown to cause an increase in the host order parameter with increasing concentration, whereas a decrease has been observed for guests that are smaller than the host molecules.²⁴

The comparison of the host order parameters in Table 4.5 from the guest-host simulations with that of 0.878 calculated for the host alone is also consistent with the experimental observations. For 15SB3 and 26B3OH, which have experimental order parameters higher than E7, the calculations show that the simulated host order parameters are greater than that of E7 alone. In contrast, for 15NB3 and 15NB3OH, which have lower experimental order parameters than E7, the simulated host order parameters are lower than that calculated for E7 alone. A slight inconsistency in this trend is observed for 26B3, which has a slightly higher experimental order parameter than E7, but the calculated order parameter of E7 in the guest-host simulation is slightly lower than that of E7 alone.

The comparison of the values of the calculated order parameters, S_θ , of the dyes with that of the host in each simulation also matches the trend described above, as the amine dyes have lower order parameters than the host, whereas the 2,6-disubstituted dyes have order parameters higher than the host. The exception to this trend is 15SB3, which has a lower calculated order parameter than the host in the guest-host simulation, but has a higher experimental order parameter than the experimental order parameter of the host.

The MD simulations also enable an analysis of the range of molecular structures explored, in a dynamic context, which is not readily obtainable from the electronic structure calculations used to determine the optimised structures discussed in Chapter 3. Average aspect ratios of the dye molecules during the simulations, calculated in the same way as for the optimised structures in section 3.1.2.2, are listed in Table 4.6,

alongside those reported in Chapter 3 from the optimised DFT structures for comparison. The trends in the aspect ratios match between the two different methods of calculation, but the differences do highlight a potential limitation of assessing suitable molecules for guest-host applications using optimised structures alone, particularly in the case of flexible structures. In the case of the dyes studied in this work, the DFT analysis provides a higher aspect ratio because the optimisations were carried out for the most rod-like *all-trans* conformations, whereas the values obtained from the MD simulations show that single optimised structures are insufficient to describe the molecular shape explored in the context of a dynamic room-temperature system.

Table 4.6 Calculated average molecular lengths, widths and aspect ratios of the dye molecules during the MD simulations, averaging over all dye molecules in each simulation between 30 ns and 500 ns, alongside the aspect ratios obtained for the DFT optimised structures. Standard deviations of lengths, widths and aspect ratios from MD were *ca* 0.05 Å, 0.03 Å and 0.10, respectively.

Dye	MD			DFT
	Length / Å	Width / Å	Aspect ratio	Aspect ratio
15SB3	27.18	9.53	2.86	2.99
15NB3	26.29	10.40	2.53	2.66
15NB3OH	26.21	10.92	2.40	2.53
26B3	26.53	8.77	3.03	3.18
26B3OH	26.73	8.64	3.09	3.24

A comparison of the aspect ratios of the dyes with those of the host molecules enables analysis in the context of the generally reported effect that molecules with higher aspect ratios than the host molecules will exhibit higher order parameters than the host,²⁴ whereas guest molecules with lower aspect ratios than the host molecules will have lower order parameters than the host. Average molecular lengths, widths and aspect ratios of the E7 component molecules obtained from the MD simulation of the host alone from a pseudo-nematic starting geometry are listed in Table 4.7, along with average values obtained by weighting the component values by the number of molecules present in the simulations.

A comparison of the aspect ratios of the dye molecules with those of the weighted average of the host molecules shows that 15NB3 and 15NB3OH, which have experimental order parameters lower than that of E7, also have calculated aspect ratios lower than that of the host. In contrast, 15SB3, 26B3 and 26B3OH, which all have higher measured order parameters than the host, have larger aspect ratios than the

average of the host. These calculated parameters are therefore consistent with the experimentally observed trends.²⁷⁶

Table 4.7 Calculated average molecular lengths, widths and aspect ratios of the host molecules during the MD simulations averaging over each type of host molecule in the E7 simulation run from a pseudo-nematic starting configuration between 30 ns and 500 ns. Standard deviations of lengths, widths and aspect ratios were ca 0.05 Å, 0.04 Å and 0.20, respectively.

Component	Length / Å	Width / Å	Aspect ratio
5CB	18.92	7.35	2.58
7CB	21.24	7.61	2.80
8OCB	23.56	7.73	3.06
5CT	23.14	7.50	3.10
Weighted average	20.42	7.48	2.74

4.3.3 Combining MD with DFT results

The product of the calculated molecular order parameters, S_θ , arising from the alignment of the dyes within the E7 host presented in this chapter, and the order parameters, S_β , arising from the alignment of the TDMs within the dyes, presented in Chapter 3, enables the overall order parameters, S_ϕ , of the TDMs against the host director to be calculated. S_ϕ is a calculated value that should, in principle, be directly comparable to the S_{exp} values obtained experimentally by polarised UV-visible absorption measurements. Table 4.8 lists calculated values of S_ϕ for the dyes, alongside the S_{exp} values first given in Table 4.2 for comparison. The trend in the experimental S_{exp} values and the calculated S_ϕ values for the dyes is good, but it is evident that the calculated order parameters are uniformly higher than those obtained experimentally, as can also be seen by the graphical comparison presented in Figure 4.23. This discrepancy is likely to be largely as a result of the overestimation of the molecular alignment within the MD simulations, as obtained for the host alone and discussed above, but it may also be partly due to the S_β values being calculated for static all-*trans* geometries which may represent “best-case” conformations.

Table 4.8 Calculated dichroic order parameters, S_ϕ , of the dyes in E7 obtained from the product of calculated S_θ and S_β values.

Dye	S_ϕ	S_{exp}
15SB3	0.829	0.73
15NB3	0.794	0.61
15NB3OH	0.748	0.51
26B3	0.853	0.68
26B3OH	0.894	0.74

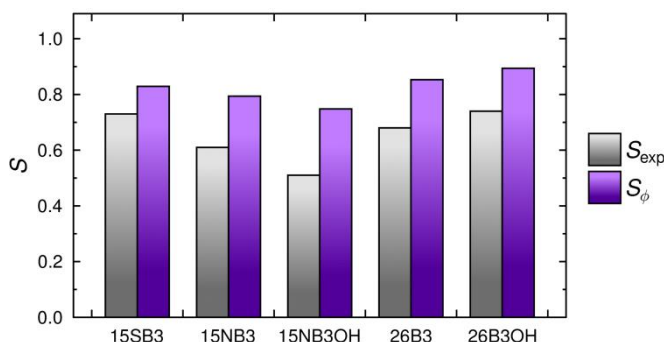


Figure 4.23 Graphical comparison of the experimental order parameters of the dyes in E7, S_{exp} , with the calculated order parameters, S_ϕ , calculated as the product of S_θ and S_β values.

A plot of S_ϕ vs. S_{exp} also enables further assessment of the match between the experimental and calculated dichroic order parameters, as shown in Figure 4.24, which would have a gradient of 1, an intercept of 0, and an R^2 value of 1 for a perfect correlation between calculated and experimental values. Figure 4.24 shows that there is a strong positive correlation between the calculated and experimental values, quantified by the value of $R^2 = 0.8299$ and the positive gradient of 0.532 from the fit, suggesting this method is appropriate for calculating trends in experimental dichroic order parameters. However, the fitted gradient of <1 and the fitted intercept of 0.476 highlight a potential limitation of the approach for replicating absolute values.

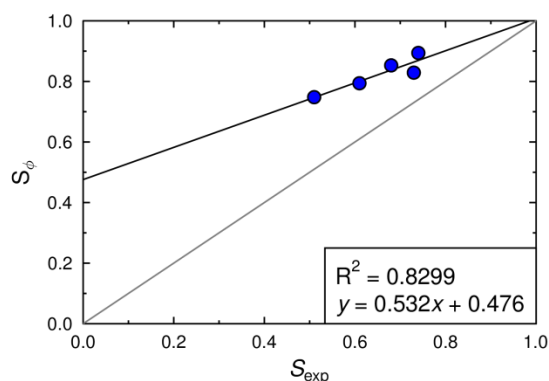


Figure 4.24 Plot of calculated dichroic order parameters, S_ϕ , vs. experimental order parameters, S_{exp} . The grey line indicates a perfect match between calculated and experimental values.

The value of an order parameter S_θ arises from a distribution of θ angles between the director and the long axes of individual molecules, as observed in the MD simulations (Figure 4.17). For discussion, it can sometimes be useful to express such a value in terms of a single θ angle, equivalent to a δ -distribution that would give the same order parameter,²⁸ as given by Equation (4.12).

$$\theta = \cos^{-1} \sqrt{\frac{2S_\theta + 1}{3}} \quad (4.12)$$

The angles, θ , calculated using Equation (4.12) for the host molecules and the dye molecules in the guest-host simulations starting from pseudo-nematic starting geometries are given in Table 4.9. The relative molecular orientations using these θ angles and TDM orientations using the β angles listed originally in Table 3.10 and again in Table 4.9 are presented schematically in Figure 4.25.

Table 4.9 Angles, θ , obtained from the average order parameters of the host molecules and dye molecules from the guest-host MD simulations starting from pseudo-nematic configurations, calculated using Equation (4.12). β angles originally given in Table 3.10 are listed again here for clarity.

Dye	$\theta_{\text{host}} / ^\circ$	$\theta_{\text{dye}} / ^\circ$	$\beta / ^\circ$
15SB3	16.4	19.3	4.4
15NB3	17.1	17.2	13.8
15NB3OH	17.3	18.9	15.9
26B3	16.9	16.4	8.4
26B3OH	16.5	15.3	1.7

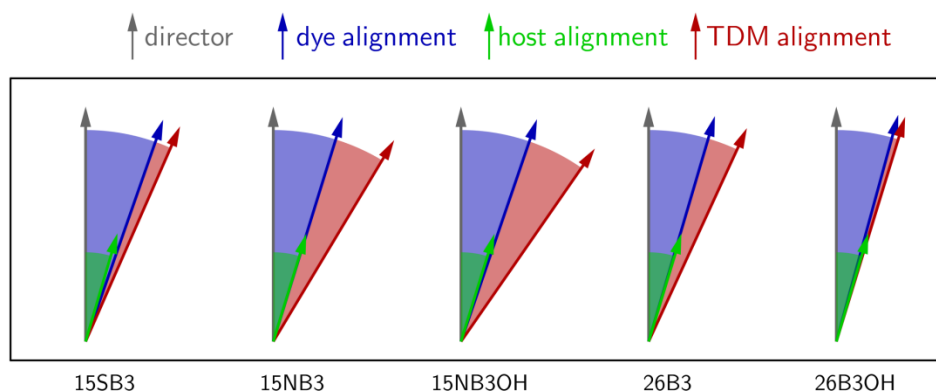


Figure 4.25 Schematic diagram of the relative calculated alignments of the dye molecular axes, the host molecular axes and the dye TDMs using the values in Table 4.9 and Table 3.10.

The orientations shown in Figure 4.25 indicate that the major limiting factor in terms of the alignments of the dye TDMs against the host director is the molecular alignment of the dyes within the host, particularly given the likely overestimation of the degree of molecular alignment in the MD simulations. However the consistency between the θ_{dye} values suggests that there is relatively little variation between the molecular alignments of the different dye molecules, which are calculated to be comparable to the molecular alignment exhibited by the E7 host species. The main cause of the variation in the calculated order parameters between the dyes is shown to be the orientations of the TDMs within the dyes. This comparison enables the lower experimental order parameters of the amine dyes to be rationalised in terms of their large β values when compared with the other dyes studied here. The high observed order parameter of 26B3OH may be attributed primarily to the small value of β , but also to slightly better orientational order of the dye within the host than the other dyes.

4.4 Conclusions

Experimental order parameters obtained from polarised UV-visible absorption spectra showed significant variation in the dichroic order parameters of the dyes in E7. The MD simulations indicate there is little variation in the molecular alignment of the dyes within the host, and subsequent combination with results of the TD-DFT calculations replicates the experimentally observed alignment trend, indicating that the primary cause of the observed variation in alignment is due to differences in TDM alignments within the dyes, defined by the β angles. The ability to consider the two contributions to the observed alignment independently, by MD and DFT calculations provides information not readily obtainable from experiment. Hence, the approach developed here may be extremely useful from the perspective of molecular design, as it may potentially enable dyes for guest-host applications to be engineered in such a way that both contributions to the overall alignment are optimised.

The combined computational approach presented here overestimates the alignment of the dye TDMs within the host, but the nature of the calculations employed means the approach provides a predictive capability, enabling the behaviour of different dyes to be compared within a nematic environment. This is an approach that can be readily extended to other guest and host systems, and could be readily applied to hypothetical systems.

The MD simulations also enabled the conformations explored by the dyes to be analysed, showing that the dyes exhibiting higher experimental order parameters than the host (15SB3, 26B3 and 26B3OH) had higher calculated aspect ratios than the host molecules, but that the dyes exhibiting lower experimental order parameters than the host (15NB3 and 15NB3OH) had lower calculated aspect ratios than the host molecules. However, this common trend was not fully matched by the trend in calculated order parameters, S_θ , for which 15SB3 was calculated to have the lowest order parameter of the dyes studied. This discrepancy is surprising, and is potentially indicative that some assumptions made in the theoretical treatment of the calculation of alignment are not valid, because it does not match the generally accepted theory that more rod-like structures exhibit increased molecular alignment.

Chapter 5

Molecular and transition dipole moment alignment

The analysis of the optical anisotropy of the dyes in aligned liquid crystal mixtures, arising from the molecular alignment of the dyes within the host and the alignment of the TDMs within the dyes, has, so far in this thesis, been carried out with a number of assumptions imposed. These assumptions include: consideration of dye alignment being uniaxial; the alignment axes of molecules being their minimum moment of inertia axes; and the transition dipole moments being fixed relative to the molecular axes. In this chapter, these assumptions are addressed, first by outlining theory relating to alignment beyond that set out in Section 1.2.5 of Chapter 1 and summarising literature related to molecular alignment in liquid crystals, and subsequently by applying these principles and approaches to the electronic structure calculations and molecular dynamics simulations presented in Chapters 3 and 4.

5.1 Introduction

It is a relatively simple task to describe the orientation of molecules within liquid crystalline phases qualitatively, but the comprehensive quantification of this behaviour is widely accepted as being an extremely complex challenge. In computational and theoretical approaches, this complexity is commonly reduced by using simplifications such as those described in Section 1.2.5, which often include considering molecules to be axially symmetric, rigid particles with uniform interaction potentials. However, such simplifications result in many aspects of the behaviour of molecules in liquid crystal phases being overlooked, as molecules exhibiting liquid crystal phases do typically exhibit lower than axial symmetry, have varying degrees of molecular flexibility, and exhibit some degree of specific electrostatic interactions, which may be significant in determining the properties of liquid crystal systems, and thus, these simplifications should not be assumed to be uniformly valid.

Experimental data of liquid crystals can be difficult to interpret, but the use of small guest molecules dissolved in a liquid crystal host can result in data that is easier to interpret,²⁷⁷ and such an approach can enable the analysis of data from liquid crystals

without directly applying assumptions to the properties of the constituent host molecules. The study of small, highly symmetric probe molecules can result in much simpler experimental data than that obtained from analysing the host molecules directly; for example, measurements of non-spherical guest molecules can provide information on the alignment of liquid-crystal phases, and can be considered to provide a simplified route to obtaining information about the intermolecular forces driving the formation of the phases.²⁷⁸

There is a wide range of literature related to the experimental study of solute molecules dissolved in liquid crystal phases, as discussed in Section 5.1.3 below, in particular in the context of their alignment within the hosts. However, somewhat surprisingly, the overlap between this work on solutes and that on guest-host systems containing dye molecules appears to be only slight. Additionally, there appears to be relatively little overlap between the literature on guest-host systems and that on the study of molecular TDM orientations in other contexts. In this introductory section, some of the approaches on rationalising the alignment behaviour of solute molecules in liquid crystal solvents are outlined first, with the focus being on those that are most relevant to the work in this thesis and on molecular dynamics simulations. A brief overview of literature concerning the analysis of TDM orientations is then given, before the aims of the work presented in this chapter are outlined.

5.1.1 Molecular alignment of solutes in liquid crystals

Molecular alignment is a key consideration of the behaviour of solutes in liquid crystals. In the context of rationalising or modelling the alignment of solute molecules, it is highly desirable to be able to define the principal alignment axes of a molecule within a molecular frame, i.e. to use a coordinate system that is unambiguously defined by the molecule itself.

At this point it is useful to extend the theory set out in Section 1.2.5, in which the second-rank order parameter, $\langle P_2 \rangle$, of a system of aligned molecules was related to the orientational distribution function, $f(\beta)$, defined for a uniaxial system comprising molecules of $D_{\infty h}$ symmetry in a phase of $D_{\infty h}$ symmetry that is aligned along the z axis of a Cartesian reference frame. From this order parameter, which is also termed S_{zz} , the

order parameters of the equivalent orthogonal axes, S_{xx} and S_{yy} , of a uniaxial molecule may be defined according to Equation (5.1),^{26, 277} with the axes shown in Figure 5.1.

$$S_{xx} = S_{yy} = -\frac{S_{zz}}{2} \quad (5.1)$$

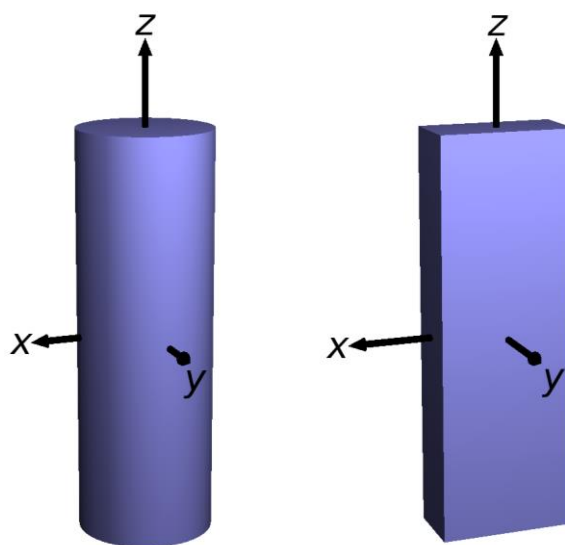


Figure 5.1 Schematic diagram of the principal axes of a shape of D_{oh} symmetry (left), for which $S_{xx} = S_{yy}$, and a shape of D_{2h} symmetry (right), for which $S_{xx} \neq S_{yy}$.

For a solute molecule of lower symmetry than D_{oh} in a uniaxial host, the molecular axes, x and y , orthogonal to the principal molecular axis, z , may not be equivalent, as also shown in Figure 5.1, and therefore the order parameters measured along these axes may also be inequivalent, i.e. $S_{xx} \neq S_{yy}$. This inequality means that these order parameters cannot be derived from S_{zz} alone, resulting in the additional order parameter, D , defined by Equation (5.3), which is required to describe the order of the system and where, by convention, $S_{xx} > S_{yy}$.²⁶ Such alignment is described as being biaxial, and D is termed the biaxial order parameter.

$$D = S_{xx} - S_{yy} \quad (5.2)$$

In a more general context, these order parameters may also be expressed as components of a tensor: the symmetric and traceless Saupe ordering tensor,²⁷⁹ $\mathbf{S}_{\alpha\beta}$, defined in Equation (5.3), where $l_\alpha, l_\beta = l_x, l_y, l_z$, which are the cosines the molecular axes, x, y and z of the solute with respect to the host director, and δ is the Kronecker delta which takes

a value of 0 unless $\alpha = \beta$, for which it takes a value of 1. Due to the fact that the tensor is traceless and symmetric, there are only five independent elements required to define the full matrix: S_{zz} , $S_{xx} - S_{yy}$, S_{xy} , S_{xz} , and S_{yz} .²⁶

$$\mathbf{S}_{\alpha\beta} = \left\langle \frac{1}{2} (3l_\alpha l_\beta - \delta_{\alpha\beta}) \right\rangle = \begin{bmatrix} S_{xx} & S_{xy} & S_{xz} \\ S_{yx} & S_{yy} & S_{yz} \\ S_{zx} & S_{zy} & S_{zz} \end{bmatrix} \quad (5.3)$$

If the principal molecular axes of a biaxial solute are coincident with the principal axes of the laboratory frame (i.e. so that the average orientation of the principal molecular axis of the guest molecule is coincident with the host director in a uniaxial system), the Saupe ordering matrix will be diagonal, and its principal components are the order parameters of the three orthogonal principal molecular axes, as expressed by Equation (5.4).²⁸⁰

$$\mathbf{S}_{\alpha\beta} = \begin{bmatrix} S_{xx} & 0 & 0 \\ 0 & S_{yy} & 0 \\ 0 & 0 & S_{zz} \end{bmatrix} = \begin{bmatrix} \frac{(S_{zz} - D)}{2} & 0 & 0 \\ 0 & -\frac{(S_{zz} + D)}{2} & 0 \\ 0 & 0 & S_{zz} \end{bmatrix} \quad (5.4)$$

The consideration of a solute molecule with lower symmetry than $D_{\infty h}$ means that the orientational distribution function must be expressed not only in terms of the angle, β , made between the principal molecular axis and the host director, but also in terms of the angle, γ , corresponding to rotation about the principal molecular axis, z , shown schematically in Figure 5.2 and given by Equation (5.5) (*cf* Equation (1.4)).

$$f(\Omega) \equiv f(\beta, \gamma) \quad (5.5)$$

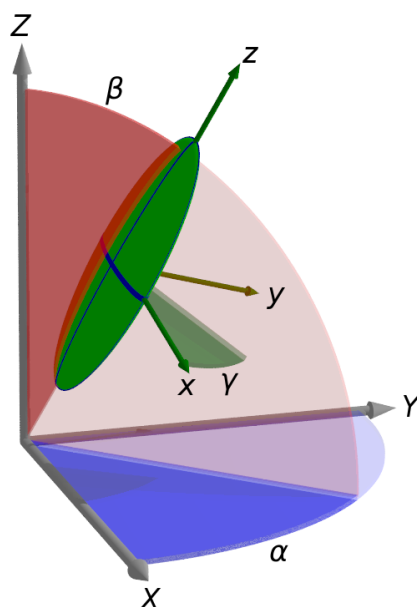


Figure 5.2 Schematic diagram showing the relative orientations of the laboratory frame axes (X , Y , and Z) and the molecular frame axes (x , y , and z), and the Euler angles, α , β and γ relating them.

Normalisation of this distribution function, $f(\beta, \gamma)$, is given by Equation (5.6), analogous to that for $f(\beta)$ described in Chapter 1 (*cf* Equation 1.5).²⁶

$$\int_0^{2\pi} \int_0^{\pi} f(\beta, \gamma) \sin \beta d\beta d\gamma = 1 \quad (5.6)$$

Just as $f(\beta)$ may be expanded as a summation of Legendre polynomials dependent on β , as described in Chapter 1, $f(\beta, \gamma)$ may be expanded as a set of orthogonal functions of β and γ . Typically, these functions are the Wigner functions, $D_{0,n}^L$, where L takes integer values and defines the rank of the matrix, and $n = L, L-1, \dots, -L+1, -L$. These terms are sometimes expressed as modified spherical harmonics, $C_{L,m}$, but there are multiple conventions concerning their relation to the Wigner functions, so the terms $D_{0,n}^L$ are used here. Thus, an expansion of $f(\beta, \gamma)$ may be given by Equation (5.7), where the coefficients, $f_{L,n}$, are defined by Equation (5.8),^{25, 281} and only even values of L need to be considered due to the symmetry of the phase,²⁶ i.e. $f(\beta, \gamma) = f(180^\circ - \beta, \gamma)$. When describing molecules of D_{2h} symmetry, non-zero terms occur when n is even.^{26, 29}

$$f(\beta, \gamma) = \sum_L \sum_{n=-L}^L f_{L,n} D_{0,n}^L(\beta, \gamma) \quad (5.7)$$

$$f_{L,n} = \left(\frac{2L+1}{4\pi} \right) \langle D_{0,n}^{L*} \rangle \quad (5.8)$$

For $n = 0$, the terms $D_{0,0}^L$ are independent of the azimuthal angle, γ , and are equal to the Legendre polynomials of rank L , as expressed by Equation (5.9).²⁶

$$D_{0,0}^L(\beta, \gamma) = P_L(\cos \beta) \quad (5.9)$$

Typically, the expansion is truncated at the second-rank level, i.e. $L = 2$, and the associated terms of the Wigner functions, $D_{0,n}^L$, for even values of n are given by Equations (5.10) - (5.12).²⁶

$$D_{0,0}^0(\beta, \gamma) = 1 \quad (5.10)$$

$$D_{0,0}^2(\beta, \gamma) = \left(\frac{3\cos^2 \beta - 1}{2} \right) \quad (5.11)$$

$$D_{0,\pm 2}^2(\beta, \gamma) = \sqrt{\frac{3}{8}} \sin^2 \beta e^{\mp i 2\gamma} \quad (5.12)$$

Using the expansions of the terms defined by Equations (5.10) - (5.12), the orientational distribution function, truncated at the second-rank level, is given by Equation (5.13).

$$f(\beta, \gamma) = \frac{1}{4\pi} + \frac{5}{4\pi} \left(\langle D_{0,-2}^{2*} \rangle \langle D_{0,-2}^2 \rangle + \langle D_{0,0}^{2*} \rangle \langle D_{0,0}^2 \rangle + \langle D_{0,2}^{2*} \rangle \langle D_{0,2}^2 \rangle \right) \quad (5.13)$$

The average values of the coefficients of the Wigner functions are obtained according to Equation (5.14), analogous to Equation (1.15) for a uniaxial molecule introduced in Chapter 1, and are components of an L th rank orientational ordering tensor that provide a set of orientational order parameters.^{25, 26}

$$\langle D_{0,n}^{L*} \rangle = \int_0^{2\pi} \int_0^\pi D_{0,n}^{L*}(\beta, \gamma) f(\beta, \gamma) \sin \beta d\beta d\gamma \quad (5.14)$$

These order parameters are not intuitively related to the molecular properties, but they may be related to the Cartesian order parameters that make up the Cartesian ordering tensor in Equation (5.4) according to Equations (5.15) and (5.16).^{281, 282}

$$S_{zz} = \langle D_{0,0}^2 \rangle \quad (5.15)$$

$$S_{xx} - S_{yy} = \sqrt{\frac{3}{2}} (\langle D_{0,2}^2 \rangle + \langle D_{0,-2}^2 \rangle) \quad (5.16)$$

5.1.2 Implications of dye biaxiality on molecular and TDM alignment

The consideration of molecular biaxiality of dyes influences the theoretical treatment of the alignment of the dye molecules, and consequently of their TDMs in a host mixture. The cone model introduced for uniaxial dyes in Chapter 1 (Fig 1.14), and used for the analysis in Chapters 3 and 4, may be altered to include the influence of the biaxial order parameter, $D = S_{xx} - S_{yy}$, and the orientation of the TDM within the dye molecule relative to the x and y axes.

The dichroic properties of a dye aligned within a liquid crystal may be considered in terms of the interaction between the electric vector, \mathbf{E} , of incident polarised light and the transition dipole moment (TDM) vector, $\boldsymbol{\mu}$, of the dye molecule. Considering the system in terms of the Cartesian axes against which these orientations are defined, the director and molecular alignment are typically defined against the axes X , Y , and Z , referred to as the laboratory frame, whereas the alignment of the TDM vector is more easily defined against the axes x , y , and z , which themselves are usually defined against (or as) the principal axes of the molecule, termed the molecular frame, as shown in Figure 5.3.

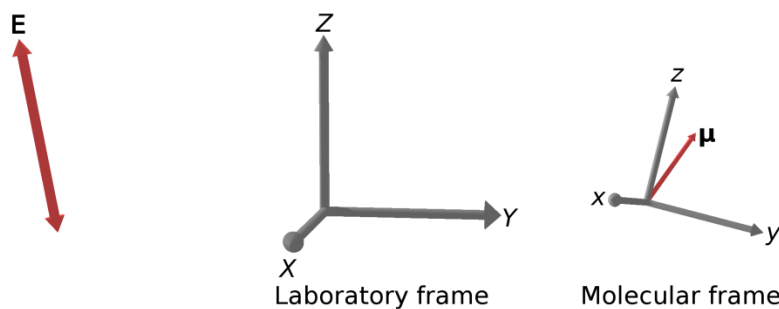


Figure 5.3 Relative orientations of the electric polarisation of incident light, \mathbf{E} , the orientation of the dye TDM, $\boldsymbol{\mu}$, the axes, X, Y, Z , defining the laboratory frame, and the axes x, y, z defining the molecular frame.

The relative orientations of two Cartesian frames may be related by a rotation described by the three Euler angles, $f(\alpha, \beta, \gamma)$, shown schematically in Figure 5.2. In general, functions of these angles may be expressed as an expansion of Wigner functions, $D_{m,n}^L(\alpha, \beta, \gamma)$, according to Equation (5.17), where the coefficients, $a_{m,n}^L$, are defined by Equation (5.18).³⁴ The second-rank terms corresponding to $D_{m,n}^2$ are listed in Appendix A3.1, from which it may be seen that these Wigner functions represent the general case from which the terms $D_{0,n}^L$ introduced in the previous section, which depend on only β, γ , arise.²⁸¹

$$f(\alpha, \beta, \gamma) = \sum_{L=0}^{\infty} \sum_{m=-L}^L \sum_{n=-L}^L a_{m,n}^L D_{m,n}^L(\alpha, \beta, \gamma) \quad (5.17)$$

$$a_{m,n}^L = \frac{2L+1}{8\pi^2} \langle D_{m,n}^{L*}(\alpha, \beta, \gamma) \rangle \quad (5.18)$$

The average value of a Wigner function $\langle D_{m,n}^{L*}(\alpha, \beta, \gamma) \rangle$ is defined by Equation (5.19) (c.f. Equations (1.15) and (5.14)).

$$\langle D_{m,n}^{L*}(\alpha, \beta, \gamma) \rangle = \int_{\alpha\beta\gamma} D_{m,n}^{L*}(\alpha, \beta, \gamma) f(\alpha, \beta, \gamma) \sin \beta \, d\alpha \, d\beta \, d\gamma \quad (5.19)$$

The Wigner functions form a group, and closure means that an orientation-dependent function described by a set of Wigner functions against a Cartesian reference frame, e.g. $D_{m,n}^L(\alpha'', \beta'', \gamma'')$, may be described in terms of a set of Wigner functions against a different Cartesian reference frame, $D_{m,n}^L(\alpha', \beta', \gamma')$, according to Equation (5.20), where $D_{m,n}^L(\alpha, \beta, \gamma)$ describes the rotation between the sets of axes against which the respective sets of angles are defined.^{29, 38}

$$D_{i,j}^L(\alpha'', \beta'', \gamma'') = \sum_k D_{i,k}^L(\alpha, \beta, \gamma) D_{k,j}^L(\alpha', \beta', \gamma') \quad (5.20)$$

Hence, in the context of the orientations shown in Figure 5.3, the orientations of the TDMs of dye molecules in the laboratory frame, as obtained by UV-visible absorption experiments that give an average second-rank order parameter, may be expressed in terms of the orientation of the electric vector of the light \mathbf{E} in the laboratory frame XYZ , the orientations of the molecular frames xyz in the laboratory frame, and the orientation of the TDM $\boldsymbol{\mu}$ in the molecular frame.

The closure relation therefore enables the second rank order parameter, $\langle P_2(\cos\phi) \rangle \equiv \langle D_{00}^2(0, \phi, 0) \rangle$ that expresses the orientation dependence of $\boldsymbol{\mu}$ with respect to \mathbf{E} , where ϕ is the angle between the two vectors, to be expressed as a product of rotations, given by Equation (5.21),^{34, 282, 283} the derivation of which is given in Appendix A3.2. The rotation from a vector to a set of axes (e.g. $\mathbf{E} \rightarrow XYZ$) only requires the terms $D_{0,n}^2$, because the rotation is independent of the angle, α , and the transformation from a set of axes to a single vector (e.g. $xyz \rightarrow \boldsymbol{\mu}$) only requires the terms $D_{m,0}^2$ as the transformation is independent of the angle, γ . $D_{m,n}^2(XYZ \rightarrow xyz)$ describes the transformation from the laboratory frame to the molecular frame, and is given as an ensemble average over all molecules.

$$\langle P_2(\cos\phi) \rangle = \sum_i \sum_j D_{0,i}^2(\mathbf{E} \rightarrow XYZ) \langle D_{i,j}^2(XYZ \rightarrow xyz) \rangle D_{j,0}^2(xyz \rightarrow \boldsymbol{\mu}) \quad (5.21)$$

Because it is easier to describe \mathbf{E} within the XYZ frame than the reverse, the complex conjugate of the first term with reversed indices may be taken to describe the reverse transformation, given by Equation (5.22),^{34, 283} which may be expressed more concisely as Equation (5.23), where $\langle D_{i,j}^2 \rangle$ are the orientational order parameters described in section 5.1.1.

$$\langle P_2(\cos\phi) \rangle = \sum_i \sum_j D_{i,0}^{2*}(XYZ \rightarrow \mathbf{E}) \langle D_{i,j}^2(XYZ \rightarrow xyz) \rangle D_{j,0}^2(xyz \rightarrow \boldsymbol{\mu}) \quad (5.22)$$

$$\langle P_2(\cos\phi) \rangle = \sum_i \sum_j D_{i,0}^{2*}(XYZ \rightarrow \mathbf{E}) \langle D_{i,j}^2 \rangle D_{j,0}^2(xyz \rightarrow \boldsymbol{\mu}) \quad (5.23)$$

As described in section 5.1.1, the non-zero Wigner rotation matrix elements D_{ij}^2 correspond to values of $i = 0, j = 0$ and $j = \pm 2$. Hence, Equation (5.23) may be expanded in full according to Equation (5.24).³⁴

$$\begin{aligned} \langle P_2(\cos \phi) \rangle &= D_{0,0}^{2*} (XYZ \rightarrow \mathbf{E}) \langle D_{0,0}^2 \rangle D_{0,0}^2 (xyz \rightarrow \boldsymbol{\mu}) \\ &+ D_{0,0}^{2*} (XYZ \rightarrow \mathbf{E}) \langle D_{0,-2}^2 \rangle D_{-2,0}^2 (xyz \rightarrow \boldsymbol{\mu}) \\ &+ D_{0,0}^{2*} (XYZ \rightarrow \mathbf{E}) \langle D_{0,2}^2 \rangle D_{2,0}^2 (xyz \rightarrow \boldsymbol{\mu}) \end{aligned} \quad (5.24)$$

Conventionally, second rank order parameters are determined against the host director, e.g. $P_2(\cos \theta)$, where θ is the angle between a molecular orientation and the director. For this reason, it is convenient to define the orientation of \mathbf{E} as (0, 0, 1) in the laboratory frame, corresponding to orientation of the Z axis which is defined as the host director. The orientation of $\boldsymbol{\mu}$ may be defined as $(\alpha, \beta, 0)$ within the molecular frame. The terms of Equation (5.24) corresponding to the description of \mathbf{E} in the laboratory frame and the description of $\boldsymbol{\mu}$ in the molecular frame, determined using the definitions of the Wigner functions given in Appendix A3.1 and Euler's formula, are listed in Table 5.1.

Table 5.1 Wigner functions defining the orientations of \mathbf{E} in the laboratory frame, and $\boldsymbol{\mu}$ in the molecular frame.

	$XYZ \rightarrow \mathbf{E} (0,0,1)$		$xyz \rightarrow \boldsymbol{\mu} (\alpha,\beta,0)$
$D_{0,0}^2$	1		$\frac{1}{2}(3 \cos^2 \beta - 1)$
$D_{-2,0}^2$	0		$\sqrt{\frac{3}{8}} \sin^2 \beta e^{2i\alpha} \equiv \sqrt{\frac{3}{8}} \sin^2 \beta (\cos 2\alpha + i \sin 2\alpha)$
$D_{2,0}^2$	0		$\sqrt{\frac{3}{8}} \sin^2 \beta e^{-2i\alpha} \equiv \sqrt{\frac{3}{8}} \sin^2 \beta (\cos 2\alpha - i \sin 2\alpha)$

Equation (5.24) may therefore be expressed as Equation (5.25), which may be further simplified to Equation (5.26) by applying Euler's formula and using the equality, $\langle D_{0,2}^2 \rangle = \langle D_{0,-2}^2 \rangle$ due to the assumption of D_{2h} molecular symmetry here.²⁵

$$\begin{aligned}
\langle P_2(\cos \phi) \rangle &= (1) \langle D_{0,0}^2 \rangle \left(\frac{1}{2} (3 \cos^2 \beta - 1) \right) \\
&+ (1) \langle D_{0,-2}^2 \rangle \left(\sqrt{\frac{3}{8}} \sin^2 \beta (\cos 2\alpha + i \sin 2\alpha) \right) \\
&+ (1) \langle D_{0,2}^2 \rangle \left(\sqrt{\frac{3}{8}} \sin^2 \beta (\cos 2\alpha - i \sin 2\alpha) \right)
\end{aligned} \quad (5.25)$$

$$\langle P_2(\cos \phi) \rangle = \langle D_{0,0}^2 \rangle \left(\frac{1}{2} (3 \cos^2 \beta - 1) \right) + 2 \left(\langle D_{0,2}^2 \rangle \right) \left(\sqrt{\frac{3}{8}} \sin^2 \beta \cos 2\alpha \right) \quad (5.26)$$

Equation (5.26) may be expressed in its Cartesian form according to Equation (5.27) describing the second-rank order parameter of the TDM in a biaxial dye molecule against the host director,²⁸³⁻²⁸⁵ using Equations (5.15) and (5.16).²⁶

$$\langle P_2(\cos \phi) \rangle = \langle S_{zz} \rangle \langle P_2(\cos \beta) \rangle + \frac{1}{2} \langle S_{xx} - S_{yy} \rangle (\sin^2 \beta \cos 2\alpha) \quad (5.27)$$

In the case of a uniaxial dye molecule, for which $S_{xx} - S_{yy} = 0$, Equation (5.27) simplifies to that given by Equation 1.20, i.e. where $\langle S_{zz} \rangle$ corresponds to $\langle P_2(\cos \theta) \rangle$ and θ is the angle between the principal molecular axis and the host director. The biaxial term is also zero for a dye molecule in which the TDM is perfectly aligned with the principal molecular alignment axis, z , i.e. where $\beta = 0^\circ$.

5.1.3 Definitions of alignment axes

A crucial factor underlying the theory set out above is that it relies on the correct definition of the principal molecular alignment axes. For a shape of $D_{\infty h}$ symmetry, such as the cylinder in Figure 5.1, the principal axis may be defined unambiguously as the z axis, but in the context of solute molecules of more complex shape, it is desirable to be able to unambiguously define the principal molecular alignment axis from the molecular structure regardless of the molecular symmetry. There are many reported studies in the context of defining molecular axes and calculating the molecular alignment of solutes in liquid crystals, the most relevant of which are outlined below in Sections 5.1.3.1 to 5.1.3.3.

5.1.3.1 Moment of inertia

A relatively early experimental NMR study on solutes in liquid crystals proposed that the inertial properties of solute molecules determined their orientation, suggesting that the minimum moment of inertia axis was best aligned with the host director.²⁸⁶ Subsequent NMR studies have applied this approach to a range of different systems with varying degrees of success: some reports have included experimental results in support of this proposed theory,^{287, 288} some reports have noted slight deviations attributable to steric effects,^{289, 290} whereas others have suggested that the approach does not apply to some systems,²⁹¹ and that shape-based approaches are more appropriate to cover a wide range of solute molecules.^{292, 293} However, it is reasonable to consider that the minimum moment of inertia axis will match that of the alignment axis in the limiting case of a calamitic molecule of high symmetry. Given that high molecular symmetry is a common assumption in the theoretical treatment of liquid crystal phases and that a moment of inertia axis is easily calculated, it has been widely used as an unambiguous quantified definition of the long molecular axes of molecules in liquid crystal phases.

5.1.3.2 Elastic tube model

One of the earliest approaches to defining molecular alignment axes based only on the shape of a solute molecule was to consider the host environment as that of an “elastic tube”, i.e. a solvent molecule dissolved in a liquid crystal is considered to be contained within an elastic tube of non-fixed dimensions, aligned along the host director.²⁹⁴ This model is shown schematically in Figure 5.4 using anthracene as an example due to its relatively simple structure and D_{2h} symmetry. Figure 5.4 illustrates an unfavourable orientation in which the tube has a large circumference, and the most energetically favourable orientation of the solute molecule is considered to be that which requires a tube of minimum circumference. The basis for this approach was that energy is required for a solute molecule to displace the liquid crystal host molecules, and that this displacement energy along the director is negligible in comparison with that required perpendicular to the director.²⁹⁴

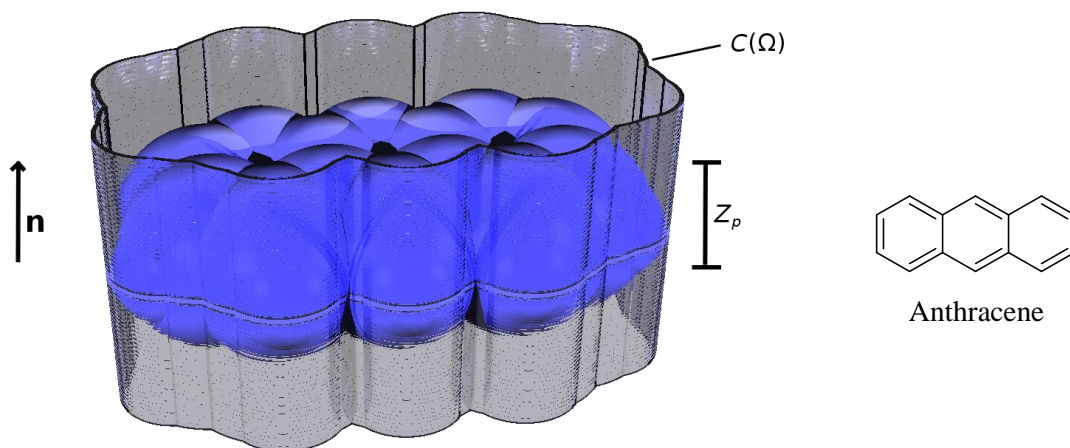


Figure 5.4 Schematic diagram of the elastic tube model applied to anthracene as a solute, in this example with an unfavourable configuration arising from a large circumference, C , when measured perpendicular to the director, \mathbf{n} .

The model could be used for a quantitative prediction of the order parameter from the solute geometry by using Hooke's law to describe the force applied by the elastic tube. Hence, the orientational potential energy $U(\Omega)$ may be related to the circumference of the tube, C , according to Equation (5.28) where k is the force constant of the elastic tube.²⁹⁴

$$U(\Omega) = \frac{1}{2} k C^2(\Omega) \quad (5.28)$$

Generally, good quantitative agreement with experimentally measured alignment was achieved using this approach,²⁹⁴ but it was found that in order to provide a good match with experimental values, fitted k values tended to be higher in the case of short molecules than long molecules, suggesting the model was not fully describing the orienting processes.²⁹⁵

To compensate for this observed discrepancy, an additional term, $Z_p(\Omega)$ was added, that describes the projection of the length of the solute molecule onto the axis of the host director, yielding Equation (5.29), where ζ is a dimensionless adjustable parameter.²⁹⁶ Qualitatively, this expression is based on solute alignment being dictated by two factors: firstly, minimisation of the circumference of the solute molecule measured perpendicular to the director, which is related to the area of the ends of the tube containing the solute, and secondly a factor proportional to the area of the side wall of the tube. Perhaps unsurprisingly, the results of the two-parameter model were found to

provide a better match with experiment than those of the one-parameter model given by Equation (5.28).²⁹⁶

$$U(\Omega) = \frac{1}{2}k \left[1 - \frac{\xi Z_p(\Omega)}{C(\Omega)} \right] C^2(\Omega) \quad (5.29)$$

Further, this two-parameter expression for the orienting potential suggests that, rather than considering an orienting potential that rotates a solute molecule towards a minimum energy orientation, the alignment may be considered to arise from anisotropic interactions between the molecular surface of the solute molecule and the host mean field.²⁷⁸

The model predicts that the most energetically favourable molecular orientation occurs when the maximum molecular surface is parallel with the director of the host, leading to the expression given by Equation (5.30),²⁹⁵ where the surface of the entire molecule is considered by integrating the circumference of the solute along the director, Z . Using this approach, the lowest energy orientation is that which maximises the surface area of the molecule oriented parallel with the director. The area of a “circumference band” of a solute, measured perpendicular to the director between two Z limits, z and z' , is equal to $A|\sin\theta|$,²⁷⁸ where A is the surface area of the band around the solute, and θ is the angle between the normal to the surface of the solute at a given point and the host director, shown schematically in Figure 5.5. Hence, Equation (5.30) may also be expressed as Equation (5.31), where the integral is carried out over the molecular surface, S .

$$U(\Omega) = -\frac{1}{2}k \int C_z(\Omega) dZ \quad (5.30)$$

$$U(\Omega) = -\frac{1}{2}k \int dS |\sin \theta| \quad (5.31)$$

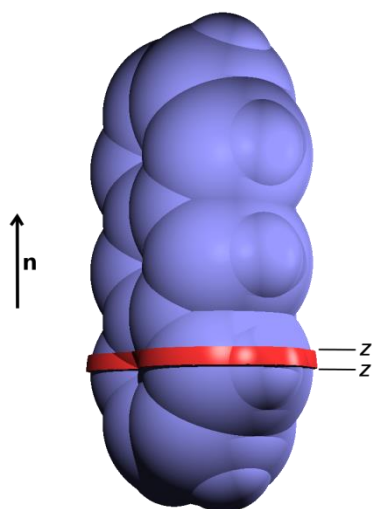


Figure 5.5 Schematic diagram of the circumference band of an anthracene molecule between z and z' limits along the host director, \mathbf{n} .

This model generally provided a better match with experiment than the previous approaches,^{278, 295} but a limitation of all models based on molecular circumference is that of transferability: ideally, a model used to describe the molecular shape of a solute is applicable to any given shape, which is not necessarily the case when measuring a molecular circumference, particularly for large, complex species.

5.1.3.3 Surface tensor model

A subsequent model used to describe the anisotropic surface interaction between a solute molecule and a nematic host is the surface tensor approach, introduced by Ferrarini *et al.*²⁹⁷ In this method, the molecular surface is used as an input variable, as in Equation (5.31), but rather than considering a one-dimensional variable describing the molecular shape, such as the circumference, it considers the molecular surface as a whole, from which a tensor defining the orientations of surface elements may be unambiguously constructed irrespective of molecular symmetry or complexity. The potential energy, U , of a given structure with a defined surface, S , at an orientation defined by Euler angles β and γ within the laboratory frame, is defined by Equation (5.32), where ψ is the angle between the normal to any point on the molecular surface and the host director, ε is a parameter representing the orienting strength of the host medium, k_B is the Boltzmann constant and T is the temperature of the system. Equation (5.32) was originally derived from the standard form of surface anchoring free energy of macroscopic surfaces.²⁹⁸

$$\frac{U(\beta, \gamma)}{k_B T} = \epsilon \int P_2(\cos \psi) dS \quad (5.32)$$

If the molecular surface is considered to comprise a set of small discrete planar surface elements, Equation (5.32) may be considered in terms of each of these surface elements tending to align parallel to the director.²⁹⁹ The variation in energy of a single vector normal to a surface element with the angle made with the director according to Equation (5.32) is shown in Figure 5.6. If a set of normal vectors to all of the surface elements is considered, then the minimum energy orientation corresponds to that which minimises the projection of these vectors along the director.

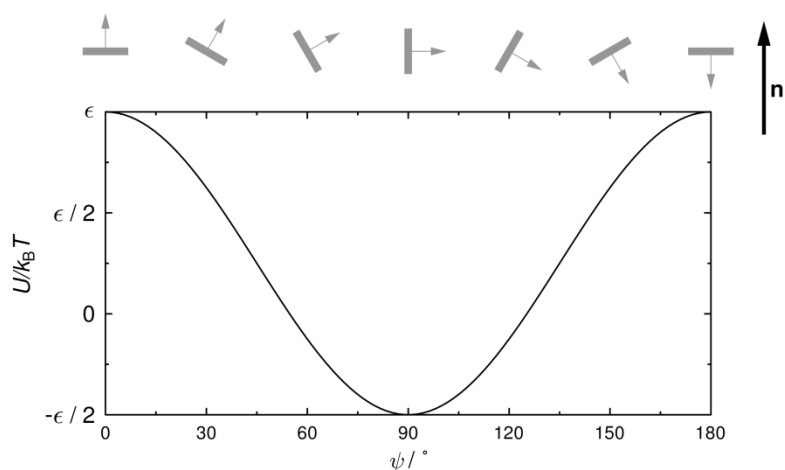


Figure 5.6 Variation in energy, $U/k_B T$, for a vector normal to a surface element (shown above) with angle, ψ , against the director, \mathbf{n} .

For a rod-like solute with $D_{\infty h}$ symmetry, the energy is at a minimum when the molecular axis, in this case the symmetry axis, is parallel to the director because at this orientation the majority of the solute surface faces perpendicular to the director, resulting in $P_2(\cos \psi) = -0.5$ for these perpendicular vectors.

For a molecular surface composed of discrete surface elements, s , with normal unit vectors, \mathbf{s} , as described above, a surface tensor, \mathbf{t} , may be constructed, as defined by Equation (5.33), where s_x , s_y , and s_z are the Cartesian components of the unit vectors (i.e. the direction cosines) associated with each surface element in the molecular frame.³⁰⁰

$$\mathbf{t} = - \begin{pmatrix} \int s_x s_x dS & \int s_x s_y dS & \int s_x s_z dS \\ \int s_y s_x dS & \int s_y s_y dS & \int s_y s_z dS \\ \int s_z s_x dS & \int s_z s_y dS & \int s_z s_z dS \end{pmatrix} \quad (5.33)$$

Equation (5.33) may be expressed in a more practical form as a summation of vectors associated with a finite number of discrete surface elements of area, a_s , given by Equation (5.34).³⁰⁰

$$\mathbf{t} = - \begin{pmatrix} \sum_s s_x s_x a_s & \sum_s s_x s_y a_s & \sum_s s_x s_z a_s \\ \sum_s s_y s_x a_s & \sum_s s_y s_y a_s & \sum_s s_y s_z a_s \\ \sum_s s_z s_x a_s & \sum_s s_z s_y a_s & \sum_s s_z s_z a_s \end{pmatrix} \quad (5.34)$$

Diagonalising \mathbf{t} results in three eigenvectors corresponding to three perpendicular molecular axes that define the orientations of maximum surface vectors, minimum surface vectors and an orthogonal axis.³⁰¹ The eigenvalues associated with these vectors give the projection of the surface area along these axes. For example, in the case of anthracene, the structure of which is shown in Figure 5.7, the van der Waals surface may be triangulated, and a normal vector assigned to each triangular surface element, shown in Figure 5.7.

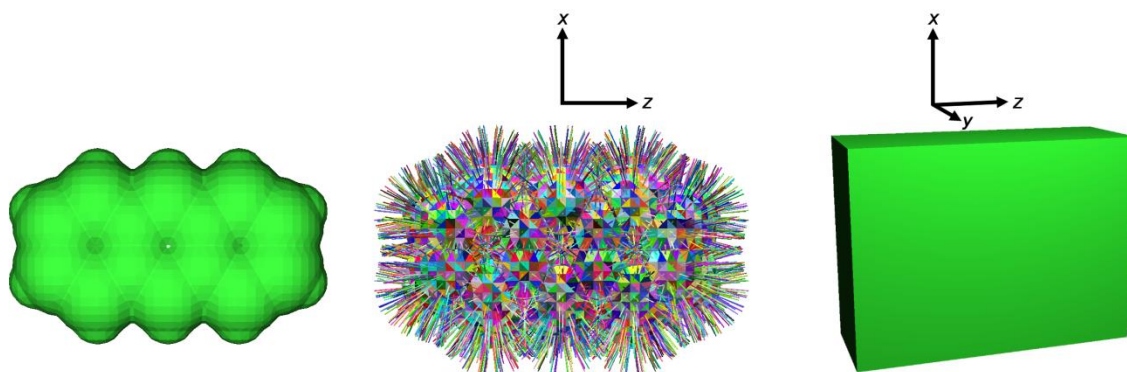


Figure 5.7 The surface of anthracene optimised at the B3LYP/6-31g(d) level (left), the triangulated surface with randomly coloured normal unit vectors shown for each surface element (centre), and the cuboid (rotated slightly out of the plane of the page for clarity) with face areas proportional to the eigenvectors of \mathbf{t} (right).

Continuing with the example of anthracene, the resulting diagonalised tensor of eigenvalues, obtained from the tensor, \mathbf{t} , from Equation (5.34) in the Cartesian frame

shown in Figure 5.7 is given by Equation (5.35). The trace of the tensor, $Tr(\mathbf{t}) = -192.3 \text{ \AA}^2$, corresponds to the negative of the total surface area, S , of the molecule.

$$\mathbf{t} = - \begin{pmatrix} 52.0 & 0.0 & 0.0 \\ 0.0 & 102.0 & 0.0 \\ 0.0 & 0.0 & 38.3 \end{pmatrix} \quad (5.35)$$

The eigenvector associated with the minimum eigenvalue, the z axis in the case above, represents the molecular axis with the maximum perpendicular surface vectors, corresponding to the molecular alignment axis. The eigenvector associated with the maximum eigenvalue, the y axis in the case above, corresponds to the molecular axis with the minimum perpendicular vectors, and the eigenvector associated with the intermediate eigenvalue is orthogonal to the other two axes, therefore the x axis in the case above. This representation of a molecular surface is intuitive, and allows a molecule of any shape or symmetry to be considered as a cuboid with surface areas corresponding to the inverse eigenvalues of \mathbf{t} , also shown for the example of anthracene in Figure 5.7. The alignment of the solute may therefore be treated with the simplifications associated with this symmetry, introduced in Sections 5.1.1 and 5.1.2.

The mathematical treatment of Equation (5.32) expressed in Cartesian form is complicated because the orientations of all the cartesian surface vectors must be considered for all combinations of the angles, β and γ , that define the molecular orientation in the laboratory frame for a uniaxial phase. The expression is simplified somewhat if the surface tensor is expressed in terms of the Wigner functions; by applying their closure relation, described in Section 5.1.2, Equation (5.32) may be expressed as Equation (5.36),^{299, 301} where the values of $T^{2,n}$ are the components of the spherical surface tensor, \mathbf{T} , that can be derived from the Cartesian surface tensor, \mathbf{t} (see below), incorporating the integration of the molecular surface described in the molecular frame, and $D_{0,2}^2(\beta, \gamma)$ describes the molecular orientation in the lab frame. The derivation of Equation (5.36) from Equation (5.32) is shown in Appendix A3.3.

$$\frac{U(\beta, \gamma)}{k_B T} = -\varepsilon \sum_n T^{2,n*} D_{0,n}^2(\beta, \gamma) \quad (5.36)$$

The Cartesian form of the surface tensor, \mathbf{T} , may be obtained from \mathbf{t} according to Equation (5.37),³⁰² where $\mathbf{1}$ is the identity matrix. The derivation of Equation (5.37) is shown in Appendix A3.4.

$$\mathbf{T} = \frac{3\mathbf{t} + S\mathbf{1}}{\sqrt{6}} \quad (5.37)$$

The interpretation of \mathbf{T} is less intuitive than that of \mathbf{t} , but the components of \mathbf{T} are still related to the shape of the molecule: a large positive value of T_{ii} indicates a large surface area perpendicular to axis i , such that the molecule has a tendency to align along the axis i , whereas a large negative value corresponds to a small surface area perpendicular to axis i . For the surface of a rod-like molecule, two values will be negative and one positive, however for a “disk-like” molecule, two values will be positive and one negative. Continuing the example of anthracene above, the Cartesian form of the surface tensor, \mathbf{T} , obtained using Equation (5.37), is given by Equation (5.38).

$$\mathbf{T} = \begin{pmatrix} 14.8 & 0.0 & 0.0 \\ 0.0 & -46.4 & 0.0 \\ 0.0 & 0.0 & 31.6 \end{pmatrix} \quad (5.38)$$

The components of the Cartesian form of \mathbf{T} may be converted into spherical components, $T^{L,m}$. In the general case of a 3×3 tensor there are 9 components of $T^{L,m}$, corresponding to $L = 0, 1, 2$, and $m = -L, -L+1 \dots L-1, L$,¹²⁷ but because \mathbf{T} , as defined from \mathbf{t} in Equation (5.37), is traceless and diagonal, the spherical components, $T^{0,0}$, $T^{1,m}$ and $T^{2,\pm 1}$, are equal to 0, and the other components may be simplified from the expressions for the general case, given in Appendix A3.5, to give Equations (5.39) and (5.40).

$$T^{2,0} = \frac{3}{\sqrt{6}} T_{zz} \quad (5.39)$$

$$T^{2,\pm 2} = \frac{1}{2} (T_{xx} - T_{yy}) \quad (5.40)$$

In the example of anthracene above, the spherical components of \mathbf{T} are $T^{2,0} = 38.7 \text{ \AA}^2$, and $T^{2,2} = T^{2,-2} = 30.6 \text{ \AA}^2$.

From the definitions of the Wigner functions in Equations (5.11) and (5.12) and the spherical terms of the surface tensor defined by Equations (5.39) and (5.40), the potential energy of a molecule at a given orientation may be expanded as Equation (5.41).

$$\frac{U(\beta, \gamma)}{k_B T} = -\varepsilon \left(T^{2,0*} \left(\frac{3 \cos^2 \beta - 1}{2} \right) + T^{2,-2*} \left(\sqrt{\frac{3}{8}} \sin^2 \beta e^{i2\gamma} \right) + T^{2,2*} \left(\sqrt{\frac{3}{8}} \sin^2 \beta e^{-i2\gamma} \right) \right) \quad (5.41)$$

Applying Euler's formula, Equation (5.41) simplifies to yield Equation (5.42).

$$\frac{U(\beta, \gamma)}{k_B T} = -\varepsilon \left(T^{2,0} \left(\frac{3 \cos^2 \beta - 1}{2} \right) + 2T^{2,2} \left(\sqrt{\frac{3}{8}} \sin^2 \beta \cos(2\gamma) \right) \right) \quad (5.42)$$

The orientational distribution function, $f(\beta, \gamma)$, may be obtained from the orientational potential energy, $U(\beta, \gamma)$, given by Equation (5.42) using a standard Boltzmann distribution to give Equation (5.43).³⁰³ The components of the Saupe ordering matrix may then be determined from this distribution, as described in section 5.1.1.

$$f(\beta, \gamma) = \frac{e^{-\frac{U(\beta, \gamma)}{k_B T}}}{\int_{\gamma=0}^{2\pi} \int_{\beta=0}^{\pi} e^{-\frac{U(\beta, \gamma)}{k_B T}} \sin \beta \, d\beta \, d\gamma} \quad (5.43)$$

To conclude the example of anthracene used in this section, the orientational distribution function calculated by using the surface tensor method and Equation (5.43), with an orienting strength of $\varepsilon = 0.04 \text{ \AA}^{-2}$ shown to be typical for nematic liquid crystals,³⁰¹ is shown in Figure 5.8. For clarity, plots of $f(\beta)$ for angles of $\gamma = 0^\circ$ and $\gamma = 90^\circ$ are also shown in Figure 5.8. Using Equations (5.19), (5.15) and (5.16), the order parameters of $S_{zz} = 0.267$ and $S_{xx} - S_{yy} = 0.329$ were obtained from the calculated distribution function, and are comparable to those determined from experiment.³⁰⁴

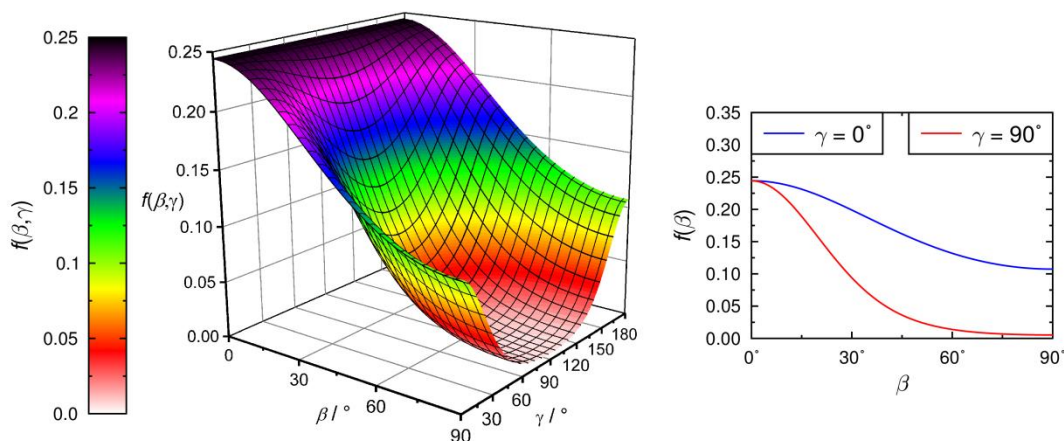


Figure 5.8 Calculated orientational distribution function of anthracene using the surface tensor method with an orienting potential of $\varepsilon = 0.04 \text{ \AA}^{-2}$.

5.1.4 Molecular surface definitions

Critical to any model based on molecular shape is the method by which the shape of a molecule is defined.³⁰⁵ A simple approximation is to consider the outer surface of a molecule constructed by a set of spheres, typically using van der Waals radii centred on atomic coordinates to obtain a van der Waals surface. However, this approach can result in different results depending on the exact approach chosen; for example, it has been shown that a united-atom approach in which a single sphere represents an entire CH, CH₂ or CH₃ group can result in a large difference in the predicted order parameter of a structure.³⁰⁶ It is also important to consider that for a model that is assuming an interaction between a molecular surface and a mean field, the molecular surface should be that which represents an accessible surface to the surrounding species, which may not be the same as the van der Waals surface.

An alternative but relatively common approach to constructing a molecular surface is to use a “rolling-ball” algorithm, which uses the principle of a probe ball of specified radius rolling over the van der Waals molecular surface.^{307, 308} A solvent accessible surface may be defined as the surface mapped out by the centre of the probe, and a solvent excluded surface (SES) may be defined by the cavity within the union of all possible probe positions. A schematic diagram of an SES is shown in two dimensions in Figure 5.9.

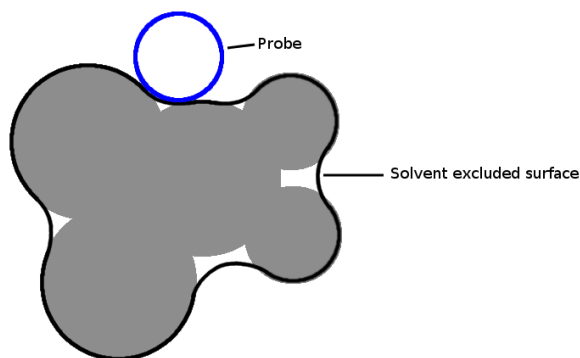


Figure 5.9 A 2D representation of a solvent excluded surface (SES) of a collection of fused spheres.

As well as being unambiguously defined for any given probe radius, the solvent excluded surface provides a surface that may be considered to be that in contact with neighbouring molecules, and is therefore applicable in the context of the models utilising the molecular surface described in Sections 5.1.3.2 and 5.1.3.3. This approach has been used to calculate molecular surfaces in the work reported here, using a probe radius of 3 Å that is consistent with previous studies.³⁰⁵ In practice, the surface is triangulated into discrete planar elements,^{128, 309} the density of which may be defined, and in this work a density of 5 vertices per Å² was used, providing an acceptable compromise between computation time and representing an accurate molecular surface.

5.1.5 Molecular alignment in MD simulations

As discussed in Chapter 1, molecular alignment is a crucial element of the analysis and verification of molecular dynamics simulations of liquid crystals and liquid crystal guest-host mixtures. Analysis of molecular alignment within pure liquid crystal simulations is typically carried out by defining the molecular axes as those of minimum moment of inertia (MOI),^{188, 241, 243, 244, 246} as used in Chapters 3 and 4, and previous studies have estimated molecular dimensions from the magnitudes of the eigenvalues of the inertia tensor.^{244, 310} However, some comparisons have been made between the alignment of different molecular axes within the same molecules in the same simulations, and subtle differences have been observed between the order parameters of the minimum MOI axes of aromatic cores and the order parameters of alkyl chains within a simulated liquid crystal phase of cyanobiphenyl molecules.²⁴³ Order parameters of molecular minimum MOI axes have been calculated to be higher than axes defined as

the bond between the C and N atoms constituting the cyano group in cyanobiphenyl liquid crystals,^{244, 251} and higher than axes defined along the aromatic cores of molecules in a simulation of E7,¹⁸⁵ suggesting that the alkyl chains add to the degree of molecular ordering. Comparisons have also been made between the minimum MOI axes and the axes of maximum polarizability for cyanobiphenyl liquid crystals,²⁵¹ which were shown to produce comparable order parameters, and between the minimum MOI axes and molecular dipole axes for a cyanobicyclohexyl liquid crystal,²⁵⁴ for which the dipole order parameter was found to be significantly lower than that obtained from the MOI axes. Some assessment of the surface tensor model has been made in the context of MD simulations of cyanobenzylideneaminocinnamates, using surface tensor values measured against the inertia reference frame, indicating that trends in experimental order parameters are not predicted as well by this method as they are from measuring the aspect ratios of the molecules.³¹⁰

Analysis of guest-host MD simulations has also focused on alignment, but typically the definitions of axes are those that are related to the experimental observables, such as bond axes for comparison with NMR data,²⁵⁸ and orbital orientations for comparison with EPR experiments,^{256, 261} although minimum MOI axes have again typically been used to model the alignment axes of the host and guest species.²⁵⁹ A study of small and generally rigid, highly symmetric solute molecules comprising 12 atoms or fewer has been carried out in 5CB, with a specific aim of assessing models of alignment.²⁵⁷ For the examples studied, it was demonstrated that molecular shape plays a greater role in the alignment of solute molecules than quadrupolar and electrostatic interactions, and it was shown that the surface tensor model did not predict simulated potential energy curves as well as Maier-Saupe theory. However, Maier-Saupe theory does not provide a definition of the principal molecular axes and therefore requires a set of axes to be defined by another method, which may be a limitation for the description of larger, more complex molecules.

The ease of calculation of the minimum MOI axis of a molecule, along with its tendency to provide a match with an intuitive definition of the long molecular axis of a rod-like molecule, means its use in the MD literature is widespread. However, the experimental studies assessing the alignment axes of solutes in liquid crystal hosts discussed in Section 5.1.3.1 and computational studies such as those outlined above

suggest that there may be merit in exploring alternative axes when considering molecular alignment in liquid crystal systems.

5.1.6 Transition dipole moment alignment

In the context of the order parameters of dye molecules, the definition of the orientation of the visible transition dipole moment vector is as vital as that used to define the molecular alignment axis. As introduced in Section 3.1.1.1, some studies have been conducted in which the orientations of the transition dipole moments within the molecular frames of dyes for guest-host applications have been calculated,¹⁴²⁻¹⁴⁵ as discussed in section 3.1.1.1, but such studies are much less common than those considering the molecular alignment axes. However, some wider literature does focus on the orientations of electronic transition dipole moments, for example in the contexts of chromophores in organic light emitting diodes,³¹¹ protein fluorescence,³¹² and energy transfer in chlorophyll,³¹³ using time-resolved spectroscopy combined with electronic structure calculations.

Some comparison has been carried out between experimentally determined TDM orientations and those obtained from calculations, generally demonstrating a good match with experimentally determined orientations using DFT^{314, 315} as well as HF and post-HF³¹⁶⁻³¹⁸ methods. Further to obtaining single TDM orientations, some of these studies focus on the dependence of TDM orientations on molecular structure and on the conformations of pendant alkyl chains,³¹⁵⁻³¹⁸ highlighting a potential shortcoming of the theoretical consideration of a fixed β angle between the molecular alignment axis and the visible TDM, which is central to the usual theoretical treatment of guest-host mixtures discussed in Chapter 1.

5.1.7 Aims

The work reported in this chapter was based on further detailed analysis of the calculations and simulations presented in Chapters 3 and 4, along with further comparison with experimental results. Initially, the aim was to assess the validity of describing the principal molecular axes using the minimum MOI axes, which were used to define the molecular axes for both the electronic structure calculations and the MD simulations in Chapters 3 and 4, respectively, by applying various other definitions of the principal molecular axes in further analysis of the MD simulations. It was intended that a comparison of the overall TDM alignment calculated using these different axis definitions with the experimental order parameters of the dyes presented in Chapter 4 would help to provide an indication of the applicability of the different models to the systems studied. By comparing possible alignment axes, the intention was to identify the model(s) that best replicated the experimental data in the context of molecular design of dye molecules for use in liquid crystal mixtures, considering the influence of molecular features on the alignment properties. Alignment models applying to the guest dye molecules could also be considered in the broader context of host molecules, potentially providing information on factors influencing the host alignment.

Further aims were to use the MD simulations, allied with comparison with experiment, to assess the influence and significance of molecular biaxiality on the overall TDM alignment of guest dyes, and also to consider the effects of molecular flexibility and conformations on the calculated TDM alignments of the dyes.

5.2 Results and discussion

The analysis of MD simulations enables an unusual approach to the consideration of molecular alignment, because the alignment may be readily characterised using any definition of the principal molecular axis, providing the axis may be unambiguously defined by the atom types and positions for any given molecular conformation. For a simulation of aligned molecules, the axis best representing the “true” molecular alignment axis may be considered to be that which has the highest associated calculated order parameter, and it is on this premise that the work presented here is based.

All of the work concerning the guest-host MD simulations in this chapter uses the trajectories of the simulations from pseudo-nematic starting configurations presented in Chapter 4, and all the analysis has been carried out on the simulations between 30 ns and 500 ns, consistent with that presented previously in Chapter 4.

5.2.1 Alignment axes

The three orthogonal axes of principal moments of inertia, \mathbf{I}_a , \mathbf{I}_b , and \mathbf{I}_c , were used as an internal molecular frame for each dye molecule to give a starting point for assessing the alignment axes of the dyes in the MD simulations. Using these reference axes, the alignment axes, \mathbf{a}_{MOI} , of the dye molecules were obtained according to Equation (5.44), where the coefficients, c_i , were each defined as the average projections of the unit vectors \mathbf{I}_i of the dye molecules onto the host director \mathbf{n} , also a unit vector, over the course of the simulation. The resultant alignment axes may be considered to be the most aligned molecular axes described by this set of reference axes within the limitations of the simulation.

$$\mathbf{a}_{\text{MOI}} = c_a \mathbf{I}_a + c_b \mathbf{I}_b + c_c \mathbf{I}_c \quad (5.44)$$

The angles, θ , between \mathbf{n} and \mathbf{a}_{MOI} and the associated order parameters, $S_\theta(\mathbf{a}_{\text{MOI}}) = \langle P_2(\cos\theta) \rangle$, of the alignment axes were then calculated against the host director for each trajectory frame and averaged over time. These order parameters are listed in Table 5.2 alongside those obtained for the minimum MOI axes, previously presented and discussed in Chapter 4, for comparison.

Table 5.2 Calculated order parameters, S_θ (MOI), of the minimum MOI axes of the dyes, originally presented in Chapter 4 (Table 4.5), and the order parameters $S_\theta(\mathbf{a}_{\text{MOI}})$ of the alignment axes of the dyes, against the host director, and the differences between these order parameters for each of the dyes, $\Delta S = S_\theta(\mathbf{a}_{\text{MOI}}) - S_\theta(\text{MOI})$.

Dye	$S_\theta(\text{MOI})$	$S_\theta(\mathbf{a}_{\text{MOI}})$	ΔS
15SB3	0.836	0.921	+0.085
15NB3	0.869	0.898	+0.029
15NB3OH	0.843	0.853	+0.010
26B3	0.880	0.900	+0.020
26B3OH	0.896	0.902	+0.006

From Table 5.2 it is clear that for each of the dyes, the \mathbf{a}_{MOI} axis exhibits a higher order parameter than that obtained from the minimum MOI axis. In some respects this result is unsurprising because the \mathbf{a}_{MOI} axes have been defined as those that are best aligned with the host director, but the differences in the obtained order parameters, ΔS , and particularly the observation that the differences are not consistent between the dyes, indicate that the minimum MOI axis may not be the best description of the principal molecular alignment axes of the dyes. The difference between the order parameters of $\Delta S = 0.085$ for 15SB3 is especially significant because its order parameter using the minimum MOI axis is the lowest of all the dyes, whereas its order parameter using the \mathbf{a}_{MOI} axis is the highest of all the dyes. This difference is of particular interest because of the results presented in Chapter 4, which showed that the calculated dichroic order parameter of 15SB3 was significantly underestimated, relative to the other dyes, when the principal molecular axis was described as the minimum MOI axis. The trend in the order parameters between the other four dyes is comparable for the \mathbf{a}_{MOI} and the minimum MOI axes.

This analysis suggests that the basis for molecular alignment of the dyes within these simulations may not be the principal moments of inertia, because a set of axes have been defined that are uniformly better aligned than those of the minimum MOI. However, the analysis does not indicate that the \mathbf{a}_{MOI} axes are the most aligned molecular axes because the choice of internal coordinate system used here may limit the description of the molecular alignment.

5.2.2 Basis for alignment

Although the analysis above is indicative that the minimum moment of inertia axes are not the best description of the molecular alignment axes of the dyes, it does not provide any information on the actual basis for alignment. For the purposes of understanding and rationalising the molecular alignment of the dyes, and to develop and improve upon the approaches presented so far in this thesis, it is desirable for a molecular axis to be defined from intrinsic molecular properties, rather than parameterising against the host director as was the case for the \mathbf{a}_{MOI} axes. However, the \mathbf{a}_{MOI} axes do provide a benchmark against which other definitions may be assessed. The following sections introduce a variety of definitions of the molecular axes, such as those based on the models discussed in Section 5.1.1 along with a brief explanation of how they were calculated here. The order parameters of these axes obtained from the MD simulations are then presented and compared.

5.2.2.1 Minimum circumference

According to the elastic tube model, giving rise to Equation (5.28) as outlined in Section 5.1.3.2, the minimum energy molecular orientation corresponds to that which has the minimum projected circumference on the plane perpendicular to the director. Hence, the principal molecular axis may be defined as that corresponding to the minimum projected circumference in the orthogonal plane. At each trajectory frame of each simulation, the van der Waals surface of each dye was constructed from atomic van der Waals radii centred on atomic positions.¹²⁹ This molecular surface was then projected into a plane orthogonal to an initial estimate of the molecular axis, in this case the minimum moment of inertia axis, and the circumference of this projected surface was calculated. A simplex algorithm was then applied to determine the orientation of a unit vector corresponding to that which had the minimum projected circumference into the orthogonal plane.

5.2.2.2 Minimum area

An alternative, similar, and intuitive approach to defining the alignment axes of molecules within a fluid system is to consider their surface areas projected on to a plane orthogonal to the director. This approach may be justified because molecular diffusion along the director is greater than diffusion perpendicular to the director in nematic phases,³¹⁹ such that a favourable orientation may be one that minimises the area along the director; hence, an alignment axis may be that which minimises this area projected on to the orthogonal plane (*cf.* the force on a moving body in a fluid³²⁰). For uniaxial particles, this axis will be the same as that which minimises the circumference, as described above, but any deviation from uniaxial symmetry may result in a difference between the orientations of the axes of minimum circumference and minimum surface area. The axis associated with the minimum projected surface area was calculated in the same way as for the circumference described above, except the area, rather than the circumference, of the projected molecular surface was calculated and minimised, again using a simplex procedure as previously reported for a similar problem in a different context.³²¹

5.2.2.3 Maximum aspect ratio

The relationship between the molecular aspect ratio and the degree of alignment within liquid crystal systems is widely accepted, as discussed in Section 3.1.2, and the general trend in the aspect ratios of the optimised structures presented in Section 3.3.2.1 matched that of the experimentally determined order parameters of the dyes, given in Table 4.2. Hence, an axis that represents the maximum molecular aspect ratio could be considered to be that which describes the principal molecular alignment axis. For each dye molecule at each trajectory frame, the aspect ratio was calculated in the same way as described in Section 3.2.2.1, using the minimum MOI axis as an initial guess for the principal axis. A simplex algorithm was then used to obtain the orientation of the axis associated with the largest aspect ratio.

5.2.2.4 Surface tensor

The principal molecular axes described by the surface tensor, \mathbf{t} , introduced in Section 5.1.3.3, enable an alignment axis to be defined on the basis of the surface tensor model of solute alignment. To define these axes during the simulations, the solvent excluded surface (described in Section 5.1.4) was calculated for each molecule at each trajectory frame during each simulation, from which the surface tensor was constructed and the eigenvector associated with the minimum eigenvalue of the surface tensor was defined as the principal molecular alignment axis.

5.2.2.5 Comparison of principal molecular axis definitions

The order parameters, $S_\theta = \langle P_2(\cos\theta) \rangle$, obtained using each of the axis definitions discussed in the sections above are listed in Table 5.3, along with the differences, Δ , from the order parameters of the \mathbf{a}_{MOI} alignment axes. These order parameters are also shown graphically in Figure 5.10.

Table 5.3 Order parameters obtained for the alignment (\mathbf{a}_{MOI}), minimum MOI, minimum circumference, minimum area, maximum aspect ratio and surface tensor axes. $\Delta = S_\theta(\mathbf{a}_{\text{MOI}}) - S_\theta$. Average Δ values are also listed.

Dye	\mathbf{a}_{MOI}		minimum MOI		minimum circumference		minimum area		maximum aspect ratio		surface tensor	
	S_θ	S_θ	S_θ	Δ	S_θ	Δ	S_θ	Δ	S_θ	Δ	S_θ	Δ
15SB3	0.921	0.836	0.085	0.868	0.053	0.853	0.068	0.906	0.015	0.894	0.027	
15NB3	0.898	0.869	0.029	0.888	0.010	0.874	0.024	0.891	0.007	0.874	0.024	
15NB3OH	0.853	0.843	0.010	0.836	0.017	0.845	0.008	0.814	0.039	0.860	-0.007	
26B3	0.900	0.880	0.020	0.877	0.023	0.883	0.017	0.842	0.058	0.899	0.001	
26B3OH	0.902	0.896	0.006	0.893	0.009	0.895	0.007	0.873	0.029	0.904	-0.002	
Average			0.030		0.022		0.025		0.030		0.009	

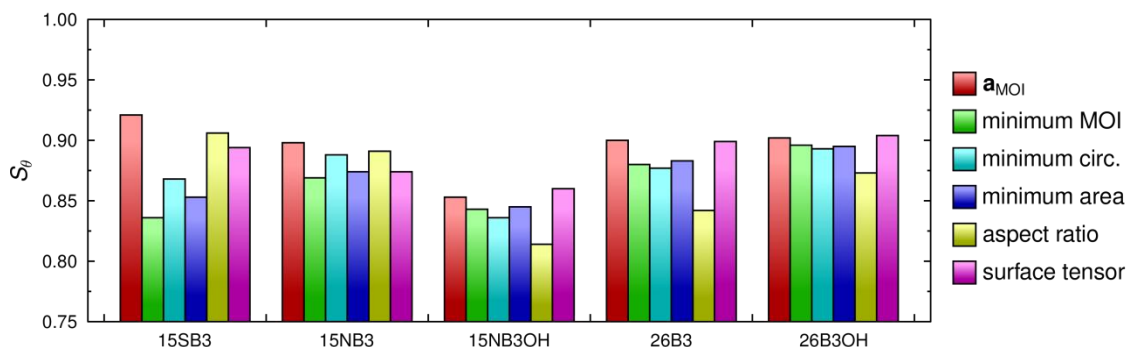


Figure 5.10 Comparison of the order parameters obtained for the alignment axes (\mathbf{a}_{MOI}), minimum moment of inertia axes (MOI), minimum circumference (circ.), minimum area, maximum aspect ratio, and surface tensor axes.

A comparison of the order parameters given in Table 5.3 and the graphical representation shown in Figure 5.10 indicates that the differences in the order parameters arising from the various principal alignment axes definitions are not consistent between the dyes. For 15NB3OH, 26B3 and 26B3OH, the aspect ratio axis gives the lowest order parameter, and may therefore be considered the worst definition of the principal molecular axes, whereas the minimum MOI, minimum circumference and maximum aspect ratio axes have similar, higher order parameters, suggesting they are better descriptions of the principal alignment axes. The highest order parameters, and therefore the best descriptions of the alignment axes for these three dyes, are shown to be the \mathbf{a}_{MOI} axes and the surface tensor axes.

In contrast, for 15SB3 and 15NB3, the aspect ratio axes have the highest order parameters of any of the axis definitions, other than the \mathbf{a}_{MOI} axes, and it is the minimum MOI and minimum area axes that have the lowest associated order parameters.

From an overall comparison of the data, and most notably the average differences of the order parameters from those of the \mathbf{a}_{MOI} alignment axes, it is evident that the surface tensor axis is generally the best of these descriptions from first principles of the principal molecular alignment axes of the dyes, for these simulations.

5.2.3 Application of the surface tensor model

5.2.3.1 Host order parameter

The potential scope of the surface tensor approach to defining the molecular alignment axes was assessed by applying the surface tensor model to the simulation of the host alone, using the simulation from an isotropic starting configuration. Figure 5.11 shows the order parameter calculated from the surface tensor axes, calculated using the same method as described in section 4.3.2 in Chapter 4 for the minimum MOI axes, alongside that of the minimum MOI axes for comparison. The slightly higher order parameter of the surface tensor axes than the minimum MOI axes indicates that the surface tensor model of the alignment axes may also provide a marginally better description of the

principal molecular alignment axes of the host molecules, and thus may be applicable in a wider context than simply the guests in the guest-host simulations studied thus far in this work.

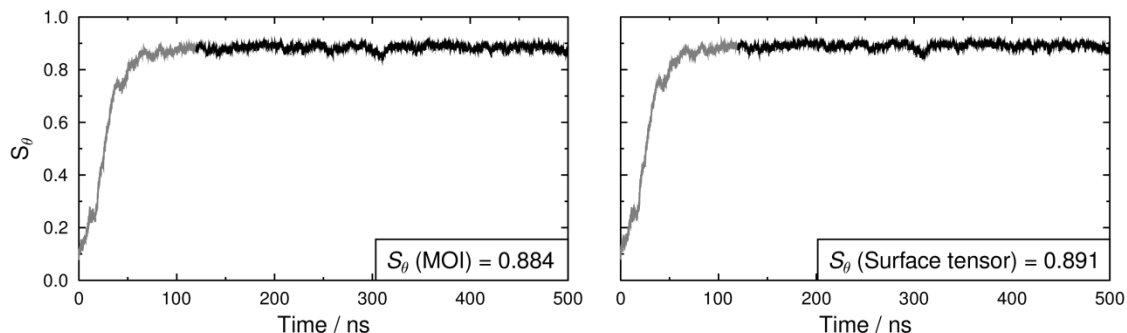


Figure 5.11 Order parameter, S_θ , vs. time for a simulation of 400 E7 component molecules starting from an isotropic starting geometry, calculated for the axes of minimum MOI (left) and the principal surface tensor axes (right). Average values were determined between 120 ns and 500 ns, shown in black.

5.2.3.2 Consideration of molecular biaxiality

Consideration of a molecular tensor such as the surface tensor enables the biaxial order parameters of the dye molecules to be assessed, in addition to the uniaxial order parameters obtained from a single molecular axis. The angles made between each of the surface tensor x and y axes (Figure 5.7) and the host director during the simulations were calculated at each trajectory frame for each dye molecule and histograms of the angles are shown in Figure 5.12, comparable to those in Figure 4.16 used for verification of the MOI axes.

A comparison of the distributions of the angles of the principal surface tensor axes against the host director shows that the distribution of angles explored is largely comparable between the dye molecules within each simulation. The order parameters, S_{xx} and S_{yy} , associated with the secondary and tertiary axes, along with the biaxial order parameters, $D = S_{xx} - S_{yy}$, are listed in Table 5.4.



Figure 5.12 Histograms of the angles made between the principal, secondary and tertiary surface axes and the host director, of individual dye molecules (represented by different colours, consistent with those used in Chapter 4) measured from the five guest-host simulations.

Table 5.4 Biaxial order parameters, $S_{xx} - S_{yy}$, of the dyes, determined from the guest-host MD simulations.

Dye	S_{xx}	S_{yy}	$S_{xx} - S_{yy}$
15SB3	-0.430	-0.464	0.034
15NB3	-0.419	-0.456	0.037
15NB3OH	-0.417	-0.443	0.026
26B3	-0.439	-0.460	0.021
26B3OH	-0.444	-0.460	0.016

The values of these biaxial order parameters from the MD simulations show that the deviations from uniaxial molecular alignment of the dyes are only slight, and they indicate that the biaxiality may be slightly greater for the 1,5-disubstituted dyes than the 2,6-disubstituted dyes.

5.2.3.3 Reassessment of dichroic order parameters

The reassessment of the molecular alignment axes of the dyes means that the β angles determined in Chapter 3 must be recalculated in order to obtain the calculated TDM order parameters, S_ϕ , against the host director using the surface tensor axes that enable a direct comparison with the experimental order parameters. The principal surface tensor axes were calculated for each of the DFT optimised dye structures presented in Chapter 3, and are shown in Figure 5.13. A comparison of these surface tensor axes with the minimum MOI axes, which are also shown in Figure 5.13, shows that the surface tensor axes lie in very similar orientations to the minimum MOI axes for each of the dyes except for 15SB3, for which a large difference in the orientations of the axes is evident. The principal surface tensor axis of a molecule tends to lie in the plane of planar molecular features such as anthraquinone or phenyl rings, and from Figure 5.13 it can be seen that the principal surface tensor axis in 15SB3 lies parallel to the plane of the substituent phenyl rings, which is not the case for the minimum MOI axis. This effect is much smaller for the other dyes, in which the substituent phenyl rings do not lie perpendicular to the anthraquinone core. Additionally, the heavy sulphur substituent atoms cause the MOI axis of 15SB3 to lie further from the long axis of the anthraquinone core than lighter substituent atoms would.

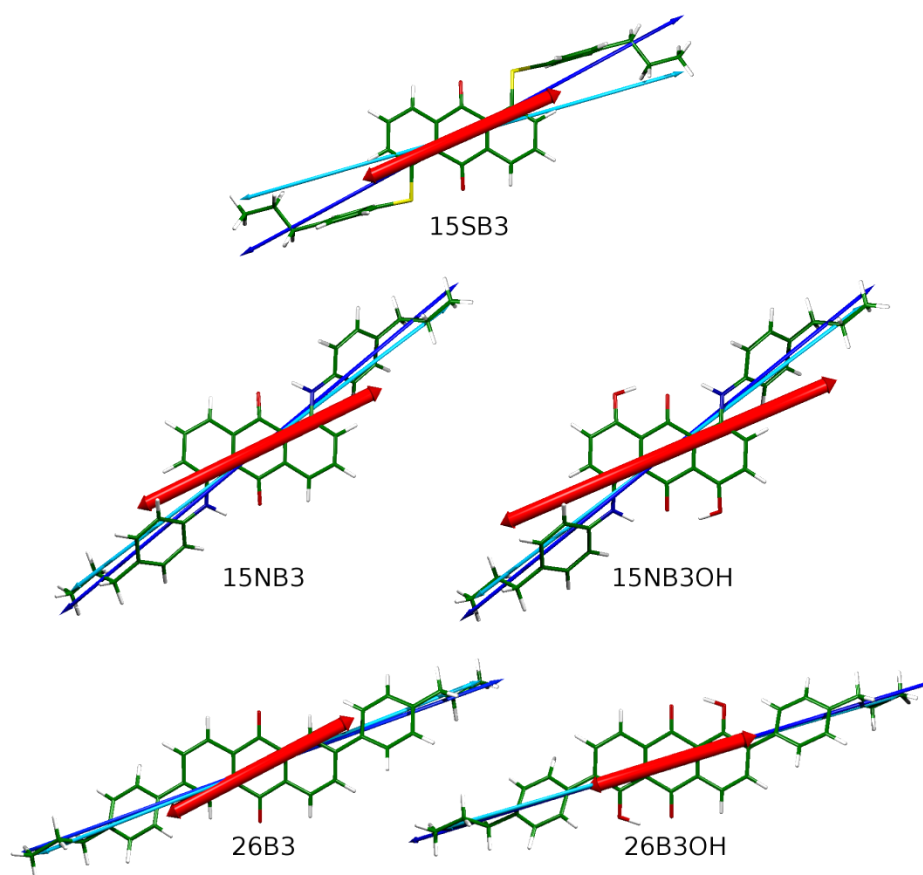


Figure 5.13 DFT optimised structures of the dyes with vectors showing the orientations of the minimum MOI axes (blue), the principal surface tensor axes (turquoise), and the visible transition dipole moment axes (red) with lengths proportional to oscillator strengths.

The β angles were recalculated, defined as the angle between the TDM vector and the principal surface tensor axis of each dye, and are listed in Table 5.5. These recalculated angles show the same trends as those determined against the MOI axes (discussed in Chapter 3 and listed in Table 3.10) except for 15SB3, which is shown to have a larger β angle relative to the other dyes when it is calculated against the principal surface tensor axis.

Table 5.5 Calculated angles, β , between the principal surface tensor axes and the visible TDMs of the dyes and their associated order parameters, S_β , and calculated uniaxial dichroic order parameters, S_ϕ (surface), determined as the product of S_θ and S_β (see Table 5.3). Uniaxial dichroic order parameters calculated using the minimum MOI axes, S_ϕ (MOI), presented in Chapters 3 and 4, are listed for comparison.

Dye	Surface tensor			MOI
	$\beta / ^\circ$	S_β	S_ϕ	S_ϕ
15SB3	7.9	0.972	0.869	0.829
15NB3	10.9	0.946	0.827	0.794
15NB3OH	13.9	0.913	0.785	0.748
26B3	7.0	0.978	0.879	0.853
26B3OH	2.8	0.997	0.901	0.894

A comparison of the S_ϕ values obtained from using the surface tensor axes with those obtained from using the minimum MOI axes shows that the surface tensor axes result in higher calculated uniaxial dichroic order parameters for all of the dyes than using the minimum MOI axes, which is largely attributable to the higher molecular alignment order parameters, S_θ , determined using the surface tensor axes.

Plotting the S_ϕ values from Table 5.5, calculated using the surface tensor approach, against S_{exp} , as shown in Figure 5.14, demonstrates that the trend between the two sets of data is good, and the value of $R^2 = 0.9211$, compared with that of $R^2 = 0.8299$ for the equivalent plot obtained from the MOI axes (Figure 4.24 in Chapter 4), demonstrates an improved linear correlation between the calculated and experimental values. However, the intercept of 0.549 is greater than that of 0.476 obtained for the MOI axes, and the gradient is smaller, indicating that although the calculations based on the surface tensor axes result in a better linear correlation between calculation and experiment, the offset between the experimental and calculated values is greater.

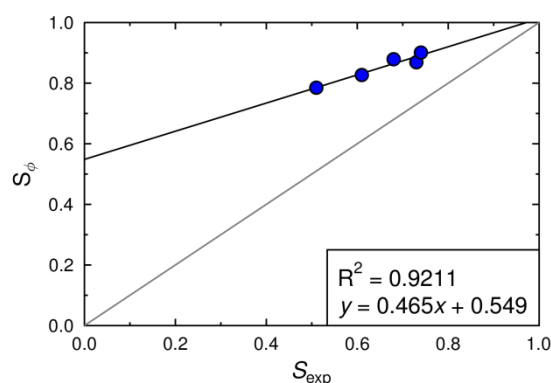


Figure 5.14 Plot of calculated order parameters, S_ϕ , vs. experimental order parameters, S_{exp} . The grey line indicates a perfect match between calculated and experimental values.

The secondary and tertiary surface axes were also obtained from the DFT optimised structures of the dyes, and the azimuthal angle, α , between the secondary axis, x , and the projection of the TDM on to the xy plane of each dye, shown schematically in Figure 5.15, is listed in Table 5.6, along with the biaxiality terms and the overall dichroic order parameters, S_ϕ , calculated for each of the dyes using Equation (5.27).

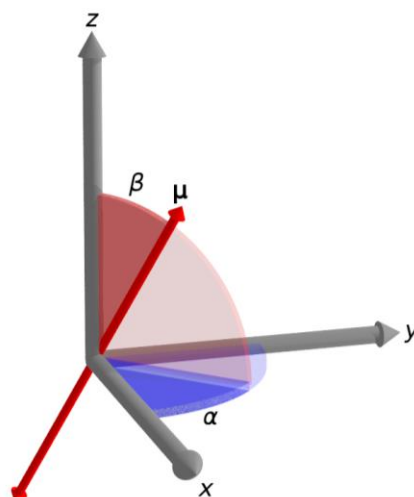


Figure 5.15 Diagram of the molecular frame, defined by the x , y and z axes, the TDM axis, μ , and the angles α and β relating them.

Table 5.6 Calculated angles, α , between the secondary surface axis, x , and the projection of the TDM into the xy plane for each of the dyes along with values of the biaxial term used to calculate the overall dichroic order parameters.

Dye	$\alpha / ^\circ$	$0.5\langle S_{xx} - S_{yy} \rangle (\sin^2 \beta \cos 2\alpha)$	S_ϕ
15SB3	0.0	0.000	0.869
15NB3	10.0	0.001	0.827
15NB3OH	10.2	0.001	0.786
26B3	36.9	0.000	0.879
26B3OH	98.7	0.000	0.901

The small values of α calculated for 15SB3, 15NB3 and 15NB3OH show that the visible TDMs of these three dyes lie close to the zx plane of the surface axes of these dyes. The large angles of α for 26B3 and 26B3OH show this is not the case for the 2,6-disubstituted dyes studied here, but when considered alongside the small values of β (Table 5.5), these α angles do not represent a large deviation of the TDMs from the xz planes of the dyes.

A comparison of the overall order parameters, S_ϕ , that include the influence of molecular biaxiality, listed in Table 5.6, with the equivalent uniaxial order parameters listed in Table 5.5 shows that there is essentially no difference between the uniaxial and biaxial order parameters, which is also highlighted by the biaxiality terms of the dichroic order parameters listed in Table 5.6.

5.2.4 Assessment of transition dipole moment orientations

In the analysis presented so far in this thesis, the visible TDMs of the dyes have been considered to be fixed against a molecular axis, in accordance with the conventional theoretical description of TDM alignment within guest-host systems.²⁴ However, as introduced in Section 5.1.6, studies in contexts other than guest-host systems have shown that molecular conformations can influence TDM orientations for some small molecules, suggesting that the consideration of a fixed TDM orientation in a molecular frame may not be entirely valid for dyes in guest-host systems.

In principle, one method of avoiding this approximation would be to calculate the orientation of the visible TDM for each dye molecule at each trajectory frame of an MD simulation, enabling the orientation of the TDM at each trajectory frame to be measured against the principal molecular alignment axis. However, the number of geometries within the trajectories is prohibitive to carrying out such DFT calculations at the level of theory used to determine the TDM orientations thus far in this thesis. Hence, exploratory calculations were carried out in order to evaluate potential methods for reducing the computation time required to evaluate the TDM orientations for the range of conformations explored in the MD simulations, and the results are described in the following subsections.

5.2.4.1 Smaller molecular structures

The first approach taken was to reduce the number of atoms in the DFT calculations by using dye structures in which the propyl chains were substituted with hydrogen atoms, labelled with the suffix “0”, rather than “3” in the names given in Table 5.7. After optimising each structure, TD-DFT calculations at the same level of theory as those presented in Chapter 3 were carried out, and the results are listed in Table 5.7 alongside those of the propyl-substituted dyes for comparison. No allowed visible transitions with comparable orbital contributions to that calculated for 26B3 were calculated for 26B0. Hence, a methyl-substituted analogue, 26B1, was tested for which such a visible transition was calculated, so for consistency a methyl substituted analogue of 26B3OH, 26B1OH, was also used. The calculated allowed visible transitions of these species are

also listed in Table 5.7. The transitions listed here for 15SB0, 15NB0, 15NB0OH, 26B1 and 26B1OH were found to arise from the same orbitals as those determined in Chapter 3 for the respective propyl-terminated dyes, supporting their use to provide suitable TDM orientations.

Table 5.7 Calculated wavelengths, λ , and oscillator strengths, f , of the allowed visible electronic transitions of the propyl-substituted dyes and their hydrogen and methyl substituted analogues, along with their projections on to the AQ, CO and ORTH axes.

	λ / nm	f	n_{AQ}	n_{CO}	n_{ORTH}
15SB3	453	0.27	0.92	0.40	0.00
15SB0	451	0.25	0.92	0.41	0.00
15NB3	552	0.35	0.90	0.45	0.04
15NB0	542	0.32	0.91	0.43	0.05
15NB3OH	634	0.55	0.91	0.41	0.06
15NB0OH	625	0.49	0.92	0.39	0.06
26B3	390	0.29	0.89	0.45	0.01
26B0	-	-	-	-	-
26B1	389	0.23	0.88	0.46	0.01
26B3OH	492	0.57	0.95	0.27	0.01
26B0OH	478	0.49	0.96	0.28	0.00
26B1OH	491	0.53	0.95	0.30	0.00

Each TDM orientation was described relative to the orientation of the anthraquinone core by defining unit vectors as the minimum MOI axis of the 14 anthraquinone carbon atoms (termed AQ), the minimum MOI axis of the 4 carbonyl atoms (termed CO), and the axis orthogonal to these (termed ORTH), shown in Figure 5.16. The coefficients, n_{AQ} , n_{CO} and n_{ORTH} were then determined as the projection of the unit TDM vector on to each of the respective anthraquinone axes, and these values are listed for each of the dyes in Table 5.7.

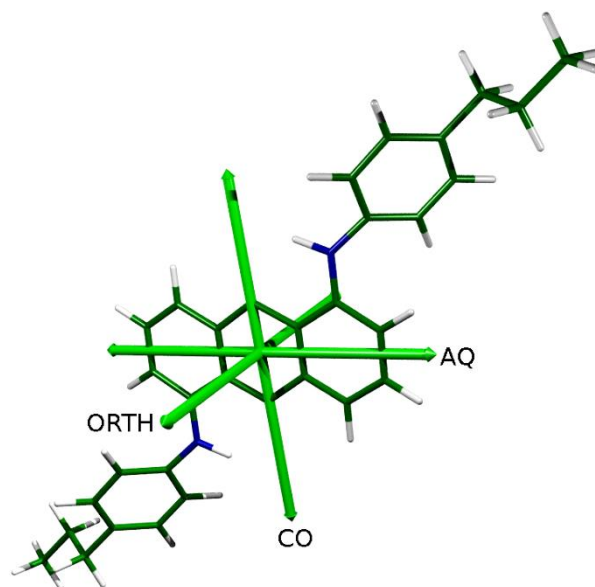


Figure 5.16 Anthraquinone (AQ), carbonyl (CO) and orthogonal (ORTH) axes shown for 15NB3.

The values in Table 5.7 demonstrate that the calculations using the smaller structures replicate those of the propyl-substituted dyes. This result is consistent with the calculated orbitals involved in the visible transitions, discussed in Chapter 3, which are located mainly on the anthraquinone core and directly substituted groups.

5.2.4.2 Level of theory and basis sets

The second approach taken to reducing the computation time of the TDM calculations was to compare the influence of the level of theory and basis-set size on the calculated visible transition energies, oscillator strengths and orientations of the allowed visible transitions. 15SB0 was chosen as a model compound for these tests, and the results are listed in Table 5.8, from which it can be seen that using the smaller 3-21G basis set had little influence on the calculated TDM orientation or oscillator strength relative to that obtained using the 6-31G(d) basis set used previously in this work, but it resulted in a higher calculated transition energy (shorter wavelength). Reducing the basis set size further to STO-3G caused a more significant difference in the calculated orientation, energy and oscillator strength relative to those obtained using 6-31G(d). The use of the semi-empirical AM1 and ZINDO methods resulted in even more significant differences in the TDM orientation compared with that calculated at the B3LYP/6-31G(d) level. It was therefore decided that the differences introduced by using lower levels of theory to

reduce the calculation time was too great to use these methods for further analysis, and the B3LYP/6-31G(d) level was used for subsequent calculations.

Table 5.8 Calculated allowed visible transitions and associated properties for 15SB0 using a range of levels of theory.

Level of theory	λ_{\max}	f	n_{AQ}	n_{CO}	n_{ORTH}
B3LYP/6-31G(d)	451	0.2501	0.92	0.41	0.00
B3LYP/3-21G	431	0.2547	0.92	0.40	0.00
B3LYP/STO-3G	395	0.1772	0.94	0.35	0.00
AM1	408	0.3246	0.86	0.52	0.00
ZINDO	337	0.4105	0.98	0.18	0.00

5.2.4.3 Fixed TDM orientations

Although the assessment of different levels of theory and of structures with fewer atoms indicated that the recalculation of TDMs at each trajectory frame is impractically computationally expensive, the definition of the TDM as a scaled sum of unit axes defined by the AQ, CO and ORTH vectors enables an approach to be taken in which the TDM orientation is defined against these axes for each dye molecule at each trajectory frame during the MD simulations. The angles β and α are then determined for each molecule at each trajectory frame against the principal surface tensor axis of the molecule. This approach does not assume any fixed angle between the TDM and the molecular alignment axis, but instead applies the assumption that the TDM is fixed only against the central anthraquinone chromophore of each dye molecule. TDMs defined in this way are subsequently referred to as “fixed TDM axes”.

Consideration of the variation in the TDM orientations within the molecular frame results in a modified expression for the TDM order parameter in the laboratory frame, given by Equation (5.45), in which the fixed β and α terms from Equation (5.27) are replaced with ensemble averages.

$$\langle P_2(\cos \phi) \rangle = \langle S_\theta \rangle \langle P_2(\cos \beta) \rangle + \frac{1}{2} \langle S_{xx} - S_{yy} \rangle \langle \sin^2 \beta \cos 2\alpha \rangle \quad (5.45)$$

The average β and α angles and their associated contributions to the dichroic order parameters, S_ϕ , of each of the dyes are listed in Table 5.9, using the S_θ values given in Table 5.3.

Table 5.9 Calculated angles, β and α , and their standard deviations, \pm , of the visible TDMs of the dyes, defined as fixed against the anthraquinone core. The associated biaxial terms and calculated overall dichroic order parameters, S_ϕ , are also listed.

Dye	$\langle\beta\rangle / ^\circ$	$\langle S_\beta\rangle$	$\langle\alpha\rangle / ^\circ$	$0.5\langle S_{xx}-S_{yy}\rangle\langle\sin^2\beta\cos2\alpha\rangle$	S_ϕ
15SB3	5.8 ± 3.0	0.981	74.3 ± 56.5	0.000	0.877
15NB3	14.0 ± 5.5	0.900	24.0 ± 28.6	0.000	0.788
15NB3OH	19.4 ± 6.4	0.821	14.2 ± 11.0	0.001	0.707
26B3	5.7 ± 2.9	0.982	127.7 ± 44.3	0.001	0.883
26B3OH	4.9 ± 2.6	0.986	70.6 ± 53.4	0.000	0.891

A comparison of the average β angles in Table 5.9 with those calculated as fixed β values (Table 5.5 in Section 5.2.3.3) shows that the TDMs are calculated to be more aligned with the principal molecular axes for 15SB3 and 26B3 when using TDMs fixed against the anthraquinone core, whereas 15NB3, 15NB3OH and 26B3OH exhibit worse TDM alignment using this approach. These differences between the calculated β angles may be attributed to the difference between the calculated structures from DFT and MD: the most common orientation of the substituent phenyl rings of 15SB3, 15NB3 and 15NB3OH during the MD simulations was found to be with the plane of the phenyl rings perpendicular to the plane of the anthraquinone core (Figure 5.19), whereas the DFT and HF optimised geometries of 15NB3 and 15NB3OH showed the plane of the phenyl substituents to be twisted to lie closer to the plane of the anthraquinone core (see Figure 3.11 in Chapter 3 and Figure A4.2 in Appendix 4.2). These differences indicate that the calculated minimum energy structures of the isolated molecules are not representative of the average molecular shapes determined from the MD simulations of these two dyes in the E7 host at room temperature. A comparison of the standard deviations of the β angles shows that the two amine dyes exhibit a larger range of β angles than 15SB3, 26B3 and 26B3OH, consistent with their greater flexibility, as discussed in Chapter 4.

The associated order parameters, S_β , in Table 5.9 differ accordingly with those calculated from fixed values of β , most significantly in terms of an increase in S_β for 15SB3 and decreases in S_β for 15NB3 and 15NB3OH, although the trend in values is

the same. The relatively small β angles, along with the small values of $S_{xx} - S_{yy}$, again result in negligible deviations arising from biaxiality in the alignments of the dyes.

Plotting the calculated overall dichroic order parameters in Table 5.9 against the experimental values, as shown in Figure 5.17 shows that this method provides an improvement in the linear correlation between calculation and experiment over that obtained when assuming the TDM vectors to be fixed against the principal molecular axes, illustrated by the higher value of $R^2 = 0.9466$ than that of 0.9211 in Figure 5.14. Additionally, the intercept of the fit is significantly lower, at 0.296 compared to 0.549 obtained previously, and the gradient of 0.815 is closer to 1 than that of 0.465 calculated previously showing a better match of the calculated values with the experimental values using this method.

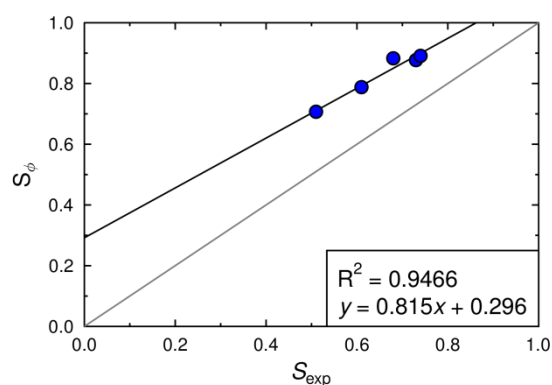


Figure 5.17 Plot of calculated order parameters, S_{ϕ} , obtained from the TDM orientations fixed against the anthraquinone cores during the MD simulations vs. experimental order parameters, S_{exp} .

5.2.4.4 Variable TDM orientations

In order to calculate the influence of specific molecular conformations on the TDM orientations without carrying out a TD-DFT calculation for each molecule at each frame of the trajectory, the conformations adopted during the MD simulations were analysed to determine the most flexible structural units, and thus the structural units responsible for the most significant variation in molecular conformations could be identified. Histograms of all of the dihedral angles within the dye molecules, excluding those involving hydrogen atoms and the alkyl chains, which were considered unlikely to have a significant influence on the TDM orientations, were analysed over the course of the

trajectories. Dihedral angles for which population distributions exhibited peaks with full width at half maximum (FWHM) values $> 20^\circ$ are shown on the structures of the dyes in Figure 5.18. The population maxima and FWHM values for these dihedral angles are listed in Table 5.10, alongside ranges either side of the peaks that were calculated to contain 95% of the populations over the course of each simulation. Dihedral angle populations of 15SB3, 15NB3 and 15NB3OH labelled ψ_2 in Figure 5.18 and the labelled dihedrals of 26B3 and 26B3OH were analysed between 0° and 180° , because the molecular symmetries meant that angles between 180° and 360° represent equivalent structures. Dihedrals $>180^\circ$ were subtracted from 360° for analysis.

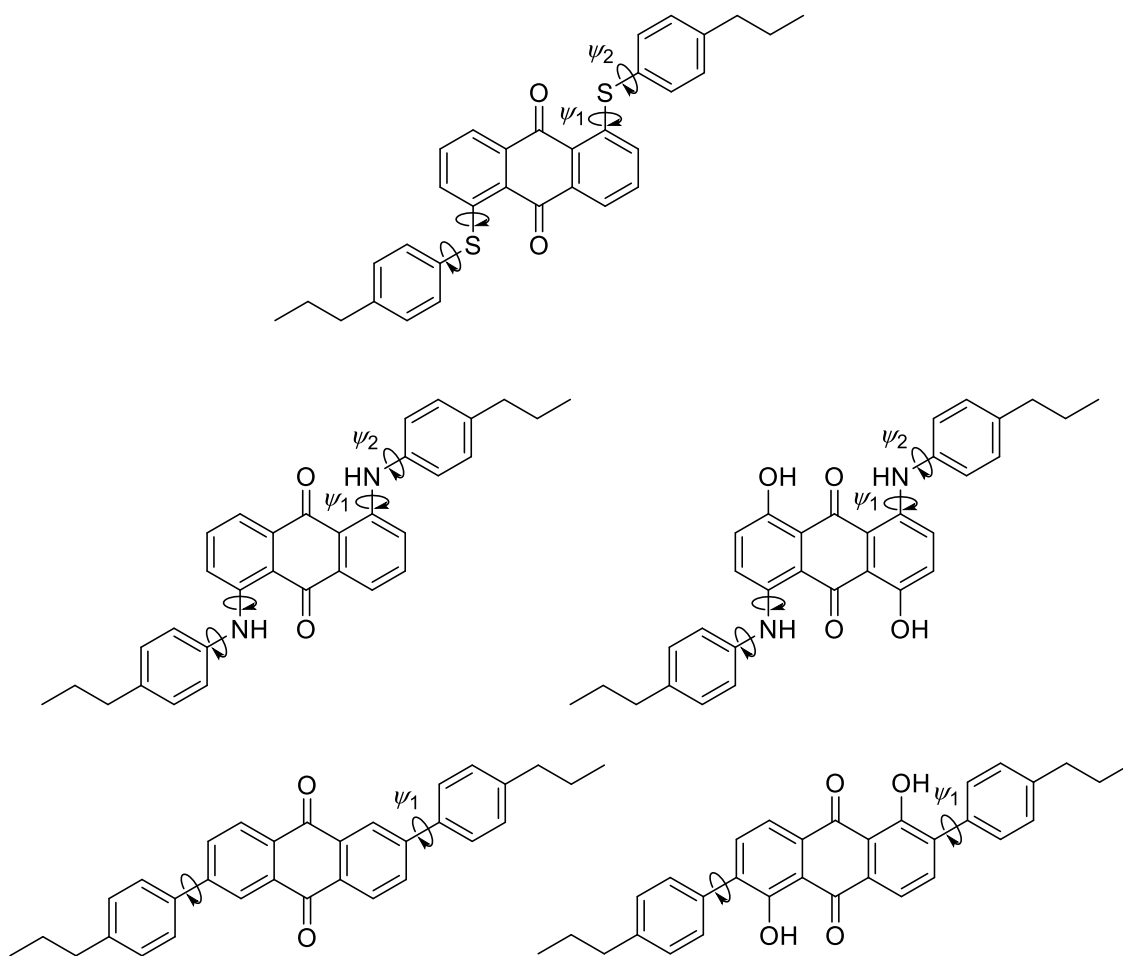


Figure 5.18 Structures of the dyes with labels indicating bonds about which the dihedral angle distributions were calculated to have a FWHM $> 20^\circ$ during the guest-host MD simulations.

Table 5.10 Most populated angles and associated FWHM values and ranges containing 95% of the populations for the dihedrals of the dyes labelled in Figure 5.18.

	ψ_1			ψ_2		
	Angle / °	FWHM / °	95%	Angle / °	FWHM / °	95%
15SB3	180	22	163-197	90	35	60-120
15NB3	180	30	151-209	90	70	33-147
15NB3OH	180	31	148-212	90	74	31-149
26B3	33, 147	23	10-56, 124-170	-	-	-
26B3OH	46, 134	22	23-69, 111-157	-	-	-

Histograms of each of the angles shown in Figure 5.18 are presented in Figure 5.19. For each population peak, five angles were defined, corresponding to the minimum and maximum of the angle range containing 95% of the population (listed in Table 5.10), and three angles evenly spaced between them, the middle of which corresponded to the most populated angle. These angles are shown as dots on the respective histograms in Figure 5.19 and were used to define geometries for TD-DFT calculations, which were carried out for all combinations of these dihedral angles for each dye. Thus, calculated visible transition dipole moments were obtained for 625 conformers of each of the model compounds 15SB0, 15NB0 and 15NB0OH, and 100 conformers of 26B1 and 26B1OH. For each TD-DFT calculation, the fully relaxed optimised structure was used, except for the dihedral angles specified above, which were rotated to their respective angles. For each geometry, the TDM orientation was defined as a scaled addition of the AQ, CO and ORTH unit vectors, using the same method as for those of the optimised structures listed in Table 5.7.

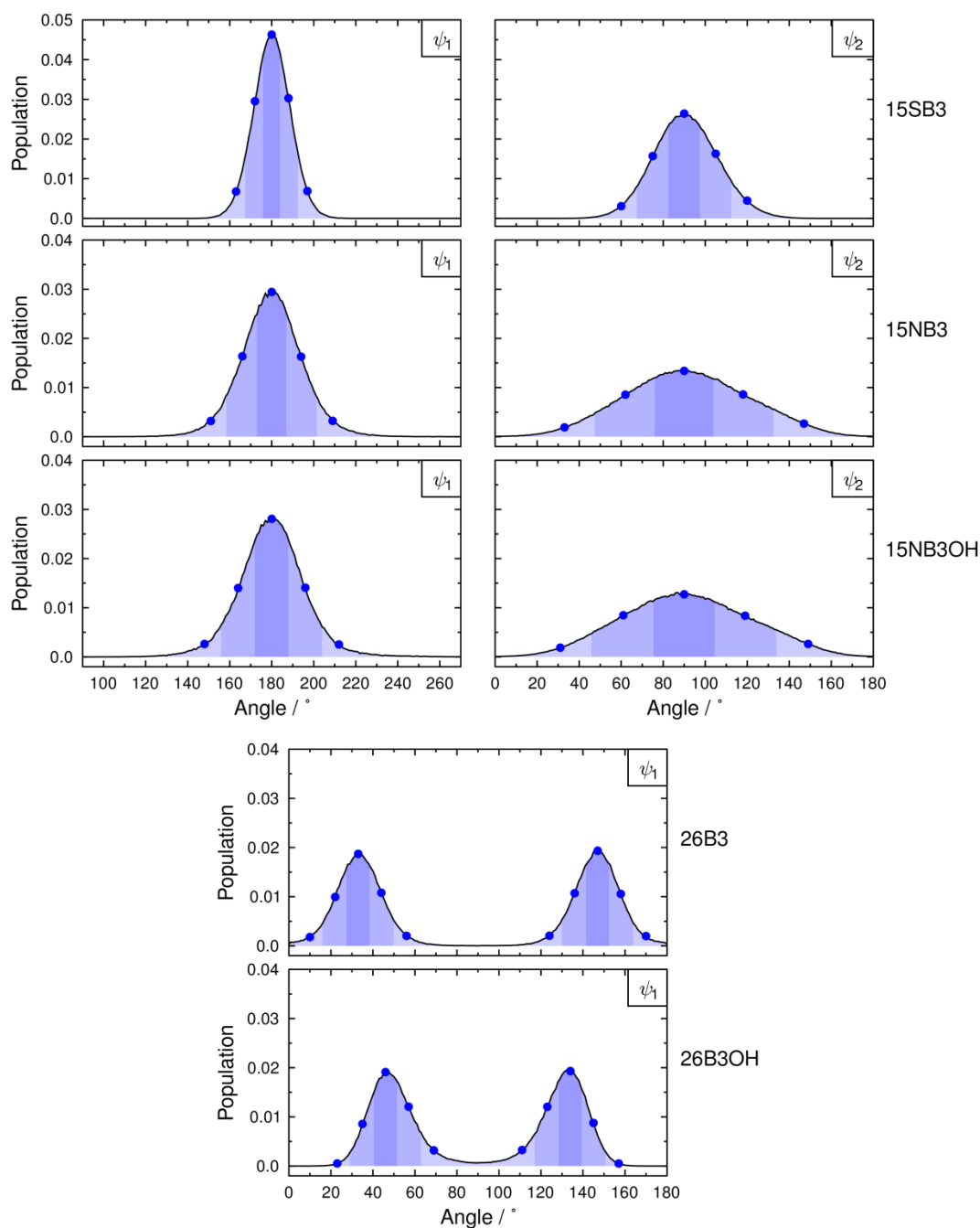


Figure 5.19 Plots of dihedral angle populations from the MD simulations for the dihedral angles labelled in Figure 5.18 with 1° histogram bin-widths. Angles used in geometries for the TD-DFT calculations of the TDM orientations are marked with blue dots. Shaded regions represent the “bins” used when assigning geometries from the MD trajectories to those for which the TDM orientations were calculated.

“Bins” were then defined around the angles used for the TD-DFT calculations, shown as shaded regions in Figure 5.19 and listed in Table 5.11, enabling each dye structure from each frame of each MD trajectory to be matched with the closest geometry for which a TD-DFT calculation had been carried out, i.e. one from a set of 625 or 100. The TDM of the dye structure from the MD trajectory could then be defined as a scaled

addition of the respective AQ, CO and ORTH unit vectors, using the nAQ, nCO and nORTH values determined for the matched geometry.

Table 5.11 Limits of the bins used to assign dye conformers in the MD simulations to those for which TD-DFT calculations had been run. The values correspond to the boundaries between shaded regions in Figure 5.19.

Dye		Dihedral bin limits / °										
15SB3	ψ_1	0	167.25	175.75	184.25	192.75	360					
	ψ_2	0	67.5	82.5	97.5	112.5	180					
15NB3	ψ_1	0	158.25	172.75	187.25	201.75	360					
	ψ_2	0	47.25	75.75	104.25	132.75	180					
15NB3OH	ψ_1	0	156	172	188	204	360					
	ψ_2	0	47.75	72.25	104.75	134.25	180					
26B3	ψ_1	0	15.75	27.25	38.75	50.25	90	129.75	141.25	152.75	164.25	180
26B3OH	ψ_1	0	28.75	40.25	51.57	63.25	90	116.75	128.25	139.75	151.25	180

Figure 5.20 shows the structures used for the TD-DFT calculations of different conformations, with the torsion angles that were varied to obtain the different conformations fixed at their most populated values from the MD simulations, and viewed along the ORTH axes. The overlaid visible TDM vectors were calculated as scaled additions of the AQ, CO and ORTH unit vectors. TDMs from conformations corresponding to <5% of the populations determined from the MD simulations are omitted to ensure the TDM vectors shown are representative of the commonly explored conformations during the MD trajectories. TDM orientations defined using this method are later termed “binned TDM axes”.

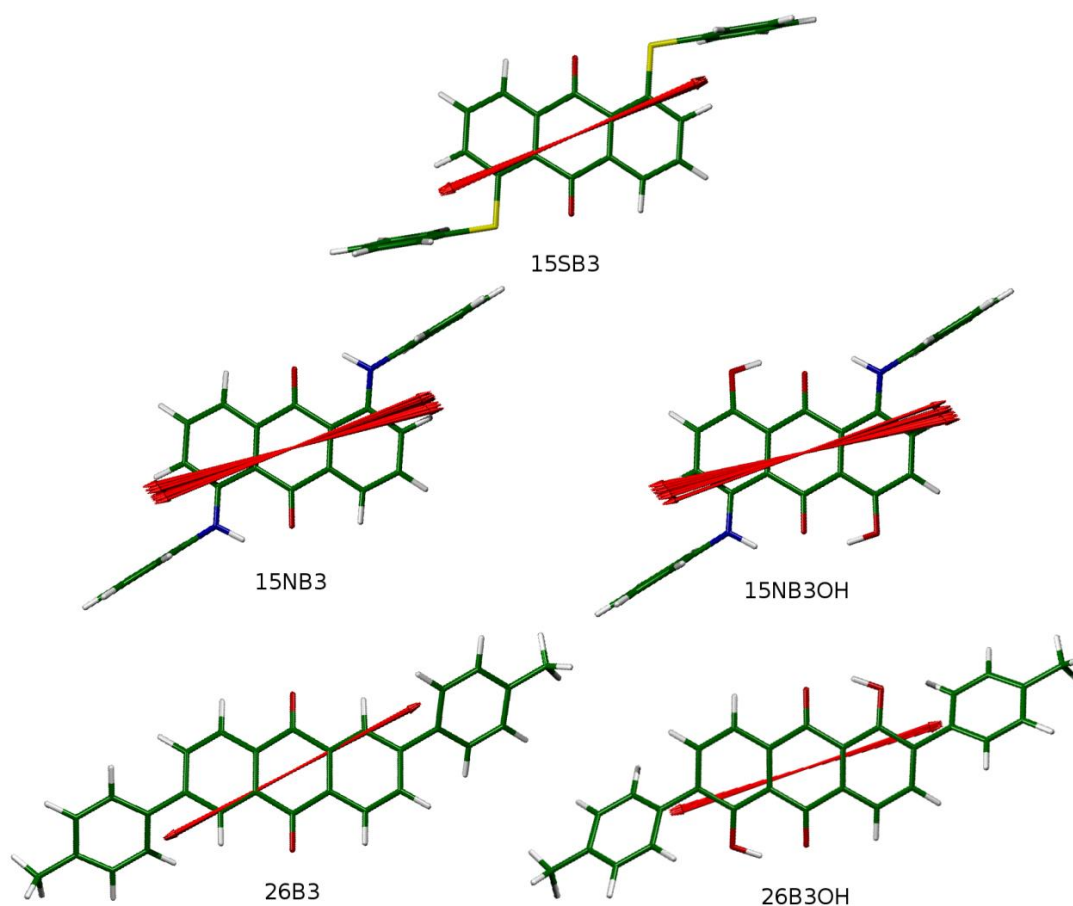


Figure 5.20 Views along the ORTH axes of structures used for calculating the influence of molecular conformation on the TDM orientations, with dihedral angles fixed at the most populated angles during the MD simulations. Red arrows are overlaid showing the orientations of the calculated TDMs, defined by scaled additions of the AQ, CO and ORTH unit vectors. TDM arrows are all of equal length, and the TDMs from conformations corresponding to <5% of the populations determined from the MD simulations are omitted here.

A qualitative analysis of Figure 5.20 shows that the calculated TDM orientations vary in the plane of the anthraquinone core most significantly for 15NB3 and 15NB3OH, that they exhibit slight variation for 15SB3 and 26B3OH, and that the least variation is exhibited by 26B3. This variation is consistent with the relative molecular flexibilities, which are calculated to be greatest for the two amine dyes, as is evident from the dihedral distributions shown in Figure 5.19. The views of the structures and the visible TDM vectors viewed along the CO axes are shown in Figure 5.21, and they indicate that the amine dyes exhibit the largest range of TDM orientations out of the plane of the anthraquinone core. Slight out-of-plane variation is observed for 15SB3, whereas almost none is observed for 26B3 and 26B3OH, which may be attributable to the directly attached phenyl substituents on the 2,6-disubstituted dyes, which do not have the out-of-plane flexibility provided by the torsions about the substituent bonds present in the 1,5-disubstituted dyes.

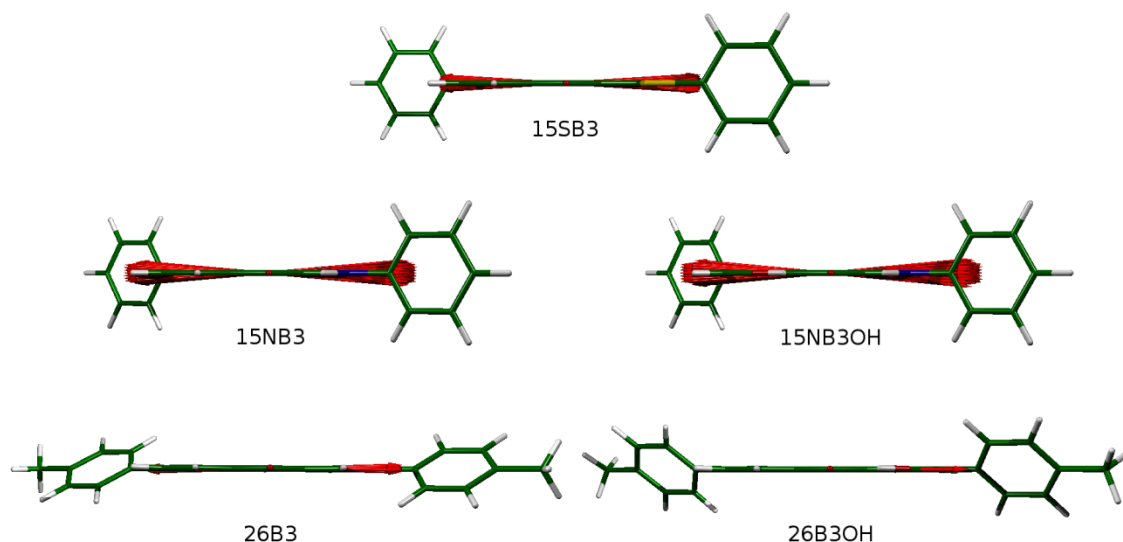


Figure 5.21 Views along the CO axes of structures used for calculating the influence of molecular conformations on the TDM orientations, with dihedral angles fixed at the most populated angles during the MD simulations. Red arrows are overlaid showing the orientations of the calculated TDMs, defined by scaled additions of the AQ, CO and ORTH unit vectors. TDM arrows are all of equal length, and the TDMs from conformations corresponding to <5% of the populations determined from the MD simulations are omitted here.

The average angles, $\langle\beta\rangle$, and associated average order parameters, $\langle S_\beta\rangle$, are listed in Table 5.12, indicating that 15SB3, 26B3 and 26B3OH exhibit remarkably similar calculated average β angles, and the angles obtained from TDM orientations determined from the binned structures described in terms of the AQ, CO and ORTH vectors are all within 0.4° of those determined from fixed TDM orientations, given in Table 5.9 for these dyes. 15NB3 and 15NB3OH have much larger calculated average angles between the surface vectors and projected TDM vectors than the other dyes, and using the binned TDM orientations, their β angles are 6.9° and 8.3° larger than those calculated using the fixed TDM orientations. The differences between the values obtained using the two approaches may be attributed to the greater range of TDM orientations exhibited by the amine dyes than the other dyes (see Figure 5.20 and Figure 5.21).

Table 5.12 Calculated angles, β and α , and their standard deviations, \pm , of the binned visible TDMs of the dyes. The associated biaxial terms and calculated overall dichroic order parameters, S_ϕ , are also listed.

Dye	$\langle\beta\rangle / ^\circ$	$\langle S_\beta\rangle$	$\langle\alpha\rangle / ^\circ$	$0.5\langle S_{xx}-S_{yy}\rangle\langle\sin^2\beta\cos 2\alpha\rangle$	S_ϕ
15SB3	5.3 ± 2.8	0.984	79.6 ± 60.7	0.000	0.880
15NB3	20.9 ± 5.5	0.799	16.1 ± 26.5	0.002	0.701
15NB3OH	27.7 ± 6.1	0.667	9.4 ± 6.5	0.003	0.576
26B3	5.3 ± 2.7	0.984	119.5 ± 47.6	0.000	0.885
26B3OH	5.3 ± 2.9	0.984	61.9 ± 51.1	0.000	0.890

The average values of the α angles and the biaxial terms of the dichroic order parameters, also listed in Table 5.12, indicate that the only influence of biaxiality is calculated for the two amine dyes, and that this is only slight. The calculated biaxial terms in Table 5.12 may be rationalised in terms of the larger β angles of 15NB3 and 15NB3OH than the other dyes causing the $\sin^2\beta$ term to be largest for the two amine dyes, although the biaxial terms of the dichroic order parameters are very small, which may be largely attributed to the small values of $\langle S_{xx} - S_{yy} \rangle$ (given in Table 5.4).

The calculated overall order parameters, S_ϕ , using the binned TDM orientations given in Table 5.12 show significantly more variation between the dyes than those calculated using the MOI axes and the surface axes with the assumption of the TDM vectors being fixed against the alignment axes, given in Table 5.9. A plot of the S_ϕ values given in Table 5.12 against S_{exp} , shown in Figure 5.22, demonstrates that by removing the constraint of TDM vectors being fixed against the principal surface axes of the dyes results in a comparable linear correlation between calculated and experimental order parameters, with R^2 values from the two methods differing by just 0.0074. However, the most noticeable difference is the reduction in the calculated order parameters of 15NB3 and 15NB3OH, bringing them closer to the values obtained experimentally, resulting in the fitted line showing a larger gradient and smaller negative intercept than that obtained from the analysis when the TDM orientations were assumed to be fixed against the anthraquinone core.

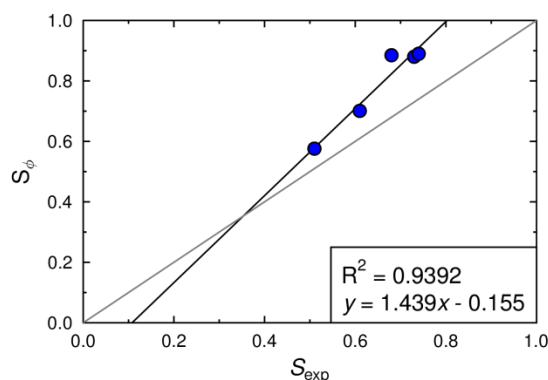


Figure 5.22 Plot of calculated order parameters, S_ϕ , obtained from the binned TDM orientations during the MD simulations vs. experimental order parameters, S_{exp} .

5.3 Conclusions

Analysis of the guest-host MD simulations using a variety of definitions of the principal alignment axes of the dyes demonstrated that the minimum MOI axes were not the best description of the principal molecular alignment axes in these systems, and that the axes defined by the surface tensor approach provided the best description obtained from first principles for this set of dyes in E7. The use of this axis definition was also supported by analysis of a simulation of the host alone, for which the surface tensor axes were shown to be better aligned than the minimum MOI axes. Investigation of the alignment of the secondary and tertiary surface axes indicated slight biaxiality in the molecular alignment of the dyes, and this effect was calculated to be slightly greater for the 1,5-disubstituted dyes than the 2,6-disubstituted dyes.

Recalculated dichroic order parameters using the surface tensor axes as the principal molecular axes resulted in an improvement in the match between calculated and experimental values over that obtained using the minimum MOI axes, providing evidence to support the use of the surface tensor axes in considering molecular alignment. The use of the surface tensor approach in defining alignment axes is not widely adopted in the literature, but the work presented here provides experimental evidence for the validity of this approach over alternative, more widely used methods.

TDM orientations considered in the context of dye flexibility and the range of molecular conformations explored during the MD simulations, rather than simply considering single optimised structures, provided further improvement in the match between calculated and experimental order parameters, highlighting the limitations of using minimum energy structures in the analysis of such systems. Further, the match between calculated and experimental dichroic order parameters was improved when the assumption of the TDMs orientations being fixed against the anthraquinone cores was removed.

Incorporating molecular biaxiality into the theoretical treatment of the dichroic order parameters provided very little difference in the calculated alignment, but did suggest that the influence of biaxiality is greatest for the amine dyes of the set studied in this work. However, such a small influence cannot be assumed in a general case, and such a

small difference in this case may additionally be partially attributable to the overestimation of the molecular alignment in the guest-host simulations carried out here.

Confidence in the calculations and analysis presented here is given by the observation that each time the methods were extended to include more detail or to remove a previous assumption, notably without incorporating any parameterisation against experimental values, a better match between calculated and experimental values was obtained. This trend indicates that previous assumptions in the theoretical treatment of fixed TDM orientations within dyes in guest-host mixtures may not be justifiable in all cases, and that inclusion of molecular flexibility and its influence on TDM orientations may be required to accurately replicate or predict experimental alignment trends.

Chapter 6

Isolated molecule studies

6.1 Introduction

The focus of this chapter is on the application of the surface tensor model to calculating the alignment of dyes in nematic hosts, through applying a mean-field approach in which only a single isolated molecule needs to be considered, rather than through the simulation of a full guest-host mixture. In this introduction, a brief outline of mean-field theory in general is given, before some of the literature concerning the calculation of order parameters by applying the surface tensor model is discussed. This is followed by an introduction to the applications of ab-initio molecular dynamics methods within the context of molecular structure and conformations, and the section concludes with an outline of the aims of the work presented in this chapter.

6.1.1 Mean field theory and the surface tensor method

The elastic tube and surface tensor approaches presented in the introduction to Chapter 5 are both examples of applications of mean field theory, which, in general, applies the concept that any given molecule in a system experiences an average potential arising from all the other molecules in the system. This concept may be extended to assume that the potential experienced by any given molecule is the same as that experienced by any other molecule in the system. If such a potential is known or, as in the case of the examples in Chapter 5, is defined for a system, then the average behaviour of a single molecule may be assumed to match that of the behaviour averaged over all molecules.^{38, 280} Thus, calculations for a single molecule may be applied to all the molecules in a system to obtain the bulk properties of the system, such as the order parameter in the context of the various models in Chapter 5. If such a theoretical approach provides a good match with experimental measurements, it may be very powerful, because the significant user-input and computational expense required to model large numbers of individual molecules explicitly are avoided. This expense can prove prohibitive to the simulation of large systems, as discussed in the context of

molecular dynamics simulations in Chapter 4, and mean-field theory can provide a method of modelling a system using a level of theory that is otherwise unfeasible.

As discussed in Chapter 5, the surface tensor method assumes that the potential acting on a molecule is determined by the anisotropy of the molecular shape. In the context in which it was applied in Chapter 5, the surface tensor of a molecule was simply used to define a set of principal molecular axes that were then used to analyse the output from the MD simulations, but much of the literature employing the surface tensor approach uses the model to predict the orientational order parameters of both guest molecules and host molecules directly from the surface tensor itself. Details of the specific steps by which such order parameters may be calculated using this method are given in Section 5.1.3.3 of Chapter 5.

Rigid solute molecules within nematic hosts are typically considered to maintain a single conformation, and order parameters of such compounds calculated from their surface tensors have been shown to provide a close match with experimental values from NMR studies,²⁹⁷ as illustrated by the examples given in Table 6.1 and shown by the plot in Figure 6.1. In the work reported here, S_{zz} will be used to define an order parameter determined from a mean field approach, in order to differentiate from the equivalent order parameter, S_θ , defined from sets of axes against a host director.

Table 6.1 Experimental order parameters of solute molecules dissolved in nematic hosts alongside calculated values obtained using the surface tensor model, using an orienting potential of $\varepsilon = 0.05 \text{ \AA}^{-2}$.²⁹⁷

Solute	S_{zz} (exp.)	S_{zz} (calc.)
4-Cyano-4'-methylbiphenyl	0.571	0.530
1,4-dibromobenzene	0.357	0.292
Iodobenzene	0.239	0.209
1,2-dichlorobenzene	0.160	0.171
1,3-chlorobromobenzene	-0.223	-0.225

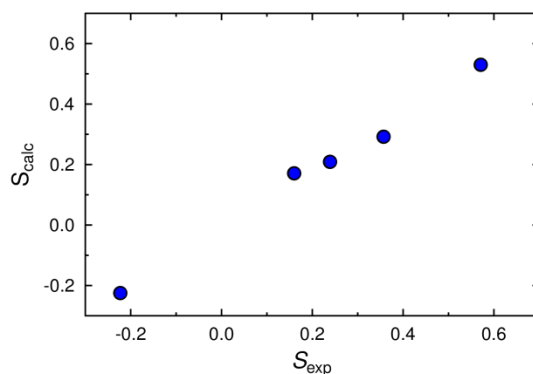


Figure 6.1 Plot of calculated order parameters, S_{calc} , obtained using the surface tensor model for the compounds listed in Table 6.1 vs. experimental order parameters, S_{exp} .

The surface tensor approach may also be applied to more flexible structures by calculating the order parameters of specific conformers and summing them with consideration to their statistical weights. The application of this approach to a series of deuterated alkanes has yielded a remarkable match between calculated values and experimental values obtained from NMR experiments, as listed in Table 6.2, although a range of ϵ values have been applied to achieve this match.²⁹⁷

Table 6.2 Experimental order parameters of CD bonds of alkanes dissolved in a nematic host, and calculated values obtained using the surface tensor model.²⁹⁷

Compound		Experimental	Calculated
n-Pentane ^a	$S_{\text{CD}}(1, 5)$	-0.0317	-0.0311
	$S_{\text{CD}}(2, 4)$	-0.1067	-0.1067
	$S_{\text{CD}}(3)$	-0.1118	-0.1119
n-Hexane ^b	$S_{\text{CD}}(1, 6)$	-0.0391	-0.0414
	$S_{\text{CD}}(2, 5)$	-0.1181	-0.1179
	$S_{\text{CD}}(3, 4)$	-0.1330	-0.1340
n-Heptane ^c	$S_{\text{CD}}(1, 7)$	-0.0377	-0.0368
	$S_{\text{CD}}(2, 6)$	-0.1297	-0.1286
	$S_{\text{CD}}(3, 5)$	-0.1464	-0.1456
	$S_{\text{CD}}(4)$	-0.1548	-0.1541

^a $\epsilon = 0.062 \text{ \AA}^{-2}$, ^b $\epsilon = 0.065 \text{ \AA}^{-2}$, ^c $\epsilon = 0.067 \text{ \AA}^{-2}$,

The surface tensor approach has also been applied to host molecules, such as deuterated 5CB; order parameters of the CD bonds in the aromatic rings and in the positions 1-5 along the alky chain were calculated as weighted averages of those obtained from the optimised structures of 27 different conformations, and are listed in Table 6.3.³⁰¹ Again, the order parameters obtained from the surface tensor model provide a close match with the experimental values determined from NMR experiments.

Table 6.3 Experimental order parameters of CD bonds in the aromatic rings of 5CB and in the 1-5 positions along the alkyl chains obtained from NMR experiments, and calculated order parameters obtained using the surface tensor model ($\epsilon = 0.05 \text{ \AA}^{-2}$).³⁰¹

C-D bonds						
	Aromatic	C1	C2	C3	C4	C5
Exp.	-0.044	-0.202	-0.137	-0.147	-0.099	-0.072
Calc.	-0.041	-0.200	-0.132	-0.144	-0.105	-0.078

These studies, of both guest and host molecules, provide examples of the predictive capability of the surface tensor approach for modelling molecular alignment within both single-component liquid crystal systems and in guest-host systems, using only the molecular structures of the constituent molecules combined with an orienting potential.

6.1.2 Ab initio molecular dynamics

The molecular dynamics simulations described and analysed in Chapters 4 and 5 were all based on fully classical force fields, because the number of atoms in the simulations were prohibitive to modelling the systems using quantum chemical approaches. However, when applying a mean-field approximation to molecular alignment of a solute in a nematic host, such as that described above, the analysis of only an individual molecule is required. This reduction in the required system size drastically reduces the computational expense of simulations using an equivalent level of theory, and therefore enables the use of significantly higher levels of theory to be applied.

As discussed in section 1.5.6 in Chapter 1, classical molecular dynamics simulations use force fields to describe inter- and intramolecular interactions, applying the assumption of the transferability of these interaction potentials between chemically similar systems. This assumption may only be avoided by parameterisation of force constants for a specific system, such as those described in Section 4.3.2.2 in Chapter 4, which is typically a non-trivial process. However, the use of ab-initio molecular dynamics (AIMD) removes the need for classical force fields altogether, providing a method which has much greater objective transferability than classical MD, and therefore may be considered more desirable, where possible, than the use of classical MD simulations.

In the context of the mean-field treatment of guest molecules outlined in Section 6.1.1, a crucial requirement of any method based on molecular shape is the sampling of an

appropriate set of molecular geometries. There are a number of reported ab-initio molecular dynamics studies relating specifically to the study of molecular conformations at non-zero temperatures, such as the study of conformations of small molecules in biological contexts,^{322, 323} and the temperature dependence of molecular conformations adopted by ethyl propionate, of industrial interest,³²⁴ that show such simulation methods can provide good matches with those indicated by experimental spectroscopy.

More closely related to the work reported here are AIMD studies concerning the structure and properties of dye molecules, reports of which typically analyse molecular conformations in the context of ensuring that representative molecular geometries are used for the calculation of electronic transition energies. The solvatochromism of several dye molecules has been rationalised using AIMD through characterisation of solvent-induced structural variation in dye molecules,³²⁵⁻³²⁷ and these studies have highlighted the potential limitations of transition energies calculated from minimum energy structures. Improved matches with experimental spectra over previous studies have been partially attributed to the consideration of room temperature molecular conformations, matching experimental conditions.³²⁸⁻³³⁰

6.2 Aims

The analysis of possible alignment axes of the dyes during the guest-host MD simulations, reported in Chapter 5, indicated that the surface tensor approach gave the best definition from first principles of the methods tested. The aim of the work presented in this chapter was to extend this surface tensor approach from defining axes in the guest-host MD simulations to calculating the molecular alignment order parameters of the dyes from the surface tensors alone. The aim of taking this approach was to explore whether molecular alignment trends between the dye molecules could be determined by considering single dye molecules, rather than by using the large guest-host MD simulations reported in Chapter 4. Such an approach would offer the benefit of much shorter simulation times than required by the large guest-host simulations, making it more practical for predictive studies, and potentially providing scope for using *ab-initio* molecular dynamics to determine the molecular conformations of the dye molecules, thereby avoiding the various assumptions made in the classical molecular dynamics simulations. The intention was to compare the results of the isolated molecule studies with those of both the guest-host MD simulations and the experimental order parameters, in order to assess the suitability of these different approaches.

6.3 Results and discussion

In the following sections three different approaches to calculating dichroic order parameters from the surface tensor approach are presented and assessed. Firstly, classical MD simulations of the isolated dye molecules are presented and discussed. Secondly, AIMD simulations of the isolated dye molecules are reported and analysed, and thirdly a similar analysis of single DFT optimised structures of the dyes is then presented. Finally, an overall comparison of the methods presented in this Chapter and in Chapter 5 is made.

6.3.1 Classical MD simulations

MD simulations of single isolated dye molecules were carried out, each was run for 10 ns, and the analysis presented here was carried out over the full trajectories. The simulations were carried out in the same way as those presented in Chapter 4, but using single dye molecules and no host molecules. Further details of the simulation parameters are given in Chapter 2.

The initial analysis carried out was intended to assess any differences between the molecular conformations explored within the guest-host and isolated molecule MD simulations. The analysis in Section 5.2.7.2 of Chapter 5 identified dihedral angle distributions that were shown to be most flexible during the guest-host simulations. Populations about these same dihedral angles (shown again for clarity in Figure 6.2) from the isolated molecule MD simulations are shown in Figure 6.3, alongside the equivalent distributions obtained from the guest-host simulations. The population maxima and associated full-width-half-maxima of the plotted populations from the isolated molecule simulations are listed in Table 6.4.

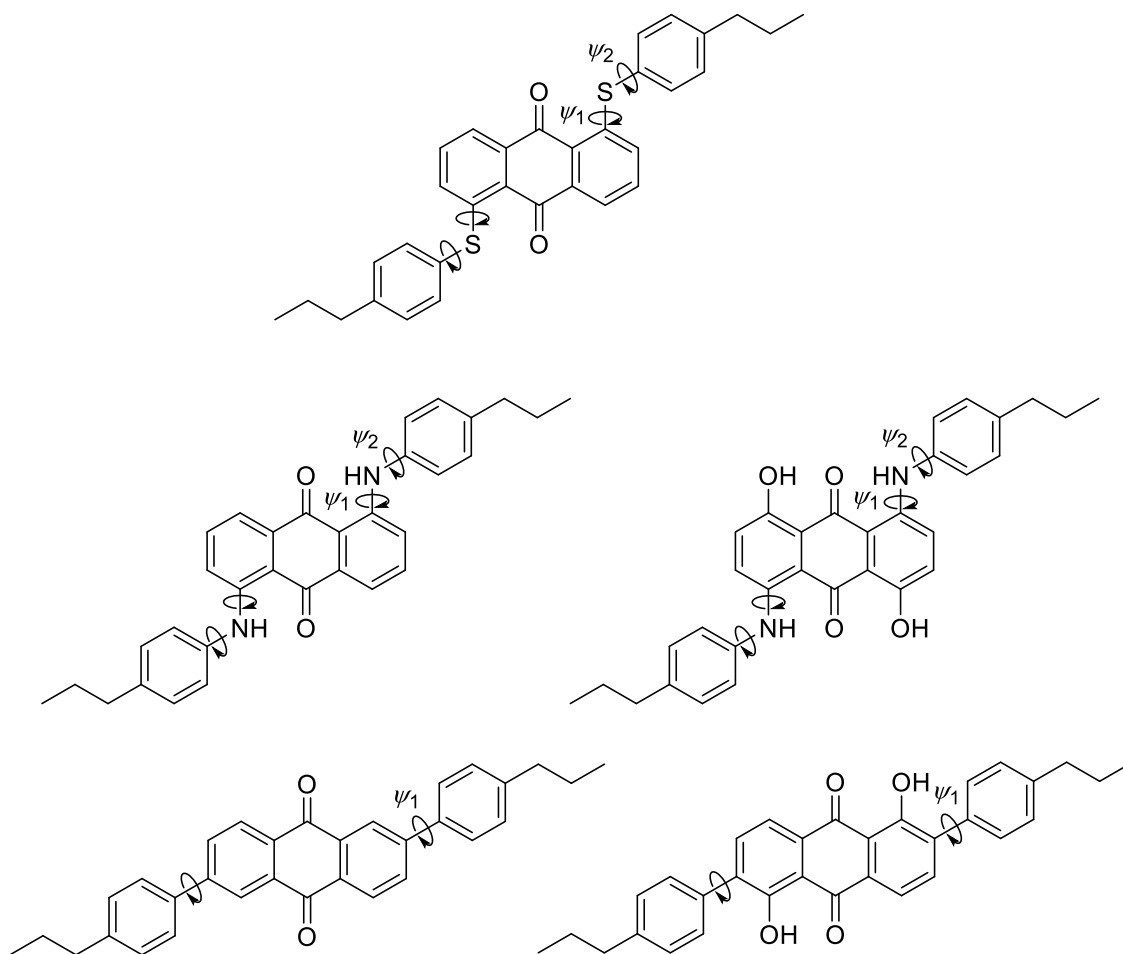


Figure 6.2 Structures of the dyes with labels indicating bonds about which the dihedral angle distributions were calculated to have a FWHM $> 20^\circ$ during the guest-host MD simulations, used for analysis of the isolated molecule MD simulations.

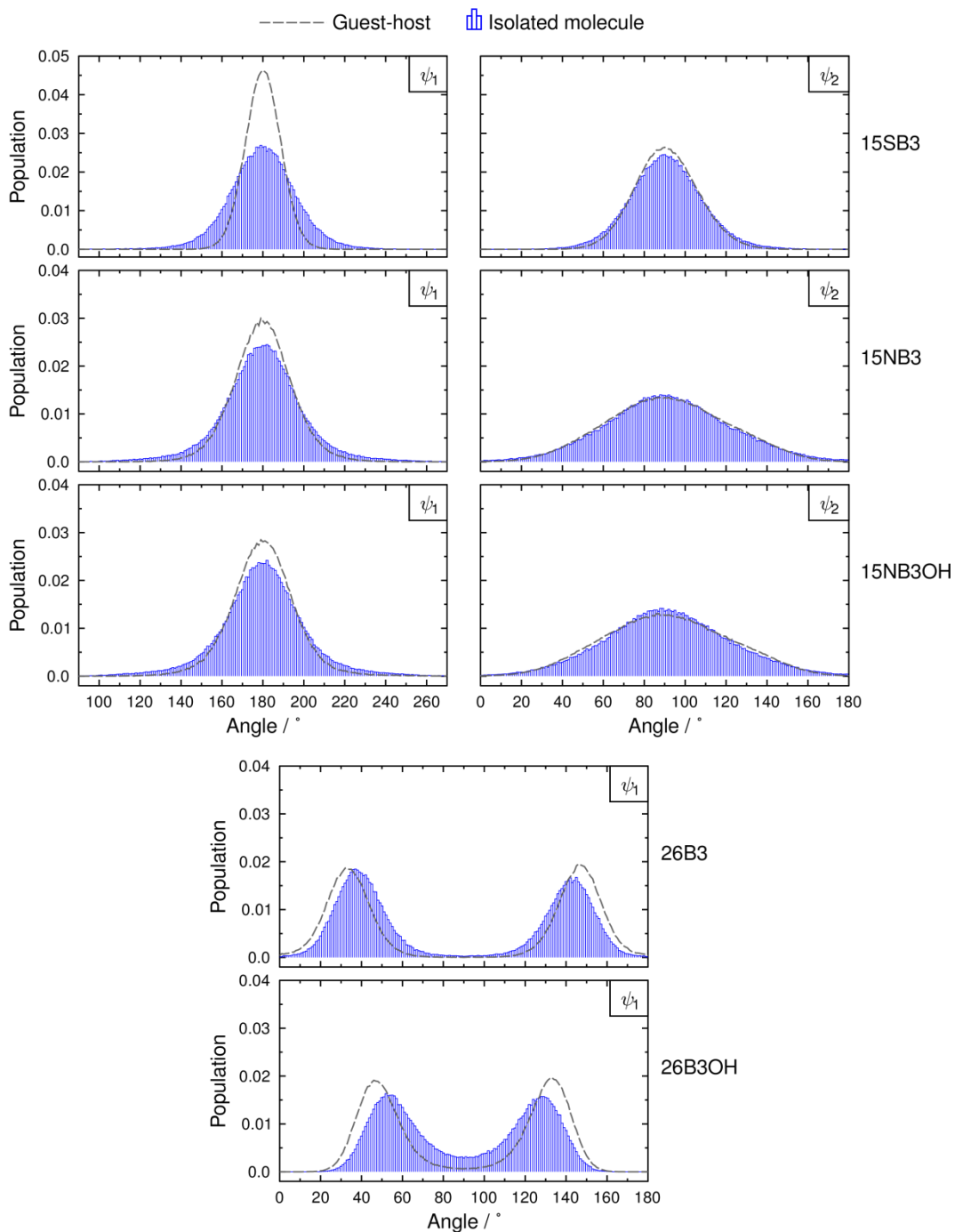


Figure 6.3 Plots of populations for the dihedral angles labelled in Figure 6.2 obtained from the the isolated molecule simulations (blue bars) and the guest-host MD simulations (dashed grey lines) using 1° bin widths.

For 15SB3, 15NB3 and 15NB3OH, the population distributions about dihedrals ψ_1 , representing torsion about the C-X bonds in the 1,5 positions on the anthraquinone core are centred about 180° from both sets of simulations, but the spread of ψ_1 angles is larger in each of the isolated molecule simulations than in the respective guest-host

simulations, shown in Figure 6.3 and by the differences in the FWHM values in Table 6.4. Differences in the populations of the ψ_1 dihedrals obtained for 26B3 and 26B3OH between the two types of simulation are also evident, and the most populated angles in Table 6.4 indicate that the planes of the phenyl substituents tend to orient further from parallel with the plane of the anthraquinone core during the isolated molecule simulations than the guest-host simulations. These differences may be attributed to a constraining influence of the nematic E7 host present in the guest-host simulations, resulting in the conformations explored in the isolated molecules to be less rod-like than those explored in the guest-host simulations, discussed further below.

Table 6.4 Most populated angles and associated FWHM values for the dihedrals of the isolated dye molecules labelled in Figure 6.2. Δ values indicate the differences between these there and the equivalent angles from the guest-host MD simulations given in Table 5.10.

Dye	ψ_1				ψ_2			
	Angle / °	Δ	FWHM / °	Δ	Angle / °	Δ	FWHM / °	Δ
15SB3	180	+0	33	+11	90	+0	37	+2
15NB3	180	+0	35	+5	90	+0	63	-7
15NB3OH	180	+0	35	+4	90	+0	64	-10
26B3	37, 143	+4, -4	27	+4	-	-	-	-
26B3OH	53, 127	+7, -7	28	+6	-	-	-	-

The distributions of the ψ_2 dihedral angles in Figure 6.3 indicate that there is very little difference between the distributions obtained from the guest-host simulations and the isolated molecule simulations, suggesting these torsions are less influenced by the presence of host molecules than the ψ_1 torsions discussed above. This consistency is also evident from the most populated angles listed in Table 6.4, and the differences in FWHM values may be attributed to the relatively broad distributions about ψ_2 .

Although some differences are evident between the two sets of simulations, the highlighted differences are relatively subtle, with population maxima shown to be either identical or similar between the simulations, and the dihedral angles selected here were those for which the widest ranges of angles were explored. The subtleties of the differences observed, combined with visual inspection of the trajectories, which showed that the general molecular conformations explored were similar between the guest-host and isolated molecule simulations, suggest that the conformers obtained from the isolated simulations are broadly representative of those explored by the dyes in the host.

6.3.1.1 Surface tensor analysis and molecular alignment

Prior to analysing the isolated molecule MD simulations, surface tensor analysis of the guest-host MD simulations reported in Chapter 4 was carried out using the method described in Chapter 5, enabling the eigenvalues of the surface tensor \mathbf{t} , to be determined for each dye at each frame of each MD trajectory. Average values of the inverse eigenvalues, $-t_{ii}$, relating to the surface areas of the molecules facing along axis i , as introduced in Chapter 5, and the total surface areas calculated as the sum of the inverse eigenvalues are listed in Table 6.5. These values provided a benchmark with which analysis of the isolated molecule simulations could be compared.

Table 6.5 Average inverse surface tensor eigenvalues, $-\langle t_{ii} \rangle$, and standard deviations obtained for the dye molecules during the guest-host MD simulations. The surface areas, SA, are also listed, calculated according to $SA = -\langle t_{xx} \rangle - \langle t_{yy} \rangle - \langle t_{zz} \rangle$.

Dye	$-\langle t_{xx} \rangle / \text{\AA}^2$	$-\langle t_{yy} \rangle / \text{\AA}^2$	$-\langle t_{zz} \rangle / \text{\AA}^2$	SA / \AA^2
15SB3	181.3 \pm 5.6	236.7 \pm 4.8	52.8 \pm 3.3	470.8
15NB3	172.3 \pm 6.7	229.9 \pm 6.8	54.7 \pm 3.9	456.9
15NB3OH	171.5 \pm 6.5	238.4 \pm 6.8	58.6 \pm 4.4	468.5
26B3	149.3 \pm 6.0	245.3 \pm 7.1	44.7 \pm 3.8	439.3
26B3OH	162.0 \pm 6.2	240.8 \pm 6.6	44.9 \pm 3.2	447.7

The values in Table 6.5 demonstrate that the surface tensor model shows the 2,6-disubstituted dyes to be the most rod-like, indicated by the relative values of $-t_{zz} \ll -t_{xx} < -t_{yy}$. The smaller surface areas facing the x -axes than the y -axes for each of the dyes are indicative of deviations from symmetry about the z -axis, and thus, are an indication of deviation from uniaxial molecular shape. A comparison of the standard deviations suggests the fluctuations of the surface tensor eigenvalues of the dyes, caused by variation in the molecular shapes, are generally consistent between the dyes. The generally slightly higher values of the standard deviations for 15NB3 and 15NB3OH may be attributable to the higher calculated flexibility of the amine-substituted dyes in comparison with the other three dyes, discussed in Section 4.3.2.2 of Chapter 4.

The inverse eigenvalues calculated from the isolated molecule MD simulations, determined in the same way as for the guest-host simulations, are plotted against time in Figure 6.4. These plots show that the eigenvalues fluctuate about constant values during the simulations, indicating that the molecular shapes explored are likely to be

representative of a statistical average, and providing support that the simulation times of 10 ns are sufficiently long.

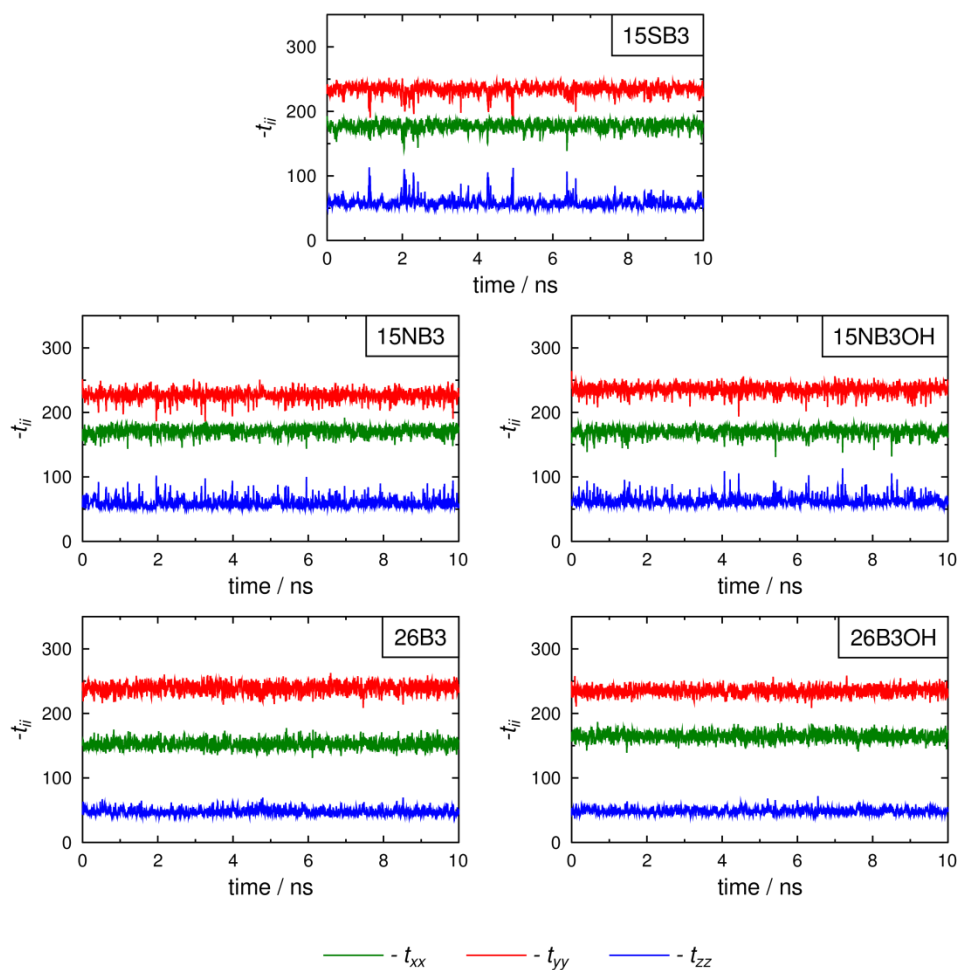


Figure 6.4 Inverse eigenvalues, t_{ij} , of the surface tensors, \mathbf{t} , obtained from the MD simulations of the isolated dye molecules. Eigenvalues at every 50th point of the trajectories are plotted for clarity.

The average eigenvalues, their standard deviations and the molecular surface areas from the isolated molecule MD simulations are listed in Table 6.6. The differences between these eigenvalues and those obtained from analysis of the guest-host MD simulations, also listed in Table 6.6, show that each of the dyes has a larger surface area facing the z -axis in the isolated molecule simulations than the guest-host simulations, consistent with the dyes being slightly less rod-like on average during the isolated molecule simulations than the guest-host simulations. This difference may again be attributed to the lack of host molecules resulting in less constrained dye geometries in the isolated molecule simulations, which may also account for the slight decrease in the surface area of each of the dyes facing the y -axis. However, these differences are slight: the $\langle t_{xx} \rangle$ and

$\langle t_{yy} \rangle$ values differ by *ca* 2% between the simulations, and the $\langle t_{zz} \rangle$ values differ by *ca* 6-9% between the simulations for each of the dyes.

Table 6.6 Average inverse surface tensor eigenvalues, $-\langle t_{ii} \rangle$, and standard deviations obtained for the dye molecules during the isolated molecule MD simulations. The surface areas, SA, are also listed, calculated according to $SA = -\langle t_{xx} \rangle - \langle t_{yy} \rangle - \langle t_{zz} \rangle$. Δ values in each case are calculated as the difference between the value obtained from the isolated molecule simulation and the respective value from the guest-host simulation.

Dye	$-\langle t_{xx} \rangle / \text{\AA}^2$	Δ	$-\langle t_{yy} \rangle / \text{\AA}^2$	Δ	$-\langle t_{zz} \rangle / \text{\AA}^2$	Δ	SA / \AA^2	Δ
15SB3	177.6 ± 7.1	-3.7	234.2 ± 7.6	-2.5	58.1 ± 7.5	+5.3	469.9	-0.9
15NB3	171.1 ± 6.9	-1.2	226.3 ± 7.7	-3.6	58.9 ± 7.0	+4.2	456.3	-0.6
15NB3OH	169.9 ± 6.8	-1.6	235.2 ± 7.5	-3.2	62.7 ± 7.0	+4.1	467.8	-0.7
26B3	152.3 ± 6.9	+3.0	239.4 ± 8.1	-5.9	47.7 ± 4.7	+3.0	439.4	+0.1
26B3OH	164.5 ± 6.8	+2.5	234.9 ± 6.9	-5.9	48.6 ± 4.3	+3.7	448.0	+0.3

Histograms of the surface tensor values obtained over the course of the two sets of simulations, shown in Figure 6.5, demonstrate that the trends between the eigenvalues of the dyes are consistent between the two simulations, indicating that the descriptions of the molecular shape provided by the two different simulations are likely to be consistent in the context of a comparison of the dyes.

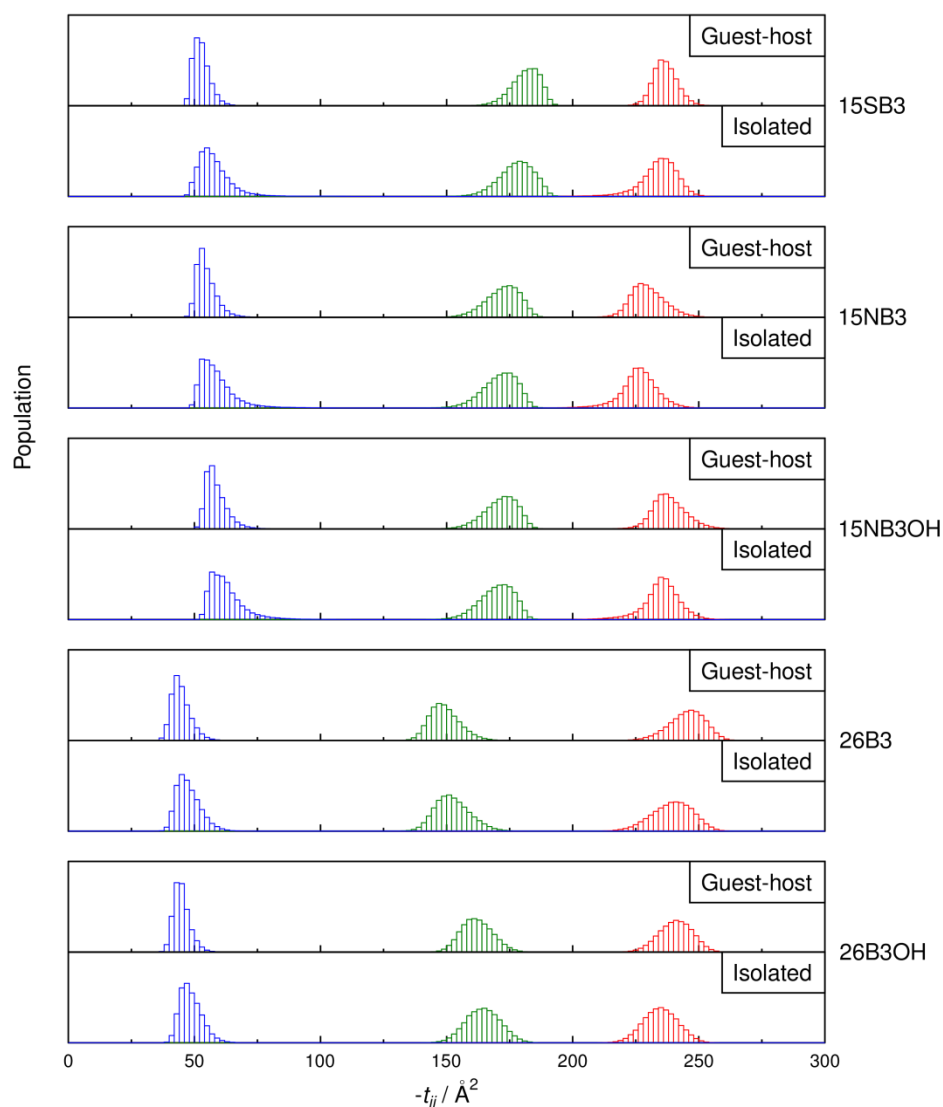


Figure 6.5 Histograms of the surface tensor eigenvalues measured during the guest-host and the isolated molecule MD simulations. t_{zz} values are shown in blue, t_{xx} values are shown in green, and t_{yy} values are shown in red using bin widths of 2\AA^2 .

As described in Chapter 5, the surface tensor model provides a simplification of a molecular structure to that of a cuboid with face areas of $-t_{xx}$, $-t_{yy}$, and $-t_{zz}$. Cuboids constructed from the average eigenvalues during the isolated molecule simulations are shown in Figure 6.6, and comparison of these cuboids shows the most rod-like structures to be the two 2,6-disubstituted dyes, whereas the two amine dyes are shown to be the least rod-like.

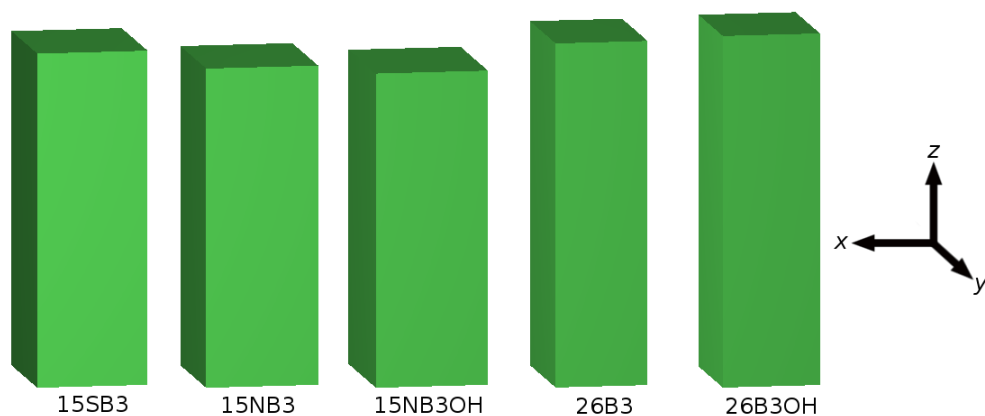


Figure 6.6 Cuboids, drawn to scale, with face areas proportional to $-t_{xx}$, $-t_{yy}$, and $-t_{zz}$, of each of the dyes, as determined from the MD simulations of isolated molecules.

6.3.1.2 Molecular alignment order parameters

For each trajectory frame of the isolated molecule MD simulations, the order parameters, S_{zz} and $S_{xx} - S_{yy}$, were calculated from the t_{ii} values using the approach outlined in the introduction to Chapter 5. The average values of these order parameters from the isolated molecule simulations, obtained by using an orienting strength of $\varepsilon = 0.04 \text{ \AA}^{-2}$ shown to be typical for nematic liquid crystals,³⁰¹ are listed in Table 6.7. A comparison with the order parameters obtained from the principal surface tensor axes within the guest-host simulations, described in Chapter 5, and listed in Table 6.7 for comparison, shows that the general trend in the S_{zz} values between the dyes calculated from the surface tensors from the isolated molecule simulations matches that of the order parameters of the surface tensor axes against the host director in the guest-host simulations. The uniformly higher values obtained from the guest-host simulations may be attributable to the overestimation of the host order parameter, discussed in Section 4.3.2.1. A comparison of the biaxial order parameters, $S_{xx} - S_{yy}$, shows no strong correlation between the approaches, but the values obtained from both methods are very small, indicating approximately uniaxial alignment for all the dyes. As presented in Chapter 5, the influence of biaxiality on the dichroic order parameters of the dyes has thus far been calculated to be minimal, and these differences are therefore unlikely to be significant in terms of the calculated dichroic order parameters of the dyes.

Table 6.7 Average values of the order parameters, S_{zz} and $S_{xx} - S_{yy}$, determined from the surface tensor eigenvalues at each frame of the trajectories of the isolated molecule MD simulations, using an orienting strength of $\varepsilon = 0.04 \text{ \AA}^{-2}$, and those obtained from the surface tensor axes in the guest-host simulations given in Tables 5.3 and 5.4 in Chapter 5.

Dye	Isolated MD ^a		Guest-host MD ^b	
	$\langle S_{zz} \rangle$	$\langle S_{xx} - S_{yy} \rangle$	$\langle S_{\theta} \rangle$	$\langle S_{xx} - S_{yy} \rangle$
15SB3	0.804	0.043	0.894	0.034
15NB3	0.791	0.047	0.874	0.037
15NB3OH	0.787	0.057	0.860	0.026
26B3	0.793	0.068	0.899	0.021
26B3OH	0.806	0.050	0.904	0.016

^a Calculated from surface tensor values.

^b Calculated from principal surface tensor vectors vs. the host director.

6.3.1.3 Transition dipole moment alignment

The contributions of the TDM vector alignments, S_{β} , to the overall dichroic order parameters calculated from the isolated molecule MD simulations were determined in the same way as described for the guest-host MD simulations in Section 5.2.6 of Chapter 5, by describing the TDM vector relative to the anthraquinone core of each conformer.

Initially, the TDM orientations were defined as fixed against the AQ, CO, and ORTH axes, calculated for each frame of each isolated molecule MD trajectory. The average angles, β and α , describing the orientations of the TDM vectors in the molecular frames are listed in Table 5.9, alongside their associated order parameters and the dichroic order parameters, S_{ϕ} , calculated using the respective S_{zz} values in Table 6.7.

Table 6.8 Average β and α angles of the fixed visible TDMs of the dyes, calculated from the isolated molecule MD simulations and their standard deviations. The associated order parameters and calculated dichroic order parameters, S_{ϕ} , are also listed.

Dye	$\langle \beta \rangle / ^{\circ}$	$\langle S_{\beta} \rangle$	$\langle \alpha \rangle / ^{\circ}$	$0.5 \langle S_{xx} - S_{yy} \rangle \langle \sin^2 \beta \cos 2\alpha \rangle$	S_{ϕ}
15SB3	7.4 ± 3.9	0.968	83.1 ± 53.8	0.000	0.778
15NB3	15.1 ± 6.5	0.882	15.1 ± 19.3	0.001	0.699
15NB3OH	18.5 ± 6.8	0.832	18.5 ± 13.5	0.003	0.657
26B3	5.6 ± 2.8	0.982	110.1 ± 51.6	0.000	0.779
26B3OH	5.6 ± 3.1	0.981	73.3 ± 55.8	0.000	0.791

A comparison of the average values of β obtained from the isolated molecule MD simulations with those obtained from the guest-host MD simulations (Table 4.8) shows very little difference between the values, with all angles differing by $< 1.6^{\circ}$ between the

two sets of simulations, consistent with the similar molecular geometries obtained from the two sets of simulations, discussed in section 6.3.1.1. Again, the trends in the β values between the dyes are consistent, with both methods showing the TDM vectors to be most aligned in 26B3 and 26B3OH, followed by 15SB3, 15NB3, and 15NB3OH, which is calculated by both methods to have the poorest TDM alignment of these dyes.

The large standard deviations obtained for the α angles of 15SB3, 26B3 and 26B3OH may be attributed to the small β angles, resulting in subtle changes in conformation having a large influence on the orientation of the projection of the TDM on to the molecular xy plane. The variation in α is calculated to be much smaller for 15NB3 and 15NB3OH, consistent with their larger β angles. The biaxial terms of the dichroic order parameters, listed in Table 5.9, again demonstrate virtually no influence of the calculated biaxiality of the molecular alignment on the calculated dichroic order parameters of the dyes.

The calculated dichroic order parameters in Table 5.9 are shown plotted against experimental values in Figure 6.7, enabling an assessment of the correlation between calculation and experiment. The value of $R^2 = 0.9420$ combined with the positive gradient shows a strong positive linear correlation between the calculated and experimental values, comparable to that of $R^2 = 0.9466$, obtained from the guest-host simulations, when applying the same assumption of the TDM vectors being fixed against the anthraquinone core. This match illustrates that this mean field approach appears valid for the dyes in this particular set of liquid crystal mixtures, and the slightly lower order parameter values obtained here compared with those from the guest-host MD simulations may be attributed to the overestimation of the molecular alignment in the guest-host systems, discussed in Section 4.3.2.1 of Chapter 4.

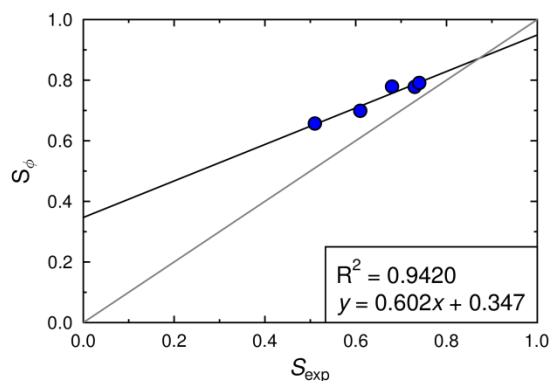


Figure 6.7 Plot of calculated order parameters, S_ϕ , obtained from the TDM orientations fixed against the anthraquinone core during the isolated molecule MD simulations vs. experimental order parameters, S_{exp} .

As described for the guest-host simulations in Chapter 5, analysis of the TDM orientations in the isolated molecule simulations was extended from assuming fixed TDM orientations against the anthraquinone cores of the dyes. Matching the dihedral angles of the dyes shown in Figure 6.2 at each trajectory frame of the simulations to the closest structures for which TD-DFT calculations had been carried out on simplified dye structures (described in detail in Section 5.2.6.3 of Chapter 5), the binned TDM orientations were determined for each frame of the isolated molecule simulation trajectories. Hence, the average angles, β and α , describing the TDMs within the molecular frame, along with the contributions to the dichroic order parameters, S_ϕ , are listed in Table 6.9 calculated using the respective S_{zz} values in Table 6.7..

Table 6.9 Average angles, β and α , of the binned visible TDMs of the dyes, calculated from the classical isolated molecule MD simulations and their standard deviations. The associated order parameters and calculated dichroic order parameters, S_ϕ , are also listed.

Dye	$\langle\beta\rangle / ^\circ$	$\langle S_\beta\rangle$	$\langle\alpha\rangle / ^\circ$	$0.5\langle S_{xx}-S_{yy}\rangle\langle\sin^2\beta\cos2\alpha\rangle$	S_ϕ
15SB3	6.5 ± 3.6	0.975	96.4 ± 58.7	0.000	0.784
15NB3	21.7 ± 6.3	0.783	12.1 ± 9.2	0.003	0.622
15NB3OH	26.6 ± 6.5	0.687	9.4 ± 9.4	0.006	0.546
26B3	5.8 ± 3.0	0.981	115.2 ± 49.9	0.000	0.778
26B3OH	6.4 ± 3.6	0.976	54.5 ± 50.0	0.000	0.787

With the exception of 15SB3, a comparison of the average β values in Table 6.9 to those in Table 6.8 shows that the binned TDM axes are all less well aligned with the surface tensor alignment axes than those assuming fixed orientations against the AQ core. The most significant differences when using binned TDM orientations rather than fixed TDM orientations are for 15NB3 and 15NB3OH, shown by increases in $\langle\beta\rangle$ of 6.6° and

8.1°, respectively, consistent with the increases of 6.9° and 8.3° from the equivalent analyses of the guest-host simulations. The values of the biaxial terms of the dichroic order parameters in Table 6.9 show that the influence of biaxiality is slightly greater when using binned TDMs rather than fixed TDM axes, which is attributable to the larger calculated β angles, although differences are still very small.

Again, the calculated results were plotted against the experimental dichroic order parameters, shown in Figure 6.8, enabling a comparison with experiment as well as an assessment of this specific method of calculation compared with the previous methods. The value of $R^2 = 0.9350$ indicates a similar linear correlation between calculated values and those from experiment to that which was obtained from assuming fixed TDM orientations against the AQ core. However, the intercept of -0.039 and gradient of 1.1351 obtained when using binned TDMs represent a significant improvement over the match with experiment compared with the plot of the order parameters from fixed TDMs shown in Figure 6.7.

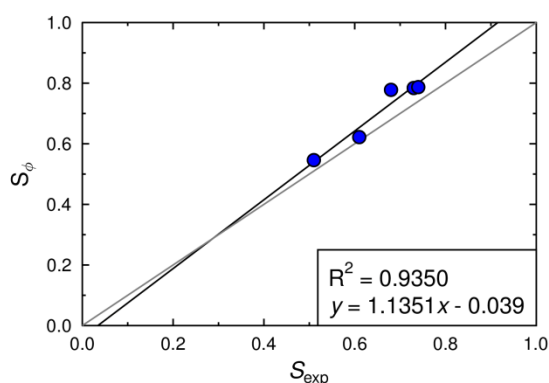


Figure 6.8 Plot of calculated order parameters, S_{ϕ} , obtained from the TDM orientations of binned conformers during the isolated molecule MD simulations vs. experimental order parameters, S_{exp} .

6.3.1.4 Benefits and drawbacks

Plots of dichroic order parameters calculated from the surface tensor axes obtained from the isolated molecule MD simulations, S_{ϕ} (Iso), against those from the guest-host MD simulations, S_{ϕ} (GH) are given in Figure 6.9. The strong positive linear correlations show that for these systems, the isolated molecule studies replicate the calculated trend in order parameters from the guest-host simulations at a fraction of the computational

cost, highlighting the suitability of mean-field theory and the surface tensor approaches to calculating the trend in the molecular alignments of the dyes.

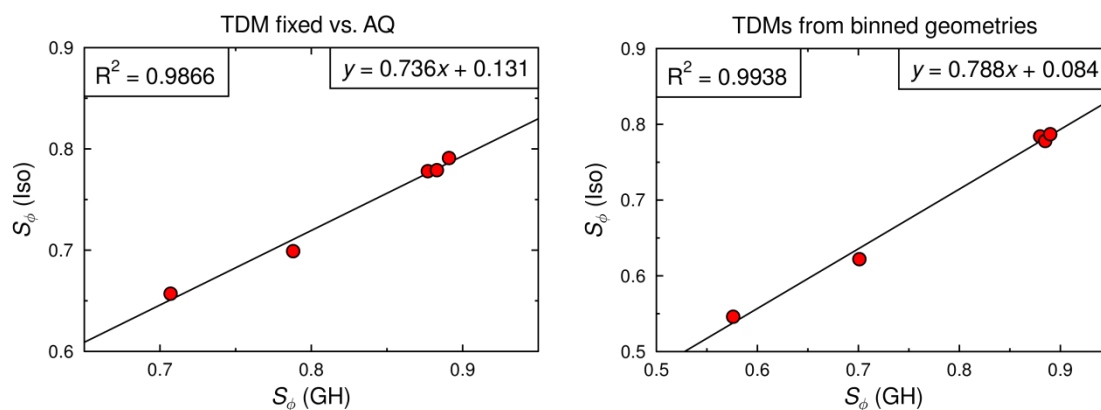


Figure 6.9 Plots of dichroic order parameters calculated from the isolated molecule MD simulations, assuming fixed TDM orientations against the anthraquinone core (left) and using TDM orientations from binned geometries (right) against those calculated from principal surface tensor axes of the dyes in the guest-host simulations.

These matches suggest that, for these systems, the molecular alignment is largely driven by the molecular shape of the dye molecules rather than by specific interactions between guest and host molecules. Thus, for this set of dyes in E7, this mean-field approach represents a computational method which is capable of calculating both the molecular alignment of the dyes within the host and the TDM alignment within the dyes, at significantly less computational expense than the guest-host MD simulations presented and discussed in Chapters 4 and 5. However, the method does rely on invoking the approximations inherent to mean-field approaches, in addition to the approximations present in the classical treatment of the molecular motion within the MD simulations, and consequently the method may be less applicable to other guest-host systems for which a mean-field approach is less appropriate. Additionally, although the MD simulation time for isolated molecules is vastly less than that of the guest-host simulations, the set-up time of such simulations in general is not significantly less than that required for the guest-host simulations, because atom-types, atomic charges and intramolecular force-constants describing the dye molecules must still be defined, and potentially parameterised.

6.3.2 Ab initio molecular dynamics simulations

The results of the classical MD simulations presented in the previous section serve to demonstrate the suitability of simulations of isolated molecules to modelling dye alignment for these guest-host systems but, unlike the guest-host MD simulations described in Chapter 4, they do not require long simulation times. The use of isolated dye molecules is hugely positive in terms of the time saving offered by the approach, and it also presents an opportunity to carry out comparable simulations utilising a more rigorous description of the isolated dye molecules.

In order to test such an approach, Car-Parrinello molecular dynamics (CPMD) simulations were carried out on each of the isolated dye molecules, enabling simulation of the conformations explored by the dye molecules, again thermostatted at 300 K, but requiring the input of only the atoms and their initial positions, rather than the connectivities and associated force constants required by the classical MD simulations. The inevitable disadvantage of CPMD simulations when compared with classical MD simulations is that of computation time, and consequently the calculation of only much shorter trajectories was possible; CPMD simulations were run for 50 ps, and full details of the methods used for the simulations are given in Chapter 2. Although the trajectories obtained by the CPMD method are much shorter than those obtained using classical MD, it was hoped that these CPMD simulations would provide an improved description of the molecular conformations explored by the dyes at 300 K, whilst avoiding the necessary classical approximations inherent to MD simulations.

To assess the conformations explored during the CPMD simulations, histograms of the dihedral angles labelled in Figure 6.2 were calculated, and are presented in Figure 6.10, alongside those obtained from the isolated-molecule classical MD simulations presented in Section 6.3.1.

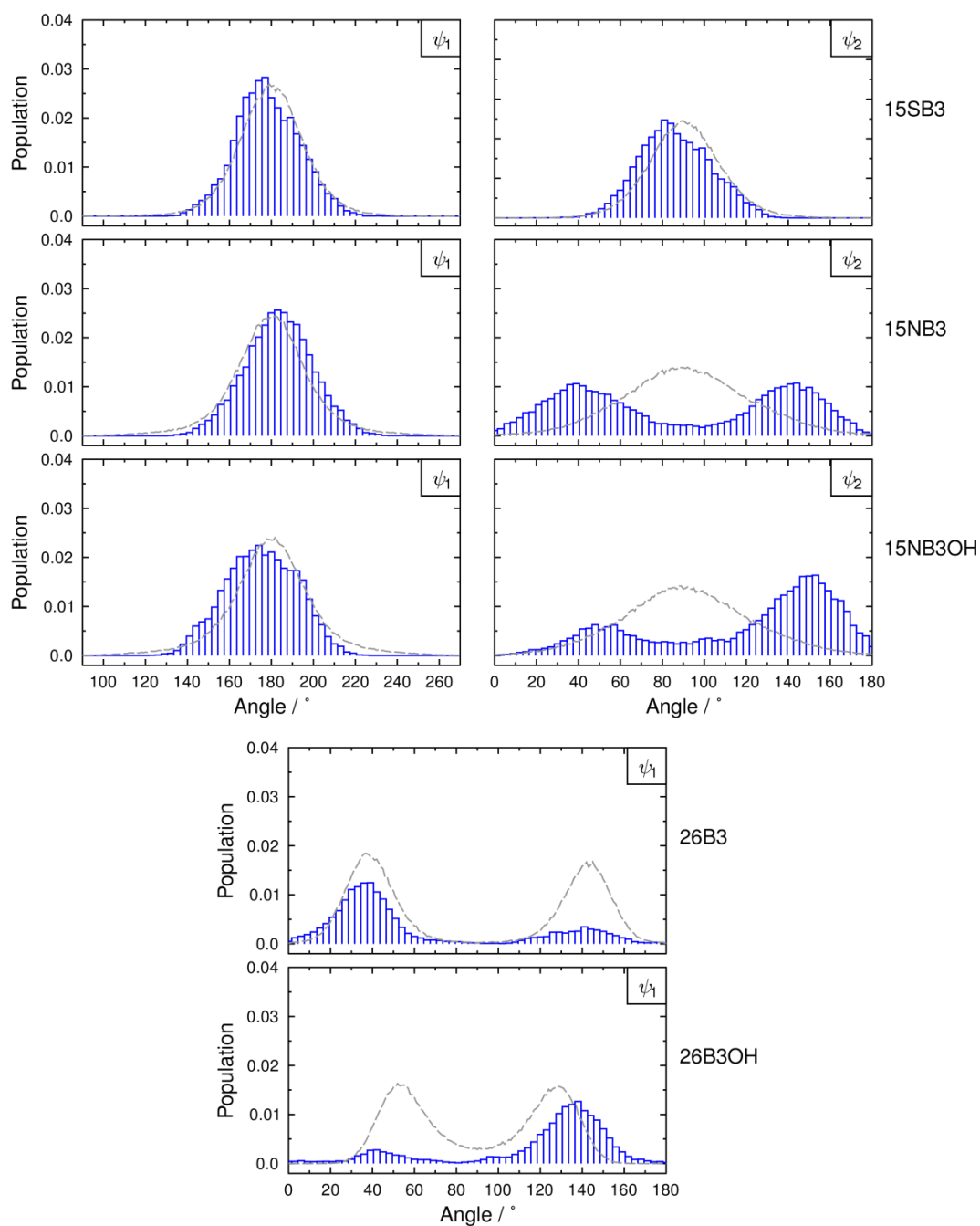


Figure 6.10 Histograms of populations of the dihedral angles labelled in Figure 6.2 obtained from the CPMD simulations (blue bars, 3° bin-width) and the isolated molecule classical MD simulations (grey lines, 1° bin-width).

For 15SB3 it is evident that the populations about both of the dihedrals analysed are consistent between the classical MD and CPMD simulations, demonstrating that the force constants used for the MD simulations are appropriate for replicating the populations determined by this level of theory in the CPMD simulations, and that the CPMD simulations have been run for a sufficient time-scale to essentially match the populations of the longer trajectories obtained from classical MD.

A comparison of the populations about ψ_1 in 15NB3 and 15NB3OH again demonstrates a good match between the two methods, from which the same conclusions may be drawn as for 15SB3. However, a comparison of the populations about ψ_2 in 15NB3 and 15NB3OH shows a marked difference between the methods: from classical MD the populations are both centred around 90° , whereas from CPMD both dihedral populations exhibit two peaks at *ca* 40° and 140° , of which the asymmetry for 15NB3OH may be attributed to the shorter trajectory obtained from CPMD. Given the force constants for these dihedrals used in the classical MD simulations were parameterised as part of this work (see Chapter 4) from the energies of conformations determined using Hartree-Fock theory, this difference may be attributed to a combination of the different levels of theory from which the populations are derived, and the approximations associated with describing the molecules classically. The double minima of the potential energy wells determined from HF calculations (see Appendix A2.4) were calculated to be separated by only a very small energy barrier (*ca* 0.1 kJ mol^{-1}), meaning the double minima did not result in separate maxima in the classical MD simulations, but the double maxima of the dihedral populations from the CPMD simulations indicate that the energy barrier may be greater using the level of theory applied in this latter approach.

The distributions obtained for the dihedrals in 26B3 and 26B3OH from the CPMD simulations are both asymmetric, and again this may be attributed to the shorter trajectories calculated using this approach than with classical MD. The population maxima, at *ca* 35° and 145° in 26B3, and *ca* 40° and 140° in 26B3OH, are similar to those obtained from the classical MD simulations, more so for 26B3 than 26B3OH.

The histograms from the CPMD simulations shown in Figure 6.10 are all less smooth than those obtained from the classical MD simulations, which may also be attributable to the shorter trajectories obtained using CPMD. Ideally the trajectories would be extended in order to remove any asymmetry and obtain smoother population distributions, but the timescale was prohibitive within the work reported here.

6.3.2.1 Surface tensor analysis and molecular alignment

Surface tensor analysis was carried out for each trajectory frame of the CPMD simulations and the inverse of the eigenvalues, t_{ii} , of the surface tensors are plotted vs. time in Figure 6.11. The eigenvalues are generally consistent over time with some fluctuation, suggesting that, overall, the simulations are likely to approach a reasonable statistical average of eigenvalues. However, in some cases, very slight gradients are evident, such as the t_{xx} values in for 15NB3 and the t_{yy} values for 26B3, again suggesting that ideally, simulations may be carried out for longer to verify the values obtained.

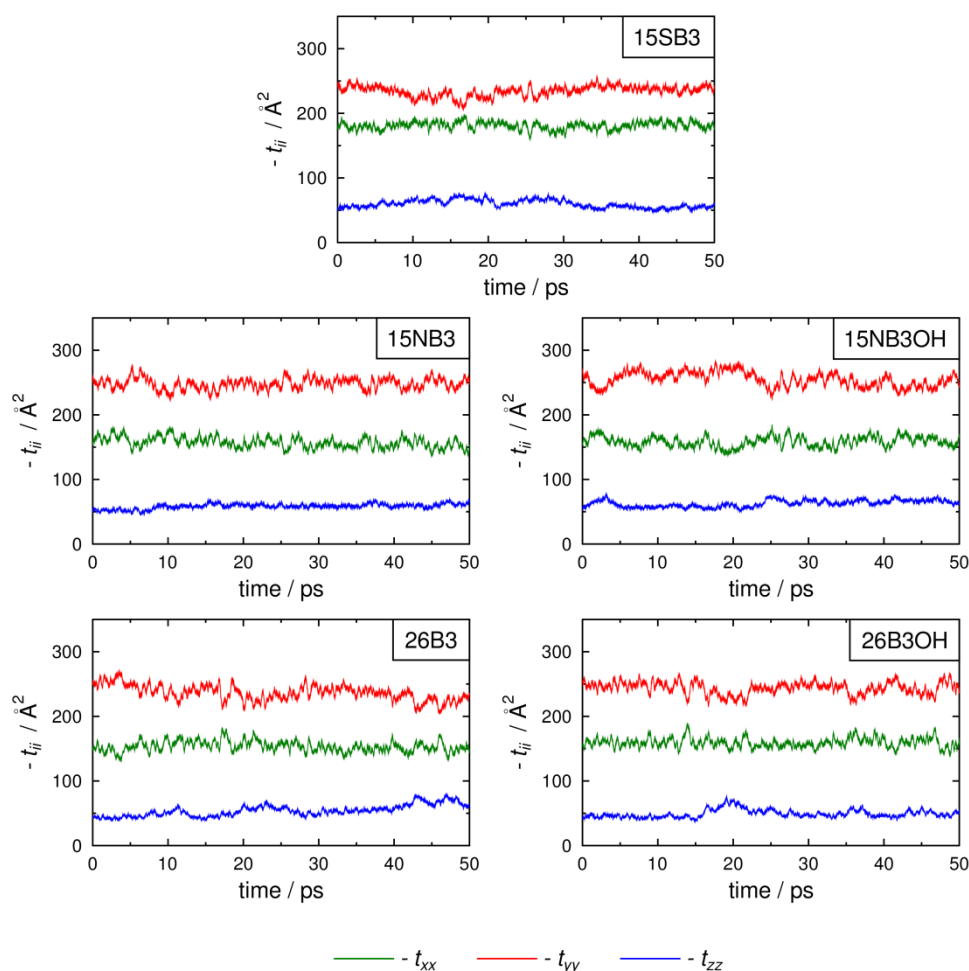


Figure 6.11 Inverse eigenvalues, $-t_{ii}$, of the surface tensors, \mathbf{t} , obtained from the CPMD simulations of the isolated dye molecules.

Histograms of the surface tensor eigenvalues are shown in Figure 6.12, alongside those obtained from the classical isolated molecule MD simulations for comparison. For

15SB3, the difference between the histograms is small, consistent with the comparable dihedral populations presented in Figure 6.10. A comparison of the respective histograms for 15NB3 and 15NB3OH shows that the $-t_{yy}$ values are larger from the CPMD simulations, whereas the $-t_{xx}$ values are smaller. This difference is again consistent with the dihedral distributions about the N-C bonds to the phenyl substituents: in the classical MD simulations the maximum populations were at 90° , corresponding to the most rod-like conformations, whereas the maxima from the CPMD simulations were at *ca* 45° , meaning the phenyl substituents lie closer to the plane of the anthraquinone core, corresponding to more planar structures with larger $-t_{yy}$ values and smaller $-t_{xx}$ values. The histograms of 26B3 are similar between the two simulations, again consistent with the comparable dihedral populations in Figure 6.10. The histograms of 26B3OH show that the CPMD simulations indicate the conformers explored are generally slightly more planar than those explored during the classical MD simulations, manifested in the smaller $-t_{xx}$ and larger $-t_{yy}$ values. This difference is also consistent with the dihedral angle populations, which indicate that the planes of the substituent phenyl groups make smaller angles against the plane of the anthraquinone, and thus exhibit a more planar structure in the CPMD simulation than the classical MD simulation.

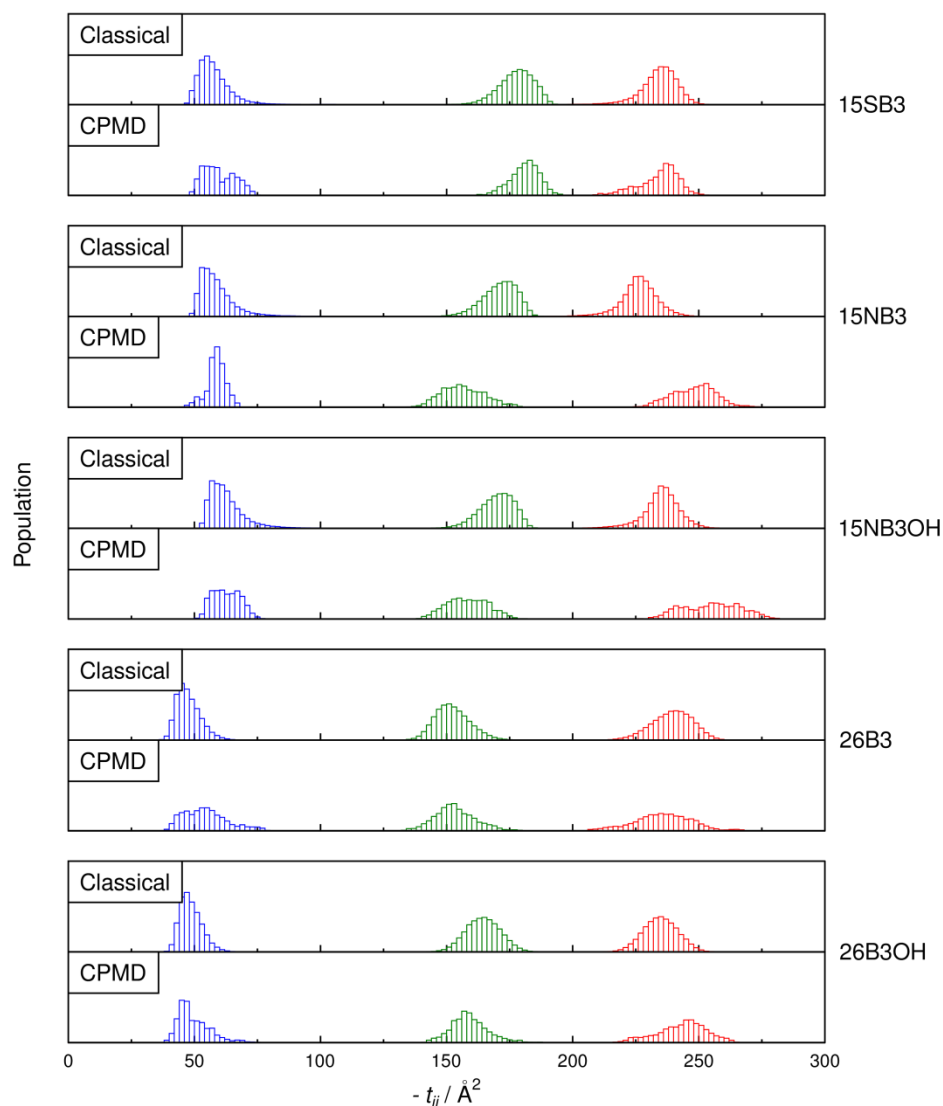


Figure 6.12 Histograms of the surface tensor inverse eigenvalues measured during the isolated molecule CPMD simulations alongside those from the isolated molecule classical MD simulations for comparison. t_{zz} values are shown in red, t_{xx} values are shown in green, and t_{yy} values are shown in blue, using 2° bin widths..

The average t_{ii} values obtained from the CPMD simulations for each of the dyes are listed in Table 6.10 along with the differences between these values and those from the isolated molecule classical MD simulations listed in Table 6.6. Given the completely different methods upon which the simulations are based, it is unsurprising that more variation is generally observed between the values from the CPMD simulations and the values from the classical MD simulations than between values from the isolated molecule MD and the guest-host MD simulations (Table 6.5). Trends between the values of the dyes are not uniform between the two approaches, but the differences reflect the variations in geometries discussed above.

Table 6.10 inverse surface tensor eigenvalues, $-\langle t_{ii} \rangle$, and standard deviations obtained for the isolated dye molecules during the CPMD simulations. The surface areas, SA, are also listed, calculated according to $SA = -\langle t_{xx} \rangle - \langle t_{yy} \rangle - \langle t_{zz} \rangle$. Δ values are calculated as the difference between the values obtained from the CPMD simulations and the isolated molecule MD simulations.

Dye	$-\langle t_{xx} \rangle / \text{\AA}^2$	Δ	$-\langle t_{yy} \rangle / \text{\AA}^2$	Δ	$-\langle t_{zz} \rangle / \text{\AA}^2$	Δ	SA / \AA^2	Δ
15SB3	181.1 \pm 10.3	+3.5	234.3 \pm 12.2	+0.1	59.8 \pm 7.0	+1.7	475.2	+5.3
15NB3	156.6 \pm 10.7	-14.5	248.2 \pm 12.7	+21.9	58.7 \pm 6.0	-0.2	463.5	+7.2
15NB3OH	158.3 \pm 10.6	-11.6	255.1 \pm 13.8	+19.9	62.7 \pm 6.7	+0.0	476.1	+8.3
26B3	153.4 \pm 10.4	+1.1	235.8 \pm 13.5	-3.6	54.4 \pm 8.0	+6.7	443.6	+4.2
26B3OH	159.1 \pm 10.3	-5.4	243.4 \pm 12.9	+8.5	49.7 \pm 6.7	+1.1	452.2	+4.2

Order parameters, S_{zz} and $S_{xx} - S_{yy}$, were calculated for each frame of each trajectory of the CPMD simulations, again using an orienting potential of $\varepsilon = 0.04 \text{\AA}^{-2}$, consistent with that used previously, and the average order parameters from the trajectories are listed in Table 6.11. Consistent with the differences in the average surface tensor eigenvalues, discussed above, there are slight differences between these order parameters and those obtained from the isolated molecule classical MD simulations, listed in Table 6.7. With the exception of 15SB3, all the molecular order parameters, S_{zz} , are calculated to be slightly lower from the CPMD trajectories, consistent with the slightly less rod-like shapes indicated by the surface tensor eigenvalues. These differences in the calculated molecular shapes are also evident in the biaxial order parameters, which are generally calculated to be higher by the CPMD simulations, most significantly in the cases of 15NB3, 15NB3OH and 26B3OH, each of which was shown to be more planar in the CPMD simulations.

Table 6.11 Averages of the order parameters S_{zz} and $S_{xx} - S_{yy}$, determined from the surface tensor eigenvalues at each frame of the trajectories of the isolated molecule CPMD simulations, using an orienting strength of $\varepsilon = 0.04 \text{\AA}^{-2}$.

Dye	$\langle S_{zz} \rangle$	$\langle S_{xx} - S_{yy} \rangle$
15SB3	0.807	0.039
15NB3	0.780	0.078
15NB3OH	0.776	0.083
26B3	0.777	0.074
26B3OH	0.800	0.062

6.3.2.2 Transition dipole moment alignment

Using the same approaches as those described for the isolated molecule classical MD simulations in section 6.3.1.3, TDM vector orientations were calculated for each frame

of each CPMD trajectory, from which the angles, β , and associated order parameters, S_β , were calculated.

Initially, analysis was carried out assuming fixed TDM orientations against the anthraquinone cores. These values are listed in Table 6.12, calculated using the respective S_{zz} values in Table 6.11.

Table 6.12 Average angles, β and α , of the fixed visible TDMs of the dyes, calculated from the isolated molecule CPMD simulations and their standard deviations. The associated order parameters and calculated dichroic order parameters, S_ϕ , are also listed.

Dye	$\langle\beta\rangle / ^\circ$	$\langle S_\beta\rangle$	$\langle\alpha\rangle / ^\circ$	$0.5\langle S_{xx}-S_{yy}\rangle\langle\sin^2\beta\cos2\alpha\rangle$	S_ϕ
15SB3	7.6 ± 3.5	0.967	66.9 ± 33.2	0.000	0.780
15NB3	11.8 ± 4.1	0.928	22.2 ± 15.9	0.001	0.725
15NB3OH	19.3 ± 4.8	0.827	14.6 ± 9.7	0.004	0.646
26B3	5.4 ± 2.6	0.983	111.3 ± 35.3	0.000	0.764
26B3OH	5.9 ± 2.8	0.980	53.4 ± 32.6	0.000	0.784

When compared with the equivalent values obtained from the isolated molecule classical MD simulations in Table 6.8, the calculated β angles are shown to be similar, with all the calculated angles differing by $<3.3^\circ$ between the two types of simulation. This similarity results in very similar calculated values of S_β between the MD and CPMD simulations, all of which are within 0.05. The calculated angles, α , and biaxiality terms arising from these calculated TDM orientations are also listed in Table 6.12, and again due to the small β angles, the contributions of biaxiality are minimal for 15SB3, 26B3 and 26B3OH. The contributions are slightly greater for the amine dyes but, as for the classical MD simulations, only a very slight influence is calculated for these dyes. The calculated dichroic order parameters are very similar to those obtained from the isolated molecule classical MD simulations, and the values are plotted against the experimental values in Figure 6.13. The gradient of < 1 and the intercept > 0 is consistent with those obtained using the same approximation of the TDMs being fixed vs. the anthraquinone core previously, both from the guest-host MD simulations (Figure 5.17 in Chapter 5) and from the classical isolated molecule MD simulations (Figure 6.7). The R^2 value of 0.9741, represents an increase over any of the previous R^2 values and may potentially be attributed to the fewer assumptions made in the CPMD simulations in comparison with the classical MD simulations.

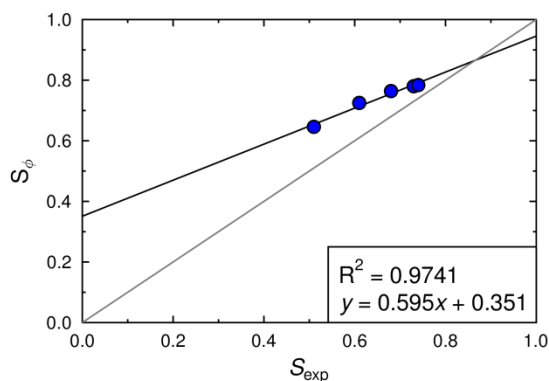


Figure 6.13 Plot of calculated order parameters, S_ϕ , obtained from the TDM orientations fixed against the anthraquinone core during the CPMD simulations vs. experimental order parameters, S_{exp} .

The average angles, β and α , describing the TDMs within the molecular frame determined for the binned TDMs in the CPMD trajectories, along with the contributions to the dichroic order parameters, S_ϕ , are listed in Table 6.13, calculated using the respective S_{zz} values in Table 6.11.

Table 6.13 Average angles, β and α , of the binned visible TDMs of the dyes, calculated from the isolated molecule CPMD simulations and their standard deviations. The associated order parameters and calculated dichroic order parameters, S_ϕ , are also listed.

Dye	$\langle\beta\rangle / ^\circ$	$\langle S_\beta \rangle$	$\langle\alpha\rangle / ^\circ$	$0.5\langle S_{xx} - S_{yy} \rangle \langle \sin^2\beta \cos 2\alpha \rangle$	S_ϕ
15SB3	7.1 ± 3.4	0.971	78.8 ± 35.2	0.000	0.784
15NB3	16.1 ± 4.0	0.878	14.7 ± 9.4	0.002	0.687
15NB3OH	24.6 ± 4.9	0.733	11.6 ± 7.7	0.007	0.575
26B3	5.6 ± 3.0	0.982	118.3 ± 33.7	0.000	0.763
26B3OH	7.6 ± 3.7	0.968	34.9 ± 25.2	0.000	0.775

As found for the classical MD simulations, the CPMD simulations give average β angles that are generally larger from binned TDM orientations than fixed TDM orientations, most notably for the two amine dyes. The slight increase in β evident for 26B3OH is consistent with the slightly different geometries explored during the CPMD simulation than during the classical MD simulation, highlighted by the dihedral angle distributions as discussed above.

Calculated contributions of biaxiality to the order parameters, listed in Table 6.13, are again shown to be negligible, resulting in slightly higher calculated order parameters for the amine dyes than those obtained by applying the approximation of uniaxial alignment.

A plot of the calculated dichroic order parameters obtained using binned TDMs against the experimental values, shown in Figure 6.14 demonstrates another strong positive correlation between calculation and experiment. The linear correlation is very slightly poorer than that obtained for the fixed TDM orientations, shown by a value of $R^2 = 0.9628$, but the intercept is significantly smaller and the slope closer to 1, which is consistent with the equivalent plots obtained from the isolated molecule classical MD simulations. The linear correlation of the dichroic order parameters obtained using binned TDM orientations with experiment is better for the values obtained from the CPMD simulations than that obtained from the equivalent analysis of the classical MD simulations, consistent with the matches obtained using fixed TDM orientations.

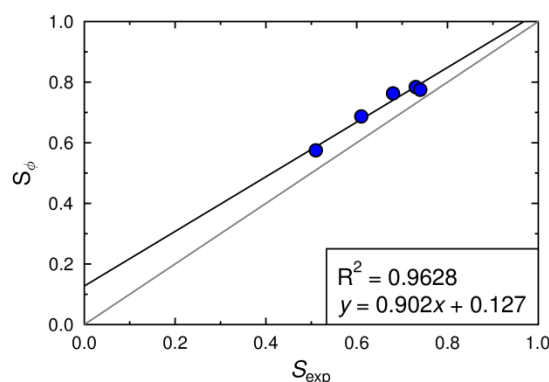


Figure 6.14 Plot of calculated order parameters, S_{ϕ} , obtained from the TDM orientations of binned conformers during the CPMD simulations vs. experimental order parameters, S_{exp} .

6.3.2.3 Benefits and drawbacks

The application of mean-field theory through CPMD simulations of the isolated dyes enables the calculation of dichroic order parameters of dyes, incorporating the influence of room-temperature conformations, without applying any assumptions relating to the transferability of force constants to the systems. Although the fits with experimental data are not very different from those obtained from isolated molecule classical MD simulations, significantly fewer assumptions are made in the CPMD simulations, and hence it may be considered a less subjective method of modelling the alignment properties of the dyes. The clear drawback to CPMD simulations in comparison with classical MD simulations is that of computation time, but

consideration should be made as to whether this disadvantage is offset by the significantly greater set-up time required for classical MD simulations, and with the ever-increasing speed of computation, ab-initio molecular dynamics will become a more accessible method in the future.

6.3.3 DFT optimised structures

Good matches between experimental dichroic order parameters and those obtained from applying the surface tensor model to the guest-host MD simulations, and to the results from the isolated molecule simulations using both classical MD and CPMD simulations, suggest that this mean-field approach to modelling dye alignment is effective for these systems. However, both classical MD and CPMD are not rapid methods of assessing dye alignment, even when applying the assumption of fixed TDMs within the dyes: either a topology must be defined, and potentially parameterisation of force constants carried out for classical MD simulations, or long computation times are typically required for CPMD simulations. It may therefore be relevant to consider whether surface tensor analyses of isolated structures obtained from DFT optimisations are capable of providing estimates of dichroic order parameters of the dyes, in order to provide a rapid method of assessing the alignment of potential dye structures in liquid crystal hosts.

6.3.3.1 Surface tensor analysis and molecular alignment

Using the DFT optimised structures of isolated dye molecules presented in Chapter 3, surface tensors were calculated, and the order parameters calculated from the eigenvalues are listed in Table 6.14. The molecular alignment order parameters, S_{zz} , of the DFT optimised structures are all higher than the respective values obtained from the surface tensor analyses of both the isolated molecule classical MD simulations and CPMD simulations. This difference is likely to be a result of the DFT optimised geometries being all-*trans*, rod-like conformations, whereas the MD and CPMD simulations explore more varied, typically less rod-like, geometries. The order parameters from the DFT optimised structures are lower than those obtained from the orientations of the principal surface tensor axes against the host director in the guest-

host simulations, discussed in Section 5.2.2.5 of Chapter 5, and this may be attributed to the overestimation of molecular alignment in the guest-host simulations.

Table 6.14 Order parameter, S_{zz} and $S_{xx} - S_{yy}$, determined from surface tensor analysis of the DFT optimised structures, using an orienting strength of $\varepsilon = 0.04 \text{ \AA}^{-2}$.

Dye	S_{zz}	$S_{xx} - S_{yy}$
15SB3	0.820	0.042
15NB3	0.798	0.073
15NB3OH	0.791	0.083
26B3	0.803	0.068
26B3OH	0.813	0.060

6.3.3.2 Transition dipole moment alignment

The dichroic order parameters of the dyes calculated from the DFT optimised structures using the surface tensor method are listed in Table 6.15, using the β and α values given in Chapter 5 in Tables 5.5 and 5.6, respectively, shown again here for clarity and S_{zz} values from Table 6.14.

Table 6.15 Calculated angles, β and α , of the binned visible TDMs of the dyes, calculated from the DFT optimised structures. The associated biaxial order parameters and calculated dichroic order parameters, S_ϕ , are also listed.

Dye	$\beta / ^\circ$	S_β	$\alpha / ^\circ$	$0.5\langle S_{xx} - S_{yy} \rangle \langle \sin^2 \beta \cos 2\alpha \rangle$	S_ϕ
15SB3	7.9	0.972	0.0	0.000	0.797
15NB3	10.9	0.946	10.0	0.001	0.756
15NB3OH	13.9	0.913	10.2	0.002	0.725
26B3	7.0	0.978	36.9	0.000	0.785
26B3OH	2.8	0.996	98.7	0.000	0.810

A plot of these calculated dichroic order parameters versus the experimental values, shown in Figure 6.15, shows a very strong linear correlation, giving a value of $R^2 = 0.9886$, which represents the highest for any of the approaches yet tried. It is not clear as to why the fit using this approach should be better than the methods presented previously, but the intercept is significantly larger than those obtained using the isolated molecule MD and CPMD methods, and the gradient is significantly lower, showing that the surface tensor analysis of the DFT structures does not provide a better match with experiment than the other methods discussed in this chapter.

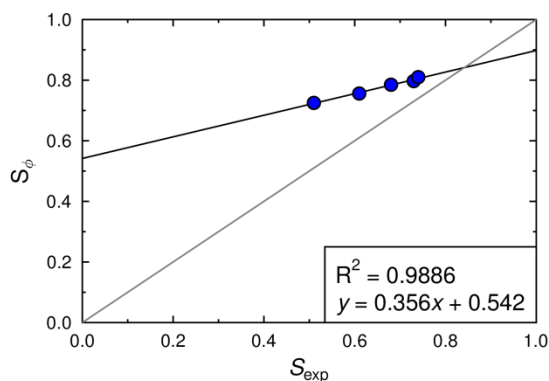


Figure 6.15 Plot of calculated order parameters, S_ϕ , obtained from the surface tensor analysis of the DFT optimised dye structures and the calculated TDM orientations vs. the experimental order parameters, S_{exp} .

6.3.3.3 Benefits and drawbacks

The match in the trend between the values calculated from surface tensor analysis of the DFT optimised structures and the experimental values does suggest that, as a minimum, such an approach may be a useful method of assessing the relative dichroic order parameters of dyes. Benefits are that it does not require any user input other than defining atom types, a starting geometry for the optimisation, a level of theory and basis set, and an orienting potential. Additionally, the whole process for dyes of this size may be completed in a matter of minutes, rather than hours, days, or months, which was required for some of the other approaches discussed in this thesis. The approach is susceptible to drawbacks, primarily from dye flexibility, which may be much more important in some structures than others, but it may provide a starting point from which further, more time consuming, analysis can be directed in an informed way.

6.3.4 Overall comparison of methods

All of the methods tested so far provide linear correlations between experimental and computational dichroic order parameters with R^2 values greater than 0.9 and positive gradients, indicating that all the methods are capable of predicting experimental alignment trends. However, there is some variation between the quality of these fits, and the values of the intercepts and the gradients of the fitted lines provide additional information about the quality of the matches between calculated and experimental values.

The R^2 values, intercepts and gradients of all the fits between the different calculated dichroic order parameters and the experimental order parameters are listed in Table 6.16, and comparisons of these values are also shown graphically in Figures 6.16 – 6.18.

Table 6.16 R^2 values, gradients and intercepts of fits between calculated dichroic order parameters and experimental order parameters of the dyes.

Method	TDM	R^2	Gradient	Intercept
GH MD	Single β angle	0.9211	0.465	0.549
	Fixed vs. aq	0.9466	0.815	0.296
	Binned	0.9392	1.439	-0.155
Isolated MD	Fixed vs. aq	0.9420	0.602	0.347
	Binned	0.9350	1.135	-0.039
CPMD	Fixed vs. aq	0.9741	0.595	0.351
	Binned	0.9628	0.902	0.127
DFT	Single β angle	0.9886	0.356	0.542

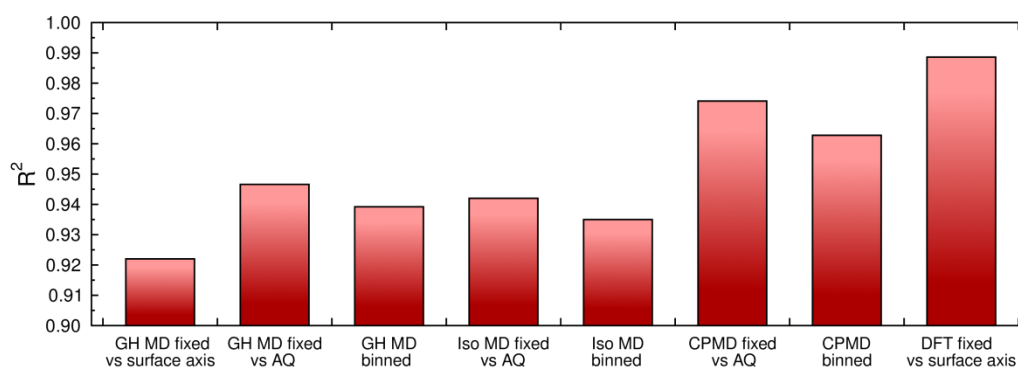


Figure 6.16 R^2 values of fits between calculated dichroic order parameters and experimental order parameters of the dyes.

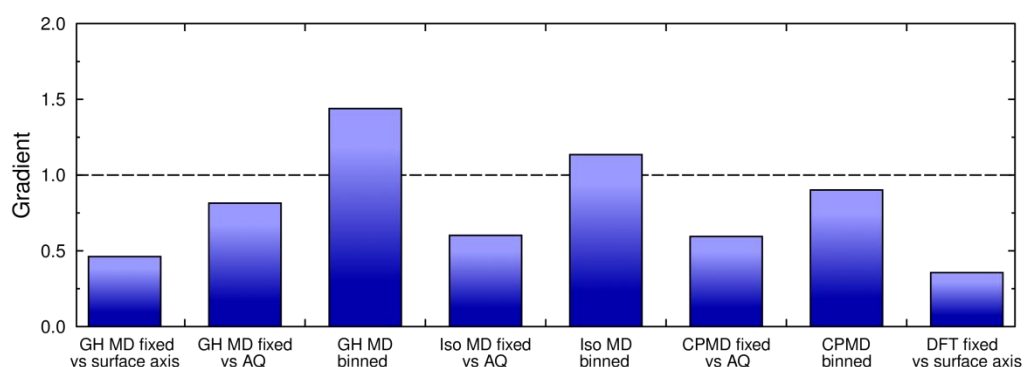


Figure 6.17 Gradients of fits between calculated dichroic order parameters and experimental order parameters of the dyes. The dashed line indicates a gradient of 1.

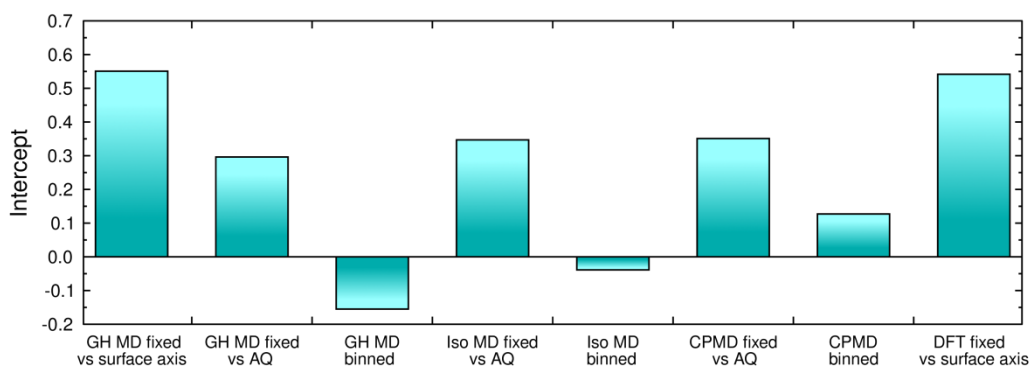


Figure 6.18 Intercepts of fits between calculated dichroic order parameters and experimental order parameters of the dyes.

Somewhat surprisingly, the best fit determined from the R^2 values is provided by surface tensor analysis of the DFT optimised structures alone, but the intercept of the fit is high and the gradient is small, showing that this method does not provide the best overall match between calculation and experiment.

A comparison of the different approaches to analysing guest-host MD simulations shows that the quality of fit is improved by referencing the TDM vector against the anthraquinone core rather than using a single value of β , both from the increase in the R^2 value, the decrease in the intercept of the fit and the gradient being closer to 1. This improvement highlights a limitation imposed by considering the TDM orientation of a dye to be fixed against the principal molecular alignment axis.

For the guest-host MD simulations, the isolated molecule MD simulations, and the CPMD simulations, using TDM vectors from binned geometries results in a very slight decrease in the R^2 values compared with the values obtained when assuming the TDMs to be fixed against the anthraquinone cores of the dyes. However the use of binned TDM orientations also results in a significant reduction in the magnitude of the intercepts for each method, which would ideally be 0. The higher R^2 values and the relatively slight differences in intercepts for the CPMD values compared with those from the classical MD simulations may potentially be attributed to the fewer assumptions invoked by the CPMD calculations compared with the classical simulations of isolated molecules, indicating that the CPMD approach may provide the best match with experiment of the MD methods tested. This conclusion is supported by the gradients of the fits, showing that the gradient closest to 1 for all the tested models is from the CPMD simulations, using binned TDM orientations.

6.4 Conclusions

The close match between the trends in dichroic order parameters obtained from the guest-host simulations in Chapter 5 and those obtained by classical isolated molecule MD simulations presented in this chapter, as well as their consistency with experimental data, demonstrates the applicability of the mean field surface tensor model to this set of guest-host systems. The consistency observed between the predictions of the order parameters by these methods indicates that the slight differences in the molecular conformations explored between the different simulations are not significant in the context of the predicted order parameters of the dyes.

The classical isolated molecule MD simulations have been shown to provide a much more rapid method of estimating experimental trends in dichroic order parameters than guest-host MD simulations, providing a comparable level of accuracy for predicting relative alignment in these systems. The reduction in computational expense provided by the isolated molecule classical MD simulations, and the applicability of mean field theory to these systems enables the use of ab-initio MD simulations in the calculation of dichroic order parameters. The results of these CPMD simulations showed experimental alignment trends could again be replicated, requiring much shorter set-up times and fewer input parameters than for the preparation of classical MD simulations. This aspect is important to give confidence in the CPMD simulations, and to provide a method that is not susceptible to potential variation in the preparation of the simulations.

Differences in the molecular conformations of the dyes between the guest-host MD simulations and the classical isolated molecule MD simulations suggest that the presence of the host molecules does have some influence on the conformations explored by the dyes. However, greater differences were observed when comparing conformations explored in the CPMD simulations to the conformations explored in the classical isolated molecule MD simulations. This difference indicates that the level of theory used here and the choice of force constants used to describe the dye molecules in this work appear to have a greater influence on the explored conformations than the presence or absence of host molecules for these systems.

Analysis of the optimised DFT structures using the surface tensor model also enabled replication of the experimentally observed alignment trends of these dyes. If shown to

be more generally applicable, this approach may provide a means of rapidly screening potential dye structures, enabling further investigations or synthesis to be targeted towards promising structures. Application to a wider range of structures may also highlight general features of highly aligned or poorly aligned dyes, helping to rationalise experimental trends, and aiding the rational design of new materials.

Chapter 7

Scope of computational methods

The work presented in this chapter assesses the scope of the computational methods developed so far in this thesis in two contexts: firstly, the classical MD methods described in Chapters 4 – 6 are applied to more structurally diverse anthraquinone dyes than those studied thus far, and secondly the use of DFT and TD-DFT calculations is applied to a wide variety of dye structures from the anthraquinone and azo dye classes.

7.1 Introduction

In this introductory section, the desirable qualities of computational methods for calculating and predicting dichroic order parameters in general are considered, followed by an outline of the general structural features of both anthraquinone and azo dyes that are known to result in a range of order parameters, before the aims of the work presented in this chapter are given.

7.1.1 Alignment prediction

Ideally, a computational method for predicting the dichroic order parameters of dyes would be accurate, applicable to any given dye structure (hypothetical or otherwise), independent of the way in which the calculation is set up, would not require the input of any experimental data, and would be rapid. Such a method would enable hypothetical dye structures to be screened prior to synthesis, enabling synthetic approaches to be targeted towards structures predicted to be most likely to exhibit a high degree of optical anisotropy in liquid crystal hosts.

The work presented in Chapters 3 – 6 indicates that a method fulfilling all of these requirements, and in particular that of being rapid while meeting the other requirements, is likely to be beyond current limitations in computational methods and computation power. However, the analysis of the five dyes studied so far, using the surface tensor approach in conjunction with single DFT optimised structures of the dyes to calculate the contribution of molecular alignment, allied with the use of TD-DFT to calculate the

contribution of TDM alignment, has shown that the calculated alignment trend between the dyes closely replicates that obtained experimentally. This method based on analysis of single optimised structures has limitations, most notably in not considering molecular flexibility and room-temperature conformations. However, it is rapid and the results in Chapter 6 showed it may have value, and if it is shown to apply more generally than to the five dyes studied in Chapters 3-6 then the method could have the potential to provide a screening approach as described above.

In the context of the behaviour of guest molecules in liquid crystal hosts, the application of mean-field theory within the surface tensor approach, discussed in Chapters 5 and 6, means that the effect of the host is considered only via the orienting potential, ε , implying that the specific consideration of different host mixtures is not necessarily required. This orienting potential may be parameterised from a set of experimental order parameters of different guests within a given host,³³¹ or an alternative and much more general approach is to apply a single ε value known to be typical for nematic hosts in general, such as in the approach used in Chapter 6. As introduced in Section 1.3 of Chapter 1, the relative alignments of dyes within a single host tend to be indicative of their behaviour in guest-host systems in general, although the absolute alignments of dyes may vary between hosts. Therefore, for predicting the relative alignments of different dyes within a given host, the use of a single orienting potential may be considered appropriate. However, for studies comparing experimental order parameters with calculated values, a single orienting potential may not be suitable if the experimental values are not all obtained for the same host at the same temperature; if the errors arising from using a single orienting potential for different hosts are significant, then the use of parameterised orienting potentials for each host may be required.

7.1.2 Dyes exhibiting negative dichroism

As discussed in Chapter 1, dichroic order parameters may range between 1 for a system in which all the TDMs are oriented along the host director, and -0.5 when all the TDMs are oriented perpendicular to the director. High order parameters approaching a value of 1 are typically desirable for the applications and devices discussed in Chapter 1, but some modes of operation can utilise dyes exhibiting negative dichroism, i.e. $S_{\text{exp}} < 0$, for

which a low order parameter approaching a value of -0.5 is typically desirable, and such dyes have also been the subject of several experimental studies.

7.1.2.1 Anthraquinone dyes

The anthraquinone dyes studied in this work and those discussed in Section 1.4.2 of Chapter 1 all exhibit experimental dichroic order parameters greater than 0.4 in E7, indicating a tendency in all cases for the visible TDMs to preferentially align parallel to the host director rather than perpendicular to it. However, the literature also includes research on anthraquinone dyes with negative dichroism,³³²⁻³³⁶ exhibiting order parameters < 0 .

Some anthraquinone dyes with amide substituents in the 1,4- positions, as shown in Figure 7.1, are known to exhibit negative dichroism.^{332, 336} The structure of the amide substituents, namely the intramolecular hydrogen bonds between the amide protons and the anthraquinone carbonyl groups as well as the planar amide groups, have been reported to result in the C-R and C-R' bonds orienting parallel with the CO axis of the anthraquinone.^{332, 336} This orientation is in contrast to that calculated for the X-C bonds to the substituent phenyl groups in the five dyes discussed in Chapters 3 – 6. It has been reported that this substituent orientation in amide-substituted dyes causes the alignment axis of the dye to also lie along the axis of the anthraquinone carbonyl groups (CO axis) for bulky R and R' groups, but the visible TDM orientation is considered to lie along the anthraquinone core (AQ axis).^{332, 336}

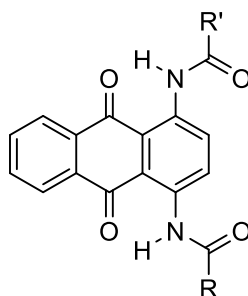


Figure 7.1 General structure of a 1,4-diamido-anthraquinone dye, derivatives of which have been shown to exhibit negative dichroism.

A semi-quantitative description of this behaviour may be obtained by applying the uniaxial approximation of dye alignment, given by $S_\phi = S_\theta S_\beta$ introduced in Chapter 1. If

the orientation of the TDM lies perpendicular to the molecular alignment axis then the contribution of the TDM order parameter, S_β , can be assumed to be *ca* -0.5 , causing the negative dichroism. The magnitude of the overall dichroic order parameter, S_ϕ , is then determined by the contribution of the molecular alignment, S_θ , which is determined by the nature of the amide substituent groups influencing the alignment of the dye molecules within the host mixture.

Examples of specific anthraquinone structures, **1** and **2**, that have been reported to exhibit negative dichroism are shown in Figure 7.2, and their reported experimental order parameters are listed in Table 7.1 along with the wavelengths at which they were measured and the nematic host mixtures used. The asymmetric dye **1** has a reported order parameter just below zero, whereas the order parameter of the symmetric dye **2** has been shown to be significantly lower, consistent with trends observed for other similar 1-amine-4-amide- and 1,4-diamide substituted dyes.^{333, 334}

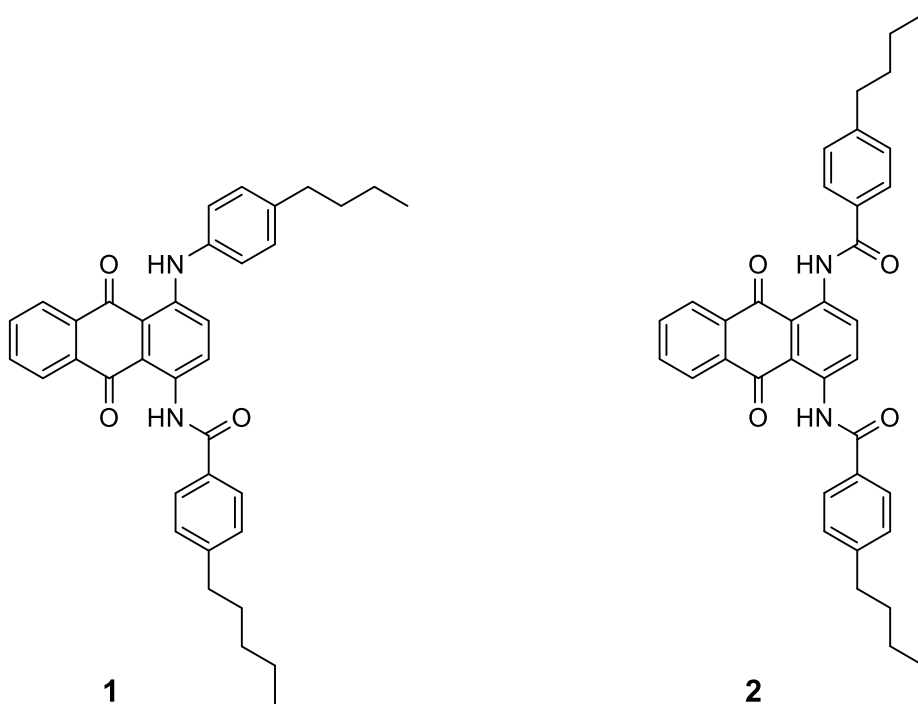


Figure 7.2 Structures of **1** and **2**.

Table 7.1 Reported dichroic order parameters, S_{exp} , of dyes **1** and **2**,^{332, 336} along with the wavelengths, λ , and nematic host mixtures^{337, 338} used for the measurements.

Dye	λ / nm	S_{exp}	Host
1	493	-0.05	ZLI-1132
2	506	-0.32	ZLI-4792

The semi-quantitative assessment described above provides a basic understanding of the optical properties of these guest-host systems but the reported analysis of structure-function relationships in these systems is relatively limited.

7.1.2.2 Azo dyes

Research into azo dyes in the context of guest-host systems has largely been driven by their rod-like molecular shapes, which provide elongated structures that result in high order parameters, as introduced in Section 1.4.1 of Chapter 1. Shorter mono-azo dyes tend to exhibit lower order parameters than longer bis-, or tris- azo dyes,²⁴ and much of the literature focusses only on azo dyes exhibiting positive dichroism.^{10, 12, 49-51}

The synthesis of heteroaromatic azo dyes that are derivatives of the structure shown in Figure 7.3, has yielded azo dyes which exhibit negative dichroism.³³⁹ In nematic hosts, such dye molecules are considered to align along the biphenyl-heteroaromatic core group, whereas the visible TDM has been suggested to align along the axis of the approximately orthogonally oriented azo group,³³⁹ resulting in a similar relative alignment of these axes to those reported for the anthraquinone dyes discussed above.

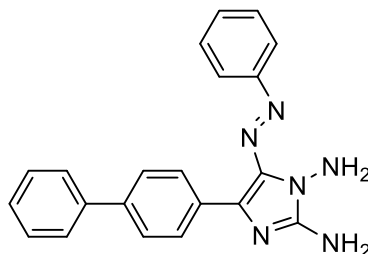


Figure 7.3 Core structure of heteroaromatic azo dyes that have been shown to exhibit negative dichroism.

This interpretation enables the alignment to be rationalised semi-quantitatively, but a detailed quantitative assessment of the contributions to the dichroic alignment appears not to have been reported.

7.2 Aims

The aim of the work presented in the first section of this chapter was to assess the scope of the methods used and developed in Chapters 4-6 by applying them to compounds **1** and **2**, which are reported to exhibit significantly different order parameters from the five dyes studied thus far in this thesis. The intention was to carry out DFT optimisations, TD-DFT calculations, classical guest-host MD simulations and classical MD simulations of the isolated dyes to assess the scope of these methods and their associated assumptions, such as the applicability of mean field theory to the MD simulations, in the context of negative dichroic dyes.

The aim of the work presented in the second section of this chapter was to assess the wider use of single DFT optimised structures and the surface tensor model as a means of rapidly assessing dichroic order parameters by analysing a number of dyes that have been reported to exhibit a range of reported experimental dichroic order parameters, using dyes from both the anthraquinone and azo dye classes.

The overall aim of the work presented in this chapter was to assess the scope of computational methods in a wider context than previously considered in this thesis, primarily using data from the literature, and thus the focus was on the methods and their scope, rather than on the details of the structures and properties of the dyes being studied. Hence, the detail in which the results are analysed in this Chapter is less than that presented in Chapters 3 – 6, because it was not the intention to develop detailed conclusions on the particular dye structures being analysed.

7.3 Results and discussion

7.3.1 1,4-disubstituted anthraquinones: assessment of methods

7.3.1.1 DFT and TD-DFT calculations

DFT optimisations of **1** and **2** were carried out from all-*trans* starting geometries and are shown in Figure 7.4. In each case, the amide substituent groups are calculated to be close to being planar, and the phenylamine substituent group in **1** adopts a comparable conformation to those calculated for 15NB3 and 15NB3OH in Chapter 3 (Figure 3.8).

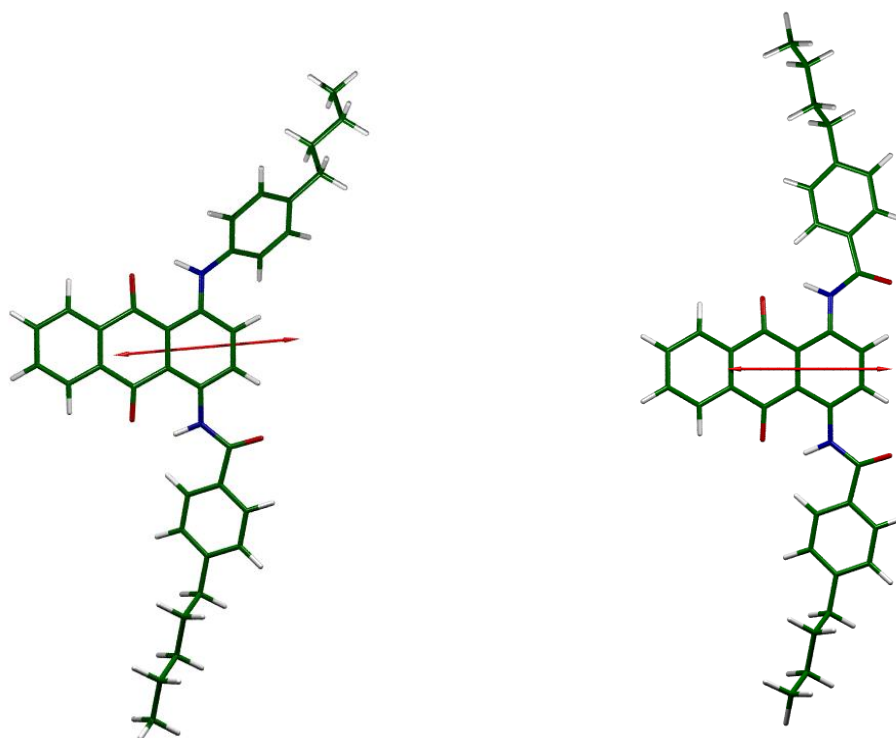


Figure 7.4 Optimised structures of **1** (left) and **2** (right) at the B3LYP/6-31g(d) level with red arrows overlaid, indicating the orientations of the TDMs associated with the strongly allowed visible transitions.

TD-DFT calculations on the optimised structures of **1** and **2** indicated one strongly allowed visible transition for each of the dyes, which are listed in Table 7.2 alongside the other calculated allowed visible transitions and their oscillator strengths. The longest wavelength transition in each of the dyes was calculated to be a HOMO \rightarrow LUMO transition, consistent with the results for the dyes presented and discussed in Chapter 3.

Table 7.2 Calculated wavelengths, λ , of the allowed visible transitions of **1** and **2**, and their associated oscillator strengths, f .

Dye	λ / nm	f
1	585	0.1723
	419	0.0312
	392	0.0616
2	511	0.1559
	395	0.0383

The longer wavelength visible absorption of **1** than **2** is consistent with the more electron-donating character of the amine group than the amide group, and with the typical substituent to anthraquinone carbonyl charge-transfer nature of the visible transitions in anthraquinone dyes. The relative calculated absorption wavelengths are not consistent with the reported wavelengths at which the dichroic order parameters were determined,^{332, 336} but a comparison with these experimental wavelengths is of limited value in the absence of spectral data in the literature.

The orientations of the long wavelength TDMs calculated for **1** and **2** are also shown overlaid on the optimised structures in Figure 7.4, from which it can be seen that the visible TDM is approximately oriented along the axis of the anthraquinone core in each of the dyes. The angle between the TDM and the anthraquinone axis (AQ) of **1** is calculated as 6.3°, and the slight offset is attributable to the asymmetry of the substituents. The calculated angle between these axes in **2** is 1.0°, showing that the TDM is more aligned with the AQ axis than in **1**, which is attributable to the symmetric structure of **2**. These calculated TDM orientations are consistent with the conclusions reported previously, that 1,4-disubstituted anthraquinone dyes are likely to have TDMs aligned along the anthraquinone core,^{332, 336} and they are also consistent with the substituent to anthraquinone carbonyl charge transfer nature of the transitions.

7.3.1.2 Guest-host MD simulations

Guest-host MD simulations were carried out on **1** and **2** in E7 using the same methods as described in Chapter 4, and simulating 5 dye molecules within 400 component molecules of E7. The use of E7 does not match the hosts used in the reported experimental studies given in Table 7.1, but the difference in the reported experimental dichroic order parameters of **1** and **2** is significant, and the negative dichroism exhibited

by such species is recognised as a general feature of the dye structures.³³² Simulations were run from pseudo-nematic starting geometries for 500 ns and averaging was carried out between 30 ns and 500 ns. Full topologies of **1** and **2** are given in Appendix A4.1.

Using the same approach as described in Chapter 4, the order parameters of the minimum moment of inertia axes of the host molecules, S_θ (MOI), were calculated at each time frame of each guest-host simulation. These order parameters are plotted against time for the two simulations in Figure 7.5, and the average order parameters of 0.875 and 0.873 are very similar to that of 0.878 obtained for the host alone, presented in Section 4.3.2.1 of Chapter 4; and they are also within the range of host order parameters calculated for the guest-host simulations of the 1,5- and 2,6-disubstituted anthraquinones also presented in Chapter 4.

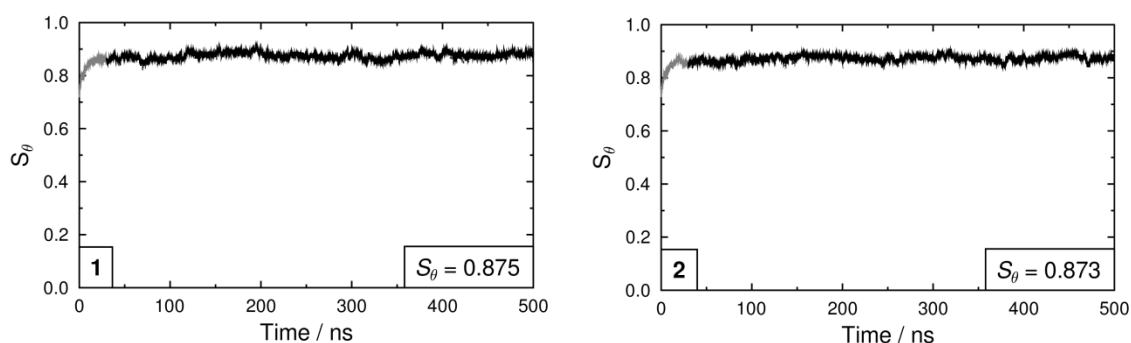


Figure 7.5 Plots of the calculated order parameters, S_θ (MOI), of the minimum MOI axes of the host molecules of E7 during the guest-host MD simulations of **1** (left) and **2** (right). Sections shown in black (≥ 30 ns) were used to calculate the average values.

The calculated molecular order parameters, S_θ (MOI), of the dyes against the host director versus time from the guest-host simulations are shown in Figure 7.6, along with their average values. These calculated order parameters indicate that **2** exhibits a higher degree of molecular alignment within the host than **1**, and the calculated order parameter of **2** fluctuates less than that of **1** during the simulation. A comparison with the equivalent order parameters of the five dyes reported in Chapter 4 shows that the calculated order parameter of **1** is lower than any of these other dyes, whereas **2** is calculated to have an order parameter within the range of these other dyes.

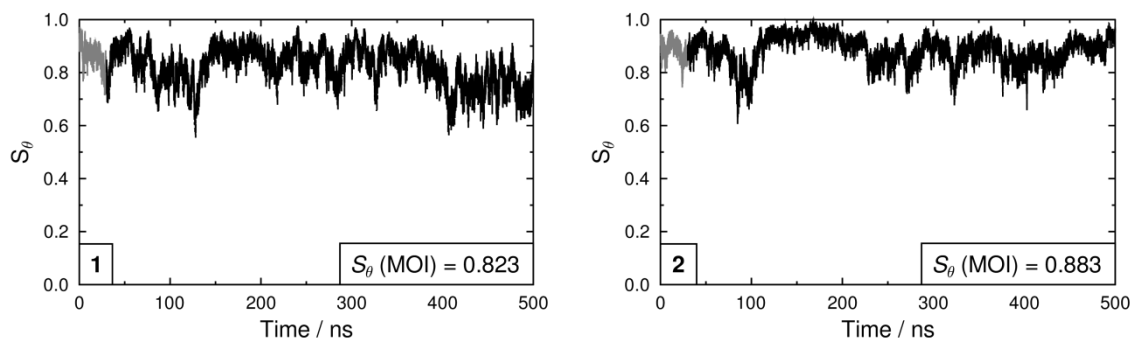


Figure 7.6 Plots of the calculated order parameters, S_θ (MOI), of the minimum MOI axes of the dye molecules during the guest-host MD simulations of **1** (left) and **2** (right). Sections shown in black (≥ 30 ns) were used to calculate the average values.

The calculated order parameters, S_θ , of the principal surface tensor axes of **1** and **2** against the host director were also calculated and are plotted versus time in Figure 7.7. A comparison of the average values from the surface tensor approach, listed in Table 7.3, with those of the minimum MOI approach indicate that, as with the previous analysis of the dyes in Chapter 5, the surface tensor axes are better aligned than the minimum MOI axes, most significantly for **1**, and the average S_θ values of the principal surface axes **1** and **2** both lie within the range of equivalent values obtained for the five dyes reported in Chapter 5. The higher order parameters of the surface tensor axes than the minimum MOI axes is consistent with the conclusion in Chapter 5 that the principal surface tensor axes provide a better description of the alignment axes than the principal MOI axes.

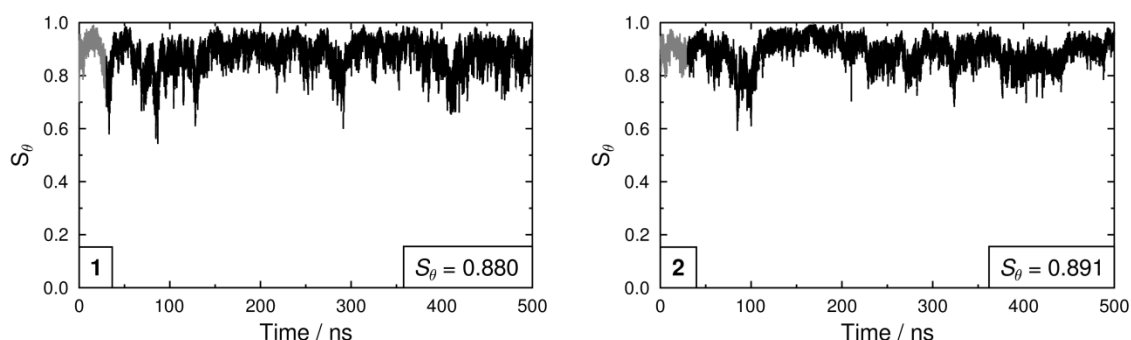


Figure 7.7 Plots of the calculated order parameters, S_θ (surface), of the principal surface tensor axes of the dye molecules during the guest-host MD simulations of **1** and **2**. Sections shown in black (≥ 30 ns) were used to calculate the average values.

Table 7.3 Average order parameters of the principal surface tensor axes of **1** and **2**, calculated from the guest-host MD simulations.

Dye	$\langle S_\theta \rangle$	$\langle S_{xx} - S_{yy} \rangle$
1	0.880	0.038
2	0.891	0.035

The average angles between the surface tensor alignment axes and the CO and AQ axes are listed in Table 7.4, and they demonstrate that the molecular alignment axes of the dyes are closer to the CO axes than the AQ axes, again providing quantification of the qualitative description of the behaviour reported for these dyes.^{332, 336} The surface tensor z axis is calculated to be better aligned with the CO axis for **2** than **1**, consistent with the greater symmetry of **2** than **1**, and its lower experimental order parameter.

Table 7.4 Average angles and standard deviations between the surface tensor alignment axes and the CO and AQ axes of **1** and **2**.

Dye	$\langle \text{Surf. vs CO} \rangle / ^\circ$	$\langle \text{Surf. vs AQ} \rangle / ^\circ$
1	27.1 \pm 9.0	64.1 \pm 9.7
2	7.5 \pm 4.0	89.2 \pm 6.5

For each molecule at each frame of the simulation trajectories, fixed TDM orientations were calculated against the AQ and CO axes as described in detail in Section 5.2.6.1 of Chapter 5. The average β and α angles describing these TDM axes within the molecular frame are listed in Table 6.9 alongside the average associated contributions to the calculated dichroic order parameters, S_ϕ , calculated using the S_θ values listed in Table 7.3.

Table 7.5 Average angles, β and α , and their standard deviations of the fixed visible TDMs of dyes **1** and **2** calculated from the guest-host MD simulations. The associated order parameter contributions and the calculated dichroic order parameters, S_ϕ , are also listed.

Dye	$\langle \beta \rangle / ^\circ$	$\langle S_\beta \rangle$	$\langle \alpha \rangle / ^\circ$	$0.5 \langle S_{xx} - S_{yy} \rangle \langle \sin^2 \beta \cos 2\alpha \rangle$	S_ϕ
1	68.9 \pm 9.7	-0.275	6.9 \pm 4.9	0.015	-0.227
2	89.4 \pm 6.5	-0.481	4.5 \pm 3.4	0.017	-0.412

The average β angles calculated for **1** and **2** show that there is a large calculated offset between the molecular alignment axes and the visible TDMs. This offset manifests as a negative order parameter contribution, $\langle S_\beta \rangle$, which is less negative for **1** than for **2**. Combining these contributions with those of the molecular alignment listed in Table 7.3, to obtain the overall dichroic order parameters demonstrates that both dyes are modelled to have negative dichroic order parameters by this method. Additionally, the

trend between the order parameters of these dyes matches that obtained experimentally, with **1** having a less negative order parameter than **2**. The contributions of biaxiality to the calculated dichroic order parameters of **1** and **2** are more significant than for the five dyes studied previously, primarily attributable to their larger β angles.

Although the scope of this comparison with experiment is limited by the different hosts used, it is noticeable that the magnitudes of the dichroic order parameters calculated from the guest-host MD simulations of **1** and **2** (Table 6.9) are greater than the experimental values (Table 7.1). This difference is consistent with the overestimation of the order parameters of the dyes presented in Chapter 5, which was attributed primarily to an overestimation of the host order parameter. Additionally, there may be a discrepancy arising from the influence of molecular flexibility on the orientations of the TDMs within dyes **1** and **2**, which was shown in Chapter 5 to result in a significant decrease in the calculated order parameters of 15NB3 and 15NB3OH; however, this more detailed level of analysis including binned TDMs rather than fixed TDMs was beyond the scope of the work reported here.

7.3.1.3 Isolated molecule MD simulations

In Chapter 6 it was demonstrated that the application of the surface tensor approach to classical molecular dynamics simulations of isolated molecules enabled the experimental trend in the order parameters of the five dyes to be replicated; this trend was also consistent with the trends obtained from the guest-host simulations. Isolated molecule MD simulations were carried out for **1** and **2**, using the same force field parameters as used to describe these dyes in the guest-host simulations, given above in Section 7.3.1.2, and with the same simulation parameters that were used for the isolated molecule simulations reported in Chapter 6.

The average inverse eigenvalues values of the surface tensors calculated for isolated molecules of **1** and **2** over the course of the 10 ns trajectories are listed in Table 7.6, and the cuboids calculated to generate these same eigenvalues are shown in Figure 7.8. The cuboids and eigenvalues demonstrate that these dyes may be described qualitatively as having rod-like structures, but they are less elongated than the five dyes studied previously in this work, and **1** is calculated to be significantly less rod-like than **2**.

Table 7.6 Average surface tensor inverse eigenvalues, $-\langle t_{ii} \rangle$, and standard deviations obtained for the dye molecules during the isolated molecule simulations.

Dye	$-\langle t_{xx} \rangle / \text{\AA}^2$	$-\langle t_{yy} \rangle / \text{\AA}^2$	$-\langle t_{zz} \rangle / \text{\AA}^2$
1	163.7 \pm 12.1	270.3 \pm 14.5	93.4 \pm 12.8
2	152.6 \pm 9.6	299.6 \pm 11.8	76.5 \pm 8.7

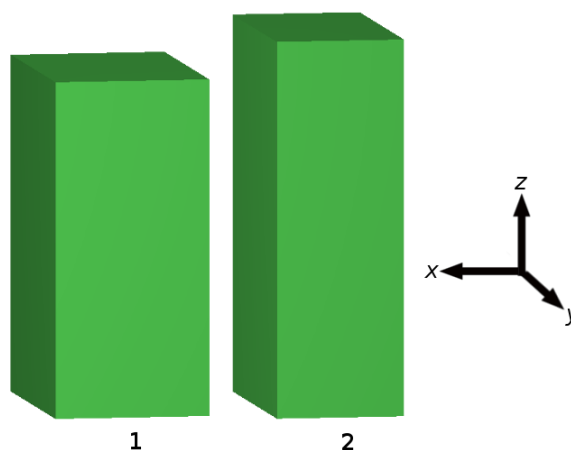


Figure 7.8 Cuboids, drawn to scale, with face areas proportional to $-t_{xx}$, $-t_{yy}$, and $-t_{zz}$, of **1** and **2**, as determined from the MD simulations of isolated molecules.

The average order parameters, $\langle S_{zz} \rangle$ and $\langle S_{xx} - S_{yy} \rangle$, of **1** and **2**, determined from the surface tensor eigenvalues at each step of the isolated molecule simulations using the approach described in Chapter 5 and an orienting potential of $\varepsilon = 0.04 \text{\AA}^{-2}$, are listed in Table 7.7. A comparison of these values shows that **2** is calculated to be better aligned than **1** and that they are both calculated to exhibit comparable biaxiality in their molecular alignment. This higher molecular alignment of **2** than **1** is consistent with the trend obtained from the guest-host simulations, and the smaller magnitudes obtained from the isolated molecule simulations than the guest-host simulations are consistent with those presented for the 1,5- and 2,6-disubstituted dyes in Chapter 6.

Table 7.7 Average values of the order parameters, S_{zz} and $S_{xx} - S_{yy}$, of **1** and **2** determined from the surface tensor eigenvalues at each frame of the trajectories of the isolated molecule MD simulations, using and orienting potential of $\varepsilon = 0.04 \text{\AA}^{-2}$.

Dye	$\langle S_{zz} \rangle$	$\langle S_{xx} - S_{yy} \rangle$
1	0.690	0.155
2	0.737	0.144

The average calculated β and α angles describing the orientations of the TDMS in the molecular frames of **1** and **2** defined by the principal surface tensor axes are given in Table 7.8 along with the order parameter contributions and the dichroic order parameters, S_{ϕ} . A comparison of these values with the equivalent values determined

from the guest-host simulations, listed in Table 7.5, shows that the average β angles for each dye are within 0.3° between the two sets of simulations, and the associated average order parameters, $\langle S_\beta \rangle$, differ by < 0.03 , attributable to comparable conformations being explored within the respective simulations. The S_ϕ values show that this isolated molecule method also predicts both dyes to have negative dichroic order parameters, with **2** again calculated to have a more negative order parameter than **1**, consistent with the experimental values and the values calculated from the guest-host simulations. These order parameters are both smaller in magnitude than those calculated from the guest-host simulations, and closer to the experimental values. This difference is consistent with the equivalent order parameters calculated using these methods for the dyes discussed in Chapters 5 and 6.

Table 7.8 Average angles, β and α , and their standard deviations of the fixed visible TDMs of dyes **1** and **2** calculated from the isolated molecule MD simulations. The associated order parameter contributions and the calculated dichroic order parameters, S_ϕ , are also listed.

Dye	$\langle \beta \rangle / ^\circ$	$\langle S_\beta \rangle$	$\langle \alpha \rangle / ^\circ$	$0.5(S_{xx} - S_{yy}) \langle \sin^2 \beta \cos 2\alpha \rangle$	S_ϕ
1	68.8 ± 7.9	-0.247	7.9 ± 6.0	0.061	-0.110
2	89.7 ± 7.4	-0.475	4.4 ± 3.3	0.069	-0.281

The consistency between the dichroic order parameters calculated from guest-host MD simulations and those calculated from isolated molecule MD simulations suggests that the application of mean-field theory to more varied structures that exhibit significantly different experimental dichroic order parameters from those discussed previously in this thesis may be valid, highlighting the potential scope of such an approach.

7.3.1.4 Surface analysis of DFT optimised structures

The application of the surface tensor model to single DFT optimised structures in order to rapidly calculate dichroic order parameters was assessed in Chapter 6. The approach was shown to provide a strong positive correlation between the calculated and experimental order parameters for the five dyes studied.

The molecular alignment order parameters, S_{zz} and $S_{xx} - S_{yy}$, calculated from the optimised structures of **1** and **2**, shown in Figure 7.4, are listed in Table 7.9. The molecular alignment order parameters, S_{zz} , are calculated to be greater than those obtained from the isolated molecule MD simulations, and may be attributed to the static

all-*trans* conformations of the optimised structures. The calculated dichroic order parameters, also listed in Table 7.9, again show both dyes to exhibit negative dichroism, with the order parameter of **2** being more negative than that of **1**, consistent with the previous calculated values.

Table 7.9 Order parameter, S_{zz} and $S_{xx} - S_{yy}$, determined from surface tensor analysis of the DFT optimised structures of **1** and **2**, using an orienting strength of $\varepsilon = 0.04 \text{ \AA}^{-2}$. Also listed are calculated angles, β and α , of the fixed visible TDMs and the associated order parameter contributions and the calculated dichroic order parameters, S_ϕ .

Dye	S_{zz}	$S_{xx} - S_{yy}$	$\beta / ^\circ$	S_β	$\alpha / ^\circ$	$0.5\langle S_{xx} - S_{yy} \rangle \langle \sin^2 \beta \cos 2\alpha \rangle$	S_ϕ
1	0.783	0.089	60.0	-0.126	4.2	0.051	-0.065
2	0.744	0.142	90.0	-0.500	2.4	0.071	-0.301

The good match between these calculated values and the experimental values supports the validity of this approach in a wider context than that considered in Chapter 6, highlighting the potential scope of this approach for an initial assessment of the dichroic order parameters of dyes in general within nematic hosts.

7.3.2 Surface tensor analysis of DFT optimised structures: scope of methods

This section extends the application of the surface tensor model to single DFT optimised structures, described above in section 7.3.1.4 and in Section 6.3.3 of Chapter 6, to dyes from different classes that exhibit a range of reported experimental dichroic order parameters. The reported experimental values from the literature that are included in this section were obtained in a range of nematic hosts, and are likely to have been recorded at a range of temperatures that were not always specified, but the application of mean-field theory used here enables a typical nematic orienting potential to be used that may be considered to apply to the different hosts.

The specific dyes considered in this section are anthraquinone dyes and azo dyes, and they were selected to provide a range of reported order parameters. Dyes with relatively short alkyl chains were generally chosen in order to minimise the influence imposed by the choice of molecular conformation for the single optimised structure.

In this section the aim was to test the method as a “black-box” approach to comparing calculated and experimental order parameters, and not to rationalise experimental or

calculated trends in detail. All the dyes were optimised from all-*trans*, rod-like conformations and rigorous testing was not carried out to determine the relative energies of different conformations, on the premise that, ideally, a black-box method should not rely on such input considerations. For each structure, the five lowest energy transitions were calculated, and those at > 300 nm with associated oscillator strengths of > 0.05 are reported. The orientations of the visible TDMs and the principal surface tensor axes were calculated, and these are shown overlaid on the optimised structures for each dye.

In the following three sections the approach is applied first to a set of anthraquinone dyes, then to a set of azo dyes, and finally a comparison is made between calculated and experimental dichroic order parameters for all of the dyes to which this computational method has been applied.

7.3.2.1 Anthraquinone dyes

Tables 7.10 – 7.12 show a variety of anthraquinone derivatives, **3** – **9**, that have been reported to exhibit a range of experimental order parameters between -0.15 and 0.78 , as listed in the tables, further demonstrating the range order parameters that are exhibited by anthraquinone dyes.

The DFT optimised structures of dyes **3** – **9** are also given in Tables 7.10 – 7.12 along with the calculated visible TDMs and the principal surface tensor axes, which show qualitatively that the degree of alignment between the TDMs and the principal surface tensor axes vary quite significantly between these dyes.

Table 7.10 Dyes **3** and **4** and their reported experimental dichroic order parameters, S_{exp} , in Lixon 5052-XX measured at wavelengths, λ_{exp} .⁶⁴ Also shown are DFT optimised structures with calculated principal surface tensor axes (turquoise) and visible TDMs (red) overlaid, along with the calculated wavelengths, λ_{calc} , and oscillator strengths, f_{calc} of the allowed visible transitions.

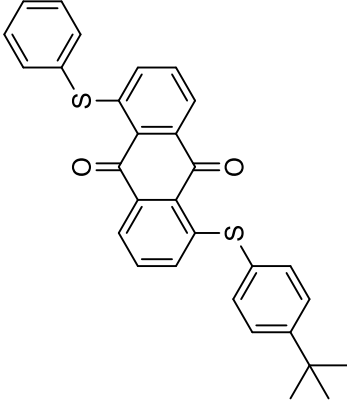
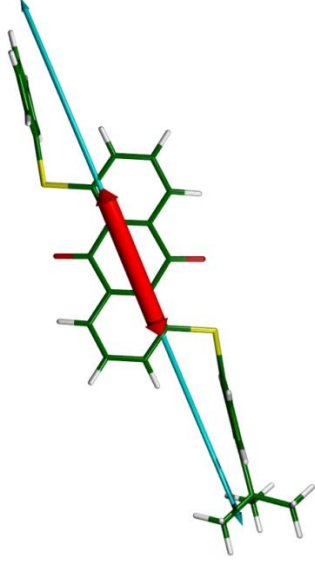
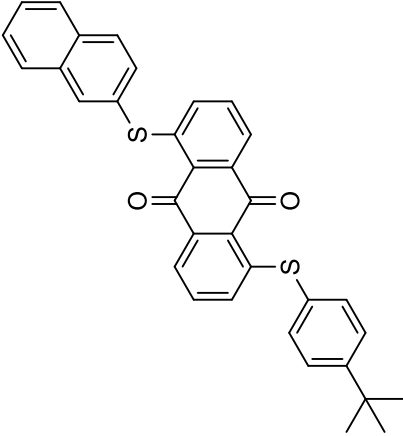
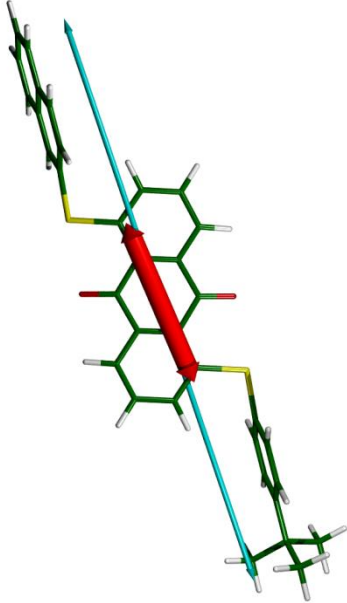
Structure	$\lambda_{\text{exp}} / \text{nm}$	S_{exp}	$\lambda_{\text{calc}} / \text{nm}$	f_{calc}
 <p>3</p>	464	0.76	453	0.2650
				
 <p>4</p>	465	0.78	457	0.2800
				

Table 7.11 Dyes **5** – **7** and their reported experimental dichroic order parameters, S_{exp} , in Lixon GR 41 measured at wavelengths, λ_{exp} .²²⁹ Also shown are DFT optimised structures with calculated principal surface tensor axes (turquoise) and visible TDMs (red) overlaid, along with the calculated wavelengths, λ_{calc} , and oscillator strengths, f_{calc} , of the allowed visible transition; those in *italics* are not shown on the optimised structures.

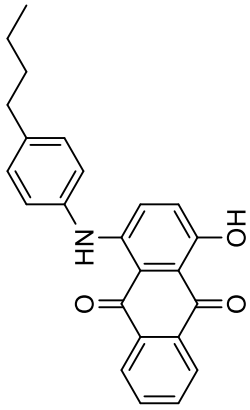
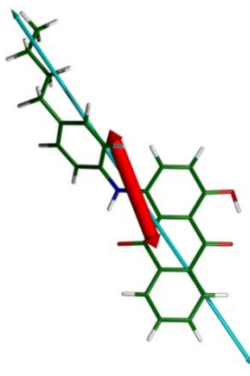
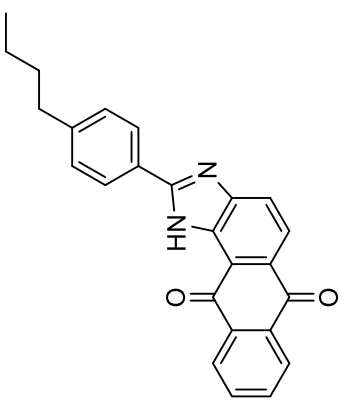
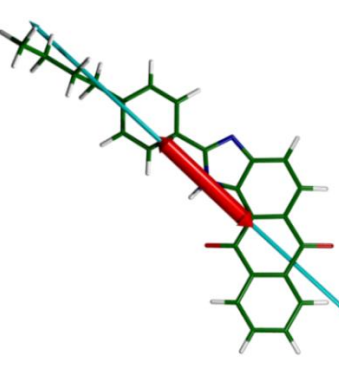
Structure	$\lambda_{\text{exp}} / \text{nm}$	S_{exp}	$\lambda_{\text{calc}} / \text{nm}$	f_{calc}
 5	590	0.59	569 368	0.2318 <i>0.0918</i>
 6	532	0.41	566	0.0979
 7	417	0.45	446 390	0.2533 <i>0.0946</i>
				

Table 7.12 Dyes **8** and **9** and their reported experimental dichroic order parameters, S_{exp} , in ZLI-1132 measured at wavelengths, λ_{exp} .³³² Also shown are DFT optimised structures with calculated principal surface tensor axes (turquoise) and visible TDMs (red) overlaid, along with the calculated wavelengths, λ_{calc} , and oscillator strengths, f_{calc} of the allowed visible transition; those in italics are not shown on the optimised structures.

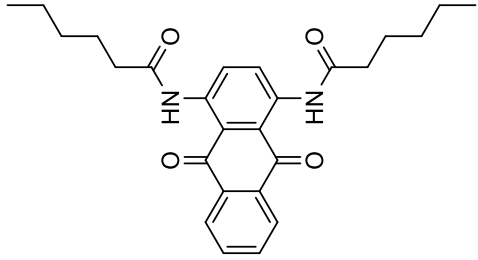
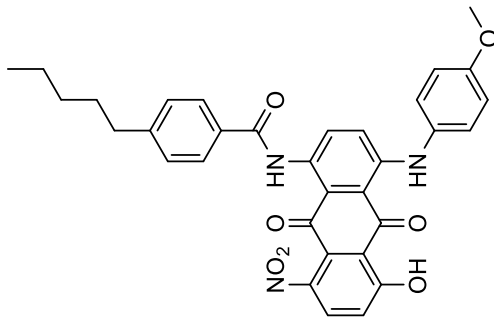
Structure	$\lambda_{\text{exp}} / \text{nm}$	S_{exp}	$\lambda_{\text{calc}} / \text{nm}$	f_{calc}
 8	493	-0.15	496	0.1789
 9	642	-0.05	623 452 415	0.2158 0.1027 0.0590

Table 7.13 gives the calculated molecular order parameters, S_{zz} and $S_{xx} - S_{yy}$, of dyes **3** – **9** showing that all of the dyes are predicted to have molecular order parameters >0.6 , consistent with their relatively rod-like structures. However, the calculated β values and associated order parameters, S_{β} , also listed in Table 7.12, show a large variation between the dyes and hence it may be considered that the TDM orientations are an important factor in the observed variation in the dichroic order parameters. This observation is consistent with the five dyes discussed in Section 4.3.3 of Chapter 4.

Table 7.13 Order parameter, S_{zz} and $S_{xx} - S_{yy}$, determined from surface tensor analysis of the DFT optimised structures of **3** to **9**, using an orienting strength of $\varepsilon = 0.04 \text{ \AA}^{-2}$. Also listed are calculated angles, β and α , of the fixed visible TDMs and the associated biaxial order parameters and calculated dichroic order parameters, S_{ϕ} .

Dye	S_{zz}	$S_{xx} - S_{yy}$	$\beta / ^{\circ}$	S_{β}	$\alpha / ^{\circ}$	$0.5(S_{xx} - S_{yy})(\sin^2\beta \cos 2\alpha)$	S_{ϕ}
3	0.775	0.051	0.3	1.000	7.5	0.000	0.775
4	0.783	0.053	4.9	0.989	28.6	0.000	0.775
5	0.640	0.172	12.8	0.926	6.2	0.004	0.597
6	0.648	0.194	21.2	0.804	10.3	0.012	0.532
7	0.604	0.229	3.1	0.996	78.5	0.000	0.601
8	0.676	0.189	88.8	-0.499	0.8	0.094	-0.243
9	0.751	0.130	65.2	-0.236	5.2	0.053	-0.125

The calculated dichroic order parameters, S_{ϕ} , from applying the surface tensor model to optimised structures of dyes **1** – **9** are shown plotted against the experimental values in Figure 7.9. This plot shows a good match between the sets of values with the value of $R^2 = 0.9742$ showing a strong linear correlation, and the gradient of 1.078 and intercept of -0.007 being close to the ideal values of 1 and 0, respectively. This good match supports the suitability of this approach to predicting order parameters and provides confidence in the scope of the approach.

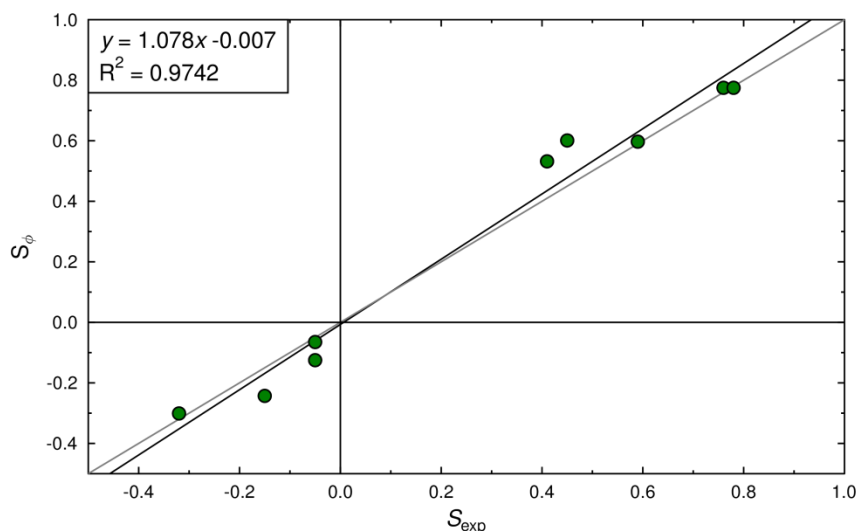


Figure 7.9 Plot of calculated dichroic order parameters using optimised DFT structures and the surface tensor approach, S_{calc} , vs. experimental dichroic order parameters, S_{exp} , for **1** to **9**. The grey line shows a perfect match between calculated and experimental values.

7.3.2.2 Azo dyes

Tables 7.14 and 7.15 give structures of azo dyes **10** – **19**, along with the experimental order parameters reported in the literature, obtained in a range of nematic hosts. The values of the order parameters between -0.18 and 0.78 demonstrate, like the anthraquinone dyes in Section 7.3.2.1, the wide range of order parameters that may be exhibited by these dyes.

A qualitative comparison of the degree of alignment of the visible TDMs and principal surface tensor axes from the optimised structures, also given in Tables 7.14 and 7.15, show the axes are very well aligned in all of the dyes, except for structure **19**. This observation is in contrast to that observed for the anthraquinone dyes above, and is consistent with the generally higher experimental order parameters of azo dyes than anthraquinone dyes reported in the literature.²⁴

Table 7.14 Dyes **10 - 13** and dyes **14 -15** and their reported experimental dichroic order parameters, S_{exp} , in E7 and Lixon GR 41, respectively, measured at wavelengths, λ_{exp} .^{50 229} Also shown are DFT optimised structures with calculated principal surface tensor axes (turquoise) and visible TDMs (red) overlaid, along with the calculated wavelengths, λ_{calc} , and oscillator strengths, f_{calc} , of the allowed visible transitions; those in italics are not shown on the optimised structures.

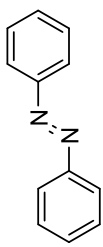
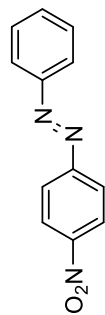
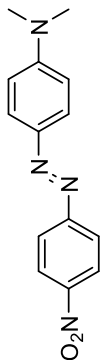
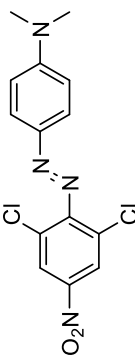
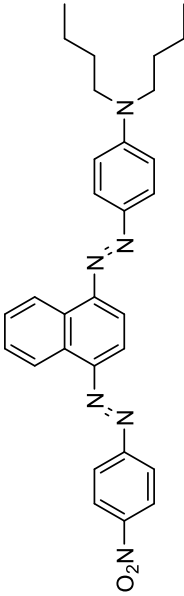
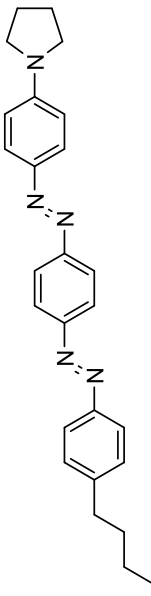
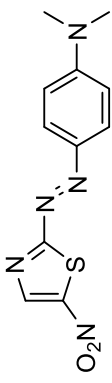
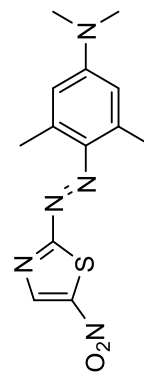
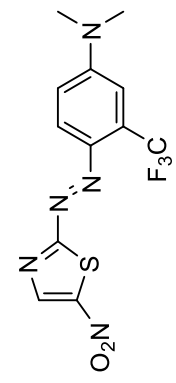
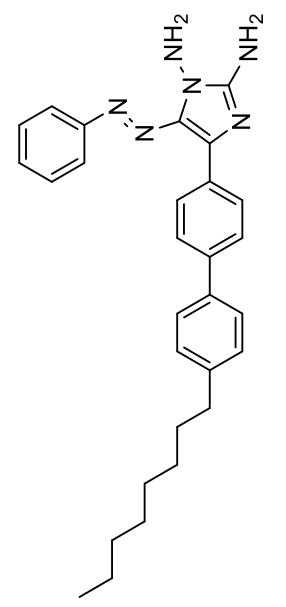
	Structure	$\lambda_{\text{exp}} / \text{nm}$	S_{exp}	$\lambda_{\text{calc}} / \text{nm}$	f_{calc}
10		450	0.37	329 302	0.7732 0.0542
11		465	0.45	356	0.8424
12		505	0.61	444 332	0.9095 0.2363
13		470	0.54	500 447 355 342	0.1136 0.4294 0.0748 0.4003
14		591	0.66	594 469 420	1.3399 0.0556 0.2546
15		509	0.78	483 376	1.5963 0.4763

Table 7.15 Dyes **16** - **18** and dye **19** and their reported experimental dichroic order parameters, S_{exp} , in E7 and 4OCB/4CB, respectively, measured at wavelengths, λ_{exp} .⁵⁰⁻³³⁹ Also shown are DFT optimised structures with calculated principal surface tensor axes (turquoise) and visible TDMs (red) overlaid, along with the calculated wavelengths, λ_{calc} , and oscillator strengths, f_{calc} of the allowed visible transitions; those in italics are not shown on the optimised structures.

	Structure	$\lambda_{\text{exp}} / \text{nm}$	S_{exp}	$\lambda_{\text{calc}} / \text{nm}$	f_{calc}
16		590	0.62	465 <i>351</i>	0.9555 <i>0.0608</i>
17		565	0.45	465	0.9297
18		575	0.52	463	0.9351
19		476	-0.18	466 430 <i>361</i>	0.3604 <i>0.4283</i> <i>0.1955</i>

The molecular order parameters, S_{zz} and $S_{xx} - S_{yy}$, of dyes **10** – **19** listed in Table 7.16 show that they are calculated to exhibit a range of molecular order parameters between 0.383 and 0.776, representing a wider range than the anthraquinone dyes **1** – **9**. The β values and associated order parameter contributions, S_β , are also given in Table 7.16 and show that all these dyes have values of $S_\beta > 0.976$, with the exception of **19**, suggesting that the primary cause of variation in the dichroic order parameters of these dyes is the molecular alignment rather than the TDM alignment. This observation is in contrast to the anthraquinone dyes discussed above.

Table 7.16 Order parameter, S_{zz} and $S_{xx} - S_{yy}$, determined from surface tensor analysis of the DFT optimised structures of **3** to **9**, using an orienting strength of $\varepsilon = 0.04 \text{ \AA}^{-2}$. Also listed are calculated angles, β and α , of the fixed visible TDMs and the associated biaxial order parameters and calculated dichroic order parameters, S_ϕ .

Dye	S_{zz}	$S_{xx} - S_{yy}$	$\beta / ^\circ$	S_β	$\alpha / ^\circ$	$0.5\langle S_{xx} - S_{yy} \rangle \langle \sin^2 \beta \cos 2\alpha \rangle$	S_ϕ
10	0.383	0.309	1.4	0.999	0.2	0.000	0.383
11	0.473	0.271	0.1	1.000	42.8	0.000	0.473
12	0.576	0.214	1.9	0.998	15.5	0.000	0.575
13	0.545	0.269	2.6	0.997	16.2	0.000	0.543
14	0.723	0.128	7.3	0.976	6.4	0.001	0.706
15	0.776	0.086	5.0	0.989	42.7	0.000	0.768
16	0.541	0.230	0.2	1.000	0.2	0.000	0.541
17	0.520	0.281	0.4	1.000	0.9	0.000	0.520
18	0.529	0.261	1.2	0.999	0.0	0.000	0.529
19	0.717	0.146	62.3	-0.176	6.5	0.056	-0.071

A plot of calculated dichroic order parameters versus the experimental order parameters is given in Figure 7.10 again demonstrating a strong linear correlation between the calculated and experimental values, shown by the value of $R^2 = 0.9724$ for the fit. The gradient of 0.859 and intercept of 0.083 for the fit are also reasonably close to the ideal values of 1 and 0, respectively. This match between calculated and experimental values demonstrates the potential scope of this method of dichroic order parameter calculation beyond the anthraquinone dyes studied previously in this thesis.

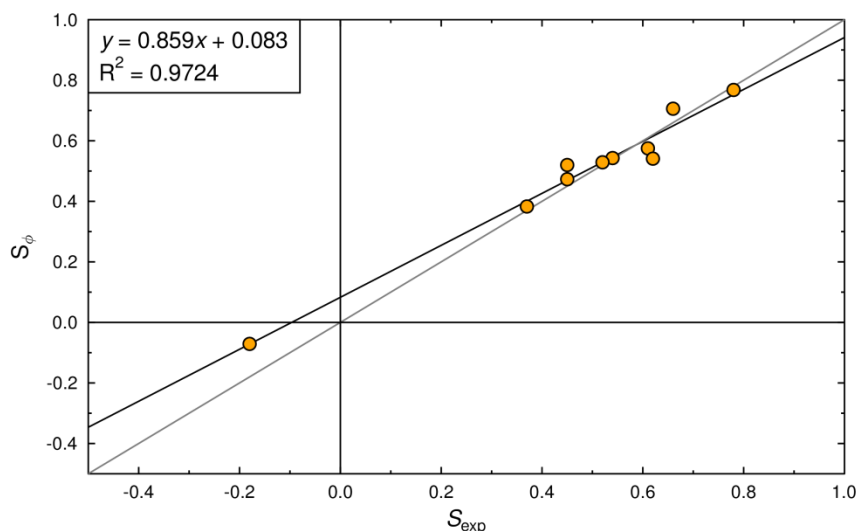


Figure 7.10 Plots of calculated dichroic order parameters, S_{calc} , vs. experimental dichroic order parameters, S_{exp} , for **10** to **19**. The grey line shows a perfect match between calculated and experimental values.

7.3.2.3 Overall comparison

The prediction of dichroic order parameters, by applying the surface tensor approach to single DFT optimised structures and calculating TDM orientations using TD-DFT calculations, has been carried out for the five anthraquinone dyes which were analysed in Chapters 3-6, and for the nine anthraquinone dyes **1** to **9** and the ten azo dyes **10** to **19** reported in this chapter. For each set of dyes, a strong positive correlation was observed between the calculated and experimental dichroic order parameters obtained in nematic hosts, despite the experimental values being obtained under a range of conditions.

The calculated dichroic order parameters determined from this approach are plotted against the experimental values for all 24 dyes in Figure 7.11, demonstrating a strong positive correlation between the calculated and experimental values, even when considering the different dye classes. The value of $R^2 = 0.9549$ shows the linear correlation is not as strong as for the individual fits (Figures 6.15, 7.9 and 7.10), but it is still indicative of a good match between calculation and experiment. The gradient and intercept values of 1.045 and 0.017, respectively, are very close to the ideal values of 1 and 0, again providing confidence in the scope of structures to which approach described here may be applied.

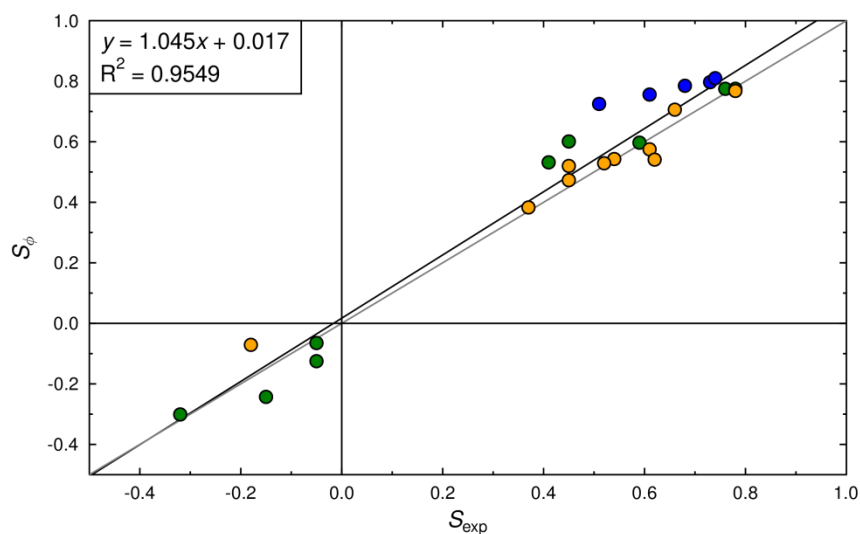


Figure 7.11 Plot of calculated dichroic order parameters from single DFT optimised structures using the surface tensor method, S_ϕ , against experimental dichroic order parameters, S_{exp} , of anthraquinone dyes **1** to **9** (green), azo dyes **10** to **19** (orange) and the dyes studied in Chapters 3 – 6 (blue). The grey line shows a perfect match between calculated and experimental values.

The results in Section 6.3.3 of Chapter 6 and in Section 7.3.1 of this chapter demonstrated that this approach of analysing a single optimised geometry did not give the best match between calculated and experimental dichroic order parameters, and consideration of molecular flexibility was shown to provide an overall improvement in the match. Thus, this analysis of single structures may not be considered the best approach tested, but it does provide a means of rapidly calculating dichroic order parameters. For some structures, in particular those with a large degree of flexibility, the importance of flexibility may be greater than those analysed here and so this analysis of single structures may be less suited to calculating dichroic order parameters.

7.4 Conclusions

In Section 7.3.1 it was demonstrated that the use of guest-host MD simulations and isolated molecule MD simulations enables the calculation of dichroic order parameters of anthraquinone dyes reported to exhibit negative dichroism. The calculated values were close to those obtained experimentally, providing confidence in the scope of the methods developed in Chapters 3 – 6 beyond the dye structures analysed previously.

In Section 7.3.2, analysis of single optimised structures of a range of dye molecules from different classes, exhibiting a wide range of reported experimental dichroic order parameters, resulted in calculated values exhibiting a strong positive correlation with the reported experimental values. Comparisons of these calculated and experimental values within the anthraquinone and azo dye classes resulted in better linear matches than those obtained when the values were compared over all the dyes studied.

The reported experimental order parameters of the dyes considered here had been obtained in a range of nematic hosts, and were likely to have been recorded at a range of temperatures, such that deviations from ideal fits between calculated and experimental values may be partially attributed to these differences in experimental conditions. The discrepancies may also be partially attributed to the “black-box” approach taken in calculating the values reported in this section because the potential contributions from different molecular conformations were not considered: improved matches may be obtained if the contributions of different conformers to the dichroic order parameters were considered, but this was beyond the intended scope of this assessment. Despite the slight discrepancies between the calculated and experimental order parameters, the general match in the trends implies that the application of a single orienting potential in the surface tensor model to dyes within different nematic hosts is less significant than the variation in the order parameters arising from the structures of the different dyes.

Strong positive correlations across the dyes studied highlight the suitability of this method for rapid assessment of potential dye structures for use within guest-host systems. The method does not take into account the molecular flexibility of the dyes, which is likely to be more significant for structures with long alkyl chains, and the method is likely to be better suited for the assessment of core dye structures.

In addition to the considerations outlined above, it is relevant to note that the full DFT, TD-DFT and surface tensor analyses for all of the structures **1** to **19** were carried out within a few days on a desktop PC, underlining the speed at which such assessments may be carried out. For comparison, several weeks/months were required for each of the guest-host MD simulations and analyses reported in Chapter 4.

Chapter 8

Conclusions and further work

The five dyes chosen for this work proved to be a good set of compounds to explore some general aspects of the behaviour of dyes as guests within liquid crystal hosts. The combination of experimental and computational studies was found to be a useful strategy to understanding such behaviour, leading to the development and testing of new computational approaches.

8.1 Structure, spectroscopy and stability

8.1.1 Structural comparisons

The optimised structures from DFT calculations discussed in Chapter 3 demonstrated a reasonable match with reported crystal structures of similar compounds, and the calculated spectra generally provided a good match with the experimental data determined as part of this work. Such calculations enable rapid structural comparisons to be made between dye molecules, and quantifiable descriptions of molecular shape such as the aspect ratios and surface tensors may be unambiguously defined, which in itself is an important quality, particularly for meaningful comparisons to be made between different studies. Within the specific systems studied in Chapter 3, the trend in aspect ratios was shown to match that of the experimental dichroic order parameters, supporting the generally observed behaviour of dyes in liquid crystal hosts, that dichroic order parameters typically increase with the molecular length: breadth ratio.

8.1.2 UV-visible absorption spectroscopy

UV-visible absorption spectroscopy showed that solutions of the dyes exhibit a range of absorption wavelengths, and polarised UV-visible absorption spectra of aligned samples of the dyes in E7 showed them to exhibit a range of dichroic order parameters. The use of time-dependent DFT calculations provided an indication of the number and orbital natures of the visible transitions exhibited by the dye molecules, along with their wavelengths and oscillator strengths, which provided a reasonably good match with

experimental values. Additionally, the calculations enabled the TDM orientations within the molecular frames of the dyes to be compared. Within the dyes studied here, the calculated deviations of the TDMs from the long molecular axes of the dyes matched the experimental trend in dichroic order parameters, and such comparisons may be extremely useful for dye design.

These studies could be extended to the calculation of vibrational fine structure of the visible transitions of the dyes, potentially leading to better prediction of band shapes and therefore potentially to an improved prediction of the experimental UV-visible absorption characteristics and the colours of the dyes.

8.1.3 Electrochemistry

The use of cyclic voltammetry enabled the determination of the first and second reduction potentials of each of the dyes, as well as the oxidation potentials of some of the dyes. Spectroelectrochemistry provided selective detection of the dye molecules and greater sensitivity than CV, enabling the use of acetonitrile as a solvent, thereby providing a means of accessing a wider range of potentials than CV, and hence the determination of both reduction and oxidation potentials for each of the dyes. These values provided an indication of the susceptibility of the dyes to reduction and oxidation, and the reversibility of the processes shown by CV gave an indication of the relative stabilities of the oxidised and reduced forms of the dyes. A relationship between dye colour and redox window was demonstrated here, and it indicated that anthraquinone dyes that absorb at long wavelengths may be more susceptible to oxidation than those absorbing at short wavelengths, whereas the susceptibility to reduction was found to be fairly consistent between each of the dyes. The calculated redox potentials of the dyes presented in Chapter 3 demonstrated a good match with the experimental values, potentially demonstrating the predictive capabilities of these calculation methods.

In the context of device design, further studies into the electrochemical stability of dyes are vital in order to extend this work to considering the stability of dyes within a device environment. Factors such as the presence of oxygen and/or water, the nature of the host and its redox properties, and the presence of any dopant species must be considered; it

is imperative that the system as a whole exhibits a high degree of stability, not just the dye molecules themselves.

8.1.4 Photochemistry

Although the photochemical stability of the dyes has not been a focus of the work presented in this thesis, this aspect of stability is vital to the practical use of guest-host systems. Similar to the electrochemical stability, discussed above, the relevant photochemical stability of a dye is its stability within the device environment, and thus the specific host and the presence of water, oxygen or other species may be relevant, and may influence the design not only of the dye molecules, but also other aspects of a guest-host system. There is significant scope for studies beyond those already reported in the literature on the photochemical stability of dyes within guest-host systems, in particular quantitative studies, and it is crucial that the photochemical stability of a guest-host system is considered, and ideally well understood, when carrying out the design of these systems in general. As mentioned in Chapter 3, photochemical properties of anthraquinones may be related to their electrochemical properties, and knowledge of such relationships may be valuable for device design.

8.1.5 Solubility

The solubility of a dye in a host mixture is crucial for obtaining high concentrations and thereby intense colours in a guest-host system. An assessment of solubility in liquid crystal hosts was beyond the scope of the work reported in this thesis, but is a vital consideration in the molecular design of dyes for guest-host systems. Ideally, quantitative structure-function relationships would enable prediction of solubility or solubility trends prior to synthesis, enabling synthesis to be targeted to the most promising candidate molecules.

8.2 Modelling alignment in liquid crystal hosts

8.2.1 Guest-host MD simulations

The guest-host MD simulations described in Chapters 4 – 6 may be considered to be the most rigorous of the methods used in this thesis to calculate molecular alignment, because no specific assumptions relating to the host alignment or the basis for alignment were made. These simulations enabled a novel approach to be taken in order to define and compare different descriptions of the molecular alignment axes of the dyes, from which the surface tensor method was found to provide a uniformly improved description of the alignment axes of the dyes compared with the more commonly used minimum MOI axes. The calculation of the order parameter of the host by using the surface tensor axes also provided a higher order parameter than that obtained by using the minimum MOI axes. Calculated dichroic order parameters of the dyes using the surface tensor axes gave an improved match with the experimental values compared with those calculated by using the minimum MOI axes, again providing support for defining the principal molecular axes as the surface tensor axes.

The combined use of MD and DFT, described in Chapters 4 and 5, provided a novel method of calculating dichroic order parameters, and also enabled the assessment of assumptions made within the theoretical models relating to dichroic order parameters; dye flexibility, in particular, was shown to have a significant influence on the calculated order parameters. When single β angles between the TDMs and molecular alignment axes were assumed, a reasonable match of the calculated dichroic order parameter trend with the experimental trend was obtained. However, the match was improved when flexibility was taken into account and a range of β angles were used, firstly by considering the visible TDM orientations as fixed relative to the anthraquinone cores, and secondly by calculating TDM orientations for a range of conformations and matching them to the dye structures at each frame of the MD trajectories.

The main focus in this thesis has been on replicating alignment trends, but the focus of further studies could be directed towards the prediction of absolute values of the dichroic order parameters. In this work, all of the calculated dichroic order parameters determined from the guest-host simulations were overestimated, and this is likely to be

attributable to the overestimation of the host order parameters, as discussed in Chapter 4. An obvious avenue for future work that is already relatively widely reported in the literature is the optimisation of host order parameters, which may help to improve the accuracy of dichroic order parameters calculated in this way. In the context of the work reported in this thesis, optimisation of the host order parameter would ideally be carried out in such a way that guest molecules could be included in the simulations without the need to use experimental values to parameterise intermolecular force constants relating to the guest molecules.

An alternative approach to improving the accuracy of the calculated dichroic order parameters would be to apply a scaling factor to the calculated molecular order parameters of the dyes based on the relative overestimation of the host compared with the experimental host order parameter. However, this approach would require some consideration; in this work, the experimental order parameter of E7 was determined from the dielectric anisotropy of an aligned sample, which may not be directly comparable with the orientational order parameter of the minimum MOI axes or surface tensor axes of component molecules within a simulation.

8.2.2 Isolated molecule studies

The application of the surface tensor model as a mean field approach enabled order parameters to be determined from simulations of isolated dye molecules, as described in Chapter 6. When the isolated dye molecules were simulated using the same classical force fields as used for the guest-host MD simulations, it was found that the geometries explored during the isolated molecule MD simulations of the dyes were similar to those explored during the guest-host MD simulations. However, detailed analysis of dihedral angle population distributions indicated some influence of the host on the molecular conformations of the dyes, and in general this influence may be more significant for guest molecules that exhibit a higher degree of flexibility than those described here. This influence may be attributed to a preferential selection of dye conformations within the guest-host MD simulations that do not disrupt neighbouring molecules from lying parallel to the director. Despite the differences in the explored conformations, the trends in the calculated dichroic order parameters between the isolated molecule simulations

and the guest-host simulations were remarkably similar, supporting the suitability of this mean field approach for modelling the alignment of these dyes in E7.

Applying this mean field approach to the analysis of CPMD simulations of isolated dye molecules also provided a good match with experimental dichroic order parameters, providing a computational method that was not reliant on the force constants inherent to the classical MD simulations. However, this benefit came at significant computational expense, and future work could focus on optimising the efficiency of such CPMD simulations.

The absolute values of the dichroic order parameters determined from the analysis of isolated dye molecule simulations were shown to be closer to the experimental values than those calculated from the guest-host MD simulations but, as discussed above, the focus in this thesis was largely on replicating trends and comparing methods. Thus, this aspect of the simulations was not a focus in this work, in which a single orienting potential, ε , was used throughout, but parameterisation could be carried out in future to determine the potential that gives rise to the best match with experiment. Additionally, the mean field approach imposes specific functional form on the orientational distribution function of the dyes, and although the surface tensor axes were found to be the best description of the alignment axes in the guest-host simulations, this does not provide any evidence for the validity of the functional form used in the surface tensor approach. A further comparison between the distribution functions predicted from the mean field approach and those obtained from the guest-host simulations may provide a measure of the validity of the mean field approach to these systems.

Isolated molecule simulations could also be extended to include the influence of the host on the conformations explored by the dyes by including an energy term corresponding to the surface tensor potential. Such an approach may be incorporated within a Monte Carlo method, as used for comparable simulations in the literature,^{340, 341} and would provide a set of molecular geometries that may be considered to be representative of those explored within a host environment.

8.2.3 Scope of methods

The study of negative dichroic dyes using classical MD simulations of guest-host mixtures and of isolated molecules, described in Chapter 7, provided evidence that the methods developed in this thesis are applicable to systems that exhibit quite different properties to those of the five dyes for which the methods were originally developed, providing further confidence in these computational methods.

Further, the calculation of the dichroic order parameters of 19 additional dyes from both the anthraquinone and azo dye classes provided a good match between calculated and reported experimental dichroic order parameters. However, from this comparison it was not possible to assess any underlying reasons for differences between the calculated and reported experimental values due to the range of conditions used in the measurements of the reported values. In order to better assess the computational methods, it would be beneficial for a study of a large number of dye molecules to be carried out in the future, in which experimental dichroic order parameters are determined under consistent conditions, providing an improved benchmark against which to assess computational methods.

8.2.4 Molecular biaxiality

The calculation of the dichroic order parameters incorporating the influences of molecular biaxiality indicated that the influence was negligible for the five dyes studied in Chapters 3 – 6, from all of the calculation methods used. This lack of influence was primarily attributed to a combination of small calculated molecular biaxial order parameters and small calculated values of β ; and, in a more general context, uniaxial alignment may be reasonably assumed when considering dyes with high dichroic order parameters. However, the analysis in Chapter 7 demonstrated that for the dyes reported to exhibit negative dichroic order parameters, the calculated contributions may be much greater. Thus, it is vital that the molecular biaxiality is taken into account when considering dyes with negative dichroism.

8.2.5 Validation of alignment contributions

The consideration of dichroic order parameters arising from separate contributions of molecular alignments and TDM alignments is very useful for their theoretical treatment, and the calculations described in this work enable a direct comparison to be made with experimental order parameters, but the relative accuracy of these calculated contributions cannot be assessed from the results obtained here. Further experimental work assessing the molecular alignment of dyes within liquid crystal hosts, such as by using NMR spectroscopy or vibrational spectroscopy, may enable the determination of experimental molecular alignment order parameters. Additionally, combining techniques such as polarised vibrational spectroscopy and polarised UV-visible absorption spectroscopy of aligned dye samples may enable the order parameter contributions arising from the orientations of the TDMs within dye molecules to be determined experimentally. Such studies would allow a valuable comparison with the calculated alignment contributions to be made, potentially enabling sources of error in the computational approaches described here to be determined and minimised.

8.3 Interdependence of molecular properties

The combination of the results presented in Chapters 3 – 6 relating to the colour, redox potentials, molecular shape, molecular flexibility, molecular alignment and transition dipole alignment of the five dyes in E7 that formed the focus of this work demonstrated a high degree of interdependence of these properties. Some of these properties, such as the colour and the redox potentials, and the flexibility and transition dipole alignments, were shown to be highly correlated: for these dyes, long wavelength absorption may be associated with low oxidation potentials, and greater molecular flexibility may generally be associated with lower dichroic order parameters. Conversely, other properties were shown to be less closely linked, but in a general context, whether properties are linked or not, their interdependence means that it is essential for all the relevant properties to be considered when choosing or designing dyes for guest-host systems. Thus, for guest-host systems of practical use to be developed, it is vital that the underlying molecular features giving rise to the various properties required are well understood, ideally through quantifiable structure-function relationships.

Appendix 1

8.3.1.1.1 Supplementary information relating to Chapter 3

A1.1 Determination of oscillator strengths

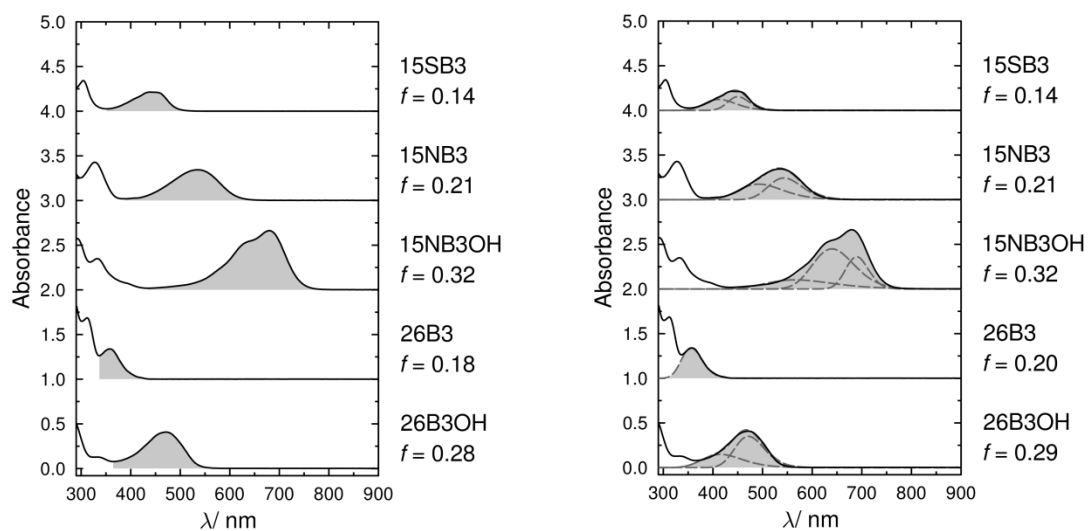


Figure A1.1 UV-vis absorption spectra of the dyes at $2.0 \times 10^{-4} \text{ mol dm}^{-3}$ in *p*-xylene, with shaded regions showing the integrated areas used to determine the oscillator strengths, f , using direct integrals (left) and fitted gaussian bands (right).

A1.2 Solvent dependence of λ_{\max} values

Table A1.1 Dielectric constants, polarizability volumes and dipole moments, μ , of the isotropic solvents used in this work.²¹⁷

	Dielectric constant	Polarisability volume / 10^{-24} cm^3	μ / D
DCM	9.08	6.48	1.60
Ethanol	24.30	5.11	1.69
Acetonitrile	37.50	4.40	3.92
Ethyl Acetate	6.02	9.70	1.78
<i>p</i> -Xylene	2.27	14.1	0.00

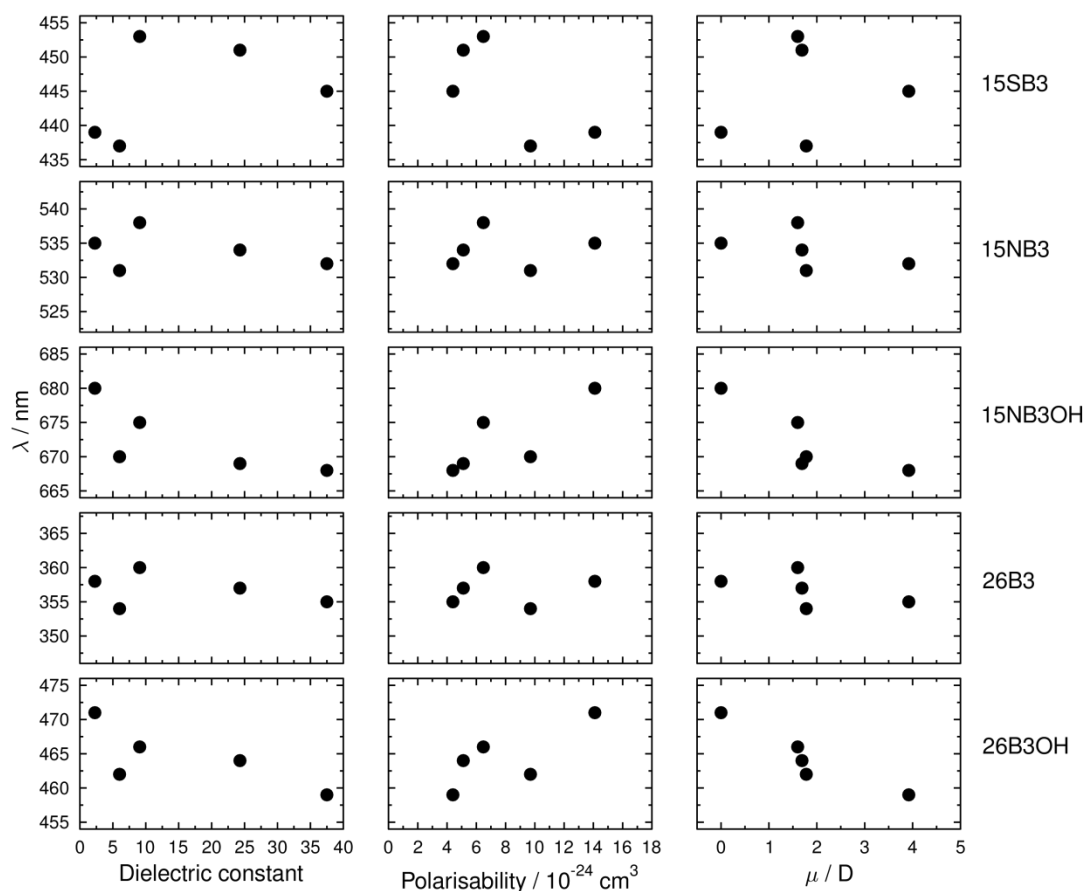


Figure A1.2 Plots of λ_{\max} of the dyes vs. solvent dielectric constant, polarizability and dipole moment, μ .²¹⁷

A1.3 Concentration dependence of UV-vis absorption spectra

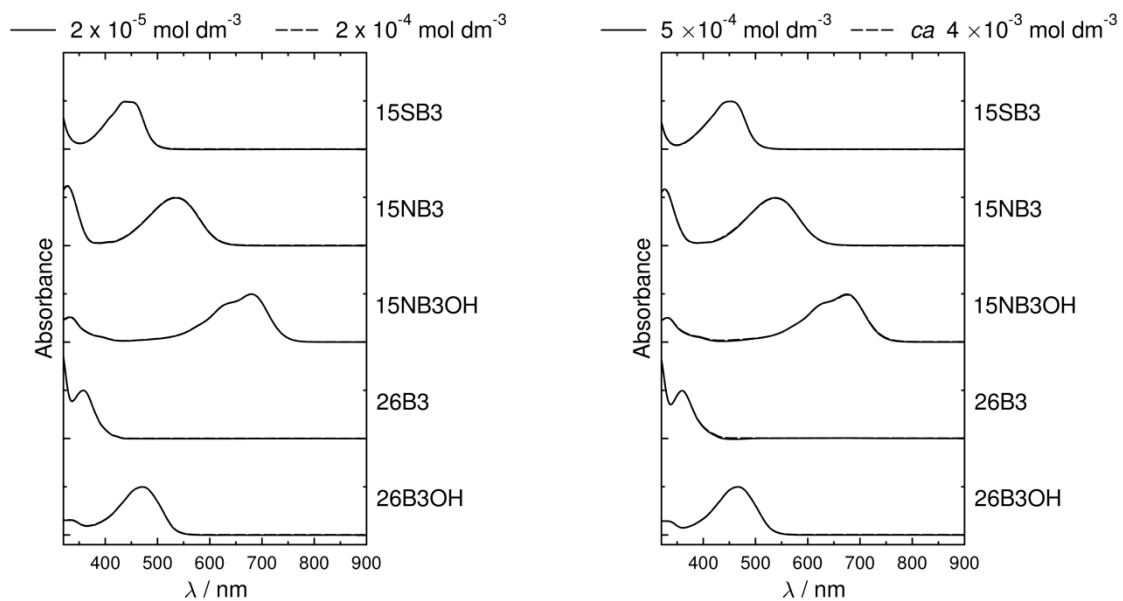


Figure A1.3 Spectral profiles of the dyes in *p*-xylene (left) and DCM (right) at the concentrations indicated above. The peak absorbances are normalised for clarity.

A1.4 Infrared spectroscopy

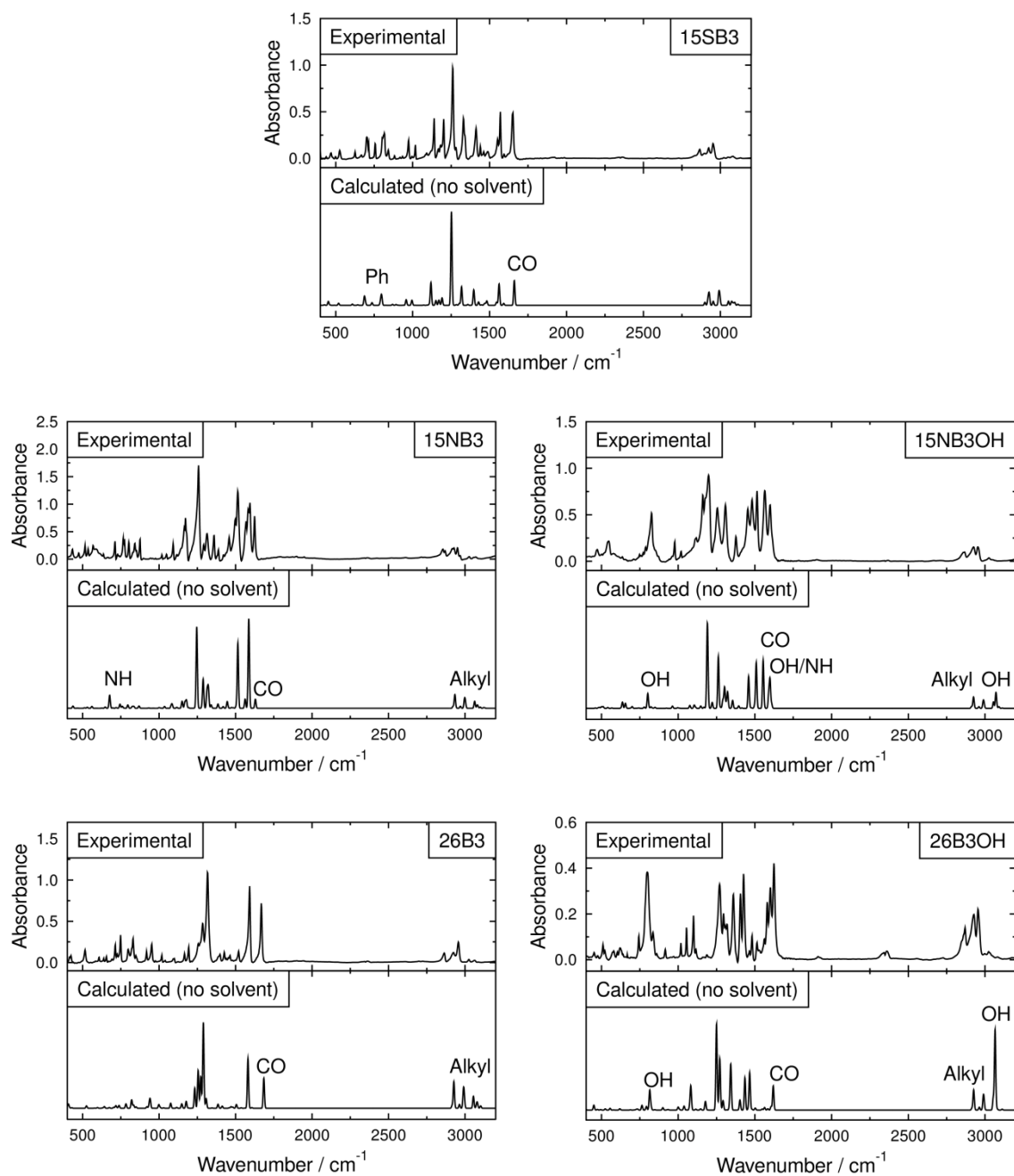


Figure A1.4 Experimental IR absorption spectra of the dyes in KBr disks along with calculated spectra determined from geometries optimised at the B3LYP/6-31g(d) level and some assignments.

A1.5 Raman spectroscopy

Experimental Raman spectra were not recorded between *ca* 1750 cm^{-1} and 2750 cm^{-1} due to the absence of calculated bands within these regions. The 26B3OH sample exhibited fluorescence, resulting in a low signal to noise ratio.

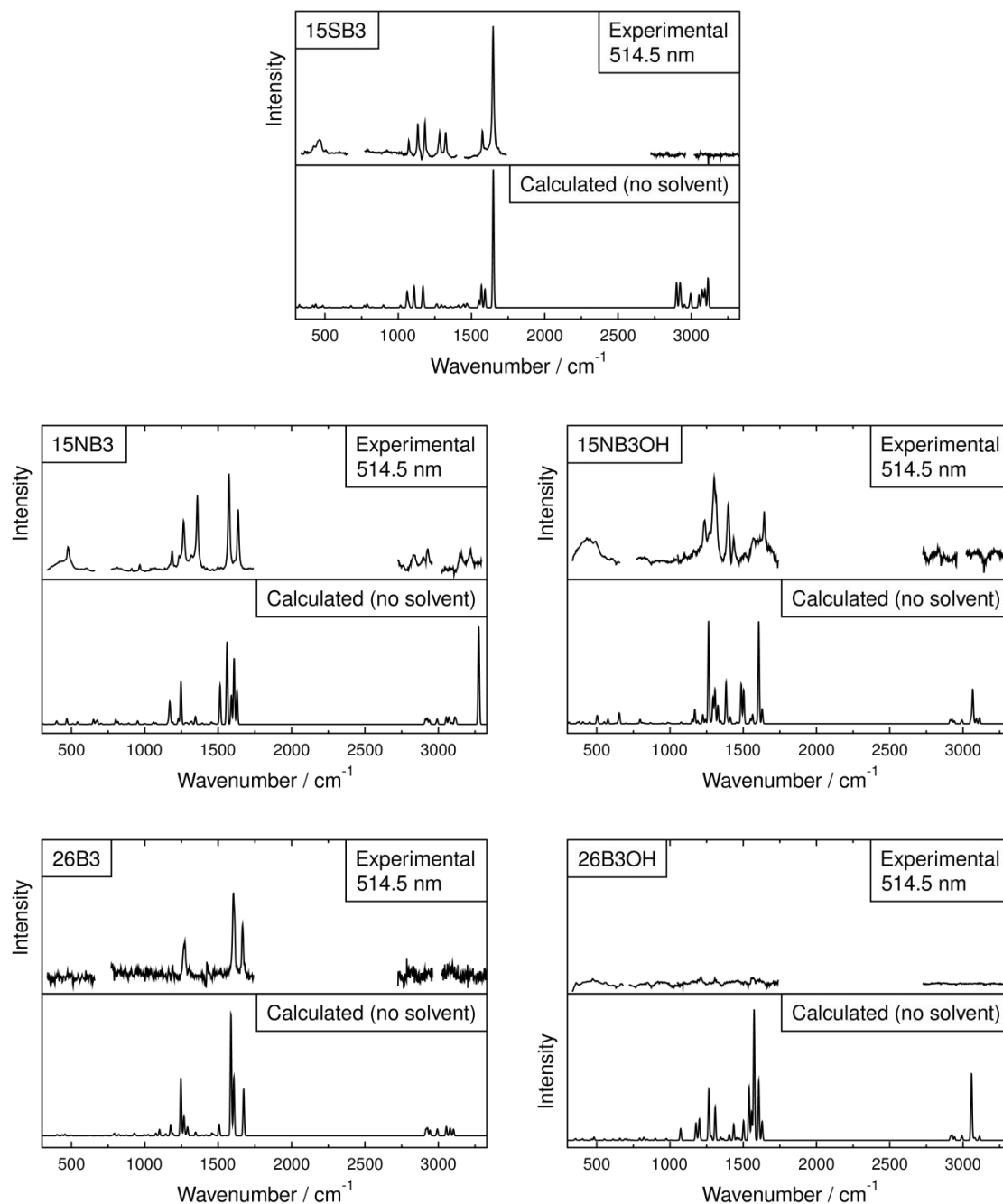


Figure A1.5 Experimental Raman spectra recorded of *ca* 5×10^{-4} mol dm^{-3} solutions of the dyes in DCM and an excitation wavelength of 514.5 nm, with regions corresponding to strong solvent peaks omitted. Calculated spectra are also shown, determined from geometries optimised at the B3LYP/6-31g(d) level.

A1.6 NMR spectroscopy

15SB3

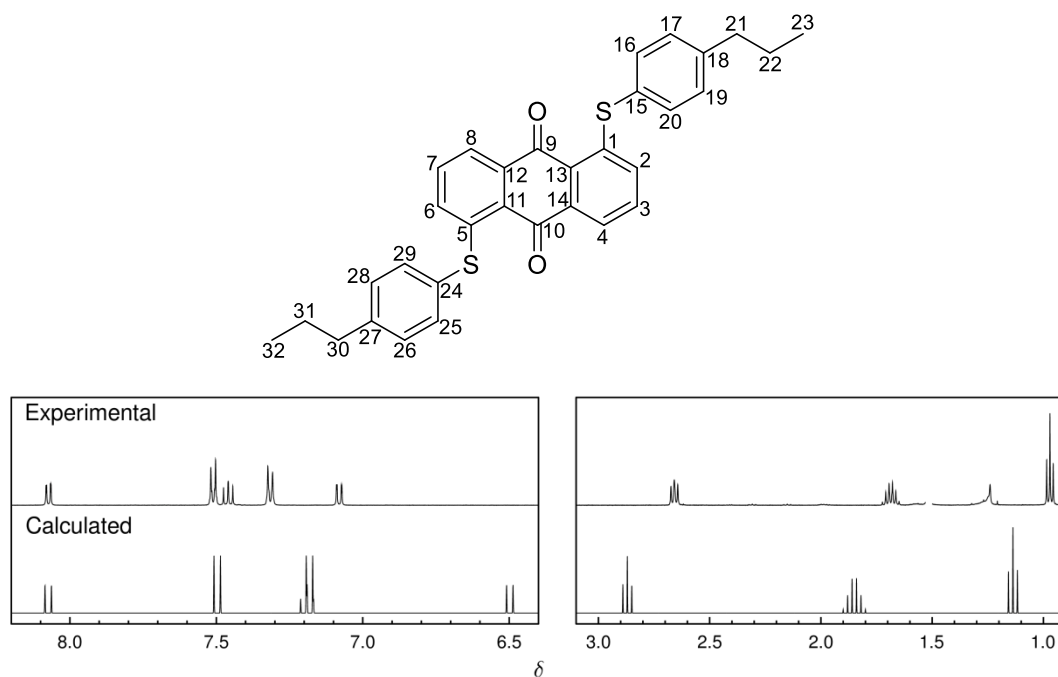


Figure A1.6 Structure of 15SB3 with numbering shown for NMR peak assignments, alongside experimental and calculated ^1H NMR spectra recorded in $\text{DCM}-d_2$.

Table A1.2 Peak assignments of the experimental ^1H NMR spectrum of 15SB3 alongside calculated chemical shift values. Calculated shifts were averaged for protons shown to be equivalent in the experimental spectrum.

Atom		Experimental ^a		Calculated
1/5	-	-	-	-
2/6	7.08	2	dd	8.2, 1.1
3/7	7.46	2	dd	8.2, 7.7
4/8	8.07	2	dd	7.6, 1.1
9/10	-	-	-	-
11/13	-	-	-	-
12/14	-	-	-	-
15/24	-	-	-	-
16/20/25/29	7.51	4	d	8.1
17/19/26/28	7.32	4	d	8.1
18/24	-	-	-	-
21/30	2.66	4	t	7.9
22/31	1.69	4	m	
23/32	0.97	6	t	7.4

^ashift/ppm, integration, multiplicity (s=singlet, d=doublet, t=triplet, m=multiplet), splitting/Hz

15NB3

The singlet at $\delta = 7.22$ in the experimental ^1H NMR spectrum was attributed to the “roofing” effect arising from coupled protons with very similar chemical shifts.

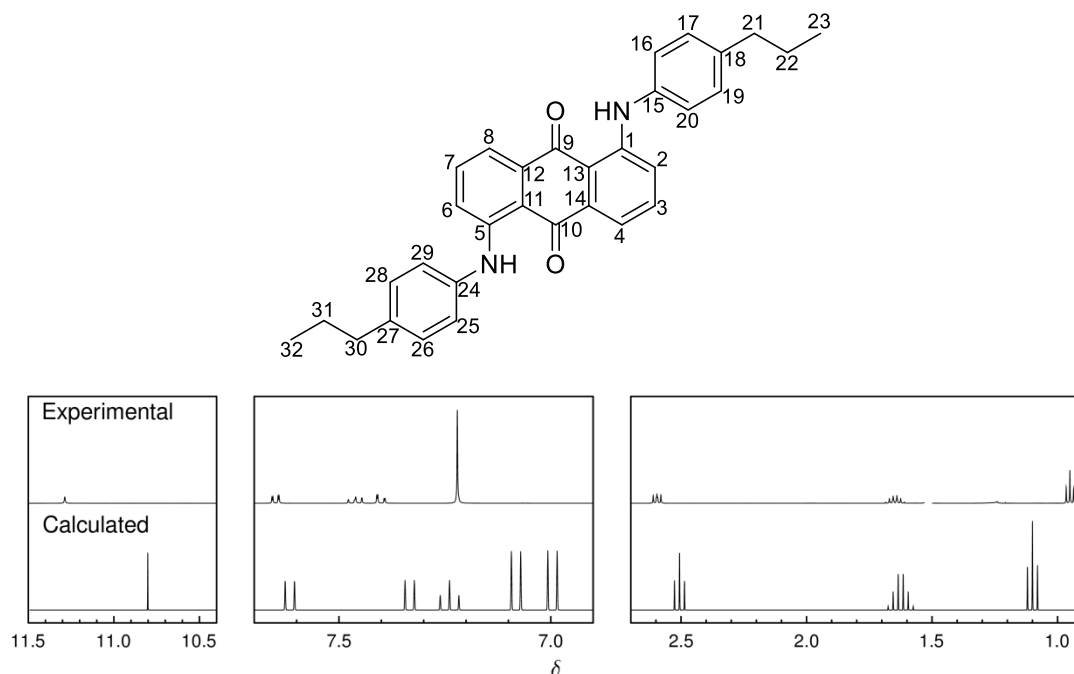


Figure A1.7 Structure of 15NB3 with numbering shown for NMR peak assignments, alongside experimental and calculated ^1H NMR spectra recorded in $\text{DCM}-d_2$.

Table A1.3 Peak assignments of the experimental ^1H NMR spectrum of 15NB3 alongside calculated chemical shift values. Calculated shifts were averaged for protons shown to be equivalent in the experimental spectrum.

Atom	Experimental ^a				Calculated
1/5	-	-	-	-	-
2/6	7.40	2	dd	8.7, 1.2	7.33
3/7	7.46	2	dd	7.4, 8.6	7.24
4/8	7.65	2	dd	7.2, 1.2	7.62
9/10	-	-	-	-	-
11/13	-	-	-	-	-
12/14	-	-	-	-	-
15/24	-	-	-	-	-
16/20/25/29	7.22	8	s		7.00
17/19/26/28					7.08
18/24	-	-	-	-	-
21/30	2.60	4	t	7.7	2.51
22/31	1.65	4	m		1.63
23/32	0.95	6	t	7.4	1.10
N1/N5	11.29	2	s		10.80

^ashift/ppm, integration, multiplicity (s=singlet, d=doublet, t=triplet, m=multiplet), splitting/Hz

15NB3OH

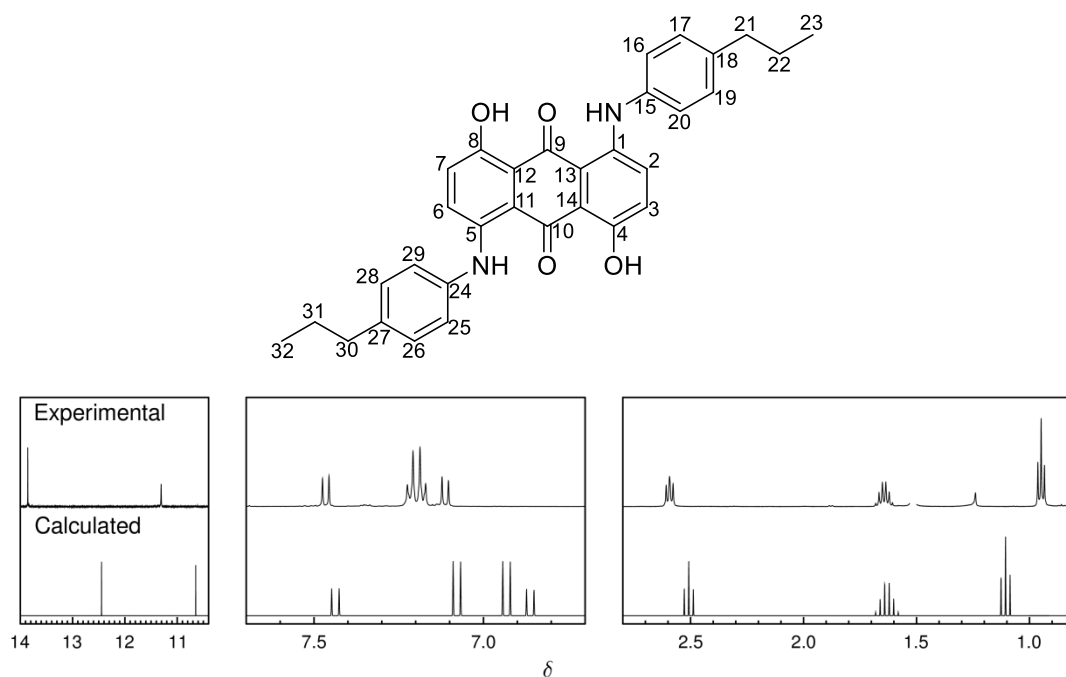


Figure A1.8 Structure of 15NB3OH with numbering shown for NMR peak assignments, alongside experimental and calculated ^1H NMR spectra recorded in $\text{DCM}-d_2$.

Table A1.4 Peak assignments of the experimental ^1H NMR spectrum of 15NB3OH alongside calculated chemical shift values. Calculated shifts were averaged for protons shown to be equivalent in the experimental spectrum.

Atom	Experimental ^a			Calculated
1/5	-	-	-	-
2/6	7.46	2	d	9.5
3/7	7.11	2	d	9.5
4/8	-	-	-	-
9/10	-	-	-	-
11/13	-	-	-	-
12/14	-	-	-	-
15/24	-	-	-	-
16/20/25/29	7.20	8	m	6.93
17/19/26/28	7.08			7.08
18/24	-	-	-	-
21/30	2.59	4	t	7.9
22/31	1.64	4	m	1.63
23/32	0.95	6	t	7.3
N1/N5	11.31	2	s	10.65
O4/O8	13.86	2	s	12.45

^ashift/ppm, integration, multiplicity (s=singlet, d=doublet, t=triplet, m=multiplet), splitting/Hz

26B3

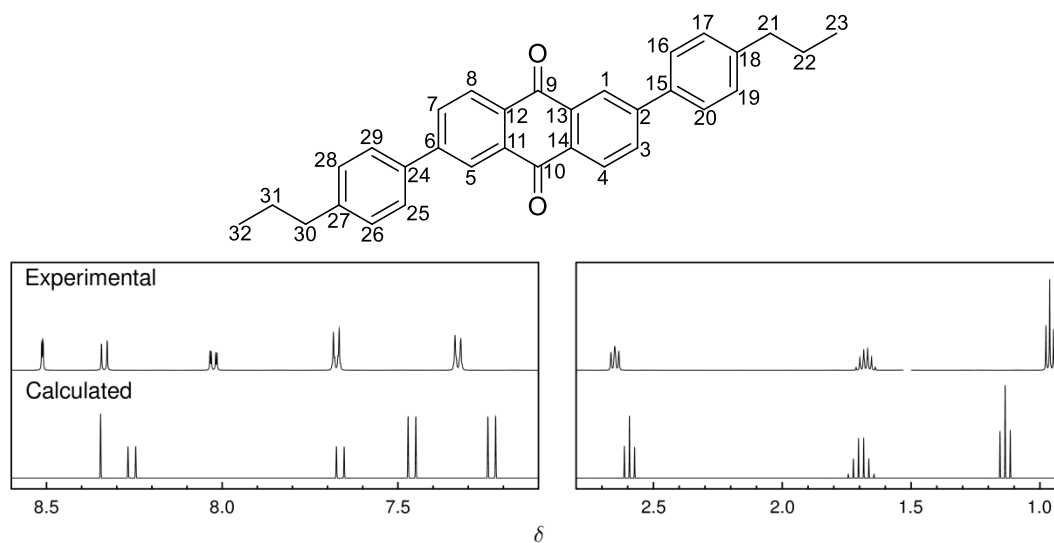


Figure A1.9 Structure of 26B3 with numbering shown for ^1H NMR peak assignments, alongside experimental and calculated ^1H NMR spectra recorded in $\text{DCM}-d_2$.

Table A1.5 Peak assignments of the experimental NMR spectrum of 26B3 alongside calculated chemical shift values. Calculated shifts were averaged for protons shown to be equivalent in the experimental spectrum.

Atom	Experimental ^a		Calculated	
1/5	8.51	2 d	1.6	8.35
2/6	-	-	-	-
3/7	8.02	2 dd	8.2, 1.9	7.66
4/8	8.34	2 d	8.1	8.26
9/10	-	-	-	-
11/12/13/14	-	-	-	-
15/24	-	-	-	-
16/20/25/29	7.68	4 d	8.3	7.46
17/19/26/28	7.33	4 d	8.3	7.23
18/24	-	-	-	-
21/30	2.65	4 t	7.8	2.59
22/31	1.68	4 m		1.69
23/32	0.96	6 t	7.4	1.14

^ashift/ppm, integration, multiplicity (s=singlet, d=doublet, t=triplet, m=multiplet), splitting/Hz

26B3OH

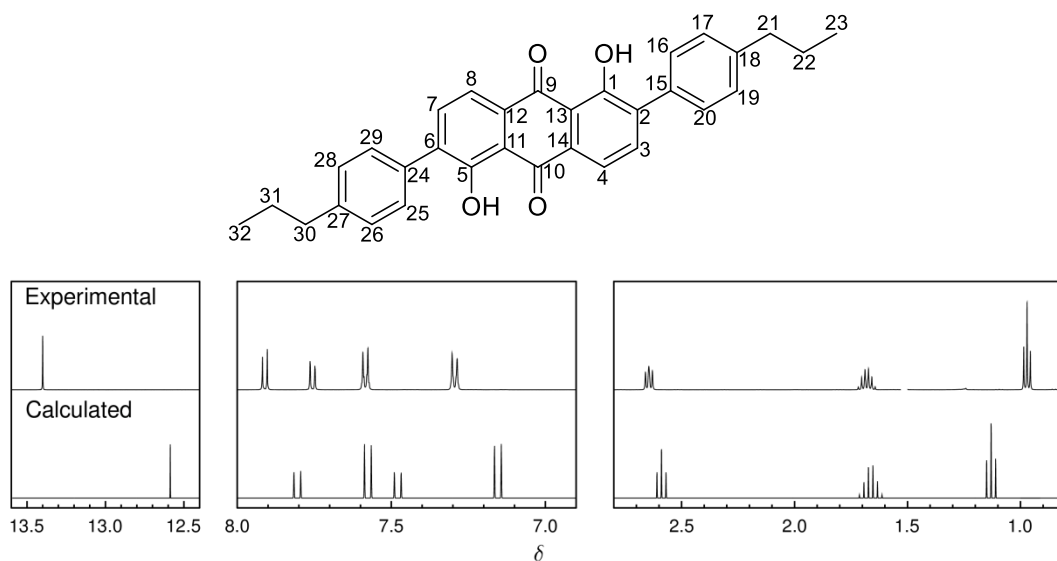


Figure A1.10 Structure of 26B3OH with numbering shown for ^1H NMR peak assignments, alongside experimental and calculated NMR spectra recorded in $\text{DCM}-d_2$.

Table A1.6 Peak assignments of the experimental ^1H NMR spectrum of 26B3OH alongside calculated chemical shift values. Calculated shifts were averaged for protons shown to be equivalent in the experimental spectrum.

Atom	Experimental ^a				Calculated
1/5	-	-	-	-	-
2/6	-	-	-	-	-
3/7	7.76	2	d	7.8	7.48
4/8	7.91	2	d	7.8	7.80
9/10	-	-	-	-	-
11/12/13/14	-	-	-	-	-
15/24	-	-	-	-	-
16/20/25/29	7.58	4	d	8.2	7.58
17/19/26/28	7.29	4	d	8.2	7.15
18/24	-	-	-	-	--
21/30	2.64	4	t	7.6	2.59
22/31	1.68	4	m		1.66
23/32	0.97	6	t	7.3	1.13
O1/O5	13.40	2	s		12.59

^ashift/ppm, integration, multiplicity (s=singlet, d=doublet, t=triplet, m=multiplet), splitting/Hz

A1.7 Aspect ratios of unsubstituted dye structures

Table A1.7 Molecular lengths, widths and aspect ratios of optimised structures of the dyes with the terminal propyl chains replaced with hydrogen atoms, labelled “0” rather than “3”. The values were calculated using the same method as that presented in the main text.

	Length / Å	Width / Å	Aspect Ratio
15SB0	20.72	9.46	2.19
15NB0	20.29	10.27	1.97
15NB0OH	20.25	10.63	1.91
26B0	20.22	8.40	2.41
26B0OH	20.39	8.40	2.43

A1.8 Cyclic voltammetry

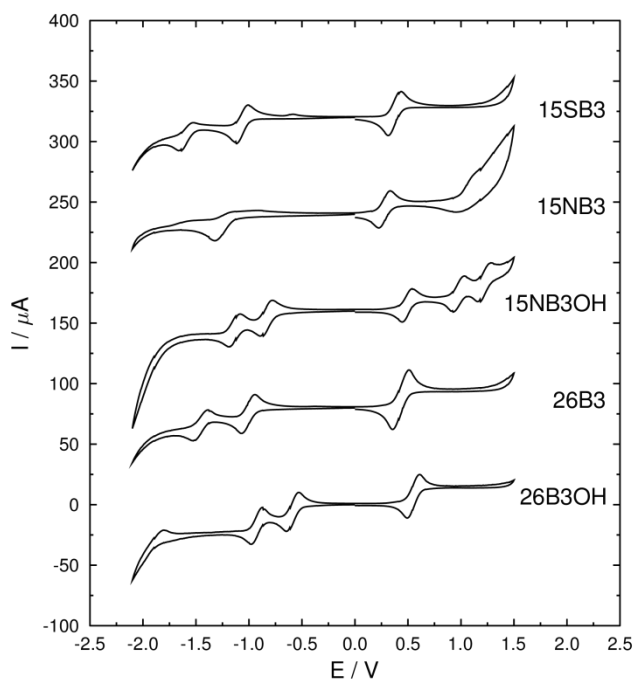


Figure A1.11 Cyclic voltammograms of the dyes at $1 \times 10^{-3} \text{ mol dm}^{-3}$ in DCM with TBAHFP at 0.1 mol dm^{-3} and ferrocene at $ca 1 \times 10^{-3} \text{ mol dm}^{-3}$ using a scan rate of 100 mV s^{-1} . The initial scan direction was to negative potential and the voltammograms are offset for clarity.

A1.9 Spectroelectrochemistry

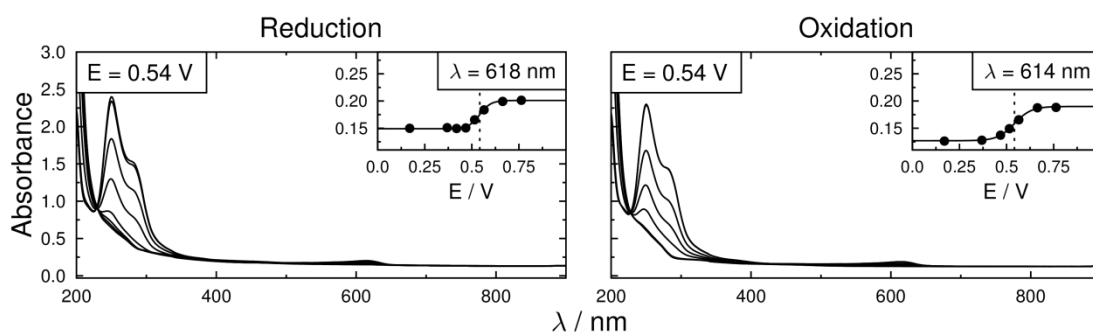


Figure A1.12 UV-vis absorption spectra of ferrocene at $ca. 5 \times 10^{-5} \text{ mol dm}^{-3}$ in acetonitrile during electrochemical reduction from +0.76 V to 0 V (left) and oxidation from 0 V to +0.76 V (right) vs. the Ag pseudo reference electrode. Inset are absorbance plots at single wavelengths (\bullet) and the fits ($—$) used to estimate the redox potential of Fc/Fc^+ . The dotted vertical lines indicate the redox potentials obtained from the fits, which are given in the plots.

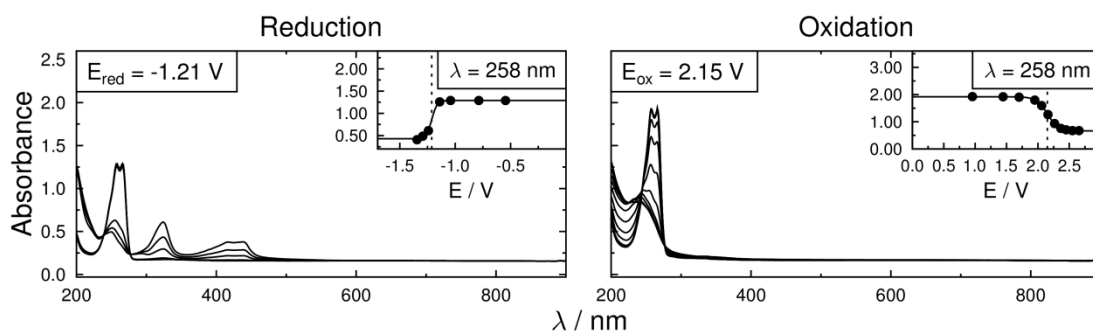


Figure A1.13 UV-vis absorption spectra of duroquinone at $ca. 5 \times 10^{-5} \text{ mol dm}^{-3}$ in acetonitrile during electrochemical reduction (left) and oxidation (right). Inset are absorbance plots at single wavelengths (\bullet) and the fits ($—$) used to estimate the redox potentials vs. the Fc/Fc^+ couple. The dotted vertical lines indicate the redox potentials obtained from the fits, which are given in the plots.

Appendix 2

Supplementary information relating to Chapter 4

A2.1 UV-visible absorption of E7

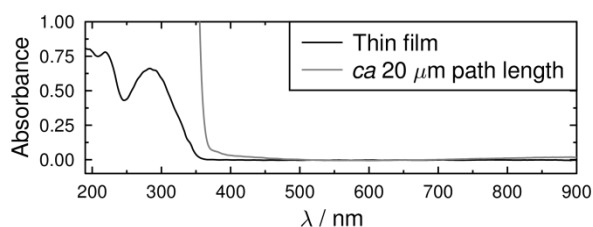


Figure A2.1 UV-visible absorption spectra of E7 in a thin film between quartz disks with no spacer, and in a cell between glass slides with a 20 μm pathlength, both recorded against a background of air.

A2.2 HF optimisations

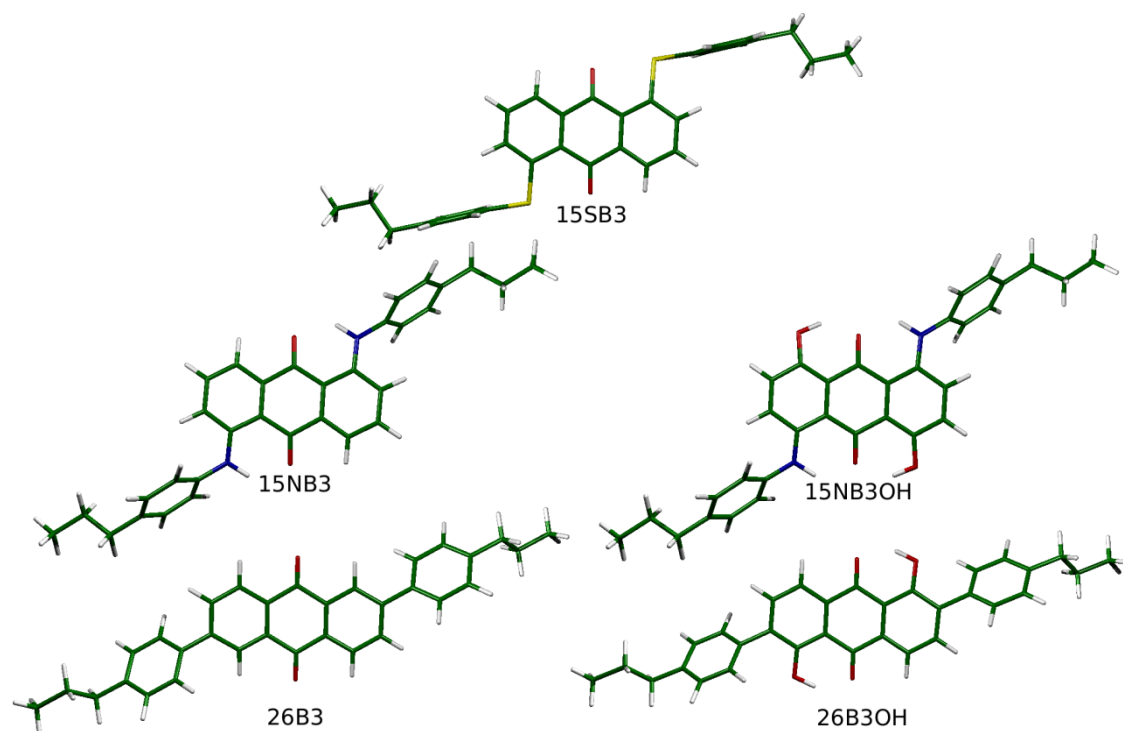


Figure A2.2 Optimised structures of the dyes in all-*trans* conformations at the HF/6-31g(d) level of theory.

A2.3 Atom types for MD simulations

Figures A2.3-A2.14 show numbered structures of the E7 constituent molecules, the model compounds, **M1** – **M3**, used for force constant parameterisation, and the five dyes. The associated OPLS atom-types, charge groups and atomic charges (if not default) are given in Tables A2.1-A2.12.

The `opls_966` atom type was defined and used to differentiate the carbon atoms in the 2- and 6- positions of the anthraquinone in **M2**, **M3**, 15SB3, 15NB3 and 15NB3OH from the other aromatic carbon atoms in the structures of these dyes. Associated force field parameters of `opls_966` were defined as identical to those associated with `opls_145`, with the exception of the parameterised dihedral force constants described in the text.

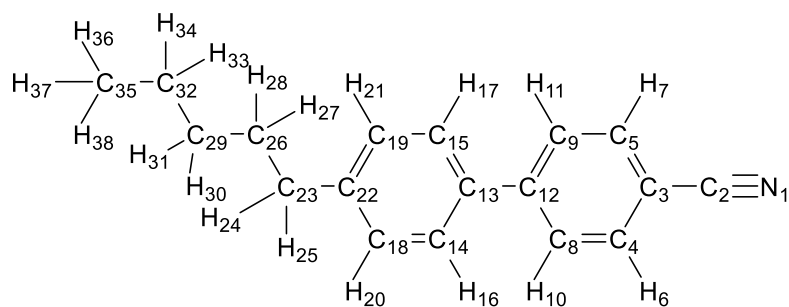


Figure A2.3 Structure and atom numbering of 5CB for the MD simulations.

Table A2.1 Atom numbers, OPLS atom types, charge groups and atomic charges (where default charges were not used) used for MD simulations of 5CB.

Atom number	Atom type	Charge group	Charge	Atom number	Atom type	Charge group	Charge
1	opls_262	1		20	opls_146	9	
2	opls_261	1		21	opls_146	10	
3	opls_260	1		22	opls_145	11	
4	opls_145	2		23	opls_149	11	
5	opls_145	3		24	opls_140	11	
6	opls_146	2		25	opls_140	11	
7	opls_146	3		26	opls_136	12	
8	opls_145	4		27	opls_140	12	
9	opls_145	5		28	opls_140	12	
10	opls_146	4		29	opls_136	13	
11	opls_146	5		30	opls_140	13	
12	opls_145B	6	0	31	opls_140	13	
13	opls_145B	6	0	32	opls_136	14	
14	opls_145	7		33	opls_140	14	
15	opls_145	8		34	opls_140	14	
16	opls_146	7		35	opls_135	15	
17	opls_146	8		36	opls_140	15	
18	opls_145	9		37	opls_140	15	
19	opls_145	10		38	opls_140	15	

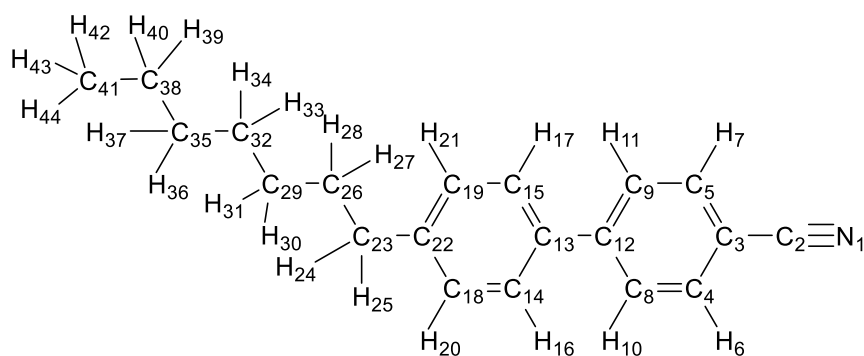


Figure A2.4 Structure and atom numbering of 7CB for the MD simulations.

Table A2.2 Atom numbers, OPLS atom types, charge groups and atomic charges (where default charges were not used) used for MD simulations of 7CB.

Atom number	Atom type	Charge group	Charge	Atom number	Atom type	Charge group	Charge
1	opls_262	1		23	opls_149	11	
2	opls_261	1		24	opls_140	11	
3	opls_260	1		25	opls_140	11	
4	opls_145	2		26	opls_136	12	
5	opls_145	3		27	opls_140	12	
6	opls_146	2		28	opls_140	12	
7	opls_146	3		29	opls_136	13	
8	opls_145	4		30	opls_140	13	
9	opls_145	5		31	opls_140	13	
10	opls_146	4		32	opls_136	14	
11	opls_146	5		33	opls_140	14	
12	opls_145B	6	0	34	opls_140	14	
13	opls_145B	6	0	35	opls_136	15	
14	opls_145	7		36	opls_140	15	
15	opls_145	8		37	opls_140	15	
16	opls_146	7		38	opls_136	16	
17	opls_146	8		39	opls_140	16	
18	opls_145	9		40	opls_140	16	
19	opls_145	10		41	opls_135	17	
20	opls_146	9		42	opls_140	17	
21	opls_146	10		43	opls_140	17	
22	opls_145	11		44	opls_140	17	

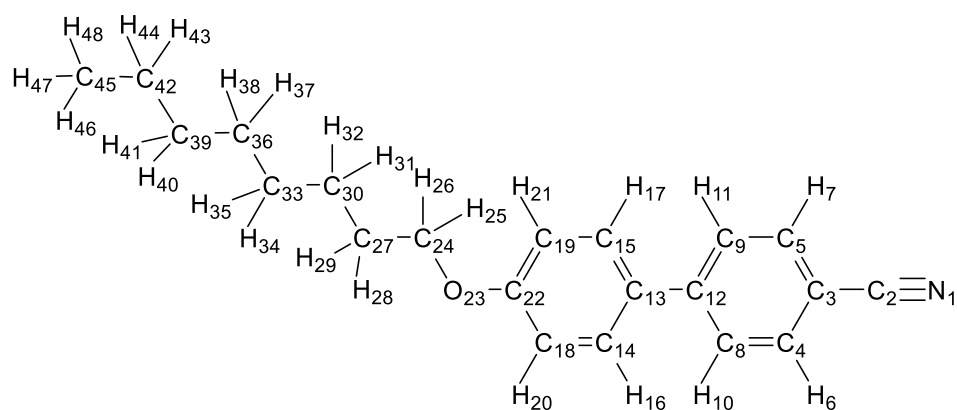


Figure A2.5 Structure and atom numbering of 8OCB for the MD simulations.

Table A2.3 Atom numbers, OPLS atom types, charge groups and atomic charges (where default charges were not used) used for MD simulations of 8OCB.

Atom number	Atom type	Charge group	Charge	Atom number	Atom type	Charge group	Charge
1	opls_262	1		25	opls_185	11	
2	opls_261	1		26	opls_185	11	
3	opls_260	1		27	opls_136	12	
4	opls_145	2		28	opls_140	12	
5	opls_145	3		29	opls_140	12	
6	opls_146	2		30	opls_136	13	
7	opls_146	3		31	opls_140	13	
8	opls_145	4		32	opls_140	13	
9	opls_145	5		33	opls_136	14	
10	opls_146	4		34	opls_140	14	
11	opls_146	5		35	opls_140	14	
12	opls_145B	6	0	36	opls_136	15	
13	opls_145B	6	0	37	opls_140	15	
14	opls_145	7		38	opls_140	15	
15	opls_145	8		39	opls_136	16	
16	opls_146	7		40	opls_140	16	
17	opls_146	8		41	opls_140	16	
18	opls_145	9		42	opls_136	17	
19	opls_145	10		43	opls_140	17	
20	opls_146	9		44	opls_140	17	
21	opls_146	10		45	opls_135	18	
22	opls_199	11		46	opls_140	18	
23	opls_179	11		47	opls_140	18	
24	opls_182	11		48	opls_140	18	

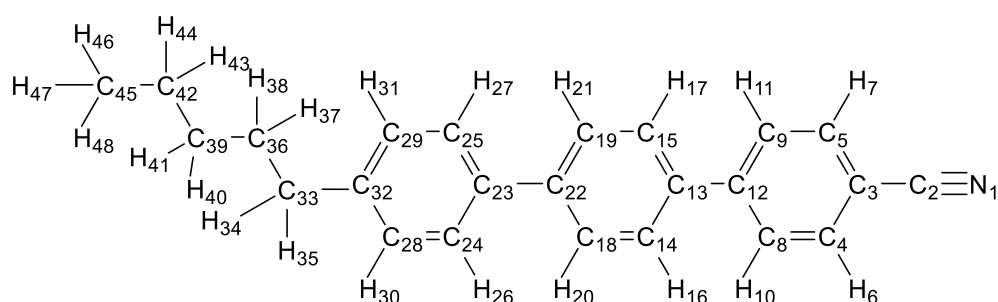


Figure A2.6 Structure and atom numbering of 5CT for the MD simulations.

Table A2.4 Atom numbers, OPLS atom types, charge groups and atomic charges (where default charges were not used) used for MD simulations of 5CT.

Atom number	Atom type	Charge group	Charge	Atom number	Atom type	Charge group	Charge
1	opls_262	1		25	opls_145	13	
2	opls_261	1		26	opls_146	12	
3	opls_260	1		27	opls_146	13	
4	opls_145	2		28	opls_145	14	
5	opls_145	3		29	opls_145	15	
6	opls_146	2		30	opls_146	14	
7	opls_146	3		31	opls_146	15	
8	opls_145	4		32	opls_145	16	
9	opls_145	5		33	opls_149	16	
10	opls_146	4		34	opls_140	16	
11	opls_146	5		35	opls_140	16	
12	opls_145B	6	0	36	opls_136	17	
13	opls_145B	6	0	37	opls_140	17	
14	opls_145	7		38	opls_140	17	
15	opls_145	8		39	opls_136	18	
16	opls_146	7		40	opls_140	18	
17	opls_146	8		41	opls_140	18	
18	opls_145	9		42	opls_136	19	
19	opls_145	10		43	opls_140	19	
20	opls_146	9		44	opls_140	19	
21	opls_146	10		45	opls_135	20	
22	opls_145B	11	0	46	opls_140	20	
23	opls_145B	11	0	47	opls_140	20	
24	opls_145	12		48	opls_140	20	

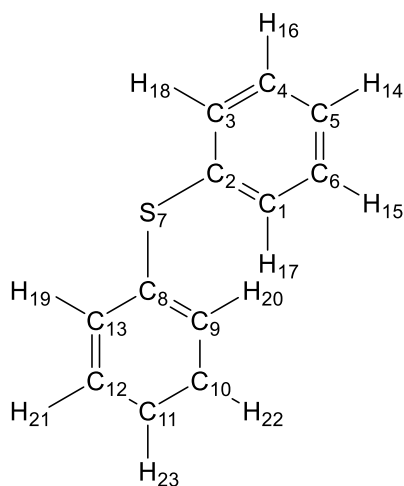


Figure A2.7 Structure and atom numbering of **M1** for the MD force constant parameterisation.

Table A2.5 Atom numbers, OPLS atom types, charge groups and atomic charges (where default charges were not used) used for MD simulations of **M1**.

Atom number	Atom type	Charge group	Charge
1	opls_145	1	
2	opls_228	2	0
3	opls_145	3	
4	opls_145	4	
5	opls_145	5	
6	opls_145	6	
7	opls_222	2	0
8	opls_228	2	0
9	opls_145	7	
10	opls_145	8	
11	opls_145	9	
12	opls_145	10	
13	opls_145	11	
14	opls_146	9	
15	opls_146	8	
16	opls_146	10	
17	opls_146	7	
18	opls_146	11	
19	opls_146	1	
20	opls_146	3	
21	opls_146	6	
22	opls_146	4	
23	opls_146	5	

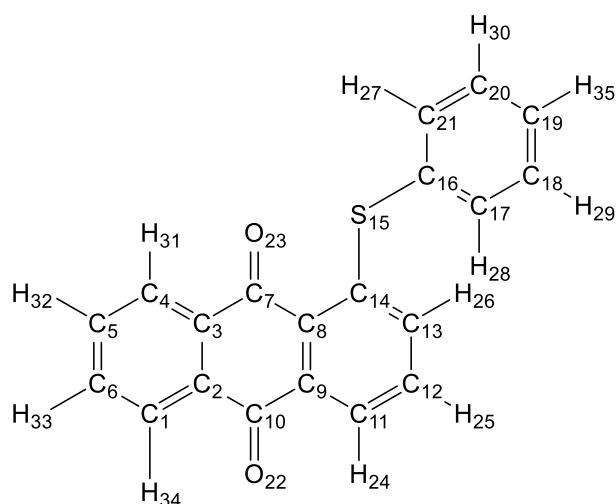


Figure A2.8 Structure and atom numbering of **M2** for the MD force constant parameterisation.

Table A2.6 Atom numbers, OPLS atom types, charge groups and atomic charges (where default charges were not used) used for MD simulations of **M2**.

Atom number	Atom type	Charge group	Charge	Atom number	Atom type	Charge group	Charge
1	opls_145	1	-0.14	19	opls_145	15	-0.14
2	opls_147	2	-0.08	20	opls_145	16	-0.14
3	opls_147	2	-0.08	21	opls_145	17	-0.14
4	opls_145	3	-0.14	22	opls_281	8	-0.48
5	opls_145	4	-0.14	23	opls_281	6	-0.48
6	opls_145	5	-0.14	24	opls_146	9	0.14
7	opls_280	6	0.55	25	opls_146	10	0.14
8	opls_147	7	-0.08	26	opls_146	11	0.14
9	opls_147	7	-0.08	27	opls_146	17	0.14
10	opls_280	8	0.55	28	opls_146	13	0.14
11	opls_145	9	-0.14	29	opls_146	14	0.14
12	opls_145	10	-0.14	30	opls_146	16	0.14
13	opls_966	11	-0.14	31	opls_146	3	0.14
14	opls_228	12	0.07	32	opls_146	4	0.14
15	opls_222	12	-0.28	33	opls_146	5	0.14
16	opls_228	12	0.39	34	opls_146	1	0.14
17	opls_145	13	-0.14	35	opls_146	15	0.14
18	opls_145	14	-0.14				

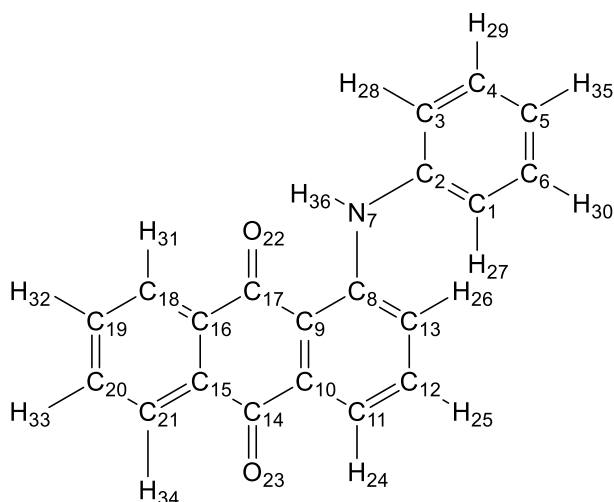


Figure A2.9 Structure and atom numbering of **M3** for the MD force constant parameterisation.

Table A2.7 Atom numbers, OPLS atom types, charge groups and atomic charges (where default charges were not used) used for MD simulations of **M3**.

Atom number	Atom type	Charge group	Charge	Atom number	Atom type	Charge group	Charge
1	opls_145	1	-0.27	19	opls_145	15	-0.12
2	opls_916	2	0.46	20	opls_145	16	-0.12
3	opls_145	3	-0.27	21	opls_145	17	-0.13
4	opls_145	4	-0.12	22	opls_281	13	-0.59
5	opls_145	5	-0.16	23	opls_281	11	-0.51
6	opls_145	6	-0.11	24	opls_146	8	0.17
7	opls_901	2	-0.89	25	opls_146	9	0.13
8	opls_916	2	0.73	26	opls_146	10	0.20
9	opls_147	7	-0.54	27	opls_146	1	0.17
10	opls_147	7	0.09	28	opls_146	3	0.17
11	opls_145	8	-0.29	29	opls_146	4	0.14
12	opls_145	9	0.04	30	opls_146	6	0.14
13	opls_966	10	-0.45	31	opls_146	14	0.15
14	opls_280	11	0.54	32	opls_146	15	0.14
15	opls_147	12	-0.04	33	opls_146	16	0.14
16	opls_147	12	-0.11	34	opls_146	17	0.15
17	opls_280	13	0.70	35	opls_146	5	0.14
18	opls_145	14	-0.11	36	opls_910	2	0.46

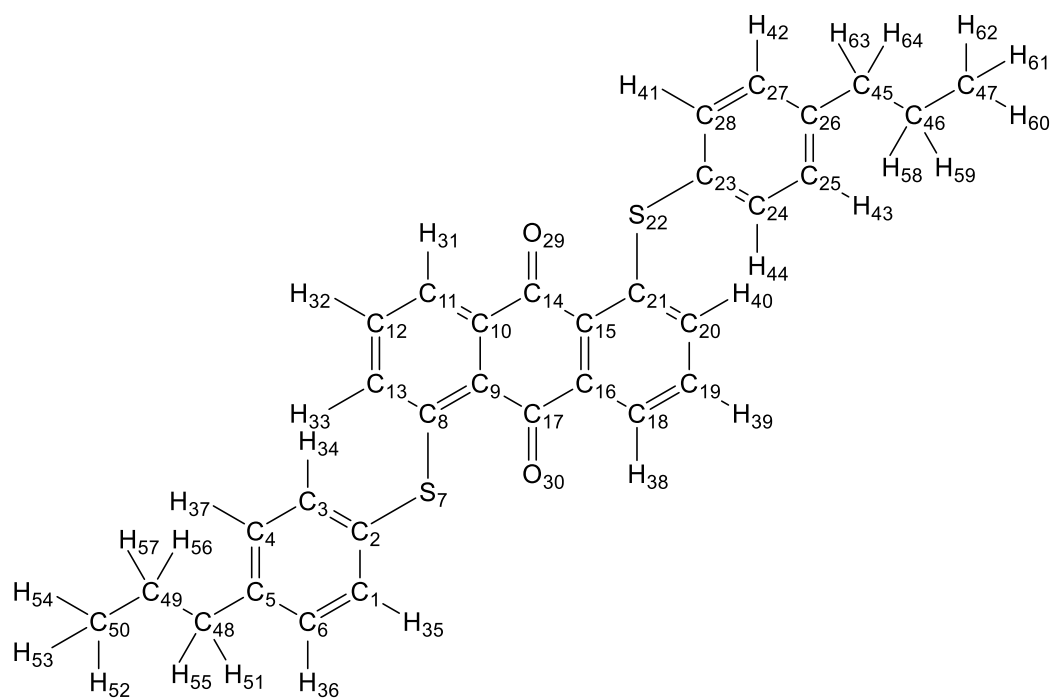


Figure A2.10 Structure and atom numbering of 15SB3 for the MD simulations.

Table A2.8 Atom numbers, OPLS atom types, charge groups and atomic charges (where default charges were not used) used for MD simulations of 15SB3.

Atom number	Atom type	Charge group	Charge
1	opls_145	1	-0.213
2	opls_228	2	0.325
3	opls_145	3	-0.213
4	opls_145	4	-0.205
5	opls_145	5	0.085
6	opls_145	6	-0.205
7	opls_222	2	-0.246
8	opls_228	2	0.037
9	opls_147	7	-0.033
10	opls_147	7	-0.124
11	opls_145	8	-0.097
12	opls_145	9	-0.152
13	opls_966	10	-0.082
14	opls_280	11	0.524
15	opls_147	12	-0.033
16	opls_147	12	-0.124
17	opls_280	13	0.524
18	opls_145	14	-0.097
19	opls_145	15	-0.152
20	opls_966	16	-0.082
21	opls_228	17	0.037
22	opls_222	17	-0.246
23	opls_228	17	0.325
24	opls_145	18	-0.213
25	opls_145	19	-0.205

26	opls_145	20	0.085
27	opls_145	21	-0.205
28	opls_145	22	-0.213
29	opls_281	11	-0.444
30	opls_281	13	-0.444
31	opls_146	8	0.139
32	opls_146	9	0.158
33	opls_146	10	0.106
34	opls_146	3	0.147
35	opls_146	1	0.147
36	opls_146	6	0.144
37	opls_146	4	0.144
38	opls_146	14	0.139
39	opls_146	15	0.158
40	opls_146	16	0.106
41	opls_146	22	0.147
42	opls_146	21	0.144
43	opls_146	19	0.144
44	opls_146	18	0.147
45	opls_149	20	-0.142
46	opls_136	23	0.276
47	opls_135	24	-0.433
48	opls_149	5	-0.142
49	opls_136	25	0.276
50	opls_135	26	-0.433
51	opls_140	5	0.056
52	opls_140	26	0.101
53	opls_140	26	0.101
54	opls_140	26	0.101
55	opls_140	5	0.056
56	opls_140	25	-0.029
57	opls_140	25	-0.029
58	opls_140	23	-0.029
59	opls_140	23	-0.029
60	opls_140	24	0.101
61	opls_140	24	0.101
62	opls_140	24	0.101
63	opls_140	20	0.056
64	opls_140	20	0.056

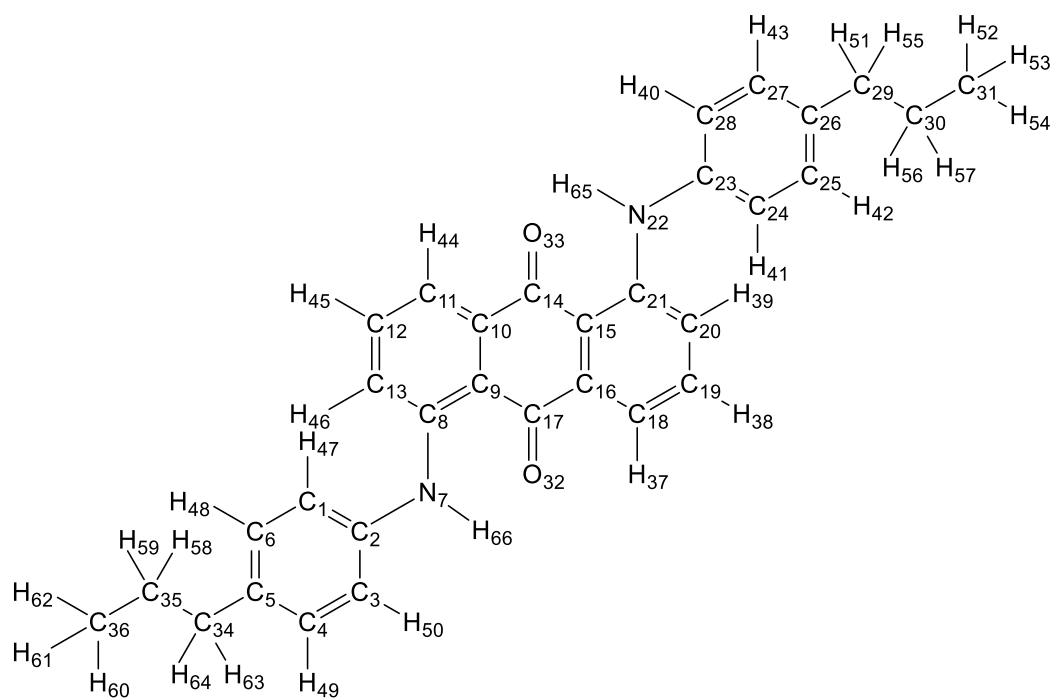


Figure A2.11 Structure and atom numbering of 15NB3 for the MD simulations.

Table A2.9 Atom numbers, OPLS atom types, charge groups and atomic charges (where default charges were not used) used for MD simulations of 15NB3.

Atom number	Atom type	Charge group	Charge
1	opls_145	1	-0.327
2	opls_916	2	0.477
3	opls_145	3	-0.327
4	opls_145	4	-0.158
5	opls_145	5	0.034
6	opls_145	6	-0.158
7	opls_901	2	-0.776
8	opls_916	2	0.611
9	opls_147	7	-0.448
10	opls_147	7	0.078
11	opls_145	8	-0.297
12	opls_145	9	0.025
13	opls_966	10	-0.399
14	opls_280	11	0.632
15	opls_147	12	-0.448
16	opls_147	12	0.078
17	opls_280	13	0.632
18	opls_145	14	-0.297
19	opls_145	15	0.025
20	opls_966	16	-0.399
21	opls_916	17	0.611
22	opls_901	17	-0.776
23	opls_916	17	0.477
24	opls_145	18	-0.328
25	opls_145	19	-0.158

26	opls_145	20	0.034
27	opls_145	21	-0.158
28	opls_145	22	-0.328
29	opls_136	20	-0.187
30	opls_136	23	0.279
31	opls_135	24	-0.329
32	opls_281	13	-0.590
33	opls_281	11	-0.590
34	opls_136	5	-0.187
35	opls_136	25	0.279
36	opls_135	26	-0.329
37	opls_146	14	0.178
38	opls_146	15	0.134
39	opls_146	16	0.184
40	opls_146	22	0.175
41	opls_146	18	0.175
42	opls_146	19	0.159
43	opls_146	21	0.159
44	opls_146	8	0.178
45	opls_146	9	0.134
46	opls_146	10	0.184
47	opls_146	1	0.175
48	opls_146	6	0.159
49	opls_146	4	0.159
50	opls_146	3	0.175
51	opls_140	20	0.061
52	opls_140	24	0.073
53	opls_140	24	0.073
54	opls_140	24	0.073
55	opls_140	20	0.061
56	opls_140	23	-0.039
57	opls_140	23	-0.039
58	opls_140	25	-0.039
59	opls_140	25	-0.039
60	opls_140	26	0.073
61	opls_140	26	0.073
62	opls_140	26	0.073
63	opls_140	5	0.061
64	opls_140	5	0.061
65	opls_910	17	0.434
66	opls_910	2	0.434

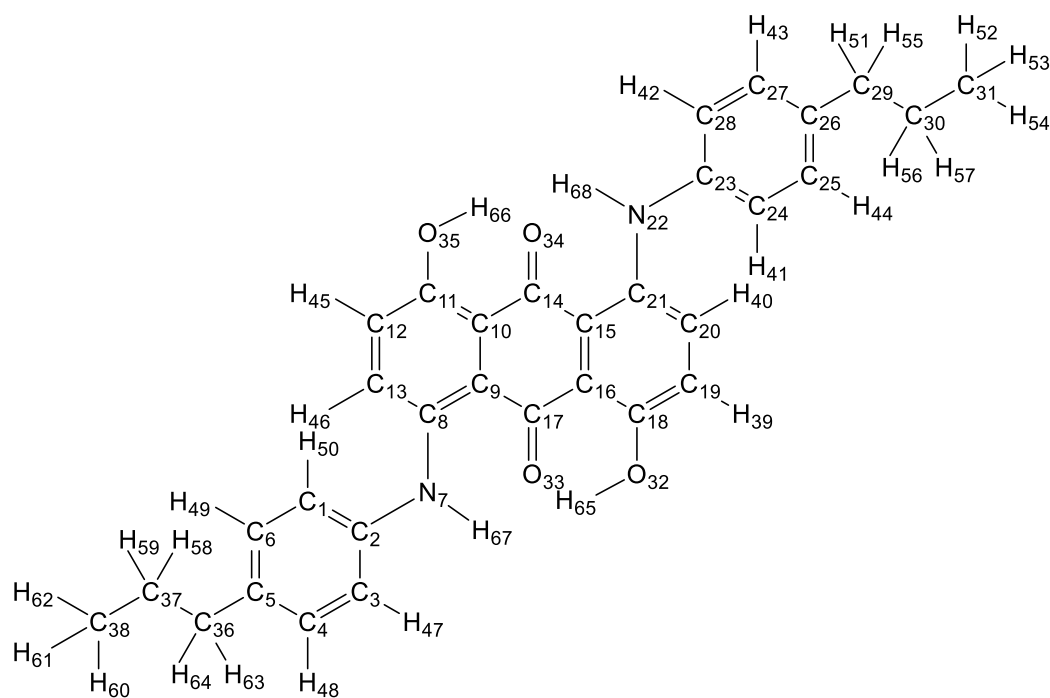


Figure A2.12 Structure and atom numbering of 15NB3OH for the MD simulations.

Table A2.10 Atom numbers, OPLS atom types, charge groups and atomic charges (where default charges were not used) used for MD simulations of 15NB3OH.

Atom number	Atom type	Charge group	Charge
1	opls_145	1	-0.343
2	opls_916	2	0.486
3	opls_145	3	-0.343
4	opls_145	4	-0.149
5	opls_145	5	0.040
6	opls_145	6	-0.149
7	opls_901	2	-0.744
8	opls_916	2	0.485
9	opls_147	7	-0.342
10	opls_147	7	-0.289
11	opls_166	8	0.414
12	opls_145	9	-0.182
13	opls_966	10	-0.270
14	opls_280	11	0.723
15	opls_147	12	-0.342
16	opls_147	12	-0.289
17	opls_280	13	0.723
18	opls_166	14	0.414
19	opls_145	15	-0.182
20	opls_966	16	-0.270
21	opls_916	17	0.485
22	opls_901	17	-0.744
23	opls_916	17	0.486
24	opls_145	18	-0.343
25	opls_145	19	-0.149

26	opls_145	20	0.040
27	opls_145	21	-0.149
28	opls_145	22	-0.343
29	opls_136	20	-0.212
30	opls_136	23	0.268
31	opls_135	24	-0.307
32	opls_167	14	-0.648
33	opls_281	13	-0.695
34	opls_281	11	-0.695
35	opls_167	8	-0.648
36	opls_136	5	-0.212
37	opls_136	25	0.268
38	opls_135	26	-0.307
39	opls_146	15	0.193
40	opls_146	16	0.176
41	opls_146	18	0.179
42	opls_146	22	0.179
43	opls_146	21	0.158
44	opls_146	19	0.158
45	opls_146	9	0.193
46	opls_146	10	0.176
47	opls_146	3	0.179
48	opls_146	4	0.158
49	opls_146	6	0.158
50	opls_146	1	0.179
51	opls_140	20	0.070
52	opls_140	24	0.068
53	opls_140	24	0.068
54	opls_140	24	0.068
55	opls_140	20	0.070
56	opls_140	23	-0.037
57	opls_140	23	-0.037
58	opls_140	25	-0.037
59	opls_140	25	-0.037
60	opls_140	26	0.068
61	opls_140	26	0.068
62	opls_140	26	0.068
63	opls_140	5	0.070
64	opls_140	5	0.070
65	opls_168	14	0.505
66	opls_168	8	0.505
67	opls_910	2	0.439
68	opls_910	17	0.439

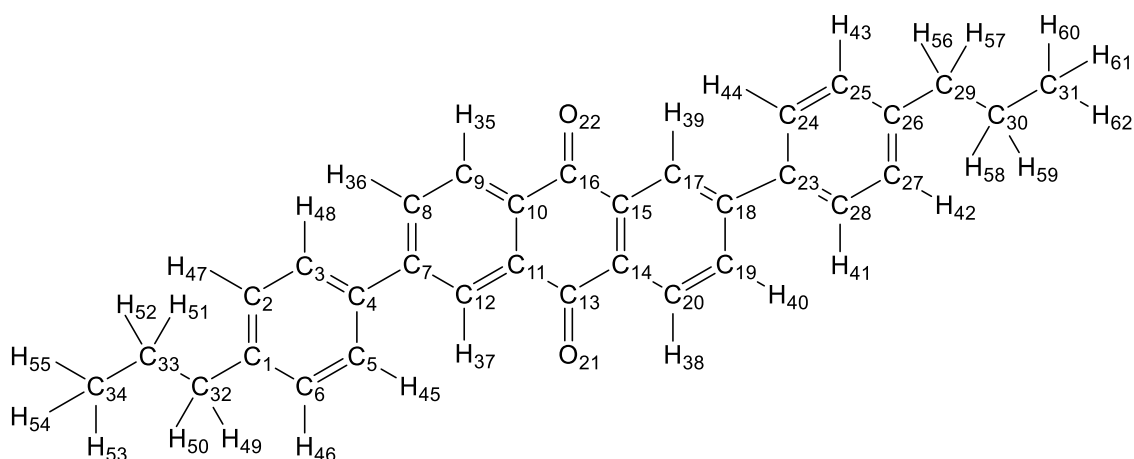


Figure A2.13 Structure and atom numbering of 26B3 for the MD simulations.

Table A2.11 Atom numbers, OPLS atom types, charge groups and atomic charges (where default charges were not used) used for MD simulations of 26B3.

Atom number	Atom type	Charge group	Charge
1	opls_145	1	0.170
2	opls_145	2	-0.238
3	opls_145	3	-0.160
4	opls_145B	4	0.055
5	opls_145	5	-0.160
6	opls_145	6	-0.238
7	opls_145B	4	0.109
8	opls_145	7	-0.191
9	opls_145	8	-0.087
10	opls_147	9	-0.121
11	opls_147	9	-0.071
12	opls_145	10	-0.169
13	opls_280	11	0.576
14	opls_147	12	-0.121
15	opls_147	12	-0.071
16	opls_280	13	0.576
17	opls_145	14	-0.169
18	opls_145B	15	0.109
19	opls_145	16	-0.191
20	opls_145	17	-0.087
21	opls_281	11	-0.522
22	opls_281	13	-0.522
23	opls_145B	15	0.055
24	opls_145	18	-0.160
25	opls_145	19	-0.238
26	opls_145	20	0.170
27	opls_145	21	-0.238
28	opls_145	22	-0.160
29	opls_149	20	-0.289
30	opls_136	23	0.301
31	opls_135	24	-0.306
32	opls_149	1	-0.289

33	opls_136	25	0.301
34	opls_135	26	-0.306
35	opls_146	8	0.148
36	opls_146	7	0.147
37	opls_146	10	0.150
38	opls_146	17	0.148
39	opls_146	14	0.150
40	opls_146	16	0.147
41	opls_146	22	0.141
42	opls_146	21	0.164
43	opls_146	19	0.164
44	opls_146	18	0.141
45	opls_146	5	0.141
46	opls_146	6	0.164
47	opls_146	2	0.164
48	opls_146	3	0.141
49	opls_140	1	0.084
50	opls_140	1	0.084
51	opls_140	25	-0.043
52	opls_140	25	-0.043
53	opls_140	26	0.068
54	opls_140	26	0.068
55	opls_140	26	0.068
56	opls_140	20	0.084
57	opls_140	20	0.084
58	opls_140	23	-0.043
59	opls_140	23	-0.043
60	opls_140	24	0.068
61	opls_140	24	0.068
62	opls_140	24	0.068

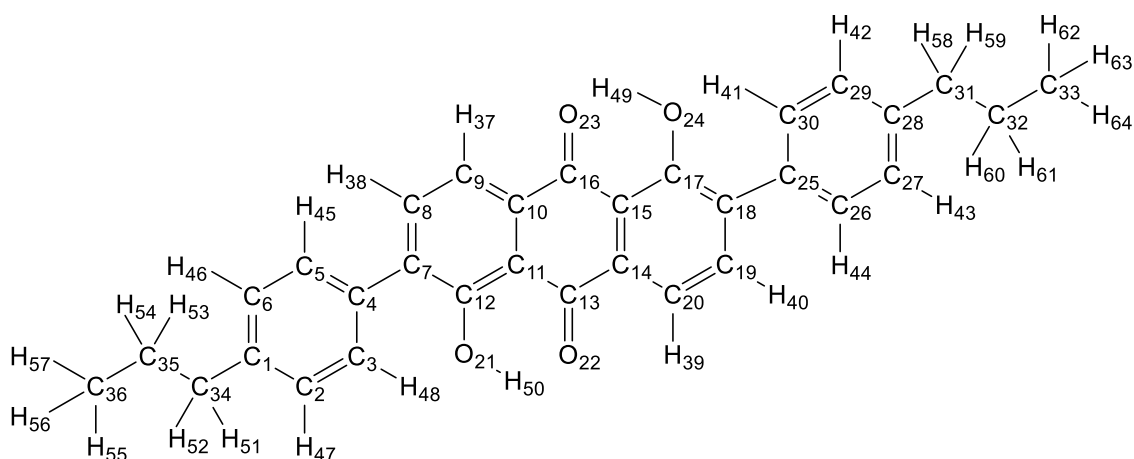


Figure A2.14 Structure and atom numbering of 26B3OH for the MD simulations.

Table A2.12 Atom numbers, OPLS atom types, charge groups and atomic charges (where default charges were not used) used for MD simulations of 26B3OH.

Atom number	Atom type	Charge group	Charge
1	opls_145	1	0.174
2	opls_145	2	-0.238
3	opls_145	3	-0.190
4	opls_145B	4	0.170
5	opls_145	5	-0.190
6	opls_145	6	-0.238
7	opls_145B	4	-0.147
8	opls_145	7	-0.061
9	opls_145	8	-0.230
10	opls_147	9	0.005
11	opls_147	9	-0.399
12	opls_166	10	0.490
13	opls_280	11	0.654
14	opls_147	12	0.005
15	opls_147	12	-0.399
16	opls_280	13	0.654
17	opls_166	14	0.490
18	opls_145B	15	-0.147
19	opls_145	16	-0.061
20	opls_145	17	-0.230
21	opls_167	10	-0.615
22	opls_281	11	-0.600
23	opls_281	13	-0.600
24	opls_167	14	-0.615
25	opls_145B	15	0.170
26	opls_145	18	-0.190
27	opls_145	19	-0.238
28	opls_145	20	0.174
29	opls_145	21	-0.238
30	opls_145	22	-0.190
31	opls_149	20	-0.302
32	opls_136	23	0.276

33	opls_135	24	-0.273
34	opls_149	1	-0.302
35	opls_136	25	0.276
36	opls_135	26	-0.273
37	opls_146	8	0.182
38	opls_146	7	0.136
39	opls_146	17	0.182
40	opls_146	16	0.136
41	opls_146	22	0.154
42	opls_146	21	0.164
43	opls_146	19	0.164
44	opls_146	18	0.154
45	opls_146	5	0.154
46	opls_146	6	0.164
47	opls_146	2	0.164
48	opls_146	3	0.154
49	opls_168	14	0.480
50	opls_168	10	0.480
51	opls_140	1	0.090
52	opls_140	1	0.090
53	opls_140	25	-0.040
54	opls_140	25	-0.040
55	opls_140	26	0.060
56	opls_140	26	0.060
57	opls_140	26	0.060
58	opls_140	20	0.090
59	opls_140	20	0.090
60	opls_140	23	-0.040
61	opls_140	23	-0.040
62	opls_140	24	0.060
63	opls_140	24	0.060
64	opls_140	24	0.060

A2.4 Potential energy wells of M2

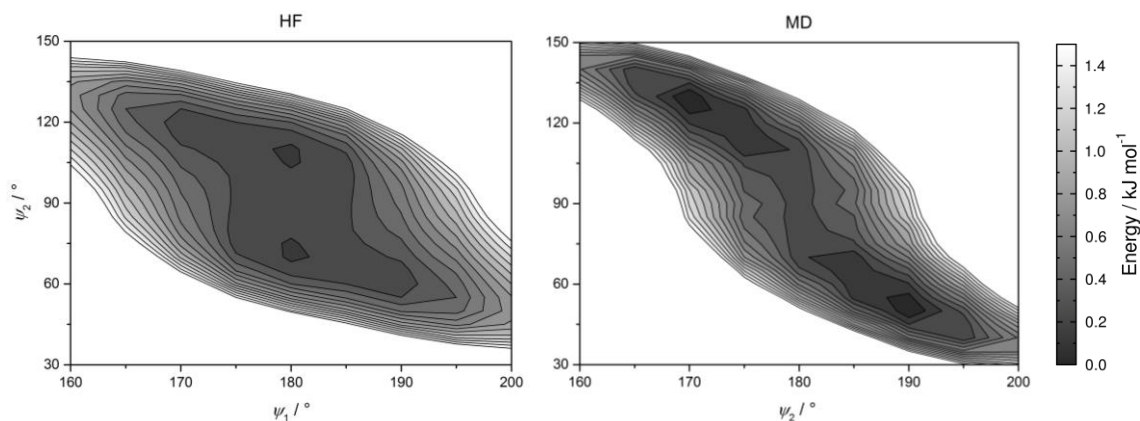


Figure A2.15 Enlarged plots of the potential energy surfaces for the two C-N-C-C dihedral angles of the **M3** from the HF calculations (left) and from MD after fitting (right), equivalent to Figure 4.15 but showing only the energy between 0 and 1.5 kJ mol^{-1} , illustrating the local minima in the base of each potential energy well.

A2.5 MD simulation verification

Figures A2.16-A2.19 are equivalent to Figure 4.19 in the main text for the different guest-host simulations.

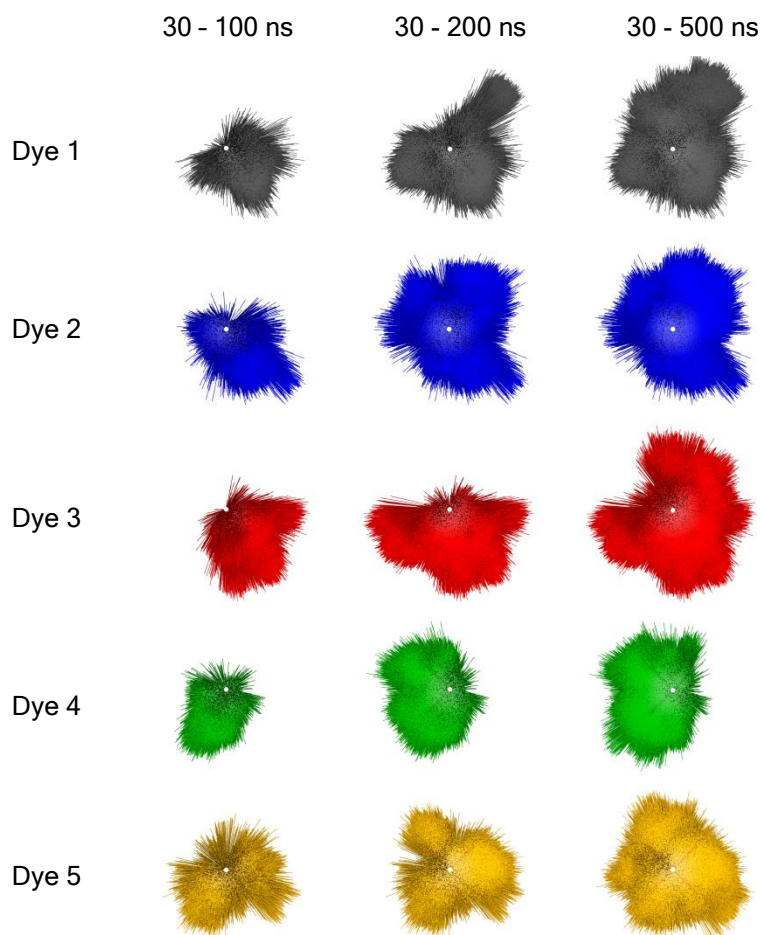


Figure A2.16 Estimates of the orientations explored by the long molecular axis of each of the five 15SB3 molecules (represented by different colours, consistent with Figure 4.16) during the guest-host simulation. Orientations are drawn as unit vectors and viewed down the host director axis (central points in white), with the time ranges during which the orientations were obtained labelled above.

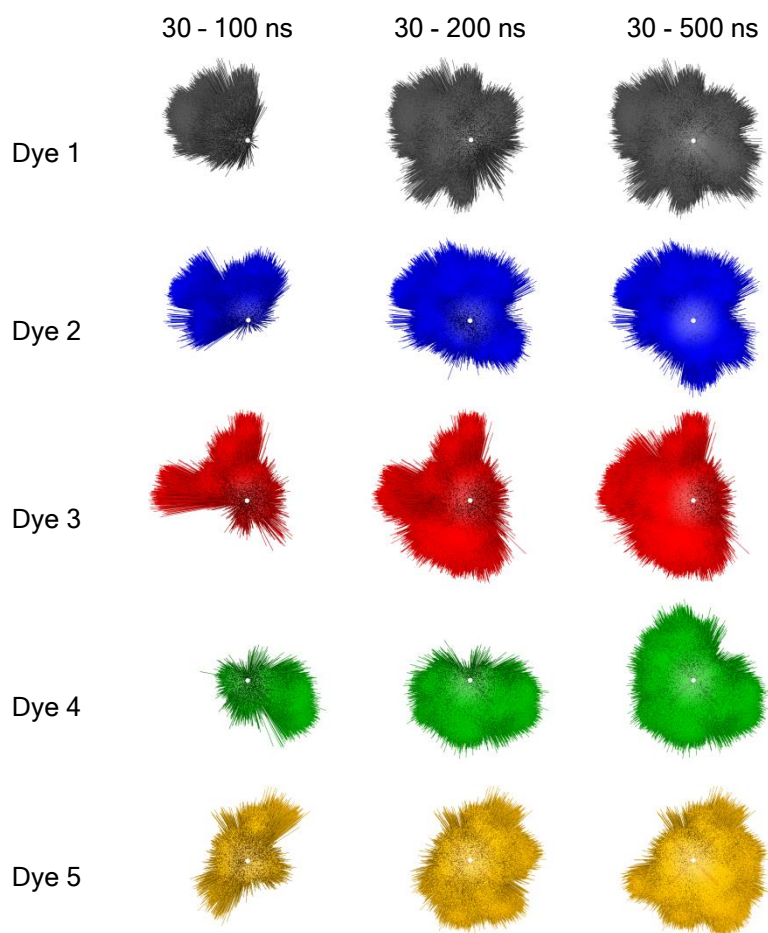


Figure A2.17 Estimates of the orientations explored by the long molecular axis of each of the five 15NB3OH molecules (represented by different colours, consistent with Figure 4.16) during the guest-host simulation. Orientations are drawn as unit vectors and viewed down the host director axis (central points in white), with the time ranges during which the orientations were obtained labelled above.

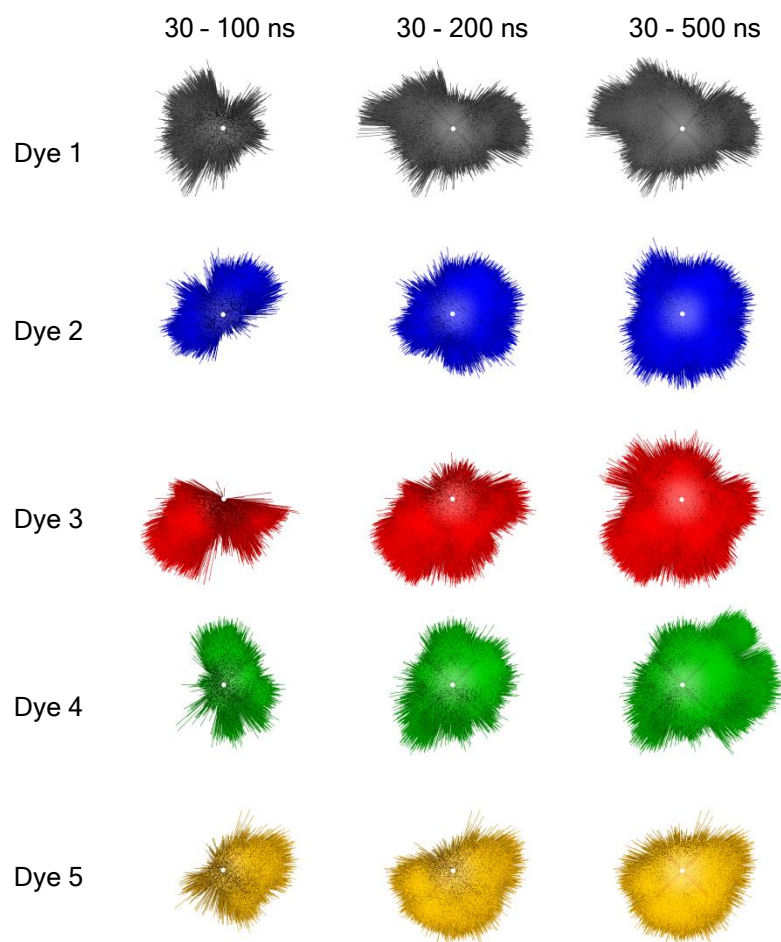


Figure A2.18 Estimates of the orientations explored by the long molecular axis of each of the five 26B3 molecules (represented by different colours, consistent with Figure 4.16) during the guest-host simulation. Orientations are drawn as unit vectors and viewed down the host director axis (central points in white), with the time ranges during which the orientations were obtained labelled above.

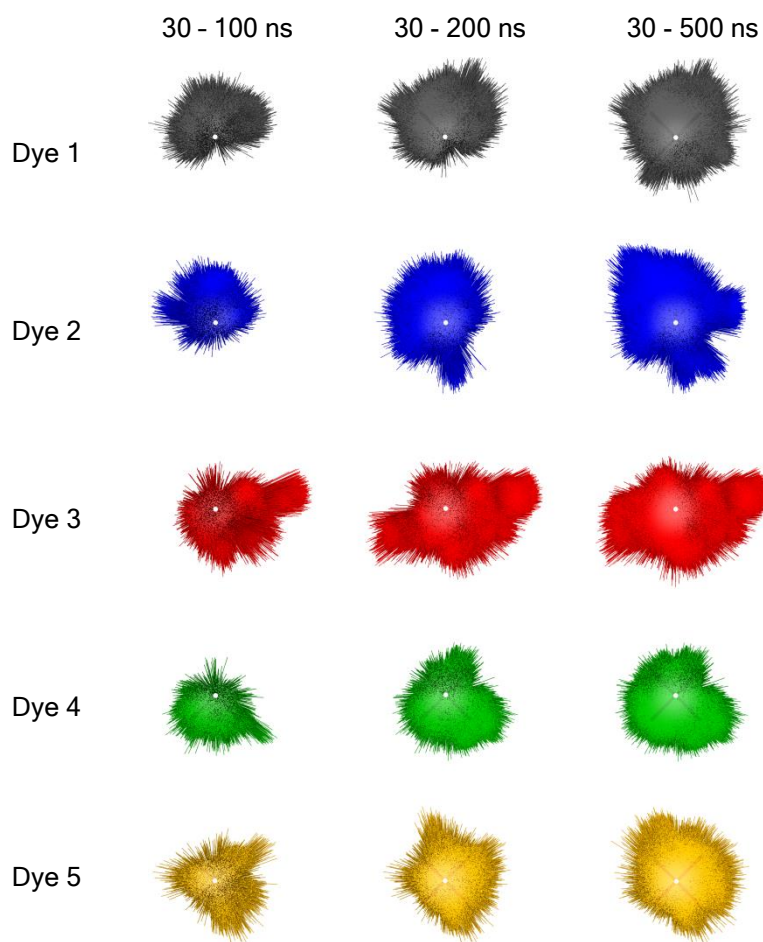


Figure A2.19 Estimates of the orientations explored by the long molecular axis of each of the five 26B3OH molecules (represented by different colours, consistent with Figure 4.16) during the guest-host simulation. Orientations are drawn as unit vectors and viewed down the host director axis (central points in white), with the time ranges during which the orientations were obtained labelled above.

A2.6 Guest-host MD simulation from isotropic starting configuration

Figure A2.20 shows the orientational order parameters, S_θ , of the host molecules and the dye molecules in the guest-host simulation of 26B3OH in E7 that was started from an isotropic configuration. The evolution of the host order parameter over time demonstrates the formation of the nematic phase over the course of *ca* 120 ns, and after this time the order parameters of 0.881 and 0.921 of the host and the dye molecules, respectively, are consistent with those of 0.879 and 0.896 from the simulation started from the pseudo-nematic configuration.

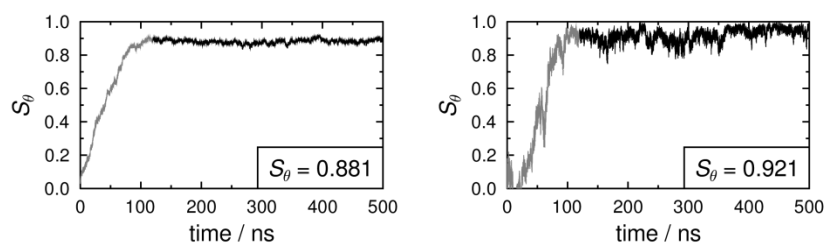


Figure A2.20 Plots of the calculated orientational order parameters, S_θ , of the host molecules (left) and the dye molecules (right) determined from the guest-host MD simulation of 26B3OH in E7 starting from an isotropic configuration. Sections shown in black (> 120 ns) were used for the calculation of the average values.

Appendix 3
Supplementary information relating to Chapter 5

A3.1 Wigner functions, $D_{m,n}^2(\alpha, \beta, \gamma)$

	n				
	-2	-1	0	1	2
-2	$\frac{1}{4}(1+\cos\beta)^2 e^{2i\alpha} e^{2i\gamma}$	$\frac{1}{2}\sin\beta(1+\cos\beta)e^{2i\alpha} e^{i\gamma}$	$\sqrt{\frac{3}{8}}\sin^2\beta e^{2i\alpha}$	$\frac{1}{2}\sin\beta(1-\cos\beta)e^{2i\alpha} e^{-i\gamma}$	$\frac{1}{4}(1-\cos\beta)^2 e^{2i\alpha} e^{-2i\gamma}$
-1	$-\frac{1}{2}\sin\beta(1+\cos\beta)e^{i\alpha} e^{2i\gamma}$	$\frac{1}{2}(2\cos\beta-1)(1+\cos\beta)e^{i\alpha} e^{i\gamma}$	$\sqrt{\frac{3}{2}}\sin\beta\cos\beta e^{i\alpha}$	$\frac{1}{2}(2\cos\beta+1)(1-\cos\beta)e^{i\alpha} e^{-i\gamma}$	$\frac{1}{2}\sin\beta(1-\cos\beta)e^{i\alpha} e^{-2i\gamma}$
$m = 0$	$\sqrt{\frac{3}{8}}\sin^2\beta e^{2i\gamma}$	$-\sqrt{\frac{3}{2}}\sin\beta\cos\beta e^{i\gamma}$	$\frac{1}{2}(3\cos^2\beta-1)$	$\sqrt{\frac{3}{2}}\sin\beta\cos\beta e^{-i\gamma}$	$\sqrt{\frac{3}{8}}\sin^2\beta e^{-2i\gamma}$
1	$-\frac{1}{2}\sin\beta(1-\cos\beta)e^{-i\alpha} e^{2i\gamma}$	$\frac{1}{2}(2\cos\beta+1)(1-\cos\beta)e^{-i\alpha} e^{i\gamma}$	$-\sqrt{\frac{3}{2}}\sin\beta\cos\beta e^{-i\alpha}$	$\frac{1}{2}(2\cos\beta-1)(1+\cos\beta)e^{-i\alpha} e^{-i\gamma}$	$\frac{1}{2}\sin\beta(1+\cos\beta)e^{-i\alpha} e^{-2i\gamma}$
2	$\frac{1}{4}(1-\cos\beta)^2 e^{-2i\alpha} e^{2i\gamma}$	$-\frac{1}{2}\sin\beta(1-\cos\beta)e^{-2i\alpha} e^{i\gamma}$	$\sqrt{\frac{3}{8}}\sin^2\beta e^{-2i\alpha}$	$-\frac{1}{2}\sin\beta(1+\cos\beta)e^{-2i\alpha} e^{-i\gamma}$	$\frac{1}{4}(1+\cos\beta)^2 e^{-2i\alpha} e^{-2i\gamma}$

A3.2 Derivation of Equation (5.21)

Three consecutive rotations described by sets of Euler angles, A , B and C , may be expressed as Wigner rotation matrices, $D_{m,n}^2(A)$, $D_{m,n}^2(B)$ and $D_{m,n}^2(C)$. The combined rotation of A and B , AB , may be expressed as Equation (A3.1).

$$D_{i,j}^2(AB) = \sum_k D_{i,k}^2(A) D_{k,j}^2(B) \quad (\text{A3.1})$$

The combined rotation ABC , may then be expressed as Equation (A3.2).

$$\begin{aligned} D_{i,l}^2(ABC) &= \sum_j D_{i,j}^2(AB) D_{j,l}^2(C) = \sum_k D_{i,k}^2(A) D_{k,l}^2(BC) \\ &= \sum_k \sum_j D_{i,k}^2(A) D_{k,j}^2(B) D_{j,l}^2(C) \end{aligned} \quad (\text{A3.2})$$

The term $D_{0,0}^2(ABC)$ is then defined according to Equation (A3.3)

$$D_{0,0}^2(ABC) = \sum_k \sum_j D_{0,k}^2(A) D_{k,j}^2(B) D_{j,0}^2(C) \quad (\text{A3.3})$$

A3.3 Derivation of $U(\beta, \gamma)$ using the surface tensor model

According to the surface tensor model, the potential energy, U , of a molecule at an orientation described by the Euler angles β and γ may be expressed as an integral over the molecular surface, S , where ψ are the angles between the unit vectors normal to the surface and the host director according to Equation A3.4 (which is given as Equation 5.33 in the main text).

$$\frac{U(\beta, \gamma)}{k_B T} = \varepsilon \int P_2(\cos \psi) dS \quad (\text{A3.4})$$

This expression may be rewritten in terms of a summation over discrete planar surface elements, s , according to Equation A3.5.

$$\frac{U(\beta, \gamma)}{k_B T} = \varepsilon \sum_s P_2(\cos \psi) \quad (\text{A3.5})$$

Using a similar approach to that described by Equations (5.21) - (5.24) in the main text, $P_2(\cos \psi)$ for a single surface unit vector may be expressed as Equation (A3.6), where $D_{i,0}^{2*}(XYZ \rightarrow \mathbf{n})$ describes the orientation of the director in the laboratory frame, $D_{ij}^2(\alpha, \beta, \gamma)$ describes the orientation of the molecular frame in the laboratory frame, and $D_{n,0}^2(\alpha', \beta')$ describes the orientation of a single surface vector in the molecular frame, which, by definition, has no dependence on γ' .

$$P_2(\cos \psi) = \sum_i \sum_j D_{i,0}^{2*}(XYZ \rightarrow \mathbf{n}) D_{i,j}^2(\alpha, \beta, \gamma) D_{j,0}^2(\alpha', \beta') \quad (\text{A3.6})$$

Assuming the director is defined as (0,0,1) in the laboratory frame, and applying the assumption of uniaxial phase symmetry (i.e. no α dependence), Equation (A3.7) is obtained.

$$P_2(\cos \psi) = \sum_j D_{0,j}^2(\beta, \gamma) D_{j,0}^2(\alpha', \beta') \quad (\text{A3.7})$$

If all the surface vectors are considered, rather than just one, Equation (A3.6) may be written as Equation (A3.8).

$$\int P_2(\cos\psi) dS = \sum_j D_{0,j}^2(\beta, \gamma) \int D_{j,0}^2(\alpha', \beta') dS \quad (\text{A3.8})$$

Therefore according to the definition of the surface tensor components, $T^{2,n}$, given by Equation (A3.9),^{342, 343} Equation (A3.5) may be expressed as Equation (A3.10), corresponding to Equation (5.36) in the main text.

$$T^{2,j} = -\int D_{j,0}^{2*}(\alpha', \beta') dS \quad (\text{A3.9})$$

$$\frac{U(\beta, \gamma)}{k_B T} = -\varepsilon \sum_j T^{2,j*} D_{0,j}^2(\beta, \gamma) \quad (\text{A3.10})$$

A3.4 Derivation of \mathbf{T} from \mathbf{t}

The spherical tensor, \mathbf{T} , with components $T^{2,n}$, must transform under rotation in the same way as the spherical harmonics of order two in order to satisfy Equation (A3.8), hence in a Cartesian basis it must be defined as a symmetric, traceless, second-rank tensor.³⁴⁴

Equation (A3.9) may be written as a sum over discrete surface elements, given by Equation (A3.11), the normal unit vectors of which are defined by the spherical polar angles α' and β' in the molecular frame.²⁹⁹

$$T^{2,j} = -\sum_s D_{j,0}^{2*}(\alpha', \beta') \quad (\text{A3.11})$$

Rather than all of the unit vectors normal to the surface elements being considered individually, their sum can be considered in terms of three vectors: one pointing in the x direction of magnitude t_{xx} , a second pointing in the y direction of magnitude t_{yy} , and a third pointing in the z direction of magnitude t_{zz} in the molecular xyz frame. These magnitudes are the inverse of the eigenvalues of the diagonal surface tensor, \mathbf{t} .

This approach enables Equation (A3.11) to be written as a sum of Wigner functions, given by Equation (A3.12) with values of α' and β' indicating the angles defining the Cartesian x , y , and z axes.

$$T^{2,j} = t_{xx} D_{j,0}^{2*}(0^\circ, 90^\circ, \gamma') + t_{yy} D_{j,0}^{2*}(90^\circ, 90^\circ, \gamma') + t_{zz} D_{j,0}^{2*}(\alpha', 0^\circ, \gamma') \quad (\text{A3.12})$$

Expanding the Wigner functions in Equation (A3.12) according to the definitions given in Appendix A3.1 gives Equations (A3.13) and (A3.14), demonstrates that $T^{2,\pm 1} = 0$. $T^{0,0} = 0$ because, as stated above, the Cartesian form of the tensor, \mathbf{T} , must be traceless.¹²⁷

$$T^{2,0} = t_{zz} - \left(\frac{t_{xx} + t_{yy}}{2} \right) \quad (\text{A3.13})$$

$$T^{2,2} = T^{2,-2} = \sqrt{\frac{3}{8}}(t_{xx} - t_{yy}) \quad (\text{A3.14})$$

The Cartesian components of \mathbf{T} , given by Equations (A3.15) – (A3.17), may then be derived from the spherical components according to Equations (A3.30) – (A3.32) in Appendix A3.5 below.¹²⁷

$$T_{xx} = -\frac{1}{\sqrt{6}}T^{2,0} + T^{2,\pm 2} \quad (\text{A3.15})$$

$$T_{yy} = -\frac{1}{\sqrt{6}}T^{2,0} - T^{2,\pm 2} \quad (\text{A3.16})$$

$$T_{zz} = \sqrt{\frac{2}{3}}T^{2,0} \quad (\text{A3.17})$$

Substituting Equations (A3.13) and (A3.14) into Equations (A3.15) – (A3.17) gives Equations (A3.18) – (A3.20).

$$T_{xx} = \frac{2}{\sqrt{6}}t_{xx} - \frac{1}{\sqrt{6}}(t_{zz} + t_{yy}) \quad (\text{A3.18})$$

$$T_{yy} = \frac{2}{\sqrt{6}}t_{yy} - \frac{1}{\sqrt{6}}(t_{zz} + t_{xx}) \quad (\text{A3.19})$$

$$T_{zz} = \frac{2}{\sqrt{6}}t_{zz} - \frac{1}{\sqrt{6}}(t_{xx} + t_{yy}) \quad (\text{A3.20})$$

Rearrangement of these expressions results in Equations (A3.21) – (A3.23), which correspond to Equation (5.37) in the main text, defining the Cartesian components of \mathbf{T} from the components of the surface tensor, \mathbf{t} .

$$T_{xx} = \frac{3t_{xx} - Tr(\mathbf{t})}{\sqrt{6}} \quad (\text{A3.21})$$

$$T_{yy} = \frac{3t_{yy} - Tr(\mathbf{t})}{\sqrt{6}} \quad (\text{A3.22})$$

$$T_{zz} = \frac{3t_{zz} - Tr(\mathbf{t})}{\sqrt{6}} \quad (\text{A3.23})$$

A3.5 Conversion between spherical and Cartesian tensors

The 9 components, T_{ij} , of an irreducible Cartesian tensor may be converted to spherical components, $T^{L,m}$, according to Equations (A3.24) - (A3.29).^{127, 345}

$$T^{0,0} = -\frac{1}{\sqrt{3}}(T_{xx} + T_{yy} + T_{zz}) \quad (\text{A3.24})$$

$$T^{1,0} = \frac{i}{\sqrt{2}}(T_{xy} - T_{yx}) \quad (\text{A3.25})$$

$$T^{1,\pm 1} = \frac{1}{2}(T_{zx} - T_{xz} \pm i(T_{zy} - T_{yz})) \quad (\text{A3.26})$$

$$T^{2,0} = \frac{1}{\sqrt{6}}(3T_{zz} - (T_{xx} + T_{yy} + T_{zz})) \quad (\text{A3.27})$$

$$T^{2,\pm 1} = \mp \frac{1}{2}(T_{xz} + T_{zx} \pm i(T_{yz} + T_{zy})) \quad (\text{A3.28})$$

$$T^{2,\pm 2} = \frac{1}{2}(T_{xx} - T_{yy} \pm i(T_{xy} + T_{yx})) \quad (\text{A3.29})$$

A symmetric second-rank Cartesian tensor may be obtained from a spherical tensor according to Equations (A3.30) to (3.35).¹²⁷

$$T_{xx} = -\frac{1}{\sqrt{3}}T_{0,0} - \frac{1}{\sqrt{6}}T_{2,0} + \frac{1}{2}(T_{2,2} + T_{2,-2}) \quad (\text{A3.30})$$

$$T_{yy} = -\frac{1}{\sqrt{3}}T_{0,0} - \frac{1}{\sqrt{6}}T_{2,0} - \frac{1}{2}(T_{2,2} + T_{2,-2}) \quad (\text{A3.31})$$

$$T_{zz} = -\frac{1}{\sqrt{3}}T_{0,0} + \sqrt{\frac{2}{3}}T_{2,0} \quad (\text{A3.32})$$

$$T_{xy} = -\frac{i}{2}(T_{2,2} - T_{2,-2}) \quad (\text{A3.33})$$

$$T_{xz} = \frac{1}{2}(T_{2,-1} - T_{2,1}) \quad (\text{A3.34})$$

$$T_{yz} = \frac{i}{2}(T_{2,1} + T_{2,-1}) \quad (\text{A3.35})$$

Appendix 4

Supplementary information relating to Chapter 7

A4.1 Atom types for MD simulations

The numbered structures of **1** and **2** are shown below, with assigned atom-types, charge groups and atomic charges listed below each structure

1

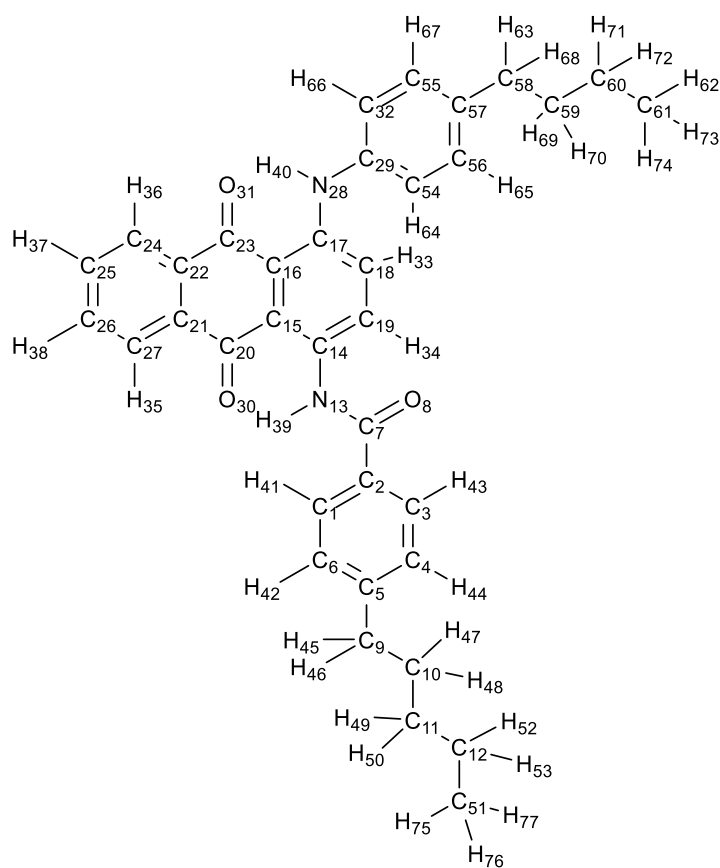


Figure A4.1 Structure and atom numbering of **1** for the MD simulations.

Table A4.1 Atom numbers, OPLS atom types, charge groups and atomic charges (where default charges were not used) used for MD simulations of **1**.

Atom number	Atom type	Charge group	Charge	Atom number	Atom type	Charge group	Charge
1	opls_145	1	-0.073	40	opls_910	11	0.360
2	opls_145	2	-0.097	41	opls_146	1	0.109
3	opls_145	3	-0.073	42	opls_146	6	0.142
4	opls_145	4	-0.224	43	opls_146	3	0.109
5	opls_145	5	0.210	44	opls_146	4	0.142
6	opls_145	6	-0.224	45	opls_140	5	0.075
7	opls_234	2	0.584	46	opls_140	5	0.075
8	opls_236	2	-0.508	47	opls_140	7	-0.014
9	opls_149	5	-0.276	48	opls_140	7	-0.014
10	opls_136	7	0.102	49	opls_140	8	-0.001
11	opls_136	8	0.015	50	opls_140	8	-0.001
12	opls_136	9	0.146	51	opls_135	22	-0.281
13	opls_265	2	-0.485	52	opls_140	9	-0.025
14	opls_266	2	0.350	53	opls_140	9	-0.025
15	opls_147	10	-0.234	54	opls_145	23	-0.239
16	opls_147	10	-0.252	55	opls_145	24	-0.190
17	opls_916	11	0.385	56	opls_145	25	-0.190
18	opls_145	12	-0.227	57	opls_145	26	0.177
19	opls_145	13	-0.189	58	opls_149	26	-0.331
20	opls_280	14	0.475	59	opls_136	27	0.083
21	opls_147	15	-0.065	60	opls_136	28	0.200
22	opls_147	15	-0.017	61	opls_135	29	-0.345
23	opls_280	16	0.452	62	opls_140	29	0.078
24	opls_145	17	-0.096	63	opls_140	26	0.087
25	opls_145	18	-0.101	64	opls_146	23	0.143
26	opls_145	19	-0.103	65	opls_146	25	0.146
27	opls_145	20	-0.085	66	opls_146	21	0.143
28	opls_901	11	-0.547	67	opls_146	24	0.146
29	opls_916	11	0.338	68	opls_140	26	0.087
30	opls_281	14	-0.456	69	opls_140	27	-0.003
31	opls_281	16	-0.491	70	opls_140	27	-0.003
32	opls_145	21	-0.239	71	opls_140	28	-0.029
33	opls_146	12	0.148	72	opls_140	28	-0.029
34	opls_146	13	0.185	73	opls_140	29	0.079
35	opls_146	20	0.112	74	opls_140	29	0.079
36	opls_146	17	0.119	75	opls_140	22	0.064
37	opls_146	18	0.118	76	opls_140	22	0.064
38	opls_146	19	0.118	77	opls_140	22	0.064
39	opls_241	2	0.273				

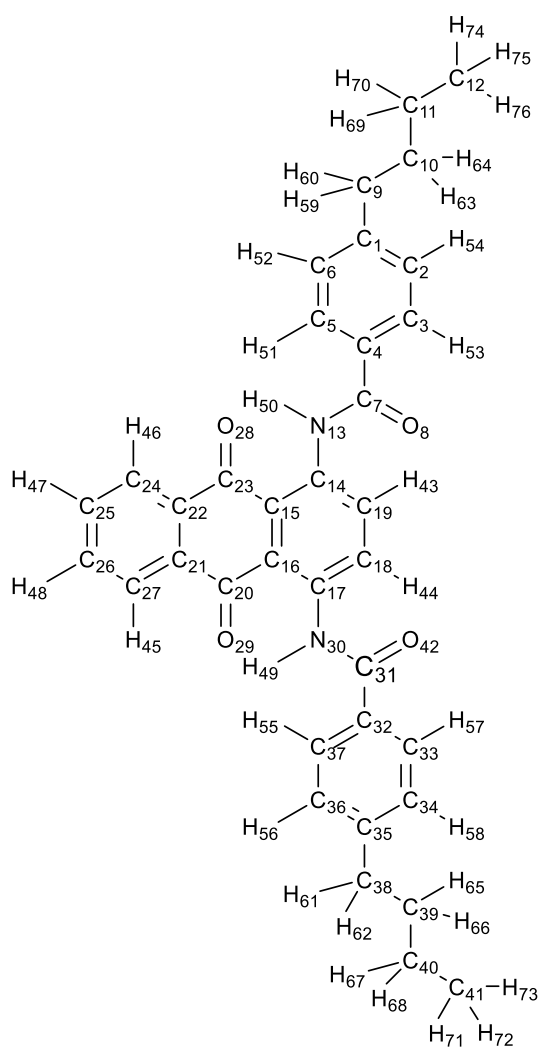


Figure A4.2 Structure and atom numbering of **2** for the MD simulations.

Table A4.2 Atom numbers, OPLS atom types, charge groups and atomic charges (where default charges were not used) used for MD simulations of **2**.

Atom number	Atom type	Charge group	Charge	Atom number	Atom type	Charge group	Charge
1	opls_145	1	0.338	39	opls_136	28	0.179
2	opls_145	2	-0.323	40	opls_136	29	0.206
3	opls_145	3	-0.040	41	opls_135	30	-0.384
4	opls_145	4	-0.187	42	opls_236	22	-0.604
5	opls_145	5	-0.04	43	opls_146	14	0.225
6	opls_145	6	-0.323	44	opls_146	13	0.225
7	opls_234	4	0.768	45	opls_146	21	0.156
8	opls_236	4	-0.604	46	opls_146	18	0.156
9	opls_149	1	-0.453	47	opls_146	19	0.139
10	opls_136	7	0.179	48	opls_146	20	0.139
11	opls_136	8	0.206	49	opls_241	12	0.318
12	opls_135	9	-0.384	50	opls_241	10	0.318
13	opls_265	10	-0.626	51	opls_146	5	0.132
14	opls_266	10	0.437	52	opls_146	6	0.179
15	opls_147	11	-0.309	53	opls_146	3	0.132
16	opls_147	11	-0.309	54	opls_146	2	0.179
17	opls_266	12	0.437	55	opls_146	27	0.132
18	opls_145	13	-0.244	56	opls_146	26	0.179
19	opls_145	14	-0.244	57	opls_146	23	0.132
20	opls_280	15	0.624	58	opls_146	24	0.179
21	opls_147	16	-0.056	59	opls_140	1	0.112
22	opls_147	16	-0.056	60	opls_140	1	0.112
23	opls_280	17	0.624	61	opls_140	25	0.112
24	opls_145	18	-0.144	62	opls_140	25	0.112
25	opls_145	19	-0.103	63	opls_140	7	-0.022
26	opls_145	20	-0.103	64	opls_140	7	-0.022
27	opls_145	21	-0.144	65	opls_140	28	-0.022
28	opls_281	17	-0.547	66	opls_140	28	-0.022
29	opls_281	15	-0.547	67	opls_140	29	-0.032
30	opls_265	12	-0.626	68	opls_140	29	-0.032
31	opls_234	22	0.768	69	opls_140	8	-0.032
32	opls_145	22	-0.187	70	opls_140	8	-0.032
33	opls_145	23	-0.040	71	opls_140	30	0.085
34	opls_145	24	-0.323	72	opls_140	30	0.085
35	opls_145	25	0.338	73	opls_140	30	0.085
36	opls_145	26	-0.323	74	opls_140	9	0.085
37	opls_145	27	-0.040	75	opls_140	9	0.085
38	opls_149	25	-0.453	76	opls_140	9	0.085

Definitions

α	Euler angle describing the initial rotation about the principal axis of the Cartesian reference frame
a	Molecular alignment axis calculated against the director
AIMD	Ab initio molecular dynamics
β	Euler angle describing the rotation about the y axis after rotation, α ; Angle between dye molecular axis and TDM
BOMD	Born-Oppenheimer molecular dynamics
C	Molecular circumference
CPMD	Car-Parrinello molecular dynamics
CV	Cyclic voltammetry
D	Biaxial order parameter, calculated as $S_{xx} - S_{yy}$
DCM	Dichloromethane
DFT	Density functional theory
ε	Molar absorption coefficient; Orienting potential
E	Orientation of electric component of linearly polarised light
E	redox potential
f	Oscillator strength
$f(\alpha, \beta, \gamma)$	Orientational distribution function
Fc	Ferrocene
FWHM	Full-width at half-maximum
γ	Euler angle describing the final rotation about the z axis after the rotations described by α and β
HF	Hartree Fock
HOMO	Highest occupied molecular orbital
IR	Infrared
λ_{\max}	Wavelength of maximum visible absorption
LCD	Liquid crystal display
LUMO	Lowest unoccupied molecular orbital
MD	Molecular dynamics
MOI	Moment of inertia
n	Director

NMR	Nuclear magnetic resonance
Ω	Abbreviation of the Euler angles, α , β and γ
s	Planar molecular surface element
S	Molecular surface
S_β	Calculated second-rank order parameter of the TDM of a dye against the principal molecular axis of the dye
S_ϕ	Calculated second-rank dichroic order parameter of the TDM of a dye
S_θ	Calculated second-rank order parameter of the principal molecular axis of a dye against the host director
S_{exp}	Experimental second-rank dichroic order parameter
S_{ii}	Second-rank orientational order parameter of the molecular i axis
$S_{xx} - S_{yy}$	Biaxial order parameter
SES	Solvent excluded surface
θ_{dye}	Angle between the dye molecular orientation and the director of the system
θ_{host}	Angle between the host molecular orientation and the director of the system
\mathbf{t}	Surface tensor describing the orientations of molecular surface elements
\mathbf{T}	Surface tensor derived from \mathbf{t}
TBAHFP	Tetrabutylammonium hexafluorophosphate
TD-DFT	Time-dependent density functional theory
TDM	Transition dipole moment
TN	Twisted nematic
$U(\alpha, \beta, \gamma)$	Energy of a molecular orientation described by the Euler angles, α , β and γ
UV	Ultraviolet
vis	Visible
x, y, z	Cartesian axes of the molecular frame
X, Y, Z	Cartesian axes of the laboratory frame

References

1. H. Kawamoto, *Proc. IEEE*, 2002, 90, 460-500.
2. H. F. Gleeson, in *Handbook of Liquid Crystals*, Eds. D. Demus, J. W. Goodby, G. W. Gray, H. W. Spiess and V. Vill, Wiley-VCH, Weinheim, 1998, vol. 1, pp. 823-838.
3. Y.-H. Lin, H.-S. Chen and M.-S. Chen, *Mol. Cryst. Liq. Cryst.*, 2014, 596, 12-21.
4. H. Coles and S. Morris, *Nat. Photonics*, 2010, 4, 676-685.
5. B. R. Kaafarani, *Chem. Mater.*, 2010, 23, 378-396.
6. A. M. Lowe and N. L. Abbott, *Chem. Mater.*, 2011, 24, 746-758.
7. G. H. Heilmeier and L. A. Zanoni, *Appl. Phys. Lett.*, 1968, 13, 91-92.
8. G. H. Heilmeier, *IEEE Trans. Electron Devices*, 1976, 23, 780-785.
9. T. Uchida and M. Wada, *Mol. Cryst. Liq. Cryst.*, 1981, 63, 19-43.
10. D. L. White and G. N. Taylor, *J. Appl. Phys.*, 1974, 45, 4718-4723.
11. H. S. Cole and R. A. Kashnow, *Appl. Phys. Lett.*, 1977, 30, 619-621.
12. T. Uchida, H. Seki, C. Shishido and M. Wada, *Proc. SID*, 1981, 22, 41-46.
13. A. B. Ebru, M. Maxim, H. Børre, G. Anatoliy and L. W. John, *Jpn. J. Appl. Phys.*, 2006, 45, 4146.
14. Y.-H. Lin, H. Ren, S. Gauza, Y.-H. Wu, Y. Zhou and S.-T. Wu, *Mol. Cryst. Liq. Cryst.*, 2006, 453, 371-378.
15. T. Suzuki, H. Fujikake, T. Murashige, H. Sato, H. Kikuchi, T. Kurita and F. Sato, *Electron. Comm. Jpn., Part 2*, 2005, 88, 21-28.
16. E. Peeters, J. Lub, J. A. M. Steenbakkers and D. J. Broer, *Adv. Mater.*, 2006, 18, 2412-2417.
17. M. R. Lufor, G. Hegde, S. Kumar, C. Tschierske and V. G. Chigrinov, *Opt. Mater.*, 2009, 32, 176-183.
18. L. De Sio, L. Ricciardi, S. Serak, M. La Deda, N. Tabiryan and C. Umeton, *J. Mater. Chem.*, 2012, 22, 6669-6673.
19. C. Carrasco-Vela, X. Quintana, E. Oton, M. A. Geday and J. M. Oton, *Opto-Electron. Rev.*, 2011, 19, 496-500.

20. M. G. Debije, *Adv. Funct. Mater.*, 2010, 20, 1498-1502.
21. Q. K. Liu, C. Beier, J. Evans, T. Lee, S. L. He and I. I. Smalyukh, *Langmuir*, 2011, 27, 7446-7452.
22. J. E. Reeve, A. D. Corbett, I. Boczarow, T. Wilson, H. Bayley and H. L. Anderson, *Biophys. J.*, 2012, 103, 907-917.
23. Š. Timr, A. Bondar, L. Cwiklik, M. Štefl, M. Hof, M. Vazdar, J. Lazar and P. Jungwirth, *J. Phys. Chem. B*, 2013, 118, 855-863.
24. B. Bahadur, in *Liquid Crystals: Applications and Uses*, Ed. B. Bahadur, World Scientific Publishing Co. Pte. Ltd., Singapore, 1992, vol. 3, ch. 11, pp. 65-208.
25. C. Zannoni, in *The Molecular Dynamics of Liquid Crystals*, Eds. G. R. Luckhurst and C. A. Veracini, Springer, New York, 1994, pp. 11-40.
26. G. R. Luckhurst, in *Physical Properties of Liquid Crystals: Nematics.*, Eds. D. A. Dunmur, A. Fukuda and G. R. Luckhurst, IET, London, 2001, pp. 57-88.
27. C. Palfy-Muhoray, *Dynamics and Defects in Liquid Crystals: A Festschrift in Honor of Alfred Saupe*, Gordon and Breach, Amsterdam, 1998.
28. A. F. Runge, S. S. Saavedra and S. B. Mendes, *J. Phys. Chem. B*, 2006, 110, 6721-6731.
29. C. Zannoni, in *Molecular Physics of Liquid Crystals*, Eds. G. R. Luckhurst and G. W. Gray, Academic Press, London, 1979, pp. 51-84.
30. I. W. Hamley, S. Garnett, G. R. Luckhurst, S. J. Roskilly, J. S. Pedersen, R. M. Richardson and J. M. Seddon, *J. Chem. Phys.*, 1996, 104, 10046-10054.
31. S. Limmer, *Fortschr. Phys.*, 1989, 37, 879-931.
32. S. Jen, N. A. Clark, P. S. Pershan and E. B. Priestley, *J. Chem. Phys.*, 1977, 66, 4635-4661.
33. A. Arcioni, R. Tarroni and C. Zannoni, *Nuovo Cimento D*, 1988, 10, 1409-1426.
34. M. van Gurp, *Colloid. Polym. Sci.*, 1995, 273, 607-625.
35. G. R. Luckhurst and C. Zannoni, *Nature*, 1977, 267, 412-414.
36. K. J. Rothschild and N. A. Clark, *Biophys. J.*, 1979, 25, 473-487.
37. J. Griffiths and K.-C. Feng, *J. Mater. Chem.*, 1999, 9, 2333-2338.
38. P. J. Collings and M. Hird, *Introduction to Liquid Crystals*, Taylor and Francis, 2004.

39. W. Haase, O. Trinquet, U. Quotschalla and J. K. Foitzik, *Mol. Cryst. Liq. Cryst.*, 1987, 148, 15-27.
40. D. Bauman, *Mol. Cryst. Liq. Cryst.*, 1988, 159, 197-218.
41. L. O. Palsson, M. Szablewski, A. Roberts, A. Masutani, G. D. Love, G. H. Cross, D. Bloor, A. J. Kay, A. D. Woolhouse, A. Masutani and A. Yasuda, *Mol. Cryst. Liq. Cryst.*, 2003, 402, 279-289.
42. D. Bauman, E. Mykowska and E. Wolarz, *Mol. Cryst. Liq. Cryst. Sci. Technol., Sect. A*, 1998, 321, 333-347.
43. G. W. Gray, in *Handbook of Liquid Crystals*, Eds. D. Demus, J. W. Goodby, G. W. Gray, H. W. Spiess and V. Vill, Wiley-VCH, Weinheim, 1998, vol. 1, pp. 257-302.
44. J. Constant, E. P. Raynes, I. A. Shanks, D. Coates, G. W. Gray and D. G. McDonnell, *J. Phys. D: Appl. Phys.*, 1978, 11, 479-489.
45. A. Ghanadzadeh Gilani, M. Moghadam, M. S. Zakerhamidi and E. Moradi, *Dyes Pigm.*, 2012, 92, 1320-1330.
46. D. Bauman and H. Moryson, *J. Mol. Struct.*, 1997, 404, 113-120.
47. D. Bauman, E. Mykowska, A. Zieba, E. Chrzumnicka, G. Czechowski and J. Jadzyn, *Phase Transitions*, 2007, 80, 599-613.
48. R. M. Christie, *Colour Chemistry*, Royal Society of Chemistry, Cambridge, 2001.
49. H. Seki, C. Shishido, S. Yasui and T. Uchida, *Jpn. J. Appl. Phys., Part 1*, 1982, 21, 191-192.
50. F. Jones and T. J. Reeve, *J. Soc. Dyers Colour.*, 1979, 95, 352-359.
51. M. Matsui, S. Okada, M. Kadowaki and M. Yamada, *Liq. Cryst.*, 2002, 29, 707-712.
52. H. Seki, T. Uchida and C. Shishido, *Jpn. J. Appl. Phys.*, 1980, 19, L501-L503.
53. G. W. Gray, *Dyes Pigm.*, 1982, 3, 203-209.
54. H. Inoue, M. Hida, N. Nakashima and K. Yoshihara, *J. Phys. Chem.*, 1982, 86, 3184-3188.
55. N. S. Allen, G. Pullen, M. Shah, M. Edge, D. Holdsworth, I. Weddell, R. Swart and F. Catalina, *J. Photochem. Photobiol. A*, 1995, 91, 73-79.
56. H. Labhart, *Helv. Chim. Acta*, 1957, 40, 1410-1420.

57. P. Dahiya, M. Kumbhakar, D. K. Maity, T. Mukherjee, A. B. R. Tripathi, N. Chattopadhyay and H. Pal, *J. Photochem. Photobiol. A*, 2006, 181, 338-347.
58. M. Umadevi, A. Suvitha, K. Latha, B. J. M. Rajkumar and V. Ramakrishnan, *Spectrochim. Acta, Part A*, 2007, 67, 910-915.
59. M. G. Pellatt, I. H. C. Roe and J. Constant, *Mol. Cryst. Liq. Cryst.*, 1980, 59, 299-316.
60. F. C. Saunders, K. J. Harrison, E. P. Raynes and D. J. Thompson, *IEEE Trans. Electron Devices*, 1983, 30, 499-503.
61. G. Heppke, B. Knippenberg, A. Moller and G. Scherowsky, *Mol. Cryst. Liq. Cryst.*, 1983, 94, 191-204.
62. K. Naito and H. Iwanaga, *Jpn. J. Appl. Phys., Part 1*, 1998, 37, 3422-3427.
63. S. Imazeki, *Mol. Cryst. Liq. Cryst.*, 1986, 140, 119-130.
64. H. Iwanaga, K. Naito and F. Aiga, *J. Mol. Struct.*, 2010, 975, 110-114.
65. H. Iwanaga, K. Naito and Y. Nakai, *Mol. Cryst. Liq. Cryst.*, 2001, 364, 211-218.
66. H. Iwanaga, *Materials*, 2009, 2, 1636-1661.
67. H. Iwanaga and K. Naito, *Jpn. J. Appl. Phys., Part 2*, 1998, 37, L356-L358.
68. H. Iwanaga and F. Aiga, *Liq. Cryst.*, 2011, 38, 135-148.
69. S. J. Cowling, C. Ellis and J. W. Goodby, *Liq. Cryst.*, 2011, 38, 1683-1698.
70. G. Pelzl, H. Zschke and D. Demus, *Displays*, 1985, 6, 141-147.
71. E. Wolarz, H. Moryson and D. Bauman, *Displays*, 1992, 13, 171-178.
72. D. Bauman and H. G. Kuball, *Chem. Phys.*, 1993, 176, 221-231.
73. T. Martyński, E. Mykowska, R. Stolarski and D. Bauman, *Dyes Pigm.*, 1994, 25, 115-129.
74. S. Kumar, *Chem. Soc. Rev.*, 2006, 35, 83-109.
75. Z. H. Chen and T. M. Swager, *Org. Lett.*, 2007, 9, 997-1000.
76. X. Zhang, H. Gorohmaru, M. Kadowaki, T. Kobayashi, T. Ishi-i, T. Thiemann and S. Mataka, *J. Mater. Chem.*, 2004, 14, 1901-1904.
77. S. E. Braslavsky, *Pure Appl. Chem.*, 2007, 79, 293-465.

78. P. Atkins, *The Elements of Physical Chemistry*, Oxford University Press, Oxford, 3rd edn., 2001.
79. C. N. Banwell, *Fundamentals of Molecular Spectroscopy*, McGraw-Hill Book Company (UK) Limited, 3rd edn., 1983.
80. L. C. Abbott, S. N. Batchelor, J. Oakes, B. C. Gilbert, A. C. Whitwood, J. R. Lindsay Smith and J. N. Moore, *J. Phys. Chem. A*, 2005, 109, 2894-2905.
81. A. M. Bond, *Broadening Electrochemical Horizons*, Oxford University Press, Oxford, 2002.
82. G. Gritzner and J. Kuta, *Pure Appl. Chem.*, 1984, 56, 461-466.
83. C. J. Cramer, *Essentials of Computational Chemistry*, Wiley, Chichester, 2004.
84. J. B. Foresman and Æ. Frisch, *Exploring Chemistry with Electronic Structure Methods*, Gaussian, Inc., Pittsburgh, 1993.
85. P. Hohenberg and W. Kohn, *Phys. Rev. B*, 1964, 136, B864-B871.
86. W. Kohn and L. J. Sham, *Phys Rev*, 1965, 140, 1133-1138.
87. A. D. Becke, *J. Chem. Phys.*, 1993, 98, 5648-5652.
88. P. J. Stephens, F. J. Devlin, C. F. Chabalowski and M. J. Frisch, *J. Phys. Chem.*, 1994, 98, 11623-11627.
89. M. R. Wilson, *Int. Rev. Phys. Chem.*, 2005, 24, 421-455.
90. S. B. Sinnott and D. W. Brenner, *MRS Bull.*, 2012, 37, 469-473.
91. W. L. Jorgensen, D. S. Maxwell and J. T. Rives, *J. Am. Chem. Soc.*, 1996, 118, 11225-11236.
92. D. Marx and J. Hutter, *Ab Initio Molecular Dynamics: Basic Theory and Advanced Methods*, Cambridge University Press, Cambridge, 2009.
93. G. Galli and A. Pasquarello, in *Computer Simulation in Chemical Physics*, Eds. M. P. Allen and D. J. Tildesley, Springer, New York, 1993, pp. 261-314.
94. R. Car and M. Parrinello, *Phys. Rev. Lett.*, 1985, 55, 2471-2474.
95. M. C. Payne, M. P. Teter, D. C. Allan, T. A. Arias and J. D. Joannopoulos, *Rev. Mod. Phys.*, 1992, 64, 1045-1097.
96. D. Vanderbilt, *Phys. Rev. B*, 1990, 41, 7892-7895.
97. S. P. Yadav, K. K. Pandey, A. K. Misra, P. K. Tripathi and R. Manohar, *Phys. Scr.*, 2011, 83.

98. H. G. Kuball, A. Strauss, M. Kappus, E. Fechterrink, A. Schonhofer and G. Scherowsky, *Ber. Bunsen-Ges. Phys. Chem.*, 1987, 91, 1266-1273.
99. L. C. Abbott, D. Phil. Thesis, University of York, 1988.
100. G. Gritzner and J. Kůta, *Electrochim. Acta*, 1984, 29, 869-873.
101. S. Haymond, J. K. Zak, Y. Show, J. E. Butler, G. T. Babcock and G. M. Swain, *Anal. Chim. Acta*, 2003, 500, 137-144.
102. M. J. Frisch, G. W. Trucks, H. B. Schlegel, G. E. Scuseria, M. A. Robb, J. R. Cheeseman, G. Scalmani, V. Barone, B. Mennucci, G. A. Petersson, H. Nakatsuji, M. Caricato, X. Li, H. P. Hratchian, A. F. Izmaylov, J. Bloino, G. Zheng, J. L. Sonnenberg, M. Hada, M. Ehara, K. Toyota, R. Fukuda, J. Hasegawa, M. Ishida, T. Nakajima, Y. Honda, O. Kitao, H. Nakai, T. Vreven, J. J. A. Montgomery, J. E. Peralta, F. Ogliaro, M. Bearpark, J. J. Heyd, E. Brothers, K. N. Kudin, V. N. Staroverov, R. Kobayashi, J. Normand, K. Raghavachari, A. Rendell, J. C. Burant, S. S. Iyengar, J. Tomasi, M. Cossi, N. Rega, J. M. Millam, M. Klene, J. E. Knox, J. B. Cross, V. Bakken, C. Adamo, J. Jaramillo, R. Gomperts, R. E. Stratmann, O. Yazyev, A. J. Austin, R. Cammi, C. Pomelli, J. W. Ochterski, R. L. Martin, K. Morokuma, V. G. Zakrzewski, G. A. Voth, P. Salvador, J. J. Dannenberg, S. Dapprich, A. D. Daniels, Ö. Farkas, J. B. Foresman, J. V. Ortiz, J. Cioslowski and D. J. Fox, *Gaussian 09, Revision B.01*, Gaussian Inc., Wallingford CT, 2009.
103. C. T. Lee, W. T. Yang and R. G. Parr, *Phys. Rev. B*, 1988, 37, 785-789.
104. A. V. Marenich, C. J. Cramer and D. G. Truhlar, *J. Phys. Chem. B*, 2009, 113, 6378-6396.
105. A. P. Scott and L. Radom, *J. Phys. Chem.*, 1996, 100, 16502-16513.
106. K. Wolinski, J. F. Hinton and P. Pulay, *J. Am. Chem. Soc.*, 1990, 112, 8251-8260.
107. H. J. C. Berendsen, D. Vanderspoel and R. Vandrunen, *Comput. Phys. Commun.*, 1995, 91, 43-56.
108. E. Lindahl, B. Hess and D. van der Spoel, *J. Mol. Model.*, 2001, 7, 306-317.
109. D. Van der Spoel, E. Lindahl, B. Hess, G. Groenhof, A. E. Mark and H. J. C. Berendsen, *J. Comput. Chem.*, 2005, 26, 1701-1718.
110. B. Hess, C. Kutzner, D. van der Spoel and E. Lindahl, *J. Chem. Theory Comput.*, 2008, 4, 435-447.
111. G. A. Kaminski, R. A. Friesner, J. Tirado-Rives and W. L. Jorgensen, *J. Phys. Chem. B*, 2001, 105, 6474-6487.

112. D. L. Cheung, S. J. Clark and M. R. Wilson, *Phys. Rev. E*, 2002, 65.
113. H. Hu, Z. Y. Lu and W. T. Yang, *J. Chem. Theory Comput.*, 2007, 3, 1004-1013.
114. G. Bussi, D. Donadio and M. Parrinello, *J. Chem. Phys.*, 2007, 126.
115. M. Parrinello and A. Rahman, *J. Appl. Phys.*, 1981, 52, 7182-7190.
116. T. Darden, D. York and L. Pedersen, *J. Chem. Phys.*, 1993, 98, 10089-10092.
117. U. Essmann, L. Perera, M. L. Berkowitz, T. Darden, H. Lee and L. G. Pedersen, *J. Chem. Phys.*, 1995, 103, 8577-8593.
118. B. Hess, *J. Chem. Theory Comput.*, 2008, 4, 116-122.
119. *CPMD V3.17 Copyright IBM Corp 1990-2013, Copyright MPI fuer Festkoerperforschung Stuttgart 1997-2001*,
120. A. D. Becke, *Phys. Rev. A*, 1988, 38, 3098-3100.
121. N. Sieffert, M. Bühl, M.-P. Gaigeot and C. A. Morrison, *J. Chem. Theory Comput.*, 2012, 9, 106-118.
122. A. Furmanchuk, O. Isayev, O. V. Shishkin, L. Gorb and J. Leszczynski, *Phys. Chem. Chem. Phys.*, 2010, 12, 3363-3375.
123. A. Furmanchuk, O. V. Shishkin, O. Isayev, L. Gorb and J. Leszczynski, *Phys. Chem. Chem. Phys.*, 2010, 12, 9945-9954.
124. S. Nose, *J. Chem. Phys.*, 1984, 81, 511-519.
125. W. G. Hoover, *Phys. Rev. A*, 1985, 31, 1695-1697.
126. G. J. Martyna, M. L. Klein and M. Tuckerman, *J. Chem. Phys.*, 1992, 97, 2635-2643.
127. R. Y. Dong, *Nuclear Magnetic Resonance of Liquid Crystals* Springer, New York, 2nd edn., 1997.
128. M. F. Sanner, A. J. Olson and J. C. Spohner, *Biopolymers*, 1996, 38, 305-320.
129. A. Bondi, *J. Phys. Chem.*, 1964, 68, 441-&.
130. R Core Team, *R: A language and environment for statistical computing*, R Foundation for Statistical Computing, Vienna, Austria, 2014, URL: <http://www.R-project.org/>
131. P. F. Bernath, *Spectra of Atoms and Molecules*, Oxford University Press, Oxford, 2005.
132. W. Humphrey, A. Dalke and K. Schulten, *J. Molec. Graphics*, 1996, 14, 33-38.

133. D. Jacquemin, E. Bremond, I. Ciofini and C. Adamo, *J. Phys. Chem. Lett.*, 2012, 3, 468-471.
134. A. D. Laurent, C. Adamo and D. Jacquemin, *Phys. Chem. Chem. Phys.*, 2014, 16, 14334-14356.
135. Z. K. Hu, M. Z. Xue, Q. Zhang, Q. R. Sheng and Y. G. Liu, *Dyes Pigm.*, 2008, 76, 173-178.
136. L. He, H. S. Freeman, L. H. Lu and S. F. Zhang, *Dyes Pigm.*, 2011, 91, 389-395.
137. J. E. Gautrot, P. Hodge, D. Cupertino and M. Helliwell, *New J. Chem.*, 2007, 31, 1585-1593.
138. D. Jacquemin, J. Preat, M. Charlot, V. Wathélet, J. M. Andre and E. A. Perpète, *J. Chem. Phys.*, 2004, 121, 1736-1743.
139. E. A. Perpète, V. Wathélet, J. Preat, C. Lambert and D. Jacquemin, *J. Chem. Theory Comput.*, 2006, 2, 434-440.
140. D. Jacquemin, E. Bremond, A. Planchat, I. Ciofini and C. Adamo, *J. Chem. Theory Comput.*, 2011, 7, 1882-1892.
141. M. A. Osman, L. Pietronero, T. J. Scheffer and H. R. Zeller, *J. Chem. Phys.*, 1981, 74, 5377-5383.
142. M. Matsui, K. Shirai, N. Tanaka, K. Funabiki, H. Muramatsu, K. Shibata, Y. Abe and Y. Ohgomori, *J. Mater. Chem.*, 1999, 9, 2755-2763.
143. M. Matsui, N. Tanaka, N. Andoh, K. Funabiki, K. Shibata, H. Muramatsu, Y. Ishigure, E. N. Kohyama, Y. Abe and M. Kaneko, *Chem. Mater.*, 1998, 10, 1921-1930.
144. D. H. Song and J. P. Kim, *Dyes Pigm.*, 2009, 80, 219-225.
145. M. Matsui, M. Suzuki, K. Mizuno, K. Funabiki, S. Okada, T. Kobayashi and M. Kadowaki, *Liq. Cryst.*, 2004, 31, 1463-1467.
146. H. Bloom, L. H. Briggs and B. Cleverley, *J. Chem. Soc.*, 1959, 178-185.
147. T. Hayashi and Tokumits.T, *Bull. Chem. Soc. Jpn.*, 1965, 38, 916-922.
148. S. N. Singh and R. S. Singh, *Spectrochim. Acta, Part A*, 1968, A 24, 1591-1597.
149. J. Spangetlarsen, D. H. Christensen and E. W. Thulstrup, *Spectrochim. Acta, Part A*, 1987, 43, 331-335.
150. B. Ball, X. F. Zhou and R. F. Liu, *Spectrochim. Acta, Part A*, 1996, 52, 1803-1814.

151. K. V. Berezin, T. V. Krivokhizhina and V. V. Nechaev, *Opt. Spectrosc.*, 2004, 97, 530-536.
152. S. H. Cho, H. Huh, H. M. Kim, N. J. Kim and S. K. Kim, *J. Chem. Phys.*, 2005, 122, 034305.
153. M. Umadevi and V. Ramakrishnan, *Spectrochim. Acta, Part A*, 2003, 59, 393-403.
154. S. W. Han, T. H. Ha, C. H. Kim and K. Kim, *Langmuir*, 1998, 14, 6113-6120.
155. K. D. Clerck, H. Rahier, B. V. Mele, P. Westbroek and P. Kiekens, *J. Appl. Polym. Sci.*, 2007, 106, 1648-1658.
156. D. Phillips, J. N. Moore and R. E. Hester, *J. Chem. Soc., Faraday Trans. 2*, 1986, 82, 2093-2104.
157. J. N. Moore, D. Phillips and R. E. Hester, *J. Phys. Chem.*, 1988, 92, 5619-5627.
158. E. Vauthey, D. Phillips and A. W. Parker, *J. Phys. Chem.*, 1992, 96, 7356-7360.
159. D. W. Cho, S. H. Kim, M. Yoon and S. C. Jeoung, *Chem. Phys. Lett.*, 2004, 391, 314-320.
160. O. F. Mohammed, D. Xiao, V. S. Batista and E. T. J. Nibbering, *J. Phys. Chem. A*, 2014, 118, 3090-3099.
161. C. Shao, Z. She, Z. Guo, H. Peng, X. Cai, S. Zhou, Y. Gu and Y. Lin, *Magn. Reson. Chem.*, 2007, 45, 434-438.
162. X.-K. Xia, H.-R. Huang, Z.-G. She, C.-L. Shao, F. Liu, X.-L. Cai, L. L. P. Vrijmoed and Y.-C. Lin, *Magn. Reson. Chem.*, 2007, 45, 1006-1009.
163. Y. Chen, X. Cai, J. Pan, J. Gao, J. Li, J. Yuan, L. Fu, Z. She and Y. Lin, *Magn. Reson. Chem.*, 2009, 47, 362-365.
164. C. Zhang, R. Wang, B. Liu and G. Tu, *Magn. Reson. Chem.*, 2011, 49, 529-532.
165. I. B. Rubin and M. V. Buchanan, *Magn. Reson. Chem.*, 1985, 23, 161-165.
166. R. Sieckmann, *Magn. Reson. Chem.*, 1991, 29, 264-266.
167. K. Danielsen, G. W. Francis and D. W. Aksnes, *Magn. Reson. Chem.*, 1996, 34, 1043-1045.
168. R. K. Harris, P. Jonsen and K. J. Packer, *Org. Magn. Resonance.*, 1984, 22, 784-788.
169. K. Danielsen, *Magn. Reson. Chem.*, 1995, 33, 823-826.

170. B. V. R. Murty, *Z. Kristallogr.*, 1959, 133, 445-465.
171. A. Prakash, *Acta Crystallogr.*, 1967, 22, 439-&.
172. L. C. Abbott, S. N. Batchelor and J. N. Moore, *J. Phys. Chem. A*, 2013, 117, 1853-1871.
173. Q. H. Meng, W. B. Zhang, Y. F. Yu and D. Y. Huang, *Dyes Pigm.*, 2005, 65, 281-283.
174. I. Yoon, K. M. Park, S. S. Lee, G. Choi and J. S. Lee, *Anal. Sci.*, 2001, 17, 1355-1356.
175. D. Jacquemin, X. Assfeld, J. Preat and E. A. Perpète, *Mol. Phys.*, 2007, 105, 325-331.
176. D. Jacquemin, V. Wathelet, J. Preat and E. A. Perpète, *Spectrochim. Acta, Part A*, 2007, 67, 334-341.
177. B. Bahadur, R. K. Sarna and V. G. Bhide, *Mol. Cryst. Liq. Cryst.*, 1981, 75, 121-132.
178. M. Villanueva-García, A. Martínez-Richa and J. Robles, *Mol. Cryst. Liq. Cryst.*, 2006, 446, 245-254.
179. J. B. Chang, J. H. Hwang, J. S. Park and J. P. Kim, *Dyes Pigm.*, 2011, 88, 366-371.
180. J. B. Chang, S. B. Yuk, J. S. Park and J. P. Kim, *Dyes Pigm.*, 2012, 92, 737-744.
181. A. Stroobants, H. N. W. Lekkerkerker and D. Frenkel, *Phys. Rev. A*, 1987, 36, 2929-2945.
182. J. A. C. Veerman and D. Frenkel, *Phys. Rev. A*, 1991, 43, 4334-4343.
183. A. Poniewierski, *Phys. Rev. A*, 1992, 45, 5605-5613.
184. J. T. Brown, M. P. Allen, E. Martín del Río and E. de Miguel, *Phys. Rev. E*, 1998, 57, 6685-6699.
185. J. Pelaez and M. Wilson, *Phys. Chem. Chem. Phys.*, 2007, 9, 2968-2975.
186. J. W. Goodby, I. M. Saez, S. J. Cowling, J. S. Gasowska, R. A. MacDonald, S. Sia, P. Watson, K. J. Toyne, M. Hird, R. A. Lewis, S. E. Lee and V. Vaschenko, *Liq. Cryst.*, 2009, 36, 567-605.
187. Y. Olivier, L. Muccioli and C. Zannoni, *ChemPhysChem*, 2014, 15, 1345-1355.

188. O. M. Roscioni, L. Muccioli, R. G. Della Valle, A. Pizzirusso, M. Ricci and C. Zannoni, *Langmuir*, 2013, 29, 8950-8958.
189. P. W. Hart and A. W. Rudie, *Tappi J.*, 2014, 13, 23-31.
190. B. Alberts, A. Johnson, J. Lewis, M. Raff, K. Roberts and P. Walter, *Molecular Biology of the Cell*, Garland Science, New York, 5th edn., 2008.
191. A. Joy, A. K. Ghosh and G. B. Schuster, *J. Am. Chem. Soc.*, 2006, 128, 5346-5347.
192. A. Joy and G. B. Schuster, *Chem. Commun.*, 2005, 2778-2784.
193. P. S. Guin, S. Das and P. C. Mandal, *Int. J. Electrochem.*, 2011, 2011, 22.
194. M. Shamsipur, A. Siroueinejad, B. Hemmateenejad, A. Abbaspour, H. Sharghi, K. Alizadeh and S. Arshadi, *J. Electroanal. Chem.*, 2007, 600, 345-358.
195. A. Sarapuu, K. Vaik, D. J. Schiffrin and K. Tammeveski, *J. Electroanal. Chem.*, 2003, 541, 23-29.
196. D. Jeziorek, T. Ossowski, A. Liwo, D. Dyl, M. Nowacka and W. Woznicki, *J. Chem. Soc., Perkin Trans. 2*, 1997, 229-236.
197. L. Ebersson and M. P. Hartshorn, *J. Chem. Soc., Perkin Trans. 2*, 1996, 151-154.
198. S. Palaniappan and P. Manisankar, *J. Polym. Res.*, 2011, 18, 311-317.
199. W. A. Badawy, K. M. Ismail and S. S. Medany, *Int. J. Chem. Kinet.*, 2011, 43, 141-146.
200. K. M. Ismail, Z. M. Khalifa, M. A. Azzem and W. A. Badawy, *Electrochim. Acta*, 2002, 47, 1867-1873.
201. M. Shamsipur, K. Alizadeh and S. Arshadi, *J. Mol. Struct.: Theochem*, 2006, 758, 71-74.
202. R. N. Capps and M. Vala, *Photochem. Photobiol.*, 1981, 33, 673-682.
203. K. E. Drabe, H. Veenvliet and D. A. Wiersma, *Chem. Phys. Lett.*, 1975, 35, 469-474.
204. N. S. Allen and J. F. McKellar, *J. Photochem.*, 1976, 5, 317-320.
205. A. N. Diaz, *J. Photochem. Photobiol. A*, 1990, 53, 141-167.
206. N. S. Allen, P. Bentley and J. F. McKellar, *J. Photochem.*, 1976, 5, 225-231.
207. S. R. Flom and P. F. Barbara, *J. Phys. Chem.*, 1985, 89, 4489-4494.

208. M. H. Vanbenthem and G. D. Gillispie, *J. Phys. Chem.*, 1984, 88, 2954-2960.
209. D. K. Palit, H. Pal, T. Mukherjee and J. P. Mittal, *J. Chem. Soc., Faraday Trans.*, 1990, 86, 3861-3869.
210. T. Yatsushashi and H. Inoue, *J. Phys. Chem. A*, 1997, 101, 8166-8173.
211. H. Pal, D. K. Palit, T. Mukherjee and J. P. Mittal, *J. Chem. Soc., Faraday Trans.*, 1993, 89, 683-691.
212. K. Tickle and F. Wilkinson, *Trans. Faraday Soc.*, 1965, 61, 1981-1990.
213. S. A. Carlson and D. M. Hercules, *Photochem. Photobiol.*, 1973, 17, 123-131.
214. H. Görner, *Photochem. Photobiol.*, 2003, 77, 171-179.
215. T. Kausche, J. Sauberlich, E. Trobitsch, D. Beckert and K. P. Dinse, *Chem. Phys.*, 1996, 208, 375-390.
216. D. K. Palit, H. Pal, T. Mukherjee and J. P. Mittal, *J. Photochem. Photobiol. A*, 1990, 52, 375-390.
217. *CRC Handbook of Chemistry and Physics*, CRC Press, Boca Raton, 71st edn., 1990.
218. M. Bailey and C. J. Brown, *Acta Crystallogr.*, 1966, 22, 488-492.
219. P. Zanello, *Inorganic Electrochemistry*, The Royal Society of Chemistry, Cambridge, 2003.
220. M. Shamsipur, B. Hemmateenejad, A. Babaei and L. Faraj-Sharabiani, *J. Electroanal. Chem.*, 2004, 570, 227-234.
221. C. Q. Bullivant, PhD thesis, University of York, 2010.
222. K. Alizadeh and M. Shamsipur, *J. Mol. Struct.: Theochem.*, 2008, 862, 39-43.
223. M. W. Lehmann and D. H. Evans, *J. Electroanal. Chem.*, 2001, 500, 12-20.
224. J. Pommerehne, H. Vestweber, W. Guss, R. F. Mahrt, H. Bässler, M. Porsch and J. Daub, *Adv. Mater.*, 1995, 7, 551-554.
225. M. Thelakkat and H.-W. Schmidt, *Adv. Mater.*, 1998, 10, 219-223.
226. L. V. Brownell, K. A. Robins, Y. Jeong, Y. Lee and D. C. Lee, *J. Phys. Chem. C.*, 2013, 117, 25236-25247.
227. P. J. Homnick, J. S. Tinkham, R. Devaughn and P. M. Lahti, *J. Phys. Chem. A*, 2013, 118, 475-486.

228. K. Toda, S. Nagaura, T. Watanabe, M. Sukigara and K. Honda, *Nippon Kagaku Kaishi*, 1975, 459-462.
229. H. Seki, T. Uchida and Y. Shibata, *Mol. Cryst. Liq. Cryst.*, 1986, 138, 349-365.
230. V. G. Gregoriou, S. Tzavalas and S. T. Bollas, *Appl. Spectrosc.*, 2004, 58, 655-661.
231. E. Libowitzky and G. R. Rossman, *Phys. Chem. Miner.*, 1996, 23, 319-327.
232. J. B. Benedict, J. H. Freudenthal, E. Hollis and B. Kahr, *J. Am. Chem. Soc.*, 2008, 130, 10714-10719.
233. E. P. Raynes, personal communication.
234. P. Photinos, in *Liquid Crystals Experimental Study of Physical Properties and Phase Transitions*, Ed. S. Kumar, Cambridge University Press, Cambridge, 2011, pp. 95-154.
235. M. R. Wilson, *Chem. Soc. Rev.*, 2007, 36, 1881-1888.
236. C. Zannoni, *J. Mater. Chem.*, 2001, 11, 2637-2646.
237. M. Allen and M. Wilson, *J. Comput. Aided Mol. Des.*, 1989, 3, 335-353.
238. J. G. Gay and B. J. Berne, *J. Chem. Phys.*, 1981, 74, 3316-3319.
239. J. M. Ilnytskyi, A. Trokhymchuk and M. Schoen, *J. Chem. Phys.*, 2014, 141, 114903.
240. J. K. Whitmer, X. Wang, F. Mondiot, D. S. Miller, N. L. Abbott and J. J. de Pablo, *Phys. Rev. Lett.*, 2013, 111, 227801.
241. Z. Wang, J. A. Lupo, S. Patnaik and R. Pachter, *Comput. Theor. Polym. Sci.*, 2001, 11, 375-387.
242. A. J. McDonald, S. Hanna and H. H. Wills, *Mol. Cryst. Liq. Cryst.*, 2004, 413, 135-144.
243. A. J. McDonald and S. Hanna, *J. Chem. Phys.*, 2006, 124, 164906.
244. G. Tiberio, L. Muccioli, R. Berardi and C. Zannoni, *ChemPhysChem*, 2009, 10, 125-136.
245. M. F. Palermo, A. Pizzirusso, L. Muccioli and C. Zannoni, *J. Chem. Phys.*, 2013, 138.
246. A. Pizzirusso, R. Berardi, L. Muccioli, M. Ricci and C. Zannoni, *Chem. Sci.*, 2012, 3, 573-579.

247. M. Bizzarri, L. Cacelli, G. Prampolini and A. Tani, *J. Phys. Chem. A*, 2004, 108, 10336-10341.
248. I. Cacelli, L. De Gaetani, G. Prampolini and A. Tani, *J. Phys. Chem. B*, 2007, 111, 2130-2137.
249. M. Cifelli, L. De Gaetani, G. Prampolini and A. Tani, *J. Phys. Chem. B*, 2008, 112, 9777-9786.
250. L. De Gaetani and G. Prampolini, *Soft Matter*, 2009, 5, 3517-3526.
251. M. R. Wilson, *J. Mol. Liq.*, 1996, 68, 23-31.
252. C. McBride, M. R. Wilson and J. A. K. Howard, *Mol. Phys.*, 1998, 93, 955-964.
253. D. L. Cheung, S. J. Clark and M. R. Wilson, *Chem. Phys. Lett.*, 2002, 356, 140-146.
254. D. L. Cheung, S. J. Clark and M. R. Wilson, *J. Chem. Phys.*, 2004, 121, 9131-9139.
255. E. D. Gerts, A. V. Komolkin, V. A. Burmistrov, V. V. Alexandriysky and S. V. Dvinskikh, *J. Chem. Phys.*, 2014, 141, 074503.
256. V. S. Oganessian, E. Kuprusevicius, H. Gopee, A. N. Cammidge and M. R. Wilson, *Phys. Rev. Lett.*, 2009, 102, 013005.
257. A. Pizzirusso, M. B. Di Cicco, G. Tiberio, L. Muccioli, R. Berardi and C. Zannoni, *J. Phys. Chem. B*, 2012, 116, 3760-3771.
258. A. C. J. Weber, A. Pizzirusso, L. Muccioli, C. Zannoni, W. L. Meerts, C. A. de Lange and E. E. Burnell, *J. Chem. Phys.*, 2012, 136, 174506.
259. A. Pizzirusso, M. E. Di Pietro, G. De Luca, G. Celebre, M. Longeri, L. Muccioli and C. Zannoni, *ChemPhysChem*, 2014, 15, 1356-1367.
260. E. Kuprusevicius, R. Edge, H. Gopee, A. N. Cammidge, E. J. L. McInnes, M. R. Wilson and V. S. Oganessian, *Chem. - Eur. J.*, 2010, 16, 11558-11562.
261. F. Chami, M. R. Wilson and V. S. Oganessian, *Soft Matter*, 2012, 8, 6823-6833.
262. L. Cwiklik, A. J. A. Aquino, M. Vazdar, P. Jurkiewicz, J. Pittner, M. Hof and H. Lischka, *J. Phys. Chem. A*, 2011, 115, 11428-11437.
263. I. Hurjui, A. Neamtu and D. O. Dorohoi, *J. Mol. Struct.*, 2013, 1044, 134-139.
264. J. R. Robalo, A. M. T. M. do Canto, A. J. P. Carvalho, J. P. P. Ramalho and L. M. S. Loura, *J. Phys. Chem. B*, 2013, 117, 5806-5819.

265. M. G. Clark, E. P. Raynes, R. A. Smith and R. J. A. Tough, *J. Phys. D: Appl. Phys.*, 1980, 13, 2151-2164.
266. A. D. Remenyuk, E. V. Astrova, R. F. Vitman, T. S. Perova and V. A. Tolmachev, *Proc. SPIE*, 2005, 5825, 400-407.
267. G. Y. Kim and C. H. Kwak, *Opt. Commun.*, 2011, 284, 5157-5163.
268. B. Bahadur, R. K. Sarna and V. G. Bhide, *Mol. Cryst. Liq. Cryst.*, 1982, 72, 139-145.
269. F. Würthner, T. E. Kaiser and C. R. Saha-Möller, *Angew. Chem. Int. Ed.*, 2011, 50, 3376-3410.
270. P. V. Soroka, V. M. Pergamenschchik, O. P. Boiko, Y. L. Slominskiy, V. Y. Gayvoronsky, L. N. Lisetski, S. V. Yakunin and V. G. Nazarenko, *Mol. Cryst. Liq. Cryst.*, 2014, 589, 96-104.
271. A. G. Gilani, M. Salmanpour and T. Ghorbanpour, *J. Mol. Liq.*, 2013, 179, 118-123.
272. A. Ghanadzadeh, A. Zeini, A. Kashef and M. Moghadam, *Spectrochim. Acta, Part A*, 2009, 73, 324-329.
273. A. Y. G. Fuh, K. L. Huang, C. H. Lin, H. C. Lin and I. M. Jiang, *Chinese J. Phys.*, 1990, 28, 551-557.
274. G. Celebre, G. De Luca, M. Longeri, D. Catalano, C. A. Veracini and J. W. Emsley, *J. Chem. Soc., Faraday Trans.*, 1991, 87, 2623-2627.
275. M. T. Sims, L. C. Abbott, S. J. Cowling, J. W. Goodby and J. N. Moore, *Chem. - Eur. J.*, 2015, 21, 10123-10130.
276. B. Bahadur, *Mol. Cryst. Liq. Cryst.*, 1991, 209, 39-61.
277. C. A. Veracini and G. N. Shilstone, in *The Molecular Dynamics of Liquid Crystals*, Eds. G. R. Luckhurst and C. A. Veracini, Springer, New York, 1994, pp. 257-270.
278. E. E. Burnell and C. A. de Lange, *Chem. Rev.*, 1998, 98, 2359-2387.
279. D. A. Dunmur and K. Toriyama, in *Handbook of Liquid Crystals*, Eds. D. Demus, J. W. Goodby, G. W. Gray, H. W. Spiess and V. Vill, Wiley-VCH, Weinheim, 1998, vol. 1, pp. 253-280.
280. D. A. Dunmur and K. Toriyama, in *Physical Properties of Liquid Crystals*, Eds. D. Demus, J. W. Goodby, G. W. Gray, H. W. Spiess and V. Vill, Wiley-VCH, Weinheim, 1999, pp. 87-112.

281. G. R. Luckhurst, in *Biaxial Nematic Liquid Crystals*, Eds. G. R. Luckhurst and S. T. J., Wiley, United Kingdom, 2015, pp. 25-54.
282. C. Zannoni, in *Nuclear Magnetic Resonance of Liquid Crystals*, Ed. J. W. Emsley, D. Reidel Publishing Company, Dordrecht, 1985, pp. 1-34.
283. M. van Gurp, H. van Langen, G. van Ginkel and Y. K. Levine, in *Polarized Spectroscopy of Ordered Systems*, Eds. B. Samori and E. W. Thulstrup, Kluwer, The Netherlands, 1987, pp. 455-490.
284. M. G. Clark and F. C. Saunders, *Mol. Cryst. Liq. Cryst.*, 1982, 82, 267-276.
285. R. Kiefer and G. Baur, *Mol. Cryst. Liq. Cryst.*, 1989, 174, 101-126.
286. J. M. Anderson, *J. Magn. Reson.*, 1971, 4, 231-235.
287. T. C. Wong and E. E. Burnell, *J. Magn. Reson.*, 1976, 22, 227-234.
288. E. T. Samulski, *Ferroelectrics*, 1980, 30, 83-93.
289. H. Fujiwara, N. Shimizu, T. Takagi and Y. Sasaki, *Bull. Chem. Soc. Jpn.*, 1985, 58, 2285-2288.
290. H. Fujiwara, M. Watanabe and Y. Sasaki, *Bull. Chem. Soc. Jpn.*, 1988, 61, 1091-1094.
291. Y. P. Lee and D. F. R. Gilson, *J. Chem. Phys.*, 1979, 70, 2042-2044.
292. A. L. Segre and S. Castellano, *J. Magn. Reson.*, 1972, 7, 5-17.
293. J. C. T. Rendell, D. S. Zimmerman, A. J. van der Est and E. E. Burnell, *Can. J. Chem.*, 1997, 75, 1156-1161.
294. A. J. van der Est, M. Y. Kok and E. E. Burnell, *Mol. Phys.*, 1987, 60, 397-413.
295. D. S. Zimmerman and E. E. Burnell, *Mol. Phys.*, 1993, 78, 687-702.
296. D. S. Zimmerman and E. E. Burnell, *Mol. Phys.*, 1990, 69, 1059-1071.
297. A. Ferrarini, G. J. Moro, P. L. Nordio and G. R. Luckhurst, *Mol. Phys.*, 1992, 77, 1-15.
298. S. V. Burylov and Y. L. Raikher, *Phys. Lett. A*, 1990, 149, 279-283.
299. A. Ferrarini, G. R. Luckhurst, P. L. Nordio and S. J. Roskilly, *J. Chem. Phys.*, 1994, 100, 1460-1469.
300. L. Feltre, A. Ferrarini, F. Pacchiale and P. L. Nordio, *Mol. Cryst. Liq. Cryst.*, 1996, 290, 109-118.

301. A. Ferrarini, G. J. Moro and P. L. Nordio, in *Physical Properties of Liquid Crystals: Nematics.*, Eds. D. A. Dunmur, A. Fukuda and G. R. Luckhurst, IET, London, 2001, pp. 103-112.
302. A. Ferrarini and P. L. Nordio, *J. Chem. Soc., Perkin Trans. 2*, 1998, 455-460.
303. A. Ferrarini, G. J. Moro and P. L. Nordio, *Phys. Rev. E*, 1996, 53, 681-688.
304. C. Benzi, M. Cossi, V. Barone, R. Tarroni and C. Zannoni, *J. Phys. Chem. B*, 2005, 109, 2584-2590.
305. A. Ferrarini, F. Janssen, G. J. Moro and P. L. Nordio, *Liq. Cryst.*, 1999, 26, 201-210.
306. R. Tarroni and C. Zannoni, *J. Phys. Chem.*, 1996, 100, 17157-17165.
307. J. Greer and B. L. Bush, *Proc. Natl. Acad. Sci. USA.*, 1978, 75, 303-307.
308. M. L. Connolly, *J. Appl. Crystallogr.*, 1983, 16, 548-558.
309. Y. N. Vorobjev and J. Hermans, *Biophys. J.*, 1997, 73, 722-732.
310. R. Berardi, L. Muccioli and C. Zannoni, *ChemPhysChem*, 2004, 5, 104-111.
311. F. Steiner, S. Bange, J. Vogelsang and J. M. Lupton, *J. Phys. Chem. Lett.*, 2015, 6, 999-1004.
312. M. Schmitt, D. Krugler, M. Bohm, C. Ratzer, V. Bednarska, I. Kalkman and W. Leo Meerts, *Phys. Chem. Chem. Phys.*, 2006, 8, 228-235.
313. M. Linke, A. Lauer, T. von Haimberger, A. Zacarias and K. Heyne, *J. Am. Chem. Soc.*, 2008, 130, 14904-14905.
314. M. Theisen, M. Linke, M. Kerbs, H. Fidder, M. E.-A. Madjet, A. Zacarias and K. Heyne, *J. Chem. Phys.*, 2009, 131, 124511.
315. C. Brand, W. L. Meerts and M. Schmitt, *J. Phys. Chem. A*, 2011, 115, 9612-9619.
316. J. A. Dickinson, M. R. Hockridge, R. T. Kroemer, E. G. Robertson, J. P. Simons, J. McCombie and M. Walker, *J. Am. Chem. Soc.*, 1998, 120, 2622-2632.
317. P. W. Joireman, R. T. Kroemer, D. W. Pratt and J. P. Simons, *J. Chem. Phys.*, 1996, 105, 6075-6077.
318. J. A. Dickinson, P. W. Joireman, R. T. Kroemer, E. G. Robertson and J. P. Simons, *J. Chem. Soc., Faraday Trans.*, 1997, 93, 1467-1472.
319. G. J. Kruger, *Phys. Rep.*, 1982, 82, 229-269.

320. G. K. Batchelor, *An Introduction to Fluid Dynamics*, Cambridge University Press, Cambridge, 2002.
321. N. H. Bakker, P. J. F. M. Lohuis, D. J. Menger, G. J. N. Trenité, W. J. Fokkens and C. A. Grimbergen, *Laryngoscope*, 2005, 115, 1809-1812.
322. J. Liang, S. Cheng, J. Hou, Z. Xu and Y.-L. Zhao, *Sci. China Chem.*, 2012, 55, 2081-2088.
323. N. A. Murugan, P. Chandra Jha and H. Ågren, *Phys. Chem. Chem. Phys.*, 2009, 11, 6482-6489.
324. B. Dutta, T. Tanaka, A. Banerjee and J. Chowdhury, *J. Phys. Chem. A*, 2013, 117, 4838-4850.
325. N. A. Murugan and H. Ågren, *J. Phys. Chem. A*, 2009, 113, 2572-2577.
326. N. A. Murugan, Z. Rinkevicius and H. Ågren, *J. Phys. Chem. A*, 2009, 113, 4833-4839.
327. N. A. Murugan, P. C. Jha, Z. Rinkevicius, K. Ruud and H. Ågren, *J. Chem. Phys.*, 2010, 132, 234508.
328. N. A. Murugan, S. Chakrabarti and H. Ågren, *J. Phys. Chem. B*, 2011, 115, 4025-4032.
329. N. A. Murugan, J. Kongsted, Z. Rinkevicius, K. Aidas and H. Ågren, *J. Phys. Chem. B*, 2010, 114, 13349-13357.
330. N. A. Murugan, Z. Rinkevicius and H. Ågren, *Int. J. Quantum Chem.*, 2011, 111, 1521-1530.
331. A. Ferrarini, G. Gottarelli, P. L. Nordio and G. P. Spada, *J. Chem. Soc., Perkin Trans. 2*, 1999, 411-417.
332. S. Imazeki, M. Kaneko, T. Ozawa and A. Mukoh, *Mol. Cryst. Liq. Cryst.*, 1988, 159, 219-231.
333. A. V. Ivashchenko, V. T. Lazareva, E. K. Prudnikova, V. G. Romyantsev and V. V. Titov, *Mol. Cryst. Liq. Cryst.*, 1985, 129, 259-266.
334. A. V. Ivashchenko, V. T. Lazareva, E. K. Prudnikova, V. G. Romyantsev and V. V. Titov, *Mol. Cryst. Liq. Cryst.*, 1985, 129, 267-275.
335. A. V. Ivashchenko, V. T. Lazareva, E. K. Prudnikova, V. G. Romyantsev and V. V. Titov, *Mol. Cryst. Liq. Cryst.*, 1985, 129, 277-283.
336. M. Matsui, Y. Sumiya, K. Shibata, H. Muramatsu, Y. Abe and M. Kaneko, *Liq. Cryst.*, 1997, 23, 821-832.

337. G. Celebre, G. De Luca and M. Longeri, *Phys. Chem. Chem. Phys.*, 2000, 2, 1883-1888.
338. S. Pestov and V. Vill, in *Springer Handbook of Condensed Matter and Materials Data*, Eds. W. Martienssen and H. Warlimont, Springer, Berlin 2005, p. 975.
339. A. V. Ivashchenko, O. S. Petrova and V. V. Titov, *Mol. Cryst. Liq. Cryst.*, 1984, 108, 51-60.
340. M. R. Wilson, *Liq. Cryst.*, 1996, 21, 437-447.
341. D. J. Earl and M. R. Wilson, *J. Chem. Phys.*, 2003, 119, 10280-10288.
342. A. Ferrarini and G. J. Moro, in *NMR of Ordered Liquids*, Eds. E. E. Burnell and C. A. de Lange, Springer, New York, 1997, pp. 241-258.
343. H. Kamberaj, R. J. Low and M. P. Neal, *Mol. Phys.*, 2006, 104, 335-357.
344. M. E. Rose, *Elementary Theory of Angular Momentum*, John Wiley and Sons Inc., New York, 1963.
345. L. J. Mueller, *Concepts Magn. Reson., Part A*, 2011, 38A, 221-235.